Title
Chemical Purity Analysis of PET Radiotracers via Microchip Capillary Electrophoresis

Author
Ly, Jimmy

Publication Date
2016

Peer reviewed|Thesis/dissertation

UNIVERSITY OF CALIFORNIA

Los Angeles

Chemical Purity Analysis of PET Radiotracers via Microchip Capillary Electrophoresis

A dissertation submitted in partial satisfaction of the requirements for the degree Doctor of Philosophy in Biomedical Engineering

by

Jimmy Ly

2016

ABSTRACT OF THE DISSERTATION

Chemical Purity Analysis of PET Radiotracers

via Microchip Capillary Electrophoresis

by

Jimmy Ly

Doctor of Philosophy in Biomedical Engineering

University of California, Los Angeles, 2016

Professor Robert Michael van Dam, Chair

Production of a positron emission tomography (PET) tracer involves three stages: production of the radioisotope, radio-labeling and purification of the tracer, and quality control (QC) testing of the final product (if the tracer is used in humans). Though the production of the positron-emitting radioisotope requires expensive and complex instrumentation (e.g. cyclotron or generator), in many cases, the radioisotope can simply be obtained from a commercial source. The radio-labeling and purification step is performed by machines called radiosynthesizers, which perform chemical synthesis and purification processes in a remote-controlled or automated manner within radiation-shielded “hot cells”. Quality control testing is performed to ensure each batch of radiopharmaceutical is safe prior to use in human subjects, and requires several analytical chemistry instruments. Though a couple of PET tracers are routinely available

in final form from commercial sources, most other tracers need to be specially manufactured and quality tested at the researcher's facility.

Advances in radiosynthesizer technology such as automation, programmability, and reagent kits simplify the production of diverse tracers. Furthermore, recent efforts in miniaturized synthesizers based on microfluidics aim to reduce equipment cost, shielding and lab space needs, and quantities of expensive reagents, to make it more affordable to produce custom batches of PET tracers on demand.

In the context of these emerging technologies, quality control testing still remains a bottleneck due to the high cost of the many expensive instruments, specially-trained staff, and documentation needed to determine the purity and ensure the levels of all potential contaminants are below acceptable limits. Several companies are developing automated systems for quality control testing to alleviate some of these issues. However, high cost and large size remain obstacles. We have therefore explored the use of microfluidic analytical chemistry techniques to address these remaining critical issues. In this dissertation, the feasibility of using capillary electrophoresis (CE) to analyze the chemical purity of PET tracers is investigated as a compact and inexpensive replacement for high performance liquid chromatography (HPLC) and other techniques that are normally used for this purpose. After establishing that CE has sufficient performance (comparable to HPLC) using several example chemical systems, the design, development, and characterization of a microscale chemical purity testing system are presented, along with a discussion of its capabilities and limitations. Overall, it appears that microchip CE could be used instead of HPLC for performing many of the required QC tests of PET tracers.

The dissertation of Jimmy Ly is approved.

Jacob J. Schmidt

Dino Di Carlo

Seyed Sam Sadeghi Hosseini

Robert Michael van Dam, Committee Chair

University of California, Los Angeles

2016

Contents

LIST OF FIGURES

List of Tables

ACKNOWLEDGEMENTS

I want to thank all of my fellow lab members in the Mike van Dam lab, whether past or present: Dr. Mark Lazari and Dr. Helen Ma for their comradery over many years; Dr. Gaurav Shah, Dr. Tim Tseng, and John Ding for assisting me in the development microchip fabrication; Henry Herman for his great electrical engineering knowledge; Kevin Quinn for his vast computer knowledge; Dr. Uday Tata for teaching me soft lithography; Dr. Shilin Cheung for her guidance throughout my PhD. journey; Prof. Sam Sadeghi for his great mentorship and guidance in academics, engineering, and life; Dr. Maxim Sergeev for his assistance and instruction on the organic synthesis side of PET tracer production; Jeffrey Collins for help with radiosynthesis related questions; Steven Pan for his hard work and dedication to the lab and sense of humor; our new graduate students Philip Chao, Jia Wang, and Noel Ha for their warm and kind friendship.

I want to thank Dr. Joseph A. Loo and Dr. Rachel Loo of the Biological Chemistry Department for allowing us to use their commercial CE system (Beckman Coulter PA 800 plus).

I want to thank the administrative team: Sandy Ma, Karen Lum, and Erika Corrin for all their help with purchase orders, room reservations, and all other “behind the scene” issues; Larry Nadeau and Anne-Marie Dieters for their administrative work with the Bioengineering Department; Stacey Chiong and Jessica Kim for their help with payroll and parking.

I want to give a special thanks to my family and friends who have stood by me through this doctoral degree. Specifically, to my brother Sammy Ly always making me proud of his accomplishment. To my best friend, Linda La, who has constantly and

unconditionally stood by me though the highs and lows, and for your strength and support I needed to make it to this point. To my mom, Lynn Ho, for all her support and for being an amazing mother. To my dad, Ty Ly, for always making sure I'm well and good and for his strict and stern guidance.

Finally, I want to thank my doctoral committee, with whom I have been able to establish a dissertation worthy of coming from both the Bioengineering and Pharmacology Departments of UCLA and to obtain my doctoral degree: Prof. Jacob Schmidt, Prof. Dino Di Carlo, Prof. Sam Sadeghi for their numerous avenues of assistance provided during my doctoral degree; and to Prof. Mike van Dam for his unwavering mentorship and guidance throughout my doctoral work. I am very fortunate to have Mike as a mentor and boss, but also a friend, and for allowing me the freedom to learn and test my boundaries, while always making sure I am goal oriented. I would not have made it without his help and tremendous support.

Portions of Chapter 2: Separation of PET Tracers and Impurities Using CE are taken from:

S. Cheung, J. Ly, M. Lazari, S. Sadeghi, P. Y. Keng, and R. M. van Dam, “The separation and detection of PET tracers via capillary electrophoresis for chemical identity and purity analysis,” Journal of Pharmaceutical and Biomedical Analysis, vol. 94, pp. 12–18, Jun. 2014.

Portions of Chapter 3: Limit of Detection of Capillary Electrophoresis System are taken from:

S. Cheung, J. Ly, M. Lazari, S. Sadeghi, P. Y. Keng, and R. M. van Dam, “The separation and detection of PET tracers via capillary electrophoresis for chemical identity and purity analysis,” Journal of Pharmaceutical and Biomedical Analysis, vol. 94, pp. 12–18, Jun. 2014.

Chapter 4: Integrated Microchip Capillary Electrophoresis Device is a modified version of a manuscript in progress.

Chapter 5: Hybrid MCE Device Optimizations and Future Work is a modified version of a manuscript in progress.

VITA

EDUCATION

M.S. in Biomedical Engineering, University of California Los Angeles, Los Angeles, CA.
Fall 2008 – Spring 2010**;** Graduating GPA: 3.33

B.S. in Physics with minor Mathematics, San Jose State University, San Jose, CA.
Fall 1999 – Spring 2004**;** Graduated Cum Laude (GPA 3.67)

SELECTED JOURNAL PUBLICATIONS

J. Ly, et al., "Fixed Volume Capillary Electrophoresis Injection Chip," In Progress.

S. Cheung, **J. Ly**, M. Lazari, S. Sadeghi, PY. Keng, RM. van Dam, "The separation and detection of PET tracers via capillary electrophoresis for chemical identity and purity analysis," Journal of Pharmaceutical and Biomedical Analysis, vol. 94, pp. 12–18, Jun. 2014.

J. Ly, M. Masterman-Smith, R. Ramakrishnan, J. Sun, B. Kokobun, RM. van Dam, "Automated Reagent-Dispensing System for Microfludic Cell Biology Assays," Journal of Laboratory Automation, vol. 18, pp. 530-541, Dec. 2013

S. Sadeghi, V. Liang, S. Cheung, S. Woo, C, Wu, **J. Ly**, Y. Deng, M. Eddings, RM. van Dam, "Reusable electrochemical cell for rapid separation of [18F]fluoride from [18O]water for flow-through synthesis of 18F-labeled tracers," Applied Radiation and Isotope, vol. 75, pp. 85-94, May 2013

K. Parvin, J. Ma, **J. Ly**, X.C. Sun, D.E. Nikles, K. Sun, L.M. Wang, "Synthesis and Magnetic of Monodisperse Fe3O4," Journal of Applied Physics, vol. 95, pp. 7121-7123, June 2004

X.C. Sun, K. Parvin, **J. Ly**, D.E. Nikles, "Magnetic Properties of mixtures of two nanosized CO-S poders produced by hydrothermal reduction," IEEE Transactions on Magnetics, vol. 39, pp. 2678-2680, Sep 2003

SELECTED CONFERENCE PROCEEDINGS AND ABSTRACTS

J. Ly, S. Cheung, R. M. van Dam. Micromolar Detection of Analytes via sub-300 nm UV Absorbance in a PDMS Microchip Capillary Electrophoresis Device. Proceedings of the 6th International Symposium on Microchemistry and Microsystems, pg 222-223. July 2014; Singapore.

S. Sadeghi, **J. Ly**, Y. Deng, N. Satyamurthy, RM. van Dam, "Electrochemical micro flow cell for rapid PET tracer synthesis," Journal of Nuclear Medicine, vol. 52 (Supplement 1), pp. 286, May 2011

S. Sadeghi, **J. Ly**, Y. Deng, R. M. van Dam, "A robust platinum-based electrochemical micro flow cell for drying of [18F] fluoride for PET tracer synthesis," Proceedings of the 14th International Conference on Miniaturized Systems for Chemistry and Life Sciences, pg 1010-1012. Oct 2010; Netherlands

1 Chapter 1: Introduction

1.1 Positron emission tomography

1.1.1 Background

In recent years, positron emission tomography (PET) has become an important nuclear medicine imaging technique used in the diagnosis and staging of patients with cancer, along with other applications such as neuroimaging, drug discovery and development, and the study of cardiovascular diseases [1]–[6]. PET images provides functional and metabolic information about actual biological processes that can used for diagnostics, subtyping of diseases (to aid in therapy selection), and early monitoring of response to treatment. In comparison, X-ray computed tomography (CT) and magnetic resonance imaging (MRI) provide primarily structural information. Often, CT or MRI structural images are combined with the PET image to pinpoint the anatomical location of metabolic abnormalities [7], providing a more holistic view of disease, treatment, and overall biological process [1].

PET depends on the detection of pairs of gamma rays produced in relation to the positron-decay of a radioisotope that is part of a biologically active PET “tracer” administered to the patient prior to the PET scan procedure. The tracer is usually introduced into the body intravenously as shown in Figure 1-1. Here an atom of fluorine-18 (half-life of 109.8 minutes) within the tracer emits a positron that travels an average distance of 0.38 mm (max 2.3 mm) as it slows down before annihilating with a nearby electron [1]. This annihilation event generates two 511 keV gamma photons simultaneously emitted at in opposite directions (180° apart) due to the near zero momentum of the position and electron during annihilation [8]. The two photons are

detected by the PET scanner, which comprises an array of gamma detectors arranged in a ring around the patient. The detected gamma pairs are used to reconstruct three-dimensional images of the location and quantity of the labeled biomolecule at a given time *in vivo* [9].

The use of PET for clinical applications such as disease detection, cancer staging, and drug efficacy has grown significantly over the past years and continues to grow [1], [10]. Currently, radiolabeled glucose analog 2-[^{18}F]fluoro-2-deoxy-D-glucose ([^{18}F]FDG) is the most commonly utilized PET tracer in clinical PET imaging due to its relative ease of production and favorable application in many disease models that involve alterations of the glucose metabolic process, such as occurs in cancer and

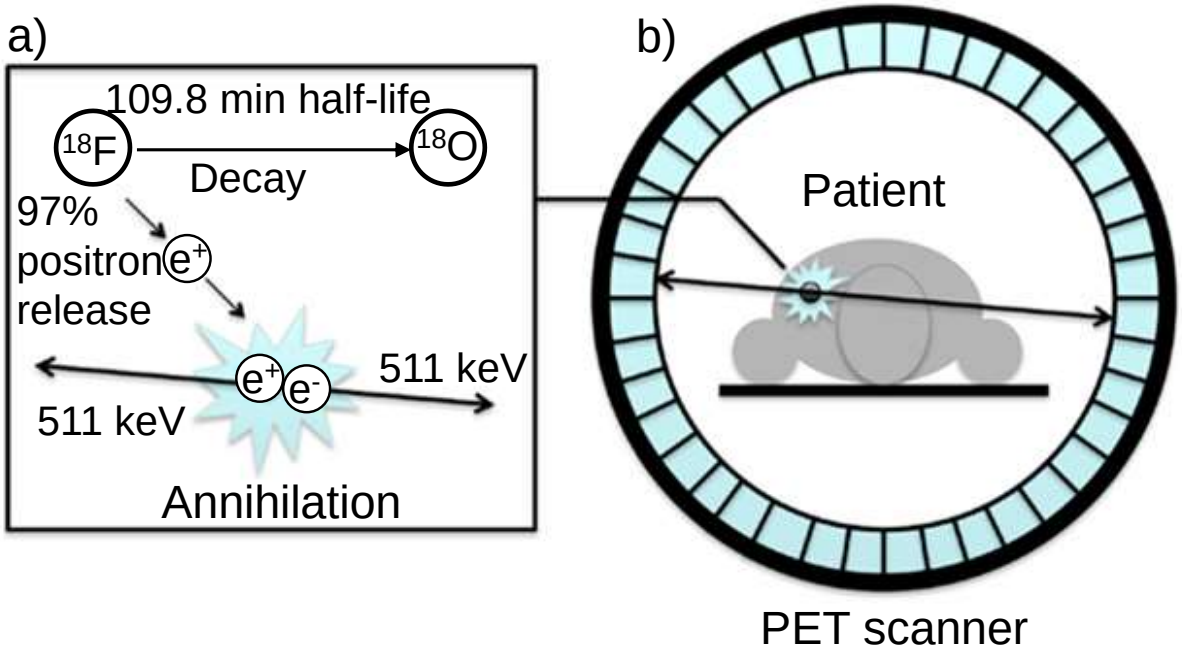

Figure 1-1 **Positron emission tomography.**

a) When a fluorine-18 atom in a PET tracer molecule decays, it releases a positron (e^+) 97% of the time (3% electron capture), which annihilates with a nearby electron (e^-) releasing two oppositely directed 511 keV gamma photons. **b)** The pair of photons is detected by a PET scanner. Based on detection of many pairs, a 3D image of the distribution of radiolabeled biomolecule can be reconstructed.

neurological disorders [11]–[14]. While thousands of other potentially clinical relevant PET tracers currently exist [15], [16], they have yet to be thoroughly evaluated due to the lack of commercial availability, which stems from a lack of widespread demand and the high cost of production. Another well-known PET tracer is 3'-deoxy-3'-[^{18}F]fluoro-L-thymidine ([^{18}F]FLT), which is an analog of the nucleoside thymidine. [^{18}F]FLT is typically used as a marker for cell proliferation as its uptake and retention is linked with DNA replication. High [^{18}F]FDG uptake in the brain makes it difficult to use [^{18}F]FDG to image brain tumors, however, [^{18}F]FLT has been shown to be more effective than [^{18}F]FDG at detecting tumors in the brain [17], [18]. Tracers such as [^{18}F]FLT and (*S*)-N-((1-Allyl-2-pyrrolidinyl)methyl)-5-(3-[^{18}F]fluoropropyl)-2,3-dimethoxybenzamide ([^{18}F]Fallypride), which is a ligand for D_2-like dopamine receptors in the striatum used for the detection of neurological diseases [19], [20], still face rigorous preclinical and clinical evaluations before they can be approved for routine clinical use.

1.1.2 Production of ^{18}F-labeled PET tracers

Production of PET tracers involves complex radiochemistry and is expensive in part because of the need for costly equipment (cyclotron, automated radiosynthesizers, shielding, and quality control instrumentation) and operating costs (personnel and reagents). There are three main stages in the production of a PET tracer final product before being injected into a patient and imaged on a PET scanner: production of the radioisotope, radio-labeling and purification of the tracer, and quality control (QC) testing of the tracer (Figure 1-2). The production of fluorine-18 is typically accomplished by bombarding oxygen-18 enriched water ([^{18}O]H_2O) with high energy (11 MeV) protons to perform a nuclear reaction (a proton in the nucleus is replaced with a neutron) , in

which oxygen-18 is converted to fluorine-18 [21]. A particle accelerator known as a cyclotron accelerates protons in a spiral trajectory to perform the bombardment [8]. Aqueous [^{18}F]fluoride is generated within the [^{18}O]H_2O at yields that depend on the cyclotron settings (beam current, bombardment time, etc.) [22]. The [^{18}F]fluoride radioisotope is then transferred out of the cyclotron to be used immediately for radiosynthesis or shipped off site for external use.

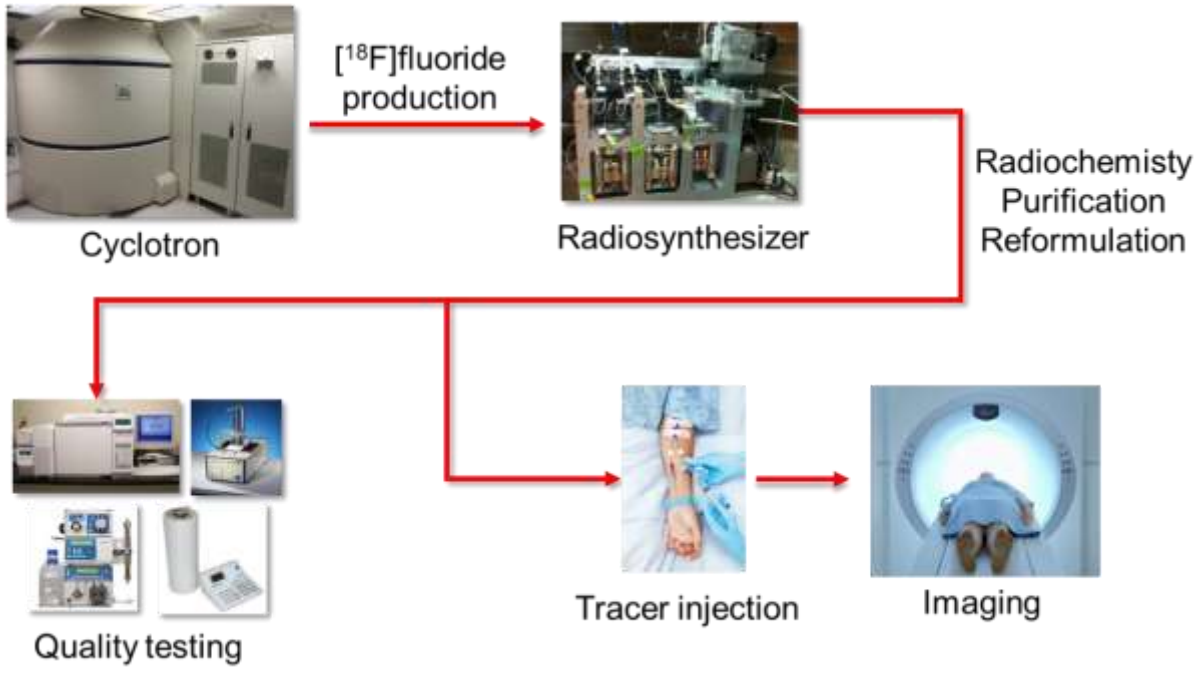

Figure 1-2 **Workflow of PET.**

A cyclotron is used to produce [^{18}F]fluoride in [^{18}O]H_2O. The resulting aqueous [^{18}F]fluoride is transferred to a radiosynthesizer (manual or automated), where the PET tracer is radiolabeled, purified, and reformulated into a solution for injection in the subject. These process are all performed within lead shielding. A sample of this solution is taken for quality control (QC) testing to ensure it is safe before being injected into the patient, who then undergoes a PET scan after a waiting period for tracer uptake to occur.

The radio-labeling and purification steps are performed by machines called radiosynthesizers, which perform multi-step chemical synthesis (and sometimes purification and formulation) processes in a remote-controlled or automated manner.

The complexity of the radiosynthesis process varies depending on the desired tracer, but there are similarities among the process for the majority of ^{18}F-labeled tracers. First, the [^{18}F]fluoride radioisotope needs to be extracted from water it is contained in, as water inhibits the reactivity of [^{18}F]fluoride by means of a strong hydration shell [23]. The most common method to extract the [^{18}F]fluoride is with solid phase extraction (SPE), which works by trapping the [^{18}F]fluoride onto a strong anion-exchange resin (SAX) using a disposable SPE cartridge (Figure 1-3). The [^{18}F]fluoride is then eluted out of the cartridge with a salt solution containing an anion with higher affinity than fluoride for the SAX, such as potassium carbonate (K_2CO_3). To fully remove any trace of water, the eluate containing the [^{18}F]fluoride is then dried by evaporation, and often further azeotropically distilled by additional additions of acetonitrile (MeCN). The addition of a phase-transfer catalyst such as cryptand 4,7,13,16,21,24-Hexaoxa-1,10-diazabicyclo[8.8.8]hexacosane, a potassium chelating agent known as Kryptofix® 2.2.2 or K222, is needed in order to allow otherwise insoluble [^{18}F]fluoride to dissolve in an organic solvent needed for downstream reaction steps. Alternative phase-transfer catalysts that can be used include tetrabutylammonium hydrogen carbonate ($TBAHCO_3$) and cesium carbonate (Cs_2CO_3).

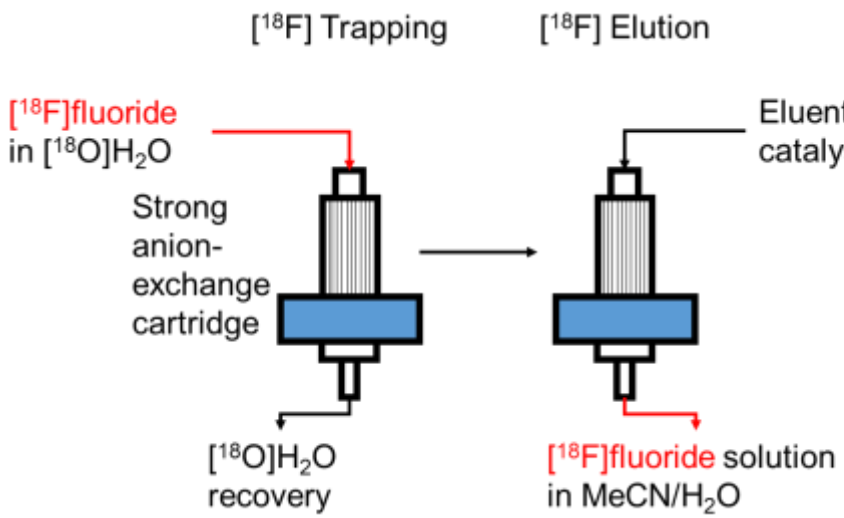

Figure 1-3 **SPE method for [^{18}F]fluoride handling.**

[^{18}F]fluoride produced in [^{18}O]H_2O is passed through strong anion-exchange cartridge to trap the [^{18}F]fluoride and recover the [^{18}O]H_2O for purification and reuse. The [^{18}F]fluoride is eluted from the cartridge using a solution containing a base (e.g., K_2CO_3) and phase-transfer catalyst (e.g., a cryptand) in a mixture of acetonitrile (MeCN) and H_2O. The final solution is then typically evaporated to remove the H_2O.

The dried [^{18}F]fluoride can now be used for nucleophilic reaction with a suitable precursor, generally at elevated temperature in an anhydrous solvent. Additional reaction steps may be required to remove protecting groups if certain groups in the precursor need to be protected to ensure that [^{18}F]fluoride is installed at the correct location. More complex assembly of PET tracers is sometimes needed, but generally the number of reaction steps is minimized to reduce losses due to radioactive decay. Sometimes the synthesized molecule is used to label fragile biological molecules, viruses, cells, or particles via a secondary labeling process under mild conditions.

An example of this process is the synthesis of [^{18}F]FLT, which consists of a nucleophilic fluorination step and a hydrolysis step. The synthesis reported by Pascali *et al.* [24] (Figure 1-4) starts by using a solution of $TBAHCO_3$ as the phase transfer catalyst to elute [^{18}F]fluoride off an anion-exchange cartridge before it is mixed with a solution of FLT precursor, (1-(2′-deoxy-3′-O-(4-nitrobenzenesulfonyl)-5′-O-(4,4′-

dimethoxytrityl)-β-D-threo-pentafuranosyl)-3-N-(tert-butyloxycarbonyl)thymine (3-N-boc-5′-ODMTr-3′-O-nosyl-lyxothymidine), in dry MeCN. The fluorination reaction proceeds at 100°C for 5 minutes, followed by a hydrolysis step with 1M hydrochloric acid (HCl) at 90°C for 3.5 minutes. The crude product is then purified and formulated into an injectable solution (e.g. saline).

Purification is needed to remove toxic reagents as well as several by-products that can be formed during the synthesis (Figure 1-4). The formation of these side products are a result of various chemical processes. Chlorothymidine (CLT) is formed when free contaminant chloride ions react with the FLT precursor. Thymidine is formed due to the hydrolysis reaction of the nosylate group before fluorination can occur, and stavudine is formed from an elimination reaction due to the good nosylate leaving group. Thymine and furfuryl alcohol are most likely formed from a proton promoted

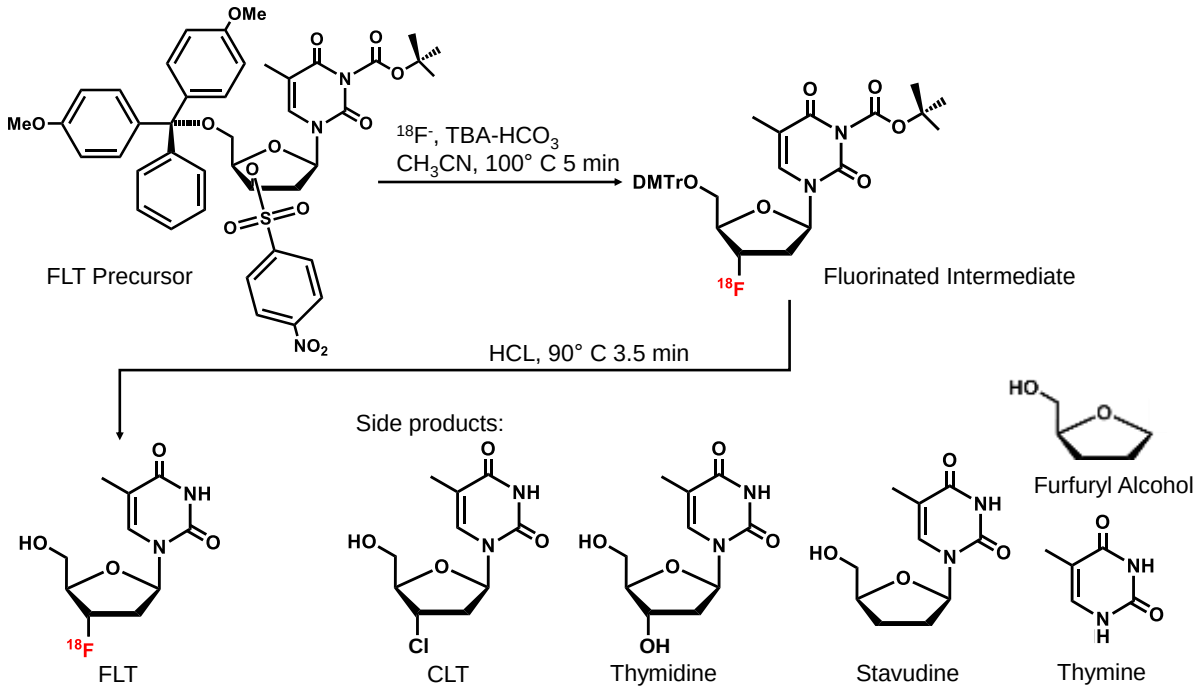

Figure 1-4 **Synthesis of [^{18}F]FLT and observed by-products**

nitrogen-carbon bond cleavage during the acidic hydrolysis step with HCl. Additional possible impurities not shown in Figure1-4 include dimethoxytrity (DMT), nosylate group and excess $TBAHCO_3$. Part of the quality control testing process (described below) is to ensure the levels of all of the compounds have been eliminated or reduced below acceptable limits.

Several automated radiosynthesizers exist in the market today to help alleviate the complexity of radiochemistry. They enable production (synthesis, purification, and formulation) by a technician rather than a radiochemist, and they prevent the need for the operator to handle the radioactive materials, thus providing safety. However, these automated systems are very expensive, and very large, and require a hot cell for proper shielding. Another problem is that many synthesizers must be customized for each different PET tracer. In such cases, the synthesizer (and hot cell) is usually dedicated to production of a single tracer (to avoid the risk of errors during configuration, and to avoid the need for validation runs each time the configuration is changed). This makes it very expensive to produce multiple tracers.

To address the latter problem, kit-based systems have been developed that enable the production of diverse tracers by simply changing a disposable cassette, i.e. without the need for system reconfiguration [25], [26]. To address the former problem, there have been significant efforts made toward the development of miniaturized radiosynthesizers based on microfluidics [27]–[29]. Over the past couple of decades, the concept of miniaturized handling of liquids and chemicals has led to the development of a wide variety of microfluidic technologies, offering not only substantial size reduction but also significantly reduced cost of the liquid handling system itself.

Leveraging these developments in the field of radiochemistry could reduce equipment costs and potentially eliminate the need for hot cells (by making self-shielding practical), enabling more research facilities to develop and study a wide range of PET tracers and their applications [25], [30]. Microfluidics systems can also reduce costs by reducing the volumes of expensive reagents consumed, and enabling synthesis with reduced amount of radioactivity [31].

When these developments are fully realized, the quality control (QC) testing process could become the bottleneck in reducing the cost of PET tracers.

1.1.3 Quality testing of PET tracers

To ensure the quality and safety of radiopharmaceuticals before use on human subjects, several requirements must be met. In the United States, these requirements are set forth by the Food and Drug Administration (FDA), which has strict guidelines to ensure the safety of compounds injected into patients. Quality control testing requirements for PET tracers, such as [^{18}F]FDG, include the characterization of appearance/color, chemical identity, pH, radioactivity, radioisotope identity, sterility, bacterial endotoxin levels, residual solvent content, chemical purity, and radiochemical

purity as shown in Table 1-1 [32], [33]. In addition, the amount of radioactivity is measured.

Table 1-1 **Common quality control tests of PET tracers.**

Techniques and abbreviations are described in the main text**.**

QC Test	Method	Requirements
Visual Characterization	Eye	Clear, colorless or slightly yellow liquid
Radionuclidic identity/purity	Gamma spectroscopy Half-life measurement	Photon energy of 0.511 MeV or 1.022 MeV 105-115 min
pH	pH meter or pH paper	4.5 to 8.5
Radioactivity	Dose calibrator	----
Sterility	Cell culture media incubation (14 days) Filter integrity test	No bacterial growth Breakthrough pressure ≥ filter specification
Bacterial Endotoxin	Limulous amoebocyte lysate test (LAL)	175 international unit/max dose in mL
Residual Solvent	GC-MS or GC-FID	Solvent dependent
Chemical Purity	UV/PAD-HPLC Colourimetric	Chemical dependent Chemical dependent
Radiochemical Purity	Radio-HPLC and/or radio-TLC	> 95% for most tracers (>90% for FDG)

Characterization of appearance/color is generally done visually: the product should be clear and colorless, and free of particulates. A slightly yellowish liquid is acceptable, though it could indicate the presence of small amounts of impurities. The pH of the product can be measured using a pH meter and should be close to physiological pH (must be in the range 4.5-8.5). The radioisotope identity can either be performed by obtaining a gamma spectrum to validate the photon energy of 0.511 MeV (or 1.022 MeV) or measuring the radioactive half-life of the product and confirming it is within an acceptable range of the expected 109.8 minutes. The sterility of the product is tested by incubating a test sample in a cell culture media for 14 days at 37°C to ensure

no bacterial growth is present. However, since this timeframe is much longer than the lifetime of the radioisotope there is a provision for early release of the product via an integrity test of the filter used for sterile filtration. To perform this test, a stream of air is passed through the filter, then into a water reservoir. An indicator will show the pressure exerted on the filter membrane by the air stream. The filter membrane should be able to withstand the maximum pressure as indicated in the specifications of the filter. If no bubbles are generated in the water reservoir, then it is assumed that the filter's integrity is still intact and would have successfully removed any microorganisms in the [^{18}F]FDG product. To test for bacterial endotoxins, the product is incubated with the lysate of ameobocytes from horseshoe crabs. If bacterial endotoxins are present, the mixture becomes cloudy.

Chemical purity analysis and residual solvent tests involve determining the amounts or concentrations of impurities and solvents in the final product, or at least confirming that they are below a permitted limit. High-performance liquid chromatography (HPLC) is a separation technique that is currently the gold standard for testing chemical/radiochemical purity. HPLC systems used in quality testing of radiopharmaceuticals typically include a ultra-violet (UV) optical absorption detector, a gamma radiation detector, and may also contain other detectors such as pulsed amperometric detection (PAD) (for detection of species with low optical absorbance), or refractive index (RI) detection (for detection of residual solvents). While HPLC has been reported to be used for residual solvent testing [32], and the detection of compounds such as Kryptofix 2.2.2 [34], due to sensitivity issues, these tests are most commonly performed using gas chromatography equipped with either mass

spectrometry or flame ionization detector (GC-MC or GC-FID) and colorimetric spot tests, respectively.

Separation on HPLC systems is performed by injecting the sample into the mobile phase, which flows through a stationary phase (HPLC column) at high pressure. The stationary phase is where the analytes are separated according to their physical and chemical properties as they pass through the column. Each species exits the column as a ‘band’ at a characteristic retention time, depending on the separation conditions. The bands can then be individually detected and quantified.

As described above, there are a large number of tests that must be performed manually on various instruments. These instruments must also be maintained and calibrated to ensure high level performance, which adds considerable labor, training, and documentation effort. Automated PET QC systems have recently emerged as a means to reduce some of this burden. For examples, systems offered by QC-1 [35] (Munster, Germany), Trace-ability [36] (Santa Monica, CA USA), and ABT Molecular Imaging Inc. [37], [38] (Louisville, TN USA) can automatically handle the majority of the needed calibrations, performance testing, and report generation. However, these automated instruments so far are still expensive and rather bulky due to their reliance on conventional analytical testing components. The QC-1 system for [^{18}F]FDG combines a HPLC/Ion Chromatography (IC) and gas chromatography (GC) device with multiple detection units (RI-detector, gamma) to perform several tests on one device. ABT uses the RI-detector to test for residual solvents in the HPLC system, and visual inspection and pH are generally done optically using absorbance detector, and pH

indicators. Trace-Ability is developing a QC plate reader to determine radionuclide identity, radioactivity concentration, and K222 concentration, using optical readouts.

While the use of HPLC and its various components is highly effective in the separation, identification, and quantification of various analytes, the overall instrumentation is expensive and bulky, and involves complicated labor-intensive protocols (especially setup and cleaning). By replacing this conventional technique with a microscale analytical approach, we can potentially avoid the need for these expensive instruments, conserve lab space, and reduce the overall cost of this aspect of PET tracer production. Microscale analytical approaches often offer sensitivity that is equal or superior to conventional analytical approaches [39], [40]. Combined with the ability to integrate multiple detectors [41], [42], the footprint and cost of the overall analytical system can be dramatically reduced using microfluidic devices to possibly perform multiple QC tests. The high sensitivity could also enable the detection of species such as Kryptofix 2.2.2 in the same platform (instead of requiring a separate colorimetric spot test [32]).

Over the past 20 years, there has been tremendous development in the area of microscale analytical techniques to leverage the high detection sensitivities, fast separation times, and small sample volumes [43]–[46]. The associated driving force led to the concept of micro-total analysis systems (μTAS) or lab-on-a-chip (LOC) devices, which strive to integrate the processes such as sample preparation, processing, and readout in a single device, replacing what used to take several laboratory instruments. Such integration reduces cost and size, and can sometimes increase throughput via parallelization, in addition to exhibiting the advantages listed above [47], [48].

Recently, a group from the PET Research Centre at the University of Hull (United Kingdom), presented a LOC device designed for radioisotope processing, synthesis, and some routine quality control tests [49]. The LOC device used modules for electrode trapping and release of [^{18}F]fluoride, as well as synthesis of [^{18}F]FDG. Chemically modified etched silica channels were used to perform separation and purification operations. A small subset of QC tests were integrated. pH was analyzed by absorption spectroscopy. Residual solvent was assessed via raman spectroscopy, but could be limited to low detection sensitivity. Chemical purity testing was not included in this platform.

A promising microscale technique for performing chemical/radiochemical purity analysis is capillary electrophoresis (CE). CE can be used to separate, identify, and quantify various analytes of interest in a sample similar to HPLC (using similar detection methods). CE can also be readily miniaturized into microfluidic chips, without the need for high pressure valves, pumps, and connectors associated with HPLC systems [50], [51], but still offering the advantages of decreased analysis time [52], [53], and increased detection sensitivity [54].

1.2 Capillary electrophoresis (CE)

1.2.1 Background

CE is an analytical technique that uses an applied potential to separate ions based on their electrophoretic mobility. This technique was described by Jorgenson and Lukacs in 1981 by using a fused silica capillary column and aqueous buffer to separate charged compounds [55], [56]. This was the first indication of the potential CE had to perform analytical separation with high separation resolution of ionic species with

short analysis times using small sample and reagent volumes. Since then, publications reporting application of CE-based methods for the characterization and quality control of biopharmaceuticals has increased dramatically as improvements in detection limits and reproducibility has been achieved [57]. CE has also been used in the analysis of technetium-99m (Tc-99m) labeled single-photon emission computed tomography (SPECT) tracers. These results demonstrated CE's advantages of short analytical times, and highly efficient separations compared to HPLC, while also reducing large amounts of radioactive eluent waste [58]. Since the duration of synthesis and purification of radiotracers should not exceed two or three times the half-life of the radionuclide used [59], there is even further advantage of the short analysis times for PET using short-lived isotopes.

1.2.2 Modes of CE

CE has been used in a diverse range of applications, including food analysis [60], [61], pharmaceutical analysis [62]–[64], bioanalysis [65], [66], and environmental pollutants analysis [67], [68]. While CE separation typically works best with samples containing different charged species, as it takes advantage of their electrophoretic mobility, the separation of a diverse range of analytes with varying properties have been developed by utilizing different modes of CE. CE requires the use of a background electrolyte (BGE; also known as "buffer") to provide stable pH control during electrophoresis, and provides the ionic strength necessary for electrical continuity. Several modes of CE are listed below.

a. **capillary zone electrophoresis (CZE):** separation of analytes via differences in their electrophoretic mobility [69] (Figure 1-5a)

b. **micellar electrokinetic chromatography (MEKC):** separation of analytes based on interaction with the background electrolyte and the micelles that acts as a pseudo-stationary phase [70] (Figure 1-6)
c. **capillary gel electrophoresis (CGE):** separation of analytes using polymers to create a molecular sieve within a capillary [71]
d. **capillary isoelectric focusing (CIEF):** separation of analytes based on difference in their isoelectric points (pI) [72]
e. **capillary isotachophoresis (CITP):** separation of analytes using different BGEs within the capillary to create zones of varying electric fields [73]
f. **capillary electrochromatography (CEC):** separation of analytes using capillaries packed with chromatographic stationary phase [74]

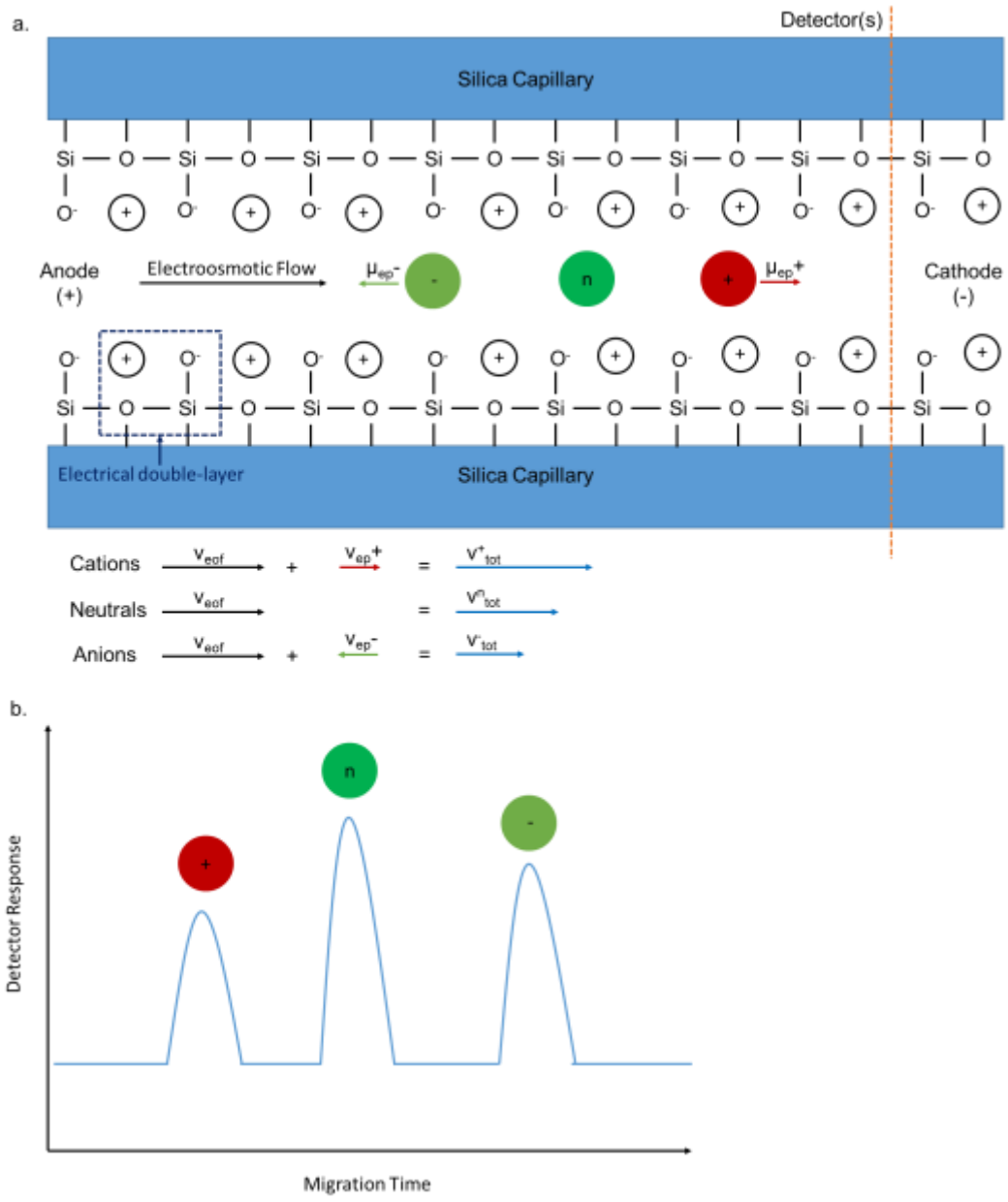

Figure 1-5 **Capillary zone electrophoresis (CZE).**

a) The negatively charged silanol groups on capillary walls attract cations from the buffer, creating an electric double layer. When applying a voltage along the length of the capillary, these cations are drawn to the cathode. This movement carries nearby mobile phase molecules, creating a bulk electroosmotic flow (EOF) with velocity v_{eof} along the capillary. Based on their electrophoretic mobilities (μ_{ep}), each species has an electrophoretic velocity, $v_{ep} = E\,\mu_{ep}$, (where E is the electrical field strength), that is superimposed on the EOF. Cations have the shortest migration time and come out first, then all neutral compounds, and finally all anions. **b)** Cartoon of CE chromatogram. Typically peaks are somewhat rounded.

The most commonly used mode of CE is CZE, due to its simplicity and its ability to

separate both anions and cations. For all modes of CE, a chromatogram (Figure 1-5b) is generated for the sample, representing the detector signal intensity (e.g. from UV or gamma detector) as a function of time. Different analytes show up as peaks in the chromatogram, each at a characteristic migration time. The separation of neutral analytes is typically performed with MEKC. Molecules can be separated based on their degree of interaction with the spontaneously-formed micelles which have an internal hydrophobic character and surface hydrophilic character.

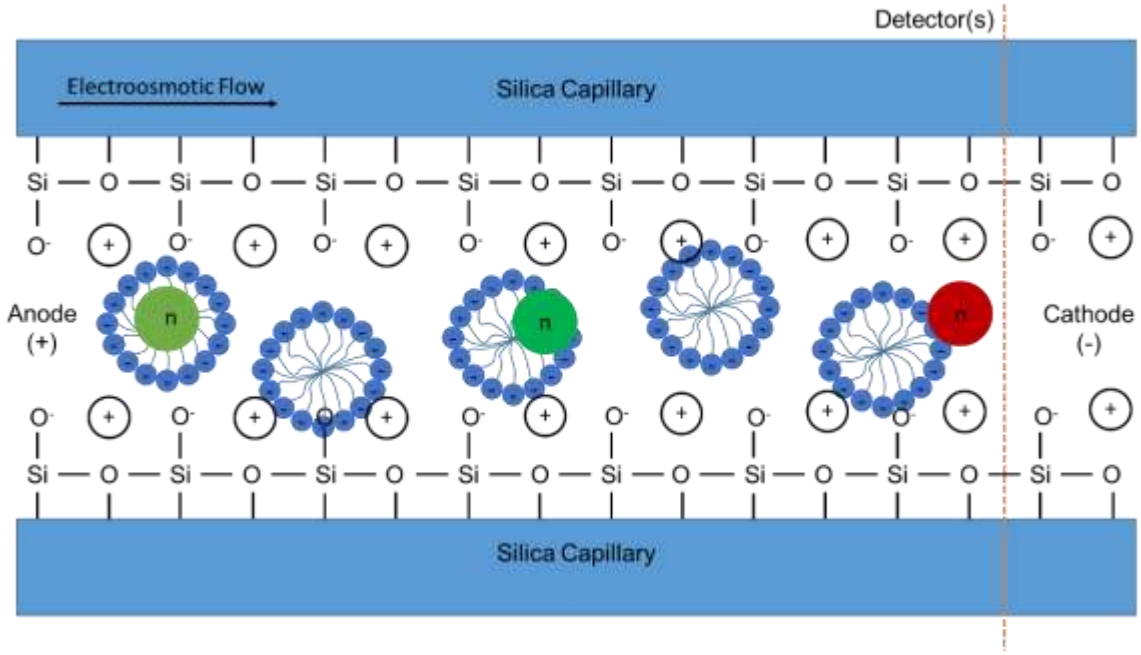

Figure 1-6 **Micellar electrokinetic chromatography (MEKC) with anionic micelles.**

Compounds are separated based upon their differing affinities for micelles, which are formed by adding a surfactant to the background electrolyte above its critical micellar concentration. In this case, micelles are negatively charged and thus move slower than the electroosmotic flow and thus retard the migration of species that interact strongly with the micelles.

1.2.3 Electroosmotic flow and electrophoretic mobility

Electroosmotic flow (EOF) is the main fluidic pumping mechanism in CE and is generated at the surface-solution interface in a capillary (or micro-fabricated channel).

An electrical double layer (composed of a “stern layer” (immobile) and a “diffuse layer” (mobile)) is formed when the mobile cations from the BGE are attracted to the fixed negative charges on the inner wall of the capillary [75]. By applying an electric potential between the two ends of the capillary, the cations in the diffuse portion of the double layer migrate towards the cathode, resulting in the bulk fluidic flow of the BGE in the same direction. The generated EOF is typically greater than the electrophoretic flow of the analytes, and thus the analytes, regardless of charge, will exhibit a net motion in the same direction as the EOF. Surfactants can be used to reverse the surface charge of the capillary wall to generate EOF towards the anode if desired [76].

The velocity profile (i.e. flow velocity as a function of position within the capillary) of EOF-driven flow is relatively flat (Figure 1-7) compared to the parabolic profile encountered in pressure-driven flow such as HPLC [77]. This has been shown to produce less diffusive effects as dispersion in the axial direction is reduced in electroosmotic flow [56], [78]–[80].

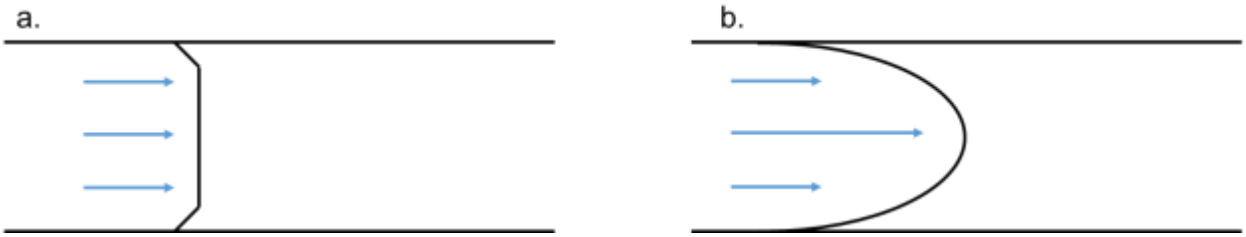

Figure 1-7 **Velocity profiles under different fluidic driving forces.**

a) electroosmotic flow, and **b)** hydrodynamic (pressure-driven) flow. Flow velocity is indicated by length of blue arrows.

The mobility of EOF (μ_{eof}) (the mobility of the bulk mobile ions in the double-layer under electric potential) is related to the zeta potential (ζ), which is the potential between the surface charge and the diffuse (mobile) layer, the viscosity (η), and the dielectric constant (ε) of the BGE as shown in Equation 1.1.

$$\mu_{eof} = \frac{\upsilon_{eof}}{E} = \frac{\varepsilon\zeta}{\eta} \quad (1.1)$$

Here, υ_{eof} is the linear velocity of the EOF and *E* is the field strength of the applied electric potential. E is defined as applied voltage (V) over length of capillary (L) as defined by Equation 1.2.

$$E = \frac{V}{L} \quad (1.2)$$

In CZE, charged analytes are separated in the BGE based on their electrophoretic mobility (μ_{ep}) in an applied field as defined by Equation 1.3.

$$\mu_{ep} = \frac{q}{6\pi\eta r} \quad (1.3)$$

The electrophoretic mobility is governed by the analyte's charge, *q*, and the frictional coefficient, *f,* defined by Stokes equation (Equation 1.4).

$$f = 6\pi\eta r \quad (1.4)$$

Stokes equation describes the frictional coefficient for a spherical particle having a hydrodynamic radius, *r,* in a solution, where *η* is the viscosity of the solution. The resulting relative velocity, $\upsilon_{ep,}$ of each analyte in this field is equal to electrophoretic mobility of the analyte multiplied by the field strength (Equation 1.5).

$$\upsilon_{ep} = \mu_{ep}E \quad (1.5)$$

When EOF is present, the total velocity, $\upsilon_{tot,}$ of an analyte is proportional to the sum of both the electrophoretic and electroosmotic mobilities (Equation 1.6).

$$\upsilon_t = \mu_{tot}E = (\mu_{ep} + \mu_{eof})E \quad (1.6)$$

To measure EOF, measuring the migration time of a neutral marker is the most common technique used [81]. The migration time, t_m, is the time it takes the analyte to migrate from the beginning of the capillary to the point of detection.

While the EOF is usually beneficial, it needs to be controlled as rapid EOF can result in the elution of analytes before separation has occurred, or can significantly prolong analytical times if EOF is too slow. Methods to control EOF include:

a. **Adjusting the electric field:** EOF changes proportionally with electric field strength as shown in Equation 1.1 [81].
b. **Adjust BGE pH:** Low (basic) pH BGE will protonate the capillary surface, which reduces the strength of the double layer and its zeta potential, and lowers EOF, as shown by Equation 1.1. High (acidic) pH, causes deprotonation of the capillary surface, which strengthens the double layer and its zeta potential, and increases EOF [81].
c. **Adjust BGE ionic strength/concentration:** High BGE concentrations limits coulombic interactions of the BGE with the capillary walls by decreasing the effective charge at the wall [82], [83], which lowers EOF.
d. **Adjust temperature:** Adjusting the BGE temperature causes changes in EOF due to BGE viscosity change (2-3%/° C) [84], [85].
e. **Additives to BGE:** Additives to the BGE can decrease or even reverse EOF depending on the additive used and its surface modification to capillary walls [76], [86], [87].

1.2.4 CE systems

The basic components of a CE system include reservoirs for sample and BGE, a capillary, electrodes, a high voltage power supply, a detector, and a device to handle data collection (and CE operation, if not operated manually) as shown in Figure 1-8. The capillary is threaded though the detector, and each end is placed in a separate BGE vial, each with an electrode connected to the high voltage power supply. Details of specific CE operations (injection, separation, and detection) depend on the mode of CE used, which will be discussed in later sections.

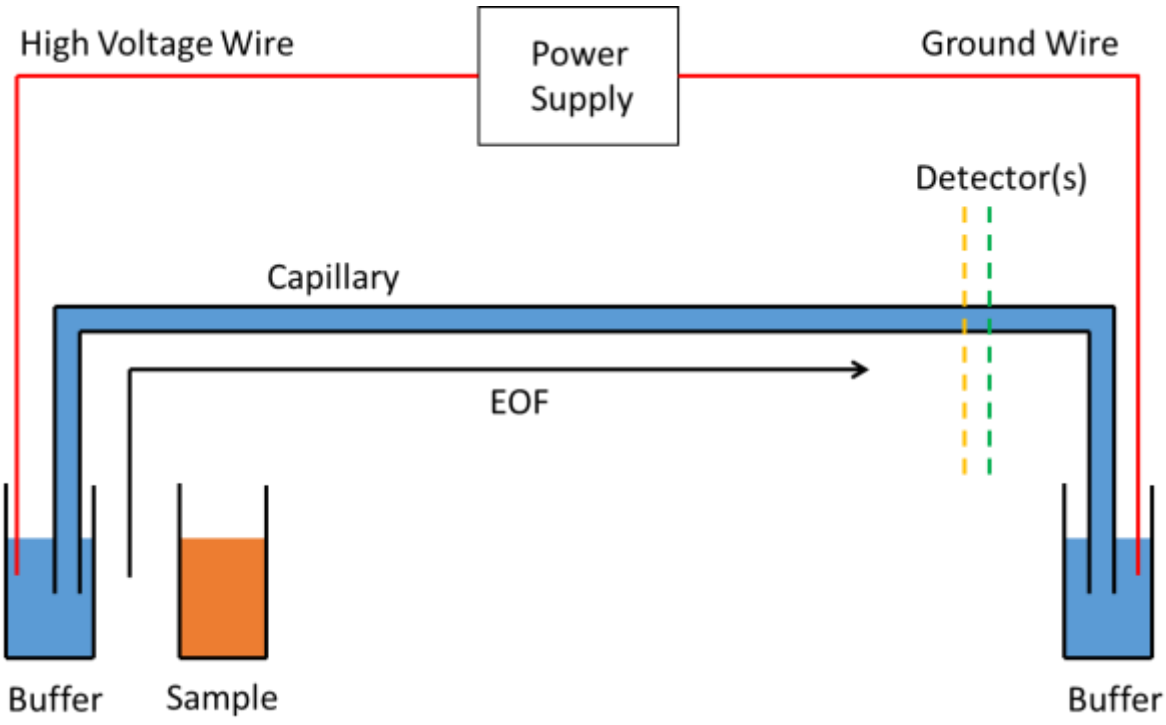

Figure 1-8 **Schematic of basic capillary electrophoresis setup.**

A capillary is inserted into two buffer (BGE) vials, and is electrically connected to a high voltage power supply. The sample is injected electrokinetically by momentarily placing the anode and entrance of capillary into the sample vial and applying an injection potential for a short time. The entrance of the capillary is then returned to the BGE vial and the separation voltage is applied to separate the sample. Detector(s) are placed on the cathode end of the capillary to detect the arrival of the separated species.

As mentioned earlier, CZE is the most common mode of CE due to its simple setup and separation mechanism as ionic analytes are separated into discrete bands due to their individual mobilities. The resolution of separation strongly depends on how different are the mobilities of each of the analytes. When working with neutral species, MEKC is commonly used to help differentiate each analyte's mobility. The formation of micelles occurs when the addition of surfactants (such as sodium dodecyl sulfate, SDS) to the BGE is above the critical micelle concentration (CMC). CMC is the concentration at which surfactants start aggregating into micelles to decrease the free energy of the system by decreasing the contact area of its hydrophilic part with the surrounding water. Sodium dodecyl sulfate (SDS) is the most commonly used surfactant, consisting of a hydrophobic head (negatively charged) and hydrophilic tail, and has a CMC of 8 mM.

The migration of the surfactant (and its micelle counterpart) depends on its overall charge. Anionic (negatively charged) surfactants, such as SDS, migrate towards the anode, which is the opposite direction of EOF. Since the EOF is typically faster than the migration velocity of the micelles, the net movement will still occur in the same direction of the EOF. During electrophoretic migration, the neutral analytes partition between the micelles and the BGE through both hydrophobic and electrostatic interactions [88]. Because the micelles migrate at a different rate than the BGE, they act as a pseudo-stationary phase, and lead to separation of analytes depending on the amount of interaction with the micelles. The use of MEKC will be vital to the separation of [^{18}F]FLT and its neutral impurities, as will be discussed in the latter sections of this chapter.

To make use of CE, the capillary must also be combined with an upstream injection method (to inject the sample) and a downstream detection method (to detect the various analytes).

1.2.4.1 Injection of sample

There are two main modalities of CE sample injection, which are electrokinetic and hydrodynamic injections. Electrokinetic injection uses electrophoretic and/or electroosmotic migration to inject sample into the separation channel. Hydrodynamic injection is performed by the application of pressure differences between two points to drive sample into the separation channel. Typically, hydrodynamic injection can be accomplished either by siphoning via capillary height difference, applying pressure to sample vial, applying vacuum to detector-side buffer reservoir, or injection by syringe.

Regardless of the injection method, an injection volume approximately 1% or less of total capillary volume is recommended for optimal separation performance [89]–[91].

1.2.4.2 Separation of analytes

Before peaks can be quantified accurately, they must be separated from each other. Separation resolution of the several analytes contained in a single sample is the major goal in separation science. The separation resolution, R_s, between two peaks is defined in Equation 1.7.

$$R_s = \frac{2(t_2 - t_1)}{w_1 + w_2} \quad (1.7)$$

Here, t_1 is the migration time of the first eluted analyte, t_2 is the migration time of the later eluted analyte, w_1 is the baseline peak width (taken between tangents drawn to the sides of the peaks) of the first eluted analyte, and w_2 is the baseline peak width of the

later eluted analyte (Figure 1-9). If peaks are symmetric and R_s > 1.5, the peaks are considered to have “baseline resolution” and are completely separated from one another [91]. If peaks display signs of tailing (i.e., non-Gaussian peaks, which occurs when analytes migrate at significantly different rates than BGE) an R_s value of 2.0 or higher is generally desired [91].

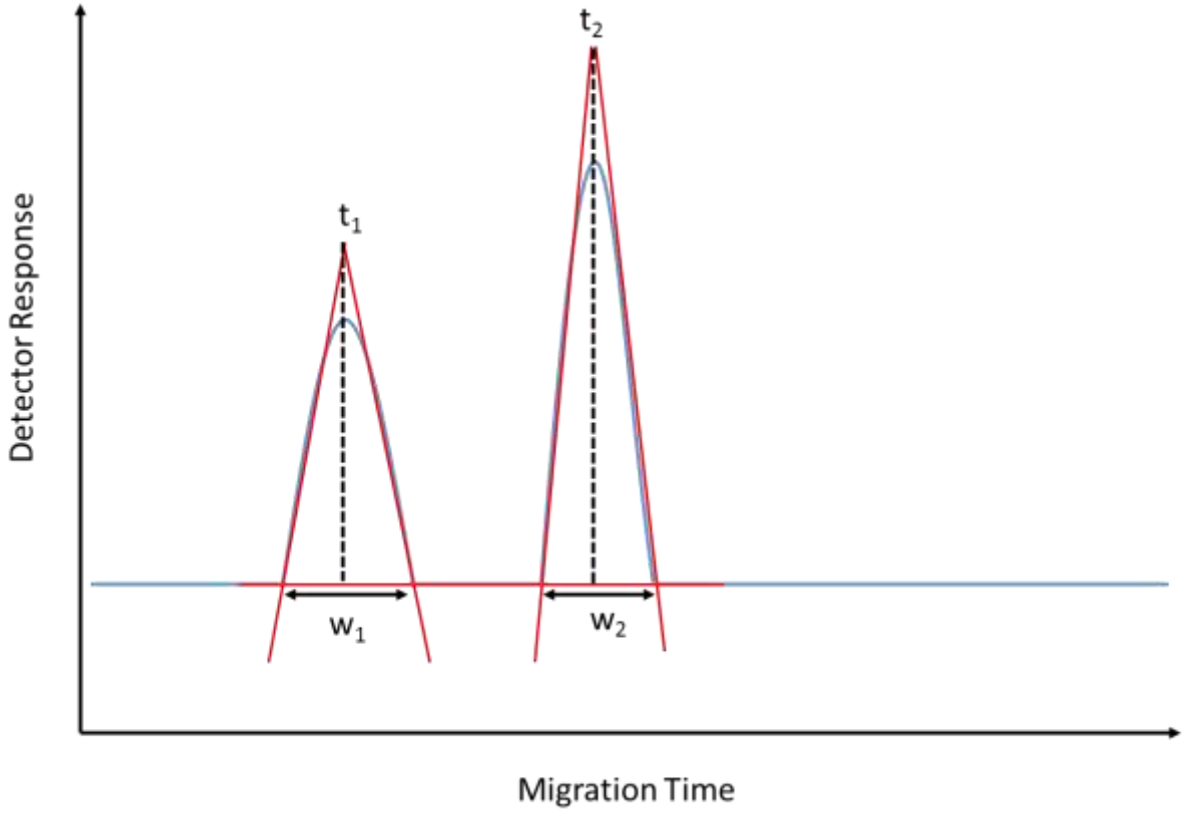

Figure 1-9 **Example of CE chromatogram**

Sample peaks are shown define migration time (t_1 and t_2) and baseline peak width (w_1 and w_2).

While CE separation is commonly performed in a capillary, microchip capillary electrophoresis (MCE) devices can implement long separation channels into a much smaller footprint of a microfluidic chip. The materials used for these MCE devices are typically either fused silica or polydimethylsiloxane (PDMS), fabricated via either glass

etching or soft lithography, respectively. Though the surface of both materials can be modified in similar ways, the material is important and can affect the EOF control and stability. EOF stability also affects reproducibility, as changes in EOF can dramatically affect peak migration times over successive runs, leading to ambiguity in the identity of peaks unless additional flanking species are co-injected with the sample.

1.2.4.3 Detection and quantitation of analytes

There are several detection modalities that can be implemented into a CE system, including optical, radiation, and electrochemical. Optical absorbance detection (UV/visible) is the most common technique used due to its relatively simple and reliable instrumentation. Optical detection uses the principle of Beer's law given in Equation 1.8.

$$A = \varepsilon l c \quad (1.8)$$

Here, *A* is absorbance, *ε* is molar absorptivity, *l* is optical path length, and *c* is molar concentration. The absorbance signal is thus proportional to concentration for a fixed system (assuming fixed path length). A radiation detector, such as a gamma detector, which uses a sealed crystal/photomultiplier assembly to detect high-energy particles, also gives a linear response, proportional to the amount of radiation (and therefore to the quantity of radioactivity). Electrochemical detectors typically use electrodes within the separation channel to detect electrical current resulting from oxidation or reduction reactions.

By monitoring the detection signal over time, a chromatogram (electropherogram) is generated, which can be analyzed to extract information about the injected sample. Quantification of the peaks in a CE chromatogram is typically

performed using peak analysis software, and will be discussed in Chapter 2. Using reference standards, the migration time can be cross-referenced to determine the identity of an analyte. The peak width information can be used to quantify resolution of pairs of peaks. The peak height is proportional to the concentration and can be used to quantify analytes present in the initial sample. Because, however, the initial injected sample spreads by diffusion and other factors, the concentration, it is generally more useful to measure the peak area to quantify the analyte. It is important that the measured area is reproducible to ensure accurate quantification. Quantitation of analyte concentration or amount requires a calibration curve to first be developed. Methods to generate these curves, and methods to determine limit of detection (LOD) will be discussed in Chapter 3.

1.2.5 Perceived limitations of capillary electrophoresis

As mentioned earlier, while microchip CE devices benefit from their small footprint, decreased analysis times, and elimination of the need for high pressure valves, pumps, and connectors associated with HPLC systems, there are a few aspects of CE that have historically been considered as limitations. The two most commonly cited issues of CE compared to HPLC systems are poor reproducibility (peak area, migration time) and poor sensitivity (optical detection) [92]. However, these issues have been mitigated in recent years by implementing improvements in materials, fabrication techniques, and operating methods.

One factor that has historically played a role in lowered reproducibility of migration times for CE is Joule heating (generation of heat due to electrical current resistance within capillary). Excessive heating has been shown to affect electrophoretic

mobilities by 2%/°C, therefore, methods to control CE temperature can be vital to migration time reproducibility [93]. Commercial CE systems, such as the Beckman Coulter PA 800 plus, circulate water around the capillary during application of electric potential to remove generated heat. Another factor that plays a role is the stability of the inner capillary surface and conditioning. For capillaries or microchips made of glass, the stability is generally quite good; however PDMS chips are subject to variable performance due to surface polymer rearrangements and fouling of the surface by unreacted oligomers [94]. To control PDMS surface conditioning/stability, one study used oxygen plasma treatment and extraction of unreacted oligomers and found an improvement in migration time relative standard deviation (%RSD) (a measure of dispersion or deviation from the average value) from 8.6% (n=40) to 3.3% (n=40) [94].

A major factor affecting reproducibility of peak area is imprecise sample injection [83], [95]–[97]. The use of PDMS micro-valves has been demonstrated to precisely control sample volumes injected into the separation channel, obtaining a peak area %RSD as low as 1.77% (n=15) on a microchip CE platform [98]. Using electrokinetic injection on a microchip CE platform, a peak area %RSD between 2.3% and 4.5%, depending on ionic species, was obtained [99].

The major factor limiting sensitivity in CE is the short optical path length due to the small diameter of the capillary through which the light travels from source to detector. Several methods to improve the sensitivity of CE microchip systems using optical detection include the use of extended optical path lengths, multi-pass path length, waveguides, and micro-lens focusing [100]–[105]. Another method to improve

sensitivity is through signal noise reduction associated with optical hardware and setup. All of these approaches will be discussed in more detail in Chapter 3.

1.3 Investigation of feasibility of using CE for chemical purity analysis of PET tracers

1.3.1 Project overview

Since CE has been shown to have similar performance (separation resolution and sensitivity) to HPLC [106], [107], and because CE has been shown to successfully separate a wide variety of analytes including peptides, proteins, nucleosides, and simple carbohydrates [108], [109], we hypothesized that CE could be used to perform the quality analysis of PET tracers based on nucleosides or carbohydrates, or other molecules. If possible, CE could provide the means to perform diverse chemical purity analysis in a compact device and consuming a tiny small sample volume.

To determine the feasibility of the use of CE in the chemical purity analysis of PET tracers, the following questions must be investigated:

- Can the tracer and all relevant impurities be separated?
- Can each species be quantified at sufficiently low levels to assess whether levels are below allowed limits?
- Can the results be achieved using a compact microfluidic implementation?

These questions were investigated using several examples of PET tracers, which are discussed in the next sections.

1.3.2 Assessment of CE separation

To determine if CE techniques can be used to separate molecules of interest to PET tracer synthesis, the separation of example PET tracers from their impurities was explored. Of the thousands of known PET tracers [16], we elected to investigate a couple of common ones. One of these is [^{18}F]FLT, which was chosen because the by-

products of synthesis (thymine, thymidine, furfuryl alcohol, stavudine, and zidovudine impurity B/chloro-L-thymidine (CLT)) [24] have been well characterized, and can be readily detected by monitoring their known UV absorbance wavelength, making them strong first candidates to test on a basic CE system with a standard UV detection module. Tables 1-2 and 1-3 show estimated expected concentration of the precursor, tracer, and various side products calculated at various stages for the [^{18}F]FLT syntheses described by Pascali *et al.* (Figure 1-4) using two different phase transfer catalysts [24]. As shown in the two tables, expected concentrations of various impurities are within the µM-mM range depending on the final volume of the sample, which are concentrations we aim to be able to detect on the microchip CE device.

In brief, [^{18}F]fluoride was captured on an anion-exchange cartridge and eluted with a 1.0 mL solution of $TBAHCO_3$ or K222/K_2CO_3 or K222/$KHCO_3$. The solution was then evaporated at 75°C until dryness before FLT precursor (BOC-FLT in 1 mL dry MeCN) was added to the mixture and allowed to react in a closed reactor at 100°C for 5 min. Due to excess of FLT precursor and phase transfer catalyst, their concentrations should remain relatively unchanged after reaction. A partial evaporation step was then performed to reduce volume to 350-500 µL before a hydrolysis step with 2 mL of 1M hydrochloric acid (HCl) at 90°C for 3.5 min. The reaction mixture was then reduced to 0.5-0.7 mL by evaporating off MeCN, and cooled to 40°C before being purified. After purification, it is expected that only FLT product remains, and all other impurities are close to zero. As shown by Tables 1-2 and 1-3, the final concentration of the product, FLT, is relatively low, whereas the range of impurity concentrations can theoretically be as high as the starting concentration of the precursor before purification. Pascali *et al.*

observed that actual concentrations of impurities after purification are in the 0.05-0.15 ppm range (or 0.05-0.15 µM range) [24]. This gives an idea of the level of detection that is needed to use CE to analyze reaction mixtures and purified samples of PET tracers.

Table 1-3 **Estimated concentrations of FLT precursor, FLT, and known side products at various stages of FLT radio-synthesis using $TBAHCO_3$ as phase transfer catalyst.**

Note: The amount of FLT was estimated from the dose produced and the specific activity reported [24]. The byproduct originates from the precursor, and since so little forms FLT, any side product may be present at nearly the original precursor concentration. Typical volumes of purified tracers are in the mL range.

	BOC-FLT ₸	$TBAHCO_3$ ‡	Thymidine	Thymine	Stavudine	Furfuryl Alcohol	FLT	CLT
Before rxn	12-30 µmol	30 µmol	0	0	0	0	0	0
After completed synthesis	12-30 µmol	30 µmol	~0-30 µmol	~0-30 µmol	~0-30 µmol	~0-30 µmol	~8.28 nmol	~0-30 µmol
After purification	~0	~0	~0	~0	~0	~0	~8.28 nmol	~0

₸ 3-N-Boc-5'-O-dimethoxytrityl-3'-O-nosyl-thymidine (FLT precursor)

‡ Tetrabutylammonium bicarbonate

Table 1-2 **Estimated concentrations of FLT precursor, FLT, and known side products at various stages of FLT radio-synthesis using K222 as phase transfer catalyst.**

Note: The amount of FLT was estimated from the dose produced and the specific activity reported [24]. The byproduct originates from the precursor, and since so little forms FLT, any side product may be present at nearly the original precursor concentration. Typical volumes of purified tracers are in the mL range.

	BOC-FLT ₸	K222 †	$K2CO_3$ or $KHCO_3$ §	Thymidine	Thymine	Stavudine	Furfuryl Alcohol	FLT	CLT
Before rxn	12-30 µmol	40-53 µmol	25.3 or 35 µmol	0	0	0	0	0	0
After completed synthesis	12-30 µmol	40-53 µmol	25.3 or 35 µmol	~0-30 µmol	~0-30 µmol	~0-30 µmol	~0-30 µmol	~8.28 nmol	~0-30 µmol
After purification	~0	~0	~0	~0	~0	~0	~0	~8.28 nmol	~0

₸ 3-N-Boc-5'-O-dimethoxytrityl-3'-O-nosyl-thymidine (FLT precursor)

† Kryptofix® 2.2.2 mixed with base solution §

§ Base solution made from potassium carbonate (K_2CO_3) or potassium bicarbonate ($KHCO_3$)

As another example, we chose 2-deoxy-2-[^{18}F]fluoro-β-D-arabinofuranosylcytosine (D-[^{18}F]FAC), which measures activity of deoxycytidine kinase (dCK), and is used to determine the therapeutic activity for several nucleoside analog drugs [110]–[112]. D-FAC is also UV active, but one of the challenges faced with detecting this compound is that during the synthesis, two stereochemical isomers are formed [111], [113], [114]. Due to the chemical similarity of the isomers, it was not clear

whether they can be separated with CE, and thus this served as an interesting test of separating ability.

Cold standards of these tracers and their impurities were used to establish the ability to separate/detect these molecules. The separation of K222 from the tracers and impurities was also explored, due to the potential to assess K222 without the need for a separate test [34]. A concern about K222 was its low molecular absorptivity, which could hinder its detection via UV absorbance. To eliminate the influence of other variables, separation was assessed on a conventional CE system (lab-built and commercial) equipped with a UV absorbance detection. These results are described in Chapter 2.

1.3.3 Characterization of UV-CE detection limits

Similarly, to eliminate extraneous variables, limit of detection (LOD) and limit of quantitation (LOQ) were assessed using a conventional CE system with a UV absorbance detector. LOD is the lowest quantity (i.e., concentration) of analyte that can be distinguished from background level. Quantitatively, the LOD is usually determined as the concentration that corresponds to a signal that is 3 times the standard deviation of background noise, whereas, LOQ is the lowest concentration at which quantitative results can be reported with high degree of confidence, and is typically measured at the concentration that corresponds to five to ten times the standard deviation in background signal noise [115]. Since HPLC is currently the accepted modality for separation/detection, its limit of detection and quantitation was used as a benchmark to gauge the performance of the CE system. These results are discussed in Chapter 3.

1.3.4 Assessment of miniaturization and integration

Since a primary motivation to consider an alternative to HPLC was the size and cost of needed instrumentation, it is critical that the above results, evaluated on conventional CE platforms, can be translated into microchip format. It is expected in fact that the microchip will provide many advantages, including features to improve injection repeatability, improve LOD, etc. The main three elements of the microscale system to be developed include injection, separation, and detection. Each component was investigated individually, and ultimately integrated into a single microscale system.

Achieving all of these objectives would provide strong evidence that CE could be used in the chemical purity analysis of PET tracers. This would, in turn, warrant further studies to explore:

- Can the methods be extended to tracers without strong UV absorption? This may require other detection methods could be employed.
- Can a radiation detector be integrated to also provide readout of radiochemical purity?
- Can the CE setup be integrated with additional simple microscale devices to perform a larger subset (or even all) of the required QC tests?

2 Chapter 2: Separation of PET Tracers and Impurities Using CE

2.1 Introduction

To establish the feasibility of using CE for the chemical purity analysis of common PET tracers, the ability to separate/identify the tracer and impurities was first evaluated. Different CE modes (CZE, MEKC) and separation conditions were explored to achieve baseline resolution of all analytes in two samples, a mixture of FLT and known synthesis byproducts, and a mixture of D-FAC isomers (briefly described in Section 1.3.2).

While it would be convenient to have a single set of conditions (buffer system, pH, applied potential, etc.) for all PET tracers, this is likely not be possible due to inherent differences of the various PET tracer synthesis protocols resulting in different sets of impurities and by-products that need to be separated and quantified. The two example systems were thus considered independently. This is not unlike current HPLC methods, which typically differ in conditions (column, flow rate, mobile phase, etc.) for each PET tracer.

A high-performance commercial CE system equipped with a UV absorbance detector was first used to test the ability of CE to separate/identify the two common tracers and their impurities, and then these results were replicated on a lower cost system built in our laboratory. Chapter 4 discusses the integration into a microchip format.

2.2 Materials and methods

2.2.1 Reagents

Sodium phosphate monobasic (NaH_2PO_4), sodium phosphate dibasic dihydrate (Na2HPO4), boric acid, sodium dodecyl sulfate (SDS), ammonium acetate, ethanol (EtOH), sodium chloride (NaCl), sodium deoxy cholate (SDC), dichloromethane (DCM), acetonitrile (MeCN), sodium hydroxide (NaOH), thymine, thymidine, furfuryl alcohol (FA), 2',3'-didehydro-3'-deoxythymidine (stavudine), and 3'deoxy-3'-fluorothymidine (FLT) were purchased from Sigma Aldrich (Milwaukee, WI, USA). Zidovudine impurity B (chlorothymidine, CLT) was purchased from LGC Standards (Wesel, Germany). Kryptofix2.2.2 (K222), 1-(2'-deoxy-2'-fluoro-α-D-arabinofuranosyl)cytosine (β-D-FAC), 1-(2'-deoxy-2'-fluoro- β-d-arabinofuranosyl)cytosine, and (α-D-FAC), 3-N-Boc-5'-O-dimethoxytrityl-3'-O-nosyl-thymidine (Boc-FLT) were purchased from ABX (Radeberg, Germany). Hydrochloric acid 0.1 N was purchased from Beckman Coulter (Brea, CA, USA). Filtered 18 MΩ water was obtained from a Milli-Q Advantage water purification system (Millipore, Billerica, MA, USA).

Stock solutions of 100 mM NaH_2PO_4 (600 mg in 50 mL water) and 100 mM Na_2HPO_4 (890 mg in 50 mL water) were made individually. 30 mM phosphate buffer (PB) was prepared by mixing 1 part 100 mM NaH_2PO_4 with 14 parts 100 mM Na_2HPO_4 and diluting the PO_4 concentration down to 30 mM accordingly. This ratio of mono and dibasic sodium phosphate has been shown to result in a buffer with a pH of 7.4 without the addition of acid or base, which was verified using a pH meter (Mettler, Toledo, Easy five, Columbus, OH, USA). 75 mM borate buffer was prepared via titration of boric acid

with NaOH to obtain a pH of 11.5. 100 mM SDS in 30 mM phosphate buffer (SDS-PB) was prepared by dissolving SDS in 30 mM PB.

2.2.1.1 Separation sample for commercial CE system and HPLC

2.2.1.1.1 FLT sample

A representative FLT sample was prepared from a mixture of FLT plus the known impurities [24] (in higher amounts than would be present in a real sample). To simulate a formulated injectable tracer dose, samples evaluated on the commercial systems were prepared in saline solution (9 g/L or 154 mM of NaCl) using 0.22 µm membrane filtered 18 MΩ deionized water. The mixture contained 200 µm K222, 100 µm FLT, 100 µm thymine, 100 µm thymidine, 100 µm FA, 100 µm stavudine, and 100 µm CLT. Due to the insolubility of the FLT precursor (Boc-FLT) in water, it could not be analyzed using CE or HPLC.

2.2.1.1.2 FAC sample

A mixed isomer sample of purified D-FAC containing known synthesis by-products consisted of a mixture of 50 µM β-D-FAC, 50 µM α-D-FAC and 50 µM K222 [116], and was also prepared in saline solution (9 g/L or 154 mM of NaCl) using 0.22 µm membrane filtered 18 MΩ deionized water.

2.2.1.2 Separation sample for lab-built CE system

2.2.1.2.1 FLT

Due to the lower sensitivity of the lab-built CE system, a higher concentration of the FLT sample mixture was prepared for the lab-built CE system. This mixture contained 3 mM FLT, 3 mM thymine, 6 mM thymidine, 5 mM FA, 6 mM stavudine, and 3 mM CLT in 18 MΩ deionized water. Also, due to th lowered sensitivity, the FLT mixture

was formulated in water as the use of saline produced a higher background noise level. K222 was also excluded from this sample mixture due to its low molecular absorptivity, which would make it undetectable in the setup.

2.2.2 Methods

2.2.2.1 Determination of monitored UV wavelength

To determine which wavelengths should be monitored for each compound, the absorption spectra was obtained for each compound using a UV absorbance detection system. Illumination was provided by a pulsed xenon light source (PX-2, Ocean Optics, Dunedun, FL, USA), which has a wavelength range from 220-750 nm. The collected light was monitored by a spectrometer (USB4000, Ocean Optics), which has a wavelength detection range from 200-900 nm. Source and detector were aligned and coupled to the fiber via a sample cell (CUV-CCE, Ocean Optics), which could be controlled with a custom LabView software using instrument drivers developed by Ocean Optics.

Before the light source was turned on, the dark noise was collected (noise that is present in all electrical devices due to small electrical current that flows through photosensitive diodes, even in the absence of light input), so it could be subtracted out. For each sample, the optical path length of the system was first filled with sample solvent (e.g. buffer) to provide a blank (or reference) signal, which would be divided from the measurement of each sample concentration to remove the effects of the capillary wall/flow cell, buffer, or any other intrinsic properties of the optical path length that can confound the signal associated with the desired analyte.

Transmission percentage (%T) was collected by taking the ratio of the sample signal (S) minus dark noise (D) over reference signal (R) minus the dark noise as shown in Equation 2.1. Equation 2.1 also shows that %T is equal to the intensity of light that passed through the sample, I, divided by the initial light intensity I_0.

$$\%T = \frac{I}{I_0} * 100 = \frac{S - D}{R - D} * 100 \qquad (2.1)$$

%T was then be converted to absorbance (A) by using Equation 2.2.

$$A = 2 - \log_{10} \%T \qquad (2.2)$$

The wavelengths with the maximum absorption value for each compound were then selected to be monitored. As shown by Figure 2-1a, FLT has a maximum absorbance at 256 nm, while furfuryl alcohol (FA) and K222 both have maximum absorbance at 224 nm. It can also be seen that K222 has a lower molar extinction coefficient than both FLT and FA at 224 nm, which will directly affect detection sensitivity for K222. Note that thymidine, thymine, stavudine, and CLT share a similar chromophore with FLT and thus have the same/similar absorbance spectrum. Figure 2-

1b shows the absorbance spectra for β-D-FAC (50 mM) and α-D-FAC (50 mM), showing a maximum absorbance at 256 nm.

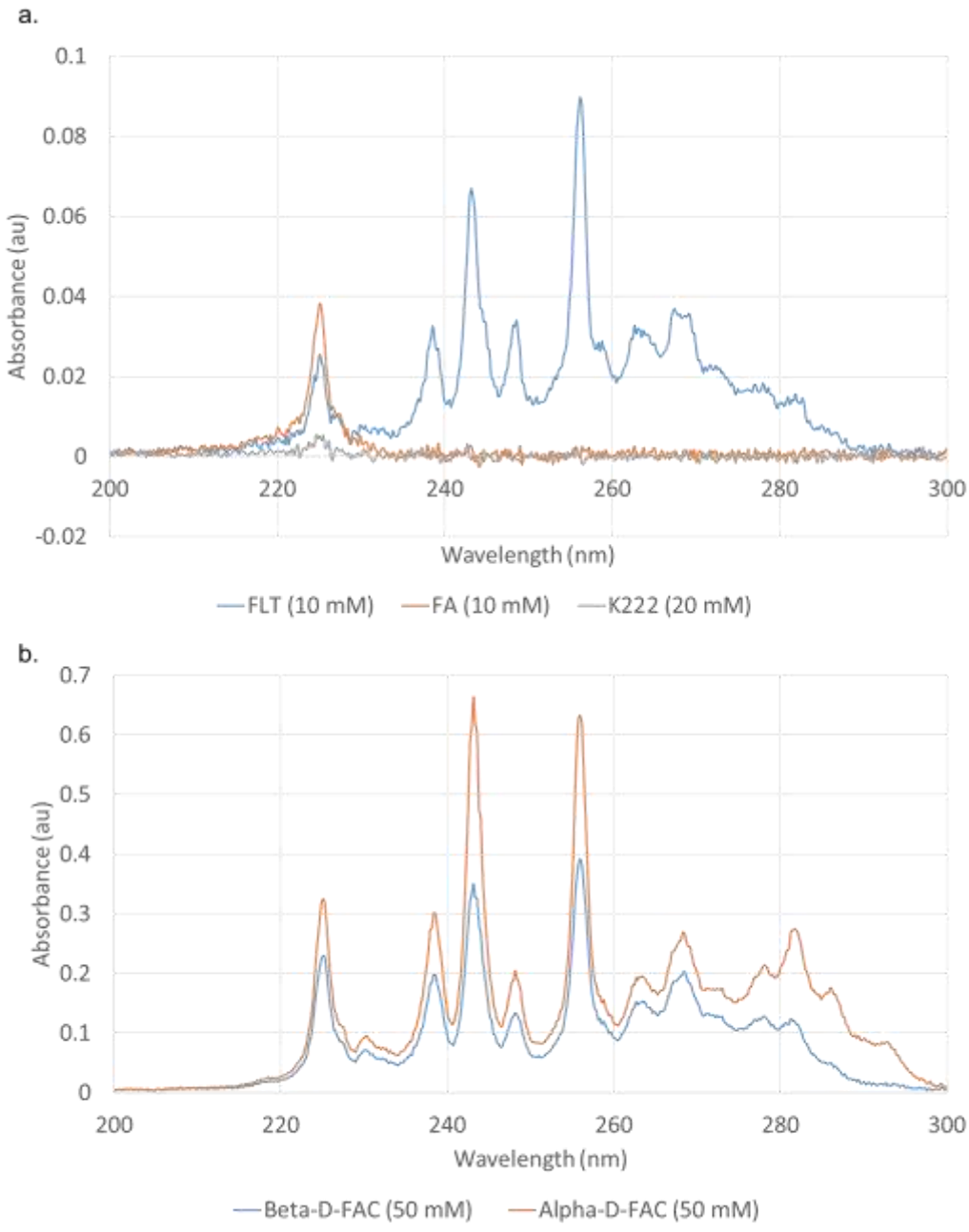

Figure 2-1 **Absorption spectra for various compounds**

(a) FLT (10 mM), FA (10 mM), and K222 (20 mM), and (b) β-D-FAC (50 mM), and α-D-FAC (50 mM). Note: Blank signal not divided out, therefore, the non-uniformity of the light source intensity at different wavelengths is apparent.

2.2.2.2 Separation using commercial CE system

Feasibility experiments were first performed on a commercial CE system (PA800-CE, Beckman Coulter, CA, USA). The PA800-CE was equipped with a 75 µm I.D. (375 µm O.D.) uncoated fused-silica capillary with a total length of 31.2 cm (21 cm from injection end to detector window). The capillary temperature was controlled via a recirculating fluid sheath around the capillary. The PA800-CE utilizes a continuous deuterium UV light source, which has a UV working range of 190-600 nm. Detection was performed using a photodiode array (PDA) detector (Beckman Coulter, CA, USA) monitoring at various absorption maxima slightly different wavelengths (205, 218, 254, and 268 nm), as determined by using similar method described in Section 2.2.2.1. All components of this commercial system are designed for high performance.

Capillary preconditioning was performed by sequentially flushing at 10 psi with the following solutions: 0.1 M HCl for 3 min, 1 M NaOH for 10 min, 0.1 M NaOH for 30 min, and the separating buffer for 30 min. In between successive separations, the capillary was flushed with the separating buffer at 5 psi for 3 min. During the experiment, the capillary and samples were maintained at room temperature (22°C). Details of BGEs used are discussed in the results section.

Samples were injected electrokinetically at +10 kV for 2.5 s and separation was performed at +12 kV. Due to a shorter capillary length of the commercial CE system compared to the lab-built CE system (described below), the electric field used in the commercial system was about 2x higher. Data analysis was performed using the instrument's built-in 32 Karat software (Beckman Coulter, CA, USA). Peaks are identified based on retention times determined from injecting standard compounds

individually. Optimization of peak integration can be performed by adjusting the Threshold value in the Intergration Events Table. The Threshold value adjusts the distance from which a point is considered a cluster point (measureable point), which can be seen as an imaginary line that runs parallel (above and below) the baseline. If a sufficient number of cluster points are grouped together, the software labels the group as a peak. A curve is then drawn through these points that extends to the baseline. The points where the curve meets the baseline are used as the start and stop points of the peak. Using these time points, the peak width, and area for each peak were determined. Migration time of the peak was taken at the peak maximum. Flat regions of the electropherogram were selected for calculation of noise in the baseline signal.

2.2.2.3 Separation using custom-built CE apparatus

A conventional (capillary-based) CE setup was built (schematic shown in Figure 1-8) based on a 75 µm I.D. (375 µm O.D.) Teflon coated fused-silica capillary with a total length of 60 cm (52 cm from injection end to detector window) from Polymicro (Phoenix, AZ, USA). Detection was based on UV absorbance. Illumination was provided by a pulsed xenon light source (PX-2, Ocean Optics, Dunedun, FL, USA), which has a wavelength range from 220-750 nm. The collected light was monitored by a spectrometer (USB4000, Ocean Optics), which has a wavelength detection range from 200-900 nm. Source and detector were aligned and coupled to the fiber via a sample cell (CUV-CCE, Ocean Optics). This setup is capable of making measurements over the wavelength range 220-750 nm. Voltage was applied to the CE system via a variable 30kV power supply (HV350REG(+), Information Unlimited) using 0.3 mm platinum lead wires (43014, Alfa Aesar) to avoid electrode corrosion.

Capillary preconditioning was performed by sequentially filling the capillary with the following solutions: 1 M NaOH, 0.1 M NaOH, and then the mobile phase using house vacuum to pull the solutions through. The solutions remained in the capillary for 10 min, 30 min, and 30 min, respectively. During the experiment, the capillary and samples were maintained at room temperature (22°C). Unlike the commercial CE system, the capillary temperature was not controlled other than being exposed to room air at ambient temperature.

CE sample injection into the separation channel was done electrokinetically. To conserve sample, a 150 µL insert (C4012-530P, Thermo Scientific) was placed inside a 2 mL vial (C4013-15A, Thermo Scientific), and filled with 120 µL of sample. To perform electrokinetic injections, the sample vial containing a known analyte mixture was placed at the beginning of the capillary with the anode. Injection potential (+12 kV) was applied for 5 seconds to inject a small sample plug into the capillary. The sample vial was then replaced with the buffer vial (C4013-15A, Thermo Scientific) filled with 1.8 mL of buffer, and the separation potential (+12 kV) was applied to carry/separate the analytes along the length of the capillary towards the detector. Note that the same separation potential is applied as for the commercial system, but the capillary length of the custom-build system is longer (~2x), leading to a lower electric field for the lab-built CE system. Though it would have been preferable to use ~24 kV potential to keep the electric field the same, the voltage was kept at 12 kV for the lab-built CE system due to the inability of the 30kV power supply to provide a stable potential above 15 kV,. The detection end of the capillary was also placed in a buffer vial filled with 1.8 mL of buffer, which is

attached to the ground of the power supply during injection and separation. Details of BGEs used are included in the results section.

For each experiment, the transmitted light at the selected wavelengths (224 nm and 254 nm) was collected by the spectrometer as a function of time and was manually synchronized to begin recording absorbance vs. time at the start of separation voltage application. This was done by starting the data collection and the application of separation voltage simultaneously. Each electropherogram (of absorbance versus migration time) was analyzed via OriginPro 8.5 peak analysis software (OriginLab, Northampton, MA, USA) to determine peak migration times (t_m), peak widths (w), as well as other values such as peak areas. Peaks are identified based on retention times determined from injecting standard compounds individually. A built-in peak fitting function was analyze the peaks using a Gaussian fit. The software allows users to highlight regions of interest for peak integration. After the peaks are fitted to the curve, peak area, peak height, peak width, and migration time (peak center) could be obtained.

2.2.2.4 Separation of sample via HPLC

To compare separation performance of both the commercial and custom CE systems, separation of similar samples was also performed on an analytical HPLC system. HPLC separations were performed on a Knauer Smartline HPLC system equipped with a Smartline 1000 pump (Knauer, Berlin Germany), Smartline 5050 manager (Knauer, Berlin Germany), Smartline Valve Drive (Knauer, Berlin Germany), and using a C18 Luna reverse phase column (4.6 mm × 250 mm, 5 µm particle size; Phenomenex, Torrance, CA, USA). Detection was performed at 224 and 254 nm with an inline UV detector (2500, Knauer, Berlin, Germany).

The HPLC mobile phase for FLT separations was 10% ethanol in water, at flow rate of 1 mL/min. The HPLC mobile phase for FAC separations was 10% ethanol in 50 mM ammonium acetate, at a flow rate of 1 mL/min. All chromatograms were collected by a GinaStar analog to digital converter (Raytest USA Inc., Wilmington, NC, USA) and GinaStar software (Raytest USA Inc., Wilmington, NC, USA). Peaks are identified based on retention times determined from injecting standard compounds individually and peak analysis was performed using GinaStar software to determine peak widths, migration times, and areas.

2.3 Results and discussion

2.3.1 Separation of FLT and by-products

2.3.1.1 Overview

The overall strategy was to initially test the separation performance of a commercial CE system with both the mixtures samples of FLT and FAC. However, due to limited access to the PA800-CE system (which belonged to another lab), some initial experiments to compare various buffer conditions were performed on the lab-built CE system first.

2.3.1.2 Lab-built CE setup

In order to use CZE to separate multiple analytes within a same sample, each analyte must have a unique charge in order to establish a velocity difference during electrophoretic separation. However, it is known that FLT and its known by-products (thymidine, thymine, FA, stavudine, and CLT) are neutral compounds with high pKa values ranging from ~9.5 and above. Therefore, it is highly likely that MEKC will be needed to separate these compounds.

In order to verify that the lab-built CE system was working properly, the use of CZE was initially tested. This would also provide the migration time of the analytes before addition of surfactants to determine its effect on elution rates. Using the lab-built CE setup, a sample of 2.5 mM thymidine (in water) was first injected. To maintain stable EOF of the BGE, it has been shown that a BGE with pH range between 7-8 is recommended to reduce undesired interactions with the capillary walls [117], and that concentrations are typically kept between 10-100 mM for adequate electrical conductivity without excessive Joule heating [91]. A commonly used BGE of 30 mM phosphate buffer (pH 7.4) made from a mixture of monobasic and dibasic sodium phosphate was selected. Thymidine (pKa of 9.8) would remain neutral in the phosphate buffer, and thus travel at the EOF rate. Using a 60 cm capillary (52 cm effective length), a migration time of 400 seconds was obtained for thymidine. This corresponds to an EOF rate of 0.13 cm/s, which is the migration rate we can expect for all neutral species. Note that for a 5 second injection, this would give an injection plug length of 0.65 cm (~29 nL). To test the inability of separation of neutral analytes, 1 mM stavudine (in water) (pKa of 14.63) was added to the thymidine sample. The inability of CZE to separate was confirmed as only one detectable peak was obtained when a single sample containing both thymidine (2.5 mM) and stavudine (1 mM) was injected and detected.

To separate thymidine and stavudine, we modified the BGE with the addition of surfactants to differentiate the migration rates of both analytes, thus operating in MEKC mode instead of CZE. The most commonly used surfactant with phosphate buffer is SDS [118]. Its critical micelle concentration is 8 mM. SDS micelles have a negative

charge and are expected to move toward the positive electrode. SDS is expected to allow separation of neutral species, but analyte migration times will increase due to interaction with SDS which is moving more slowly than the EOF. Using MEKC, several concentrations of SDS (ranging from 10-100 mM) were added to the 30 mM phosphate buffer and the ability to separate thymidine and stavudine was evaluated. At 40 mM SDS, baseline separation was achieved between the two eluting peaks (2.5 thymidine and 1 mM stavudine), which were identified by subsequently injecting one analyte at a time to determine its unique migration time (Figure 2-2). However, when a sample containing FLT and its five common by-products (6 mM thymidine, 3 mM thymine, 5 mM furfuryl alcohol, 6 mM stavudine, 3 mM FLT, and 3 mM CLT in water) was injected, baseline separation was not achieved under these conditions.

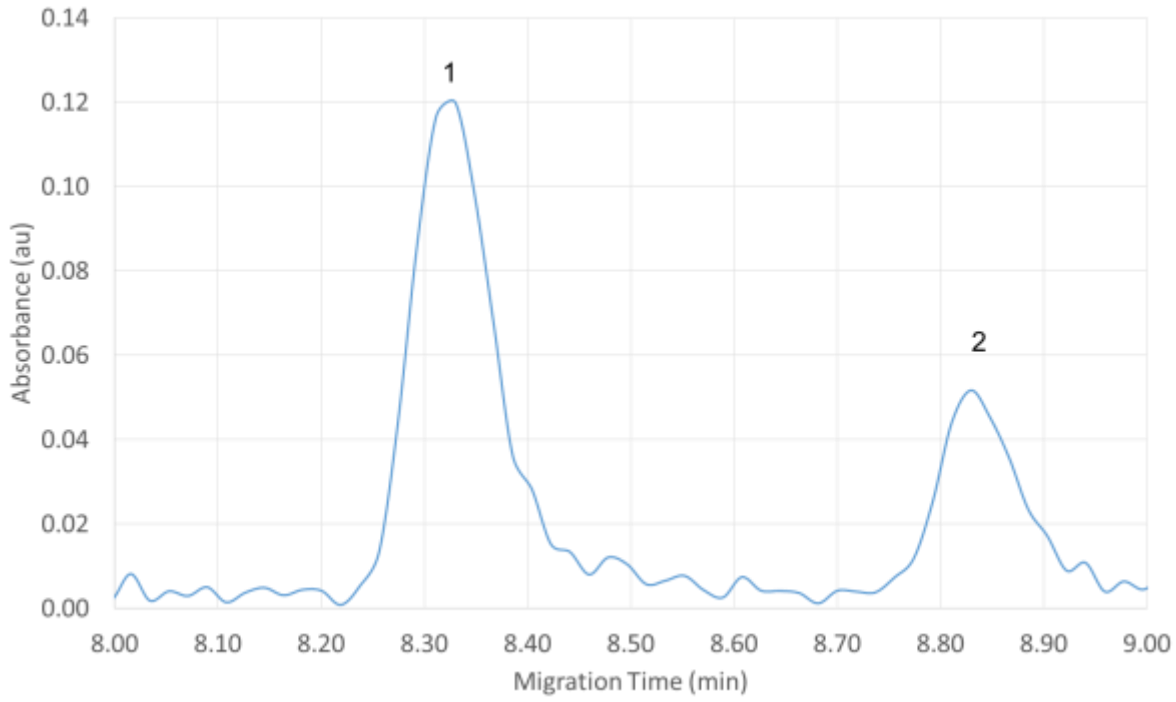

Figure 2-2 **CE chromatogram showing baseline separation of thymidine and stavudine**

2.5 mM thymidine (peak 1) and 1 mM stavudine (peak 2) monitored at 256 nm using a BGE of 30 mM PB and 40 mM SDS.

The concentration of SDS was systemically increased in order to obtain baseline separation of all 6 analytes, which was achieved at 100 mM (Figure 2-3). The resolution (R_s) between thymidine and thymine (the two closest eluting peaks) was calculated to be ~1.5 using Equation 1.7, and because the peaks are relatively symmetric, this indicates baseline separation. Using 100 mM SDS, it was found that the resolution between FLT and its two closest impurities (stavudine and CLT) was greater than 5. Due to the baseline separation, CE can be used to successfully quantify any of the individual species tested. This was repeated several times on the same day (n=15)

without flushing the capillary between injections. A summary of peak widths, migration times, and %RSD is listed in Table 2-1.

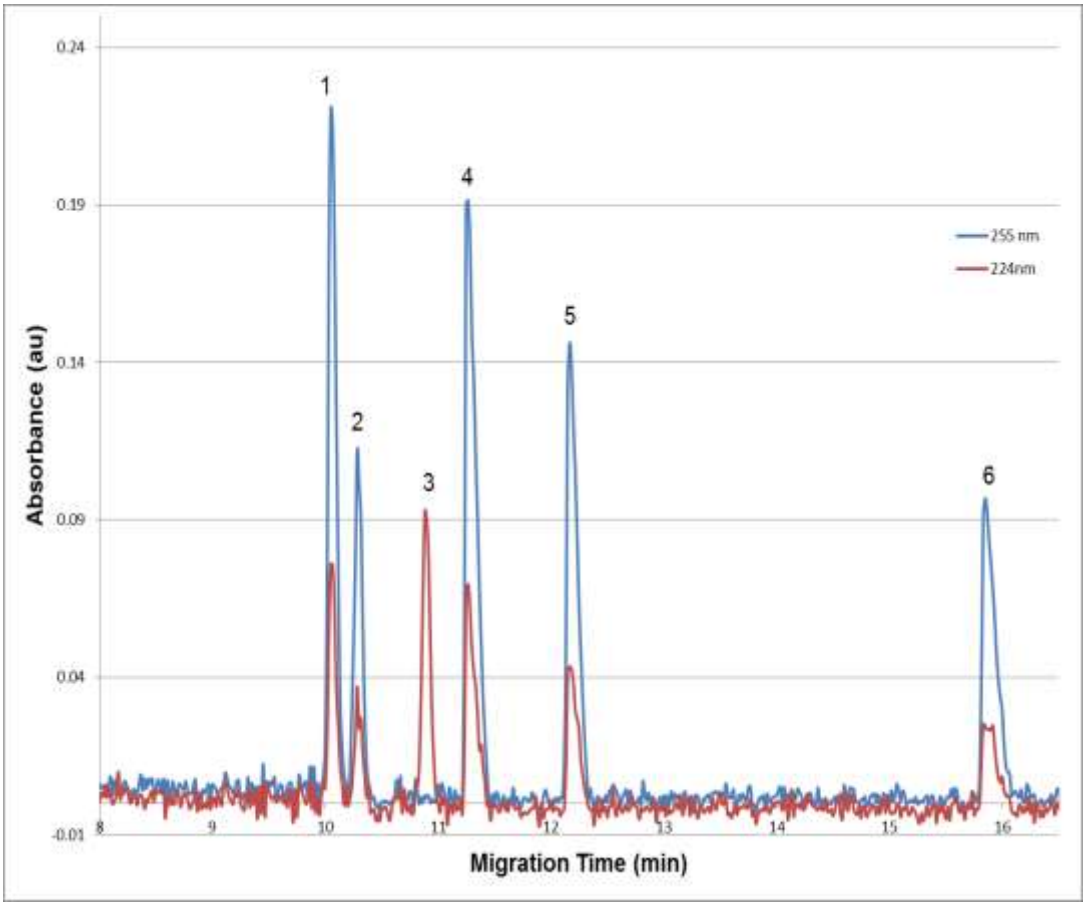

Figure 2-3 **Baseline separation of a mixture of FLT and by-products on the custom-built CE system.**

The mobile phase is 30mM phosphate buffer with 100mM SDS, and the absorbance is monitored at 224 nm (red) and 255 nm (blue). In order of elution, peaks are: (1) 6 mM thymidine, (2) 3 mM thymine, (3) 5 mM furfuryl alcohol, (4) 6 mM stavudine, (5) 3 mM FLT, (6) 3 mM CLT.

Table 2-1 **Peak width (w), migration time (t_m), and migration time reproducibility (%RSD) for the lab built CE separation of FLT and its 5 known byproducts**

BGE: 30mM phosphate BGE with 100mM SDS (n=15).

	Thymidne	Thymine	FA	Stavudine	FLT	CLT
w (min)	0.16±0.02	0.15±0.02	0.17±0.02	0.23±0.02	0.23±0.02	0.28±0.03
t_m (min) ± stdev	10.3±0.4	10.5±0.4	11.2±0.4	11.5±0.4	12.5±0.5	16.3±0.7
Reproducibility (t_m) %RSD	3.9	3.8	3.6	3.5	4.0	4.3

While the use of 100 mM SDS allowed for baseline separation resolution, it also increased migration time due the negative charge of the micelle. Without the use of SDS (i.e. the BGE was 30 mM PBS), thymidine had a migration time of 6.7 minutes. The migration time of thymidine increased to 10.3 minutes when 100 mM SDS was added (an increase of 35%).

Alternative surfactants, and additional buffers with higher pH (to protonate neutral analytes) were explored on the commercial CE system.

2.3.1.3 Commercial CE system

Using the PA800-CE system, the MEKC separation of FLT from all impurities (K222, thymidine, thymine, FA, stavudine, and CLT) was attempted using pH 7.4, 30 mM phosphate buffer with 100 mM SDS (Figure 2-4). The calculated resolution (Rs) between FLT and its two closest impurities (stavudine and CLT) was greater than 4.0, and the other peaks were baseline resolved except for thymidine and thymine. This was repeated several times on the same day without flushing the capillary between runs. A summary of peak width, migration times, and %RSD is listed in Table 2-2.

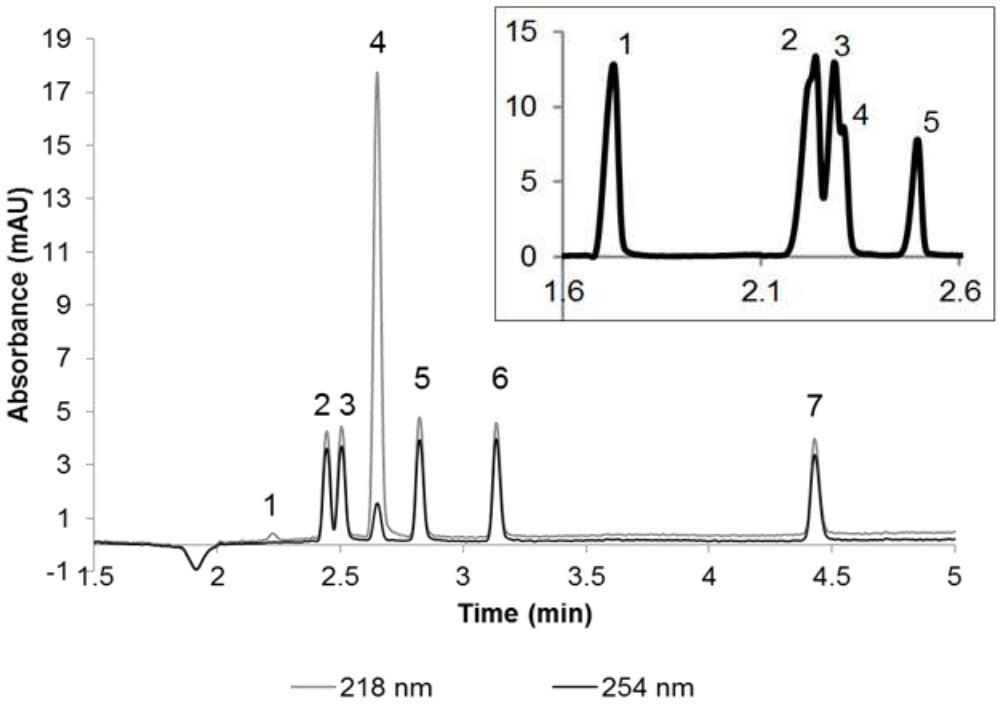

Figure 2-4 **CE electropherograms showing the attempted separation of a representative FLT sample on commercial CE system.**

Using 30mM phosphate BGE with 100mM SDS monitored at 218 nm (gray) and 254 nm (black) the order of elution was: 200 µM K222 (peak 1), 100 µM thymidine (peak 2), 100 µM thymine (peak 3), 100 µM FA (peak 4), 100 µM stavudine (peak 5), 100 µM FLT (peak 6) and 100 µM CLT (peak 7). Insert shows the separation without surfactant, but with 75 mM borate buffer (pH 11.5) to protonate the various species. In the electropherogram, the peaks are FA (peak 1), thymidine (peak 2), FLT (peak 3), CLT (peak 4) and thymine (peak 5). Reproduced with permission from reference [119].

Due to the shorter effective capillary length on the commercial system (21 cm capillary), the separation resolution of thymidine and thymine was lower on the PA800-CE system (R_s = 0.77) compared to the lab-built CE system using a 52 cm capillary (R_s = 1.48). However, an expected shorter overall analysis time was obtained on the PA800-CE system compared to the lab-built CE setup (4.5 min vs. 16 min, respectively) due to the shorter capillary length and higher applied separation field (384 versus 200 V/cm).

Table 2-2 **Peak width (w), migration time (t_m), and migration time reproducibility (%RSD) for the commercial CE separation of FLT and its 5 known byproducts.**

BGE: 30mM phosphate BGE with 100mM SDS (n=4). Adapted with permission from reference [119].

	K222	Thymidine	Thymine	FA	Stavudine	FLT	CLT
w (min)	0.050±0.000	0.065±0.016	0.065±0.016	0.070±0.017	0.070±0.018	0.085±0.016	0.10±0.027
t_m (min) ± stdev	2.18±0.09	2.45±0.1	2.5±0.1	2.6±0.1	2.7±0.1	3.0±0.2	4.2±0.3
Reproducibility (t_m) %RSD	4.1	4.1	4.0	3.8	3.7	6.7	7.1

A further decrease in overall analytical time can be achieved by lowering the ionic strength of the buffer, which increases the EOF. The ionic strength of the BGE can be significantly reduced by removing the surfactant, but because neutral species cannot be separated by CZE, a higher pH is needed to deprotonate the species into their anions. In the separation of FLT and its known by-products, the pKa of the compounds (thymine, thymidine, stavudine, FLT, and CLT) ranges from ~9.5 and above. A commonly used high pH BGE is borate buffer [91]. Various concentrations of borate buffer (pH 11.5) were tested. An example electropherogram demonstrating the attempted separation of the FLT sample with the 75 mM borate buffer is shown in the insert of Figure 2-4. The elution order differs when compared to MEKC. As FA remains uncharged, it was first to elute out with the EOF followed by the anions of thymidine, FLT and CLT. Thymidine, FLT, and CLT remained unresolved due to their similarity in chemical structures with the replacement of a hydroxyl group with a fluorine or a chlorine on the same carbon. Thymine (pKa = 10.5) was the last compound to elute out, and was well-separated from the others, possibly due to the higher negative charge density on the molecule making it more attracted to the positive (HV) electrode. Using a concentration of borate buffer below 75 mM (e.g. 50 mM) resulted in wider analyte

peaks as the BGE was not able to prevent electrodispersion (the broadening of analyte peaks due to variations in the electrical conductivity in the vicinity of the BGE and sample causing the peaks to disperse [120]). The use of borate buffer above a concentration of 75 mM (e.g. 100 mM) produced large fluctuations in the detected signal, which is possibly due to the high conductivity buffer and resulting higher current in the system and increase Joule heating. An increase in Joule heating could change the viscosity of BGE (changes EOF) and cause fluctuations in detection signal, which can cause an increase in peak migration time %RSD and also adversely affect LOD.

An alternative surfactant, sodium deoxycholate (SDC), was also tested (between 10 and 100 mM) due to its ability to form micelles (CMC = 6 mM); however, it was found not to be as effective in separating the analytes as SDS (data not shown). A zwitterionic (dipolar ion) buffer, N-cyclohexyl-3-aminopropanesulfonic acid (CAPS) designed for high pH use, was also tested due to its known advantages of low conductivity to reduce Joule heating effects. However, the use of CAPS buffer did not show an improvement in the separation (data not shown). Also, a significant increase in background noise was observed, which lowered separation resolution by making it more difficult to distinguish the separation between two peaks. At this point, the further optimization of CZE using BGEs high pH was no longer explored as the use of MEKC with a BGE pH of ~7 achieved the complete separation of desired analytes.

In summary, the successful separation of for FLT and by-products was achieved using a lab-built and commercial CE system, establishing initial feasibility of the use of CE to perform chemical purity analysis. The ability to obtain baseline separation of thymidine, thymine, FA, stavudine, FLT, and CLT on lab-built CE system that is on par

with the performance of the commercial CE system also demonstrates the ability to use low cost components to obtain comparable separation. The total analytical time for FLT and by-products obtained on both CE systems will be compared to analytical times obtained for HPLC in Section 2.3.5.

2.3.2 Separation of FAC and by-products

The separation of 200 µM K222, 200 µM α-D-FAC and 200 µM β-D-FAC (prepared as described in Section 2.2.1.1.2) was also performed on the commercial CE system (Beckman PA800-CE). Using the same PB-SDS BGE used for FLT (30 mM phosphate buffer with 100 mM SDS) the separation of β-D-FAC from its anomer α-D-

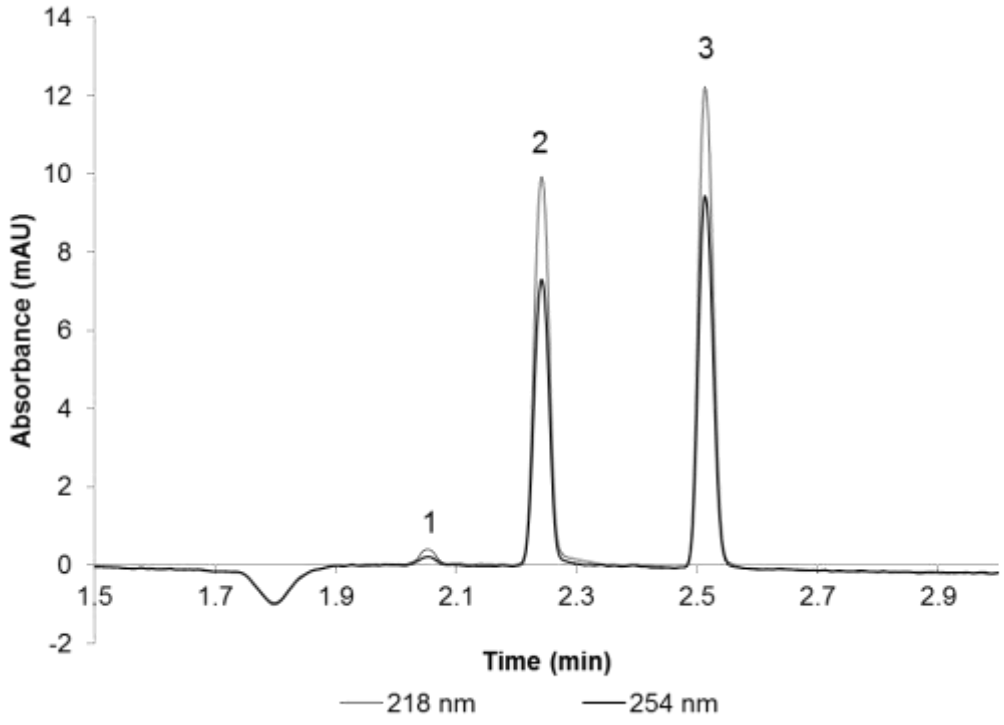

Figure 2-5 **CE electropherograms showing the separation of a representative FAC sample on commercial CE system**.

Using 30mM phosphate BGE with 100mM SDS monitored at 218 nm (gray) and 254 nm (black) the order of elution was (peak, average migration time ± stdev, n = 4): K222 (peak 1), α-D-FAC (peak 2) and β-D-FAC (peak 3). Reproduced with permission from reference [119].

FAC and K222 (Fig. 2-5) was achieved with baseline resolutions (i.e., Rs > 3.0) in less than 2.6 min. A summary of peak width, migration times, and %RSD is listed in Table 2-3.

Table 2-3 **Peak width (w), migration time (tm), and migration time reproducibility (%RSD) achieved for the separation of the mixed FAC sample on the commercial CE system (n=4).**

BGE: 30mM phosphate buffer with 100mM SDS. Adapted with permission from reference [119].

	K222	α-FAC	β-FAC
w (min)	0.065±0.000	0.065±0.018	0.065±0.019
t_m (min) ± stdev	2.04±0.04	2.22±0.04	2.48±0.05
Reproducibility (t_m) %RSD	2.0	1.8	2.0

These results demonstrate that indeed CE is capable of the separation of the FAC isomers (β and α forms). The ability to use CE to separate multiple PET related tracers and by-products further increases confidence in the feasibility to use CE to perform chemical purity analysis.

2.3.3 Separation of K222 in FLT and FAC samples

2.3.3.1 Overview

The successful separation of samples containing FLT and β-D-FAC along with their respective impurities demonstrates feasibility of CE to achieve separation that would be needed to perform chemical purity analysis. (Additional aspects of feasibility including limit of detection and miniaturization will be discussed in later chapters.)

Another potential opportunity for simplification and miniaturization of QC testing of PET tracers is to perform separation and detection of K222 in the same test, thus negating the need for a separate, dedicated testing method for this toxic impurity (intravenous LD_{50} of 35 mg/kg in rats) [121].

Successful separation of K222 from the analytes in the FLT (Figure 2-4) and FAC (Figure 2-5) samples has been demonstrated above using CE with an SDS-containing BGE. However, when examining the limit of detection (Chapter 3) it was found to be insufficient.

The use of SDS was shown to reduce overall sensitivity, however, the exact cause for this is not completely understood. It is possible that due to the longer analytical times with use of SDS, the resulting peak broadening effect lowered the overall peak height. Furthermore, because SDS is known to increase analytical times (e.g., increase of 35% for thymidine using 100 mM SDS, Section 2.3.1.2), we also considered the potential of CZE (i.e. without SDS) to accelerate the separation of K222 from PET tracers for more rapid (and higher sensitivity) detection. Though a CZE test for K222 would require a separate CE run, one could imagine that it would be possible to perform multiple parallel CE separations in a single microfluidic CE device, still providing simplicity compared to the need for a separate spot test.

It is suspected that K222 can readily be separated from the FLT or FAC impurities, even in the absence of micelles, as it would be positively charged in aqueous solutions due to the close association with a sodium or potassium ion (i.e. K222 is typically used in conjunction with K_2CO_3 in 18F-radiochemistry). Therefore, use of CZE to perform K222's separation from other components in the FLT and FAC samples with a neutral pH (PB) could possibly be achieved with reduced analytical times. Note that all other species are not expected to be separated under these conditions, so this approach would only provide a measurement for K222.

2.3.3.2 Commercial CE system

Using an FLT mixture sample (as described in Section 2.3.1.3) and FAC mixtures (section 2.3.2), the successful separation of K222 from all other species was achieved on the PA800-CE system using CZE (with 30 mM PB). Baseline resolution was achieved in both cases (Figure 2-6). The successful separation of K222 from the other species under CZE is consistent with the concept of a positive charge on K222 at this pH (pH 7.4) due to the binding of free sodium or potassium ions in the aqueous sample, whereas the other species were all predominantly neutral. However, it should be stated that if the amount of K222 is approximately 2x greater than the amount of K_2CO_3 used in the synthesis, then this test may underestimate the amount of K222 as not all of K222 would be complexed to a K^+ ion and would not be separated from the FLT or FAC components. Using CZE, a reduction in analytical time for K222 was obtained for both FLT (1.9 minutes without SDS, 4.2 minutes with SDS, %55 reduction) and FAC sample (1.81 minutes without SDS, 2.55 minutes with SDS, %28 reduction). A summary of peak width, and migration times is listed in Table 2-4. Both samples produced an analysis time for K222 of <2 min, which is better than the typical colormetric-spot test used, requiring a time of 5-15 min [34], [121]. This suggests that it may be possible to

perform the K222 test using a CE system, providing a more rapid alternative to the detected TLC or spot tests [32], [122].

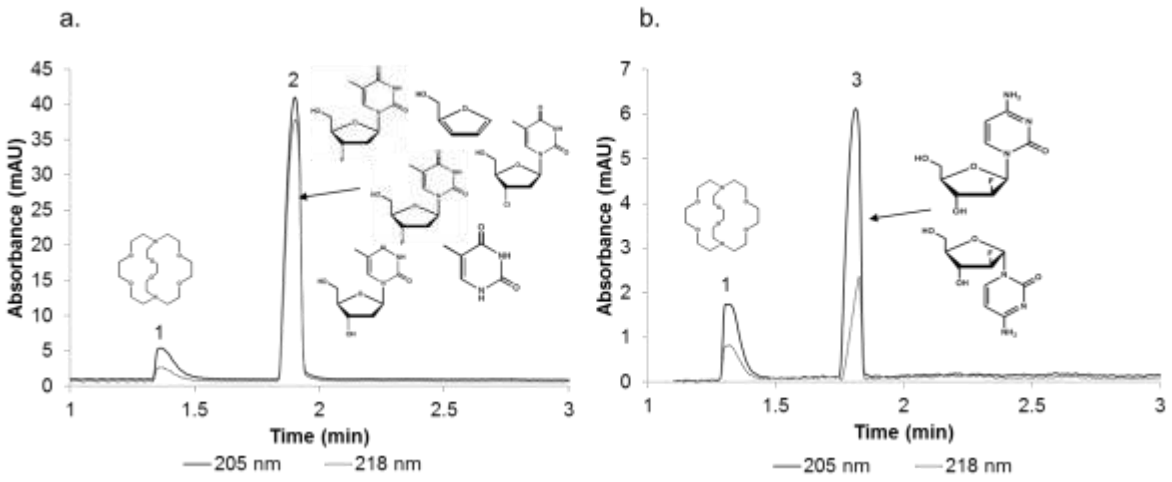

Figure 2-6 **CE showing the separation of K222 from FLT and FAC mixture samples on the commercial CE system.**

Using 30mM phosphate BGE (no SDS) monitored at 205 nm (black) and 218 nm (gray) **a)** shows the separation of K222 (peak 1, 415 µM) from other species in the FLT mixed sample (peak 2; individual analytes not resolved), and **b)** separation of K222 (peak 1, 415 µM) from the FAC sample (peak 3; isomers not resolved). In this buffer only K222 is separated in the samples. Structures of compounds are also shown. Reproduced with permission from reference [119].

Table 2-4 **Peak width (w), and migration time (tm) the commercial CE separation of (a) K222 (415 µM) and FLT sample mixture and (b) K222 (415 µM) and FAC sample mixture**

BGE: 30mM phosphate BGE without SDS (n=4). Adapted with permission from reference [119].

a.

	K222	FLT + Impurities
w (min)	0.17±0.01	0.11±0.01
t_m (min)	1.38±0.01	1.90±0.01

b.

	K222	FAC + Impurities
w (min)	0.14±0.01	0.09±0.00
t_m (min)	1.32±0.00	1.81±0.00

As mentioned above, the separation of FLT from its impurities (other than K222) and separation of the two FAC isomers were not achieved in these particular experiments due to the inability of CZE to separate neutral analytes. Therefore, to

completely separate all analytes in a mixed sample, while maintaining high sensitivity, the use of multiple buffers and CE modes may be necessary. While sequentially running the two separations in the same capillary may not be practical due to the use of different buffers, the implementation of microscale CE may enable these separations to be performed in separate channels in the same device.

2.3.4 Separation of FLT and FAC via HPLC

Separation performance was compared to an analytical HPLC system, which currently serves as a 'gold standard' for PET tracer chemical purity analysis. HPLC chromatograms showing the separation of the mixed samples of FLT and FAC (prepared as described in Section 2.2.1.1) are shown in Figure 2-7, however, K222 could not be detected via HPLC. A summary of peak widths, migration times, and %RSD of migration times for the FLT and FAC samples are listed in Table 2.5 and Table 2.6 respectively. The migration times of all analytes had a RSD ≤ 1%, which is representative of typical HPLC performance [123]. Since the separation conditions

have been optimized for QC testing of these tracers, it is not surprising that the conditions afforded baseline resolution of all species.

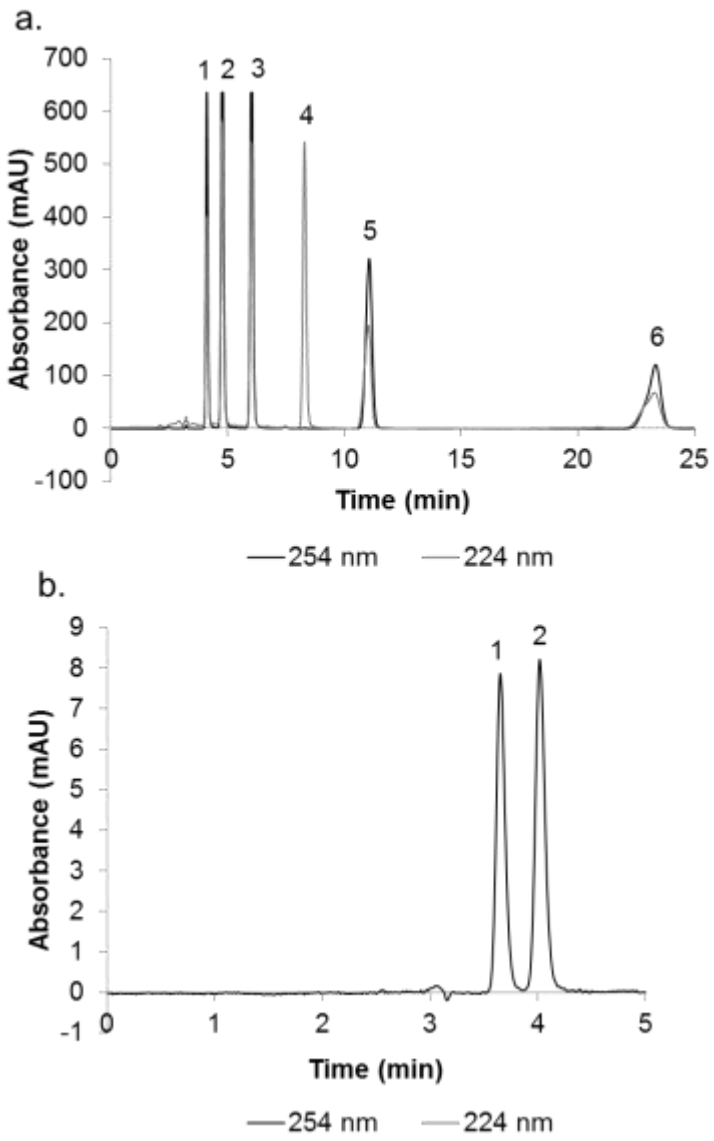

Figure 2-7 **CE showing the separation of representative FLT and FAC sample on HPLC.**

(a) Left: HPLC chromatograms at 224 nm (gray) and 254 nm (black) showing the separation of the FLT representative sample. In order of elution, thymine (peak 1), stavudine (peak 2), thymidine (peak 3), FA (peak 4), FLT (peak 5) and CLT (peak 6). (**b)** HPLC chromatogram at 254 nm showing the separation of the FAC representative sample. In order of elution, α-FAC (peak 1) and β-FAC (peak 2). Reproduced with permission from reference [119].

Table 2-6 **Peak width (w), and migration time of solute (t_m), and migration time reproducibility (%RSD) for the HPLC separation of the FLT mixture (n=4).**

Adapted with permission from reference [119].

	Thymine	Stavudine	Thymidine	FA	FLT	CLT
w (min)	0.35	0.48	0.51	0.52	0.68	1.41
t_m (min) ± stdev	4.10±0.01	5.25±0.01	6.02±0.01	9.05±0.01	11.0±0.1	23.3±0.1
Reproducibility (t_m) %RSD	0.24	0.19	0.17	0.11	0.91	0.42

Table 2-5 **Peak width (w), and migration time of solute (t_m), and migration time reproducibility (%RSD) for the HPLC separation of FAC compounds (n=6).**

Adapted with permission from reference [119].

	α-FAC	β-FAC
w (min)	0.32	0.45
t_m (min) ± stdev	3.65±0.00	4.02±0.00
Reproducibility (t_m) %RSD	0	0

While HPLC is currently the standard methodology for chemical purity analysis of FLT and FAC PET probes, K222 in the sample was not detected at any monitored wavelengths. It is suspected that K222 could not be analyzed because it was trapped in the C18 separation column under the buffer conditions (neutral/basic) used, as suggested by Deng et al. [124].

2.3.5 Comparison of CE and HPLC

The separation of the compounds of interest in both the FLT and FAC samples was demonstrated with baseline resolution using the HPLC and both CE systems (lab-built and commercial). Thus it is feasible to use CE to perform separation of the relevant compounds for these two tracers (and likely many additional ones). Furthermore, it was possible to separate K222 from the other species and detect it with good sensitivity (the limit of detection will be discussed in the next chapter). This suggests that the K222 test

can be performed in a capillary format, which may enable streamlining of the overall QC testing procedure.

An interesting observation was that the elution order of the analytes for CE compared to HPLC was different. For CE, the order was thymidine, thymine, FA, stavudine, FLT, and CLT; for HPLC, the order was thymine, stavudine, thymidine, FA, FLT, and CLT. This could be due to the different phases the analytes were partitioning into (micelles in CE versus C18 in HPLC), as well as the difference in the pseudo stationary phase separation of MEKC (micelles migrate at a different rate than the BGE) versus stationary phase separation of HPLC (porous C18 column).

Due to the insolubility of Boc-FLT in aqueous media, both the CE and HPLC methodologies were unable to inject/analyze Boc-FLT. However, due to this property of Boc-FLT, it is highly unlikely to be found in real PET samples after various purification processes, and quantitative testing of Boc-FLT doesn't seem to be something that is routinely performed during QC testing of FLT [125]. Furthermore, because the separation methods can readily distinguish CLT from FLT, it is likely that Boc-FLT would also be separated from FLT (and CLT) due to the even larger chemical difference imparted by the –Boc protecting group.

Due to the short half-lives of PET radioisotopes, it is generally preferred to have short analysis times, so the final, formulated tracer can be released more quickly after production and reduce the radioactivity loss due to radioactive decay. It should be pointed out that capillary, column, or instrument conditioning can often be performed in conjunction with other steps in the radiosynthesis, and therefore only the time taken to inject, separate, detect, and readout the results are the time limiting factors in QC tests.

In general, CE offers a significant improvement in analysis time over the use of HPLC [126], which is consistent with our findings. The lab-built CE setup offered shorter analysis times (baseline separation) for the mixed FLT sample compared to the HPLC system (lab-built CE system: 16.3 ± 0.7 min (n=15) (average run time ± stdv); HPLC: 23.2 ± 0.2 min (n = 4)). In the case of [^{18}F]FLT, 4.3% of the PET tracer decayed in the additional 6.9 min taken by the HPLC. The analysis time of the FAC sample was also lower for the commercial CE system compared to the HPLC, i.e. PA800-CE system: 3.0 ± 0.6 min (n = 4); HPLC: 4.0 ± 0.0 min (n = 6). Although it may be possible to optimize the duration of the HPLC processes using shorter columns with smaller particle sizes (e.g. 3 µm) and ultra-high pressure pumps to reduce analysis times (as in UPLCs) [26], CE still offers greater ability for miniaturization and lower costs

In comparison to the HPLC (Tables 2-5, 2-6), the reproducibility in the migration times of the commercial CE and the lab built CE systems (Tables 2-1, 2-2, 2-3) were relatively poorer; however, the RSDs were all below 7% (for the slowest migrating compound, CLT). While a shift in migration time by the %RSD values for analyte peaks such as thymidine and thymine will no longer result in baseline separation resolution, this can possibly be improved in the microchip format.

Capillary surface chemistry stability is suspected to play a crucial part to achieving more reproducible migration times as it has been observed that migration times drift through repeated use. This may be due to the unstable conditioning of the capillary wall leading to permanent alterations at the solution/glass interface. By the use of an internal standard and a better capillary conditioning method, it may be

possible to establish longer lasting capillary conditioning for analyte separation [127], [128]. These considerations will be further discussed in Chapter 5.

2.4 Conclusion

The first step in establishing the feasibility of using CE to perform chemical purity analysis on PET tracers has been shown, namely the baseline separation of analytes presented in samples of real PET tracers (FLT and D-FAC) containing a mixture of the tracer and impurities. Furthermore, the potential to combine the determination of K222 into the same system was also suggested. Shorter analysis time for the lab-built was obtained in comparison to HPLC, reducing analysis time by 30% for FLT (16.3 min on lab-built versus 23.2 min on HPLC), which suggests the QC testing may be completed more quickly using CE, reducing the loss of tracer due to radioactive decay.

One aspect that should be further investigated is the role of the sample buffer on the separation performance. In particular, most PET tracers are formulated in saline rather than water, and this could increase background noise level, which can hinder separation resolution.

The next chapter will further investigate the feasibility, and will focus on establishing whether CE has sufficient limit of detection (i.e. comparable to HPLC) for chemical impurity analysis of PET tracers.

3 Chapter 3: Limit of Detection of Capillary Electrophoresis System

3.1 Introduction

The second key to establishing the feasibility of using CE for the chemical purity analysis of common PET tracers and their impurities is to establish whether the LOD is sufficient for quantifying the anticipated species. For some species, regulatory agencies have established maximum amounts or concentrations that are permitted in injectable solutions of PET tracers for human use. For many species, clear limits have not be established and absence of detection via conventional analytical tools (e.g. radio-HPLC) seems to be considered sufficient evidence that the species has been eliminated during the purification process. Generally, chemical purity is monitored via HPLC coupled to a UV-visible absorbance detection cell. The HPLC column provides separation among the tracer and its impurities, and the detection cell enables quantitation of each species as it exits the column. Optical absorbance is a simple and readily available detection method, and is suitable for many classes of tracers, where the tracer and impurities are UV active (i.e. have significant UV absorption). Furthermore, this technique does not require modification of the sample (e.g. unlike fluorescence detection which requires chemical derivatization of the sample [105]). Other CE detection modes include refractive index (RI) [129], [130], capacitively coupled contactless conductivity (C4D) [131], [132], and pulsed amperometric detectors (PAD) [50], [133], [134], however, these are more difficult to implement. RI detectors measures the change in refractive index within the capillary. The greater the RI difference between the sample and the BGE, the higher the signal. C4D is an electrochemical detection method. In general, this methods uses two electrodes positioned outside the capillary. A high-frequency

electric field is applied to the first electrode, which passes through the solution within the capillary, and is recorded on the second electrode. The current through the circuit is affected by the impedance of the environment within the capillary. The change in current through the circuit is measured as analytes passes through the detection region. PAD is another type of electrochemical detector, which uses electrodes within the capillary channel to generate oxidation/reduction reactions. As sample passes the detector, the analytes are either oxidized or reduced, generating a measurable current. PAD applies voltage to the working potential for a short period of time, and is followed by higher or lower potentials to clean the electrode (prevents fouling) for reproducible measurements.

Given that the LODs of typical HPLC systems used in radiochemistry are considered adequate (typically in the micromolar range), we thus aim to establish whether CE can match the detection limit of HPLC for relevant analytes.

As mentioned briefly in Section 1.3.3, the LOD is the lowest quantity (i.e., concentration) of analyte that can be distinguished from background level. Quantitatively, the LOD is usually determined as the concentration that corresponds to a signal that is 3 times the standard deviation of background noise. For absorbance detection, the LOD is directly (but not necessarily linearly [135]) related to the optical path length (OPL) of the system (the ‘thickness’ of the sample through which the light passes). Figure 3-1 illustrates a chromatogram with a background signal (blue), a step function signal at 3x the noise level (orange; corresponding to LOD), and a step function signal at 10x the noise level (grey; corresponding to LOQ) with standard deviation (blue) and signal representing 3x (orange) and 10x (grey) background signal standard

deviation, which corresponds to the LOD and LOQ signal of the chromatogram, respectively.

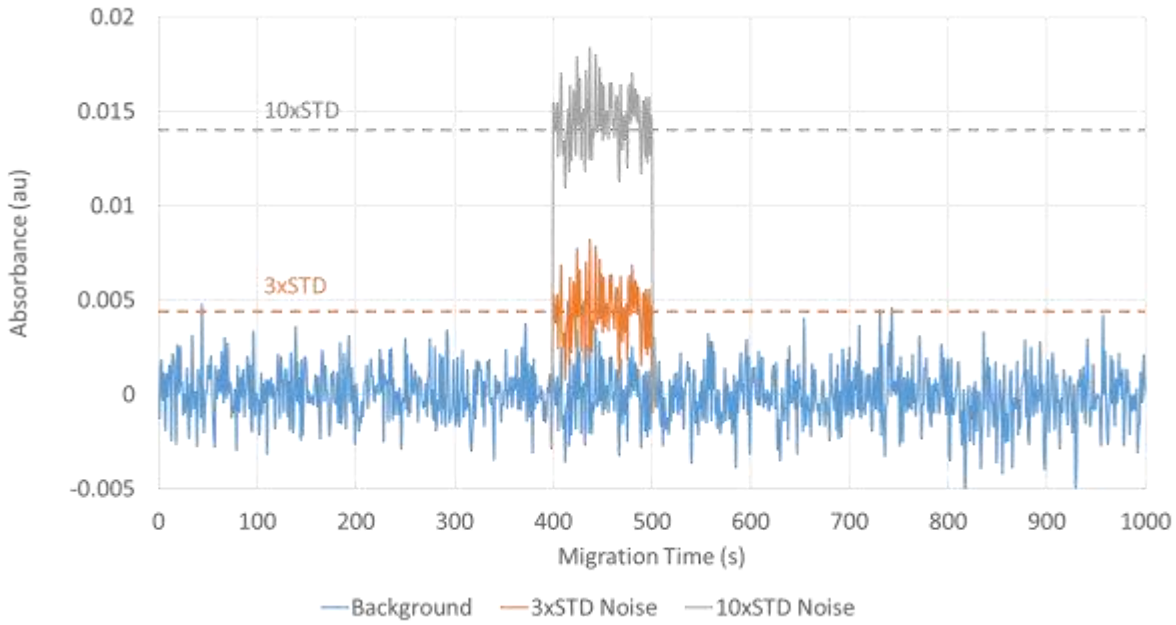

Figure 3-1 **Illustration of limit of detection (LOD) and limit of quantification (LOQ).**

Sample chromatogram illustrating background (blue) with standard deviation (SD) in noise ~ 0.00125 au, signal with mean value at 3xSD of noise (orange), and signal with mean value at 10xSD of noise (grey)

Note that for the purposes of QC testing of PET tracers, it is normally sufficient to demonstrate that the level of a contaminant is below a certain limit. In this case, the LOD should be at or below the allowed limit. This enables an absence of detection to confirm that its level is low enough. LOQ is important only if actual quantitation of the amount is desired.

In typical HPLC systems used in the field of radiochemistry, the flow cell has a path length of 10 mm (10000 µm). In the case of capillary electrophoresis in capillaries or microchannels, optical absorbance is usually measured in a direction perpendicular to the flow through a window in the capillary or chip. The OPL is the inner diameter (ID)

of the capillary or channel, which is typically limited to only about 30-100 µm. Typically, this short optical path results in a relatively high (poor) LOD in CE systems. Unfortunately, commercial HPLC flow cells are typically not suitable for use with CE due to the larger internal diameter which cannot be interfaced to the capillary without significantly disrupting the flow and leading to dispersion. However, several methods have been attempted to enhance the absorbance detection sensitivity of CE by extending the optical path length (Figure 3-2). These approaches include the use of rectangular capillaries [136], bubble cells [137], [138], multi-reflection cells [101], [139], and Z- [140], [141], U- [142], and inversed T-shaped flow cells [143], [144]. Rectangular shaped capillaries are used to increase the amount of light passing through the detection window compared to a circular capillary. A bubble cell opens up the inner diameter within the capillary (within the detection window) creating a short region with longer optical path length. The Z- and U-shaped cells uses a similar concept to the bubble cell by directing the flow to be inline with the detection window, rather than perpendicular, and thus increasing the optical path length within the detector. Similarly, the inversed T-cell splits the flow at the T-intersection, allowing the sample to increase its length within the detection window. The multi-pass approaches use mirrors around the detection region to reflect the light through the channel multiple times to increase the optical path. While capillaries with integrated bubble cells are commercially available by Agilent Technologies (Santa Clara, CA, USA), they are usually designed to be used only on their commercial CE system. Polymicro Technologies (Phoenix, AZ, USA) offers square/rectangular shaped capillaries, which offer a small increase in average

optical path through the capillary, but are typically more expensive (~3x) than standard capillaries due to the increased complexity of fabrication.

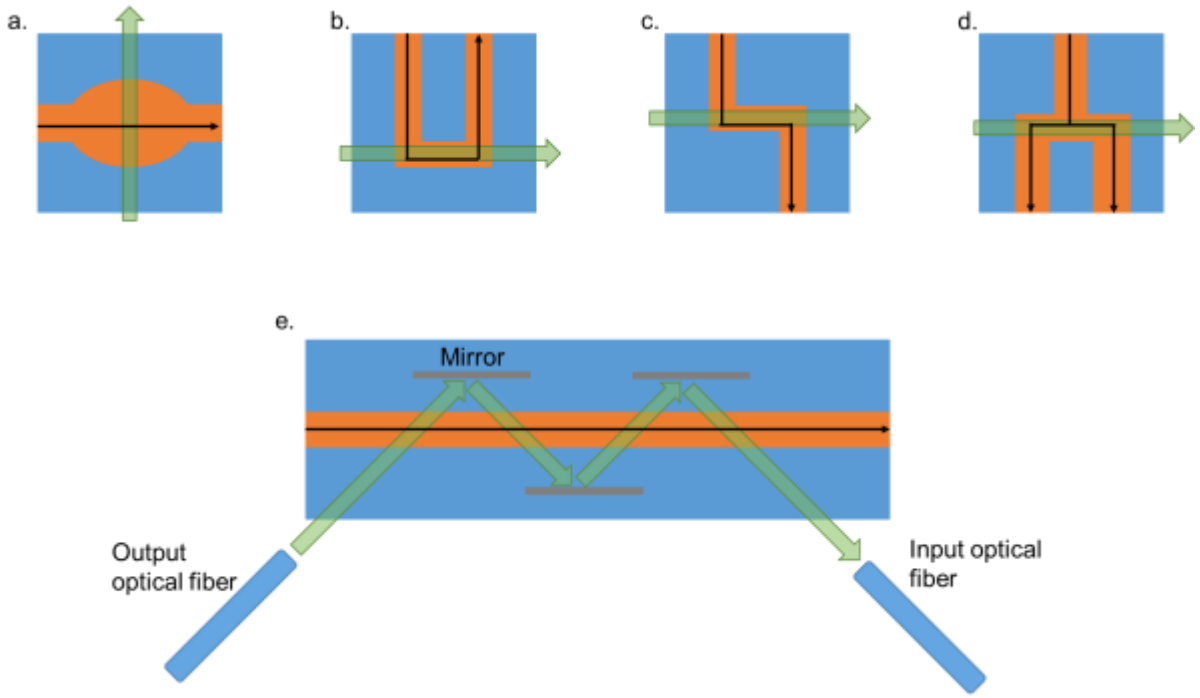

Figure 3-2 **Methods of increasing the optical pathlength.**

Single-pass absorption flow cell geometries with enhanced pathlength include: (a) bubble cell; (*b)* U-shaped cell; (*c)* Z-shaped cell; (*d)* T-shaped cell; and (*e)* multi-reflection cell. Yellow/orange indicates the liquid; g*reen arrow indicates optical detection path; black arrow indicates flow path.*

Another method to improve sensitivity is to reduce the background noise of the detection system. There are several sources of background noise, including variation in light source intensity, spectrometer dynamic range and signal to noise ratio, and mechanical stability of the optical system (i.e. light source, detection cell, and detector). Variations in light source intensity result in fluctuations in the baseline signal that contribute to the noise. Noise generated due to the spectrometer is typically caused by dark current (small electrical current that flows through photosensitive diodes, even in the absence of light input) that is present in all electrical devices. Noise can also be

introduced due to quantization error, due to the digitization of the signal. Any mechanical instability of the optical cell also affects the background noise as the optical detector will be sensitive to physical vibrations in the environment, which can impact the efficiency of light coupling at the input or output of the optical path, leading to fluctuations in the baseline signal that contribute to noise. Reducing these sources of noise can improve the LOD, and allow detection of lower sample concentrations.

An increase in intensity of the incident light can also improve sensitivity as it can increase the signal. Noise associated with the light source is also increased, but there is generally an overall improvement in the signal to noise ratio, because many sources of noise are independent of the noise in the light source.

In this chapter, we explore and compare the performance (LOD and LOQ) of optical detection in CE and HPLC using FLT and D-FAC samples (described in Chapter 2) as examples. We first evaluate a commercial CE system and find that, despite the short optical path length (75 μm) of the CE system, the LOD approaches that of the HPLC system with much longer optical path (1 cm). However, because commercial CE systems are typically designed for high-flexibility across a broad range of analytical applications, they tend to be quite expensive and bulky (comparable in size to HPLC systems). We therefore also evaluated a custom-built system using lower-cost detector components. Though the performance was adversely impacted, experiments guided potential hardware and design optimizations, many of which are best implemented in microchip format (Chapter 4), but can help a low-cost CE system match or exceed the LOD and LOQ of the commercial CE and HPLC systems.

3.2 Materials and methods

3.2.1 Detection Apparatus

The commercial CE system (PA-800 CE, Beckman Coulter) uses a capillary cartridge (Figure 3-3) to house the 75 µm ID capillary and fiber optic connections. The geometry of the detection cell is similar to the CUV-CCE (Ocean Optics) sample cell, which aligned the illuminating and detection fiber inline across the capillary. The illumination fiber is connected to an internal deuterium lamp light source, and the detection fiber interfaces with a photodiode array for detection at multiple wavelengths simultaneously.

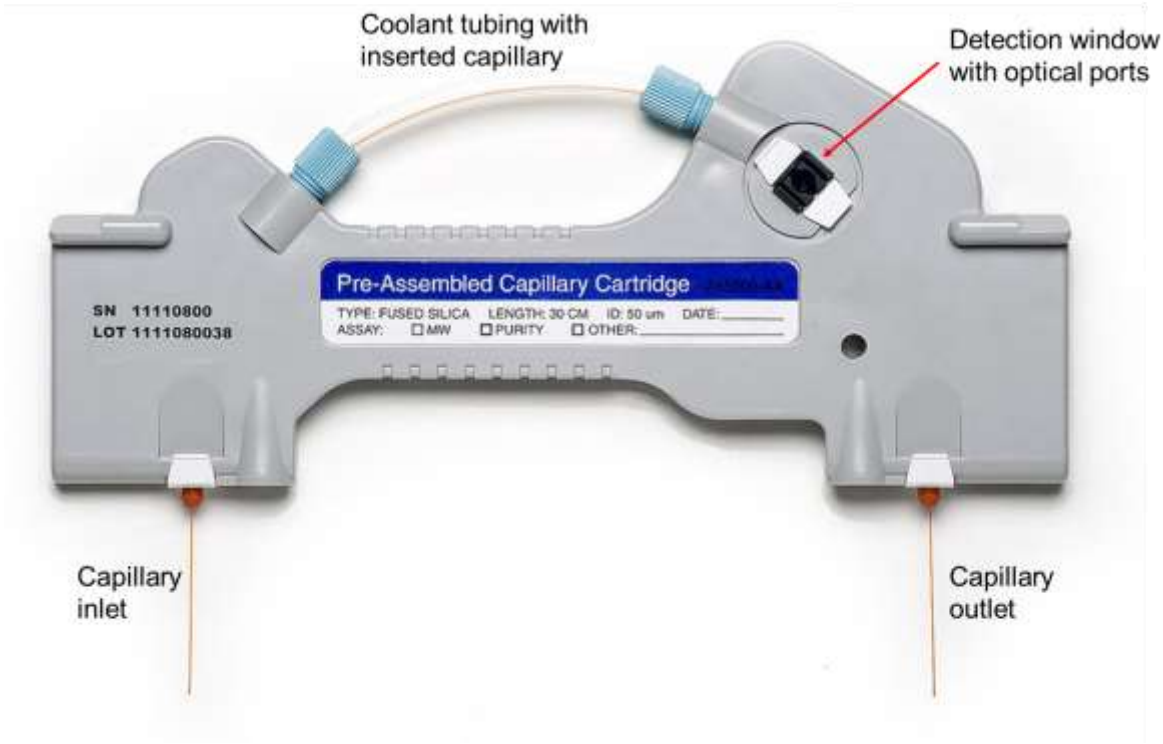

Figure 3-3 **Image of capillary cartridge used for PA-800 CE system**.

Detection window houses the capillary similarly as the CUV-CCE capillary cell shown in Figure 3-4, using the ID of the capillary as the optical path length. The detection cell of the cartridge mates to an optical system that is part of the instrument.

The lab-built setup is the same as used for experiments in Chapter 2. Detection is performed in a CUV-CCE sample cell (Ocean Optics, Dunedun, FL, USA), which is a micro-cross fitting used to interface a 75 µm ID fused glass capillary (Polymicro, AZ, USA) to optical fibers connected to a light source and a detector, illustrated in Figure 3-4. The intact capillary is inserted through the fitting, and optical fibers are aligned on opposite sides of the capillary. The setup uses 300 µm solarization-resistant optical fibers with an aluminum coating (i.e., 300 µm OD; Ocean Optical Dunedun, FL, USA). These fiber cables are connected to a light source (PX-2 pulsed xenon lamp, Ocean Optics; or DH-2000-BAL continuous deuterium lamp, Ocean Optics) and a spectrometer (USB4000, Ocean Optics; or QE-PRO, Ocean Optics). The PX-2 pulsed xenon light source represents the lower end of the price spectrum for an off-the-shelf illumination source, but has a pulse-to-pulse variation in light intensity from 3-12% depending on pulse frequency [145], which directly leads to fluctuation of the sample or background level and introduces considerable noise that can adversely affect LOD. In contrast, the DH-2000-BA has a far more stable light output intensity (output drift of less than 0.01% per hour [146]), but is 5x more expensive. Similarly, the USB4000 is the least expensive detector, with an intrinsic signal to noise ratio of 275:1. The QE-PRO has significantly expanded dynamic range and a signal to noise ratio of 1000:1, but is roughly 20x more costly. The performance of the system with the higher end hardware components (DH-2000-BAL and QE-PRO) was compared to that of the system using the lower end

components to determine its effect on LOD and LOQ. We appreciate the generous support of Ocean Optics in loaning these devices to perform this characterization.

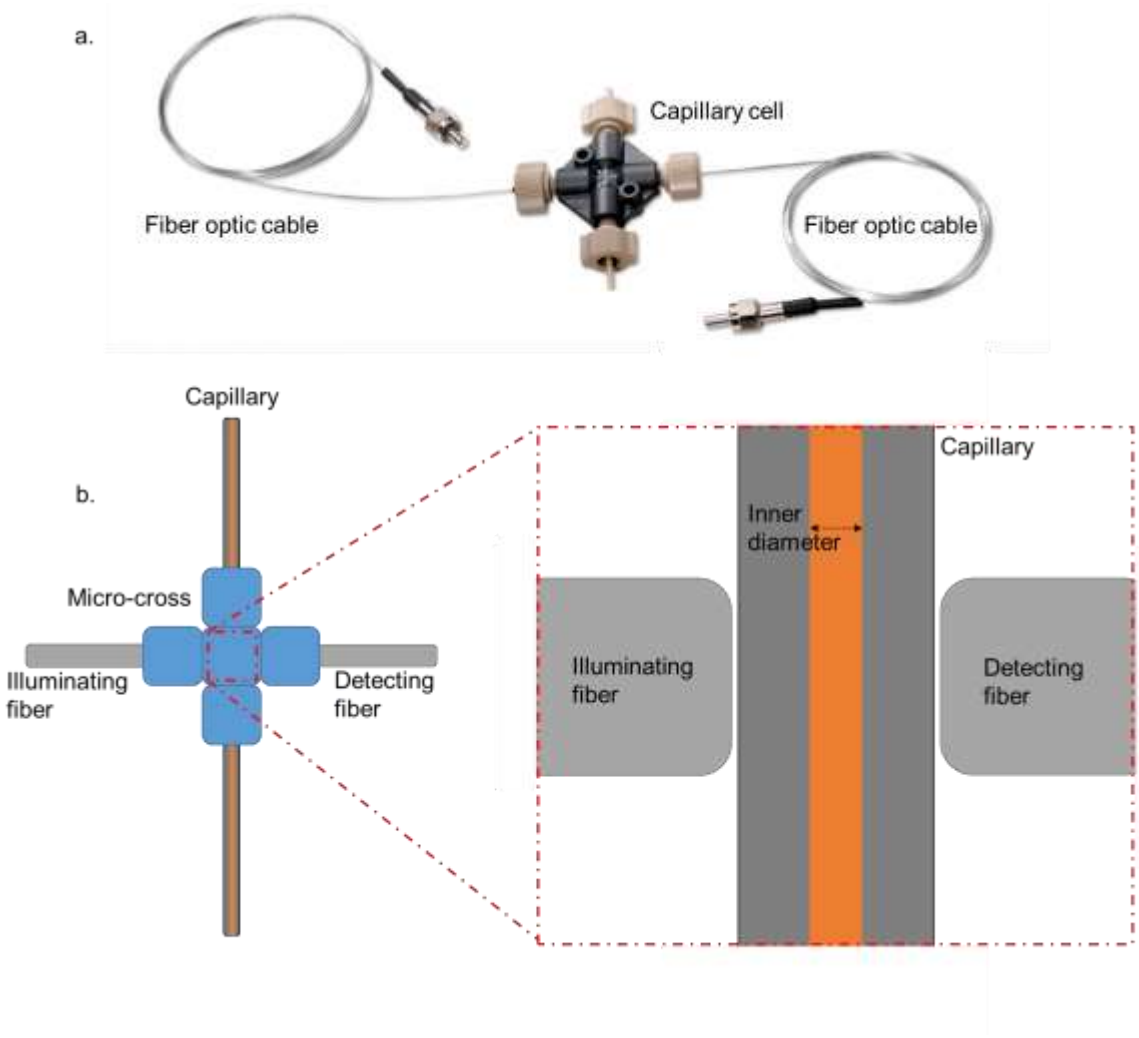

Figure 3-4 **Detector for lab-built CE system.**

a) Image of CUV-CCE capillary cell with fiber optic cables. **b)** (Left) illustration of capillary cell with inserted capillary and fiber optics cables, and (Right) schematic of internal structure. The optical path length is equal to the inner diameter of capillary.

The analytical HPLC system is equipped with a Knauer 2500 UV detection unit (Figure 3-5). Illumination is provided by an internal deuterium lamp source, and detection is performed with a photodiode array for multiple wavelength detection. The optical path length is 10 mm.

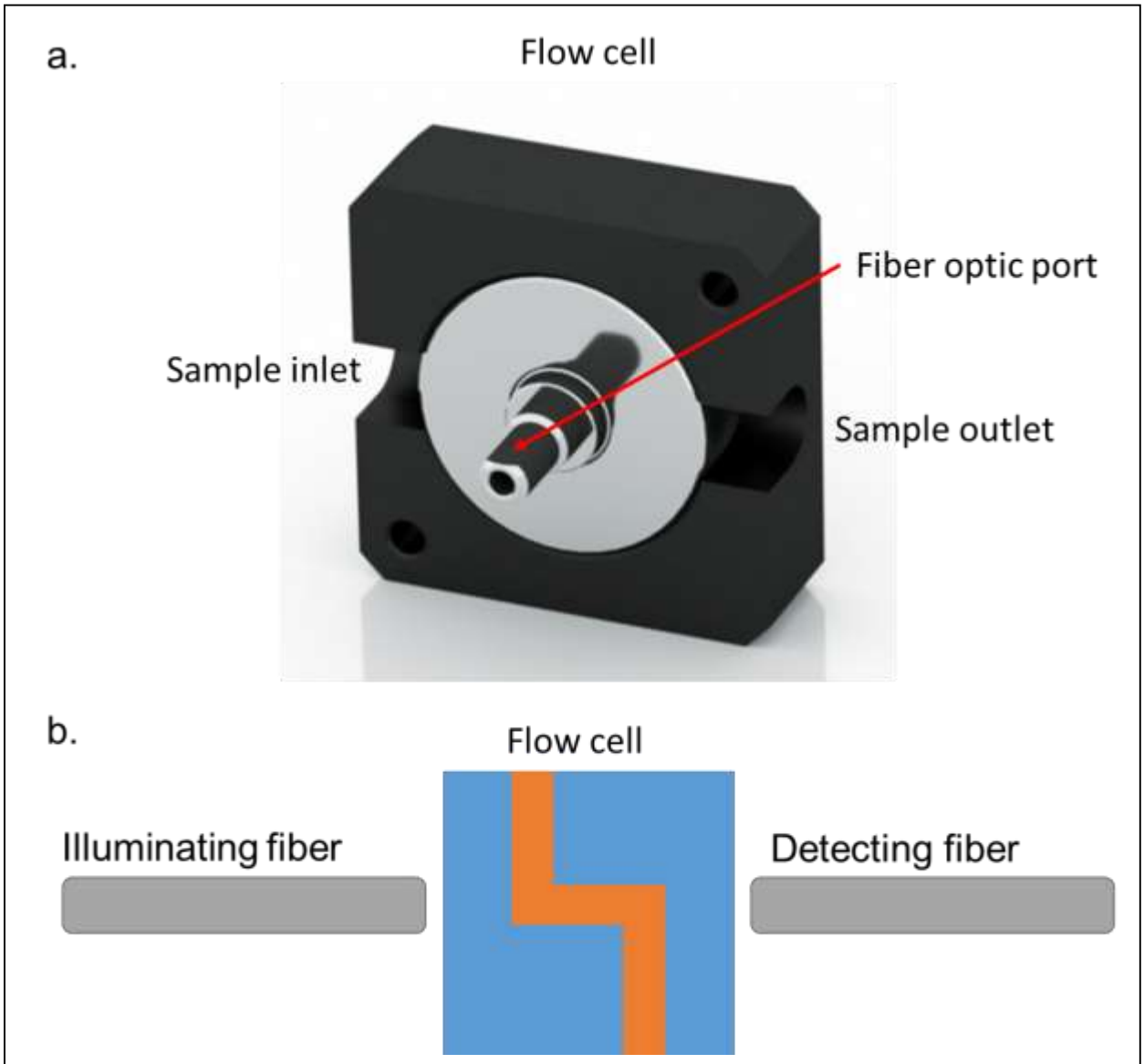

Figure 3-5 **Detection cell used in the HPLC system.**

(a) Flow cell used in Knauer HPLC system with inline UV detector (Knauer 2500 UV). **(b)** Illustration of internal optical path length and fiber optic placement.

3.2.2 Reagents

Sodium phosphate monobasic (NaH_2PO_4), sodium phosphate dibasic dihydrate (Na_2HPO_4), sodium dodecyl sulfate (SDS), thymine, thymidine, furfuryl alcohol (FA), 2',3'-didehydro-3'-deoxythymidine (stavudine), and 3'deoxy-3'-fluorothymidine (FLT) were purchased from Sigma Aldrich (Milwaukee, WI, USA). Zidovudine impurity B (chlorothymidine, CLT) was purchased from LGC Standards (Wesel, Germany). Kryptofix2.2.2 (K222), 1-(2'-deoxy-2'-fluoro-α-d-arabinofuranosyl)cytosine (β-FAC), 1-(2'-deoxy-2'-fluoro- β-d-arabinofuranosyl)cytosine, and (α-FAC) were purchased from ABX (Radeberg, Germany).

3.2.3 Methods

3.2.3.1 General procedure for determining the LOD and LOQ

First, an absorption spectrum was measured for each compound as described in Section 2.2.2.1 to determine the wavelength that would give the largest absorbance signal.

Light intensity is important in optimizing LOD and LOQ. To optimize the signal to noise ratio, the intensity is set so that the detector reads 90% of its maximum value for the blank single (i.e. to avoid saturation). (All other samples are expected to have higher absorbance, and thus lower intensity reaching the detector, than the blank sample.) The intensity of the deuterium light source could be controlled directly. However, the intensity of the PX-2 pulsed xenon light source could not be adjusted; instead intensity was adjusted by displacing the end of the illumination fiber away from the ideal installation point (i.e. in contact with the capillary wall). This displacement reduces the

efficiency of coupling of light into the sample and detector, reducing the overall intensity received.

Dark noise and blank (reference) signals were also obtained as described in Section 2.2.2.1. The absorbance signal (Equation 2.2) with the capillary filled with buffer (i.e. blank/reference) was then recorded for a period of time (~ 1 min) and averaged to calculate the standard deviation in background absorbance noise (Figure 3-2) to be used to calculate LOD and LOQ.

Next, several concentrations of each analyte (ranging from ~0.10-50.0 mM in water) were used in sequence to fill the optical path length of the system. The absorbance was measured for each sample at the desired wavelength(s) for a duration of time (~ 1 min) to ensure a stable signal and was averaged to obtain one data point. This was repeated 3 times while flushing the optical path length with blank solution between each measurement. The three data points were then averaged to obtain an overall absorbance value for the particular concentration of the particular sample.

To ensure the optical path length was completely filled with sample and that the concentration of the analyte in the detector region was the same as the initial concentration in the sample vial, a sample volume much greater than the volume of the optical path length was hydrodynamically pushed through the detection region of the system, to ensure that the previous sample was completely displaced and the optical path was filled completely with the new sample. Also, the most dilute (low concentration) samples were measured first prior to higher concentration samples.

The overall average absorbance signal (obtained as described above) of the analyte at each concentration was then plotted on a graph of signal vs. concentration

(see Appendix). Due to the linear relation predicted by Beer's law (Equation 1.8), a straight line was then fitted to the linear region of the plot, to give a calibration curve relating signal and concentration (see, for example, Figure 3-6). It should be noted that there are limitations to Beer's Law. At high concentrations the linear relationship between absorbance and analyte concentration can break down possibly due to a change in index of refraction (n) of the solution, electrostatic interactions between molecules in close proximity, or scattering of light due to particulates in the sample [147]. This limitation causes linearity of the plot to be achieved only at concentrations below ~10 mM.

Using the fitted equation, the LOD and LOQ were calculated by solving for the concentration that corresponds to 3 and 10 times the standard deviation in background absorbance noise, respectively.

3.2.3.2 Analysis of samples via lab-built conventional CE setup

The lab-built CE system was tested in two hardware combinations: (i) PX-2 pulsed xenon light source with USB4000 spectrometer and (ii) DH-2000-BAL continuous deuterium light source with QE-Pro spectrometer. Samples of FLT and known by products (thymidine, thymine, FA, stavudine, and CLT) were formulated in 18 MΩ deionized water and analyzed. Sample measurements were done as described in Section 3.2.3.1 and wavelengths were selected as described in Section 2.2.2.1. The two optimal wavelengths (224 nm to detect furfuryl alcohol and 256 nm to detect all other compounds) were monitored to generate calibration curves for LOD and LOQ determinations for each species in each of the two system configurations.

3.2.3.3 Analysis of sample on commercial CE system

The commercial CE system (PA800-CE) with a built in photodiode array detector and continuous deuterium light source was tested as described in Section 3.2.3.1. FLT related compounds (thymidine, thymine, FA, stavudine, FLT and CLT), and FAC related compounds (α-D-FAC, β-D-FAC, and K22) were formulated in water and analyzed. Wavelengths were selected as described in Section 2.2.2.1. The two optimal wavelengths (218 nm to detect furfuryl alcohol and 254 nm to detect all other FLT-related compounds) were monitored to generate calibration curves for LOD and LOQ determinations for FLT related compounds and three wavelengths (205 nm to detect K222, 218 nm and 254 nm to detect α-FAC and β-FAC) were monitored for FAC-related compounds.

3.2.3.4 Analysis of sample via HPLC

The HPLC system with a built in photodiode array detector and continuous deuterium light source was tested as described in Section 3.2.3.1. FLT related compounds (thymidine, thymine, FA, stavudine, FLT and CLT), and FAC related compounds (α-D-FAC, β-D-FAC, and K22), formulated in 18 MΩ deionized water, were analyzed. Wavelengths were selected as described in Section 2.2.2.1. The two optimal wavelengths (224 nm to detect furfuryl alcohol, and all FAC-related compounds and 254 nm to detect all other FLT-related compounds) were monitored to generate calibration curves for LOD and LOQ determinations. Sample was injected into the flow cell using an external syringe.

3.3 Results and discussion

3.3.1 Detection/quantification limits of HPLC system

As a benchmark comparison, the LOD and LOQ of both FLT and FAC sample were evaluated on the HPLC system. The standard deviation in noise for 254 nm and 224 nm were 0.1 mAU and 0.5 mAU, respectively. Measured at the absorption maximum at 254 nm, the LOD and LOQ for FLT were 2 and 5 μM, respectively. For FAC, the LOD and LOQ were 5 and 9 μM, respectively. A list of LOD and LOQ for FLT and FAC related compounds is listed in Table 3-1. Only FLT, β-FAC, furfuryl alcohol, and stavudine were tested on the HPLC system due to similar chromophores and expected extinction coefficients to related compounds (i.e., FLT and stavudine were expected to have similar LOD as thymine, thymidine, and CLT, and β-FAC was expected to have similar LOD as α-FAC). K222 could not be detected in the sample at any monitored wavelength, as it is suspect to be trapped in the C18 separation column as suggested by Deng et al. [124].

Table 3-1 **Limits of detection (LOD), and quantification (LOQ) of FLT samples on HPLC system.**

Adapted with permission from reference [119].

		FLT	β-FAC	FA	Stavudine
254 nm	LOD	2 μM	5 μM	n/a	2 μM
	LOQ	5 μM	9 μM	n/a	4 μM
224 nm	LOD	n/a	n/a	35 μM	n/a
	LOQ	n/a	n/a	116 μM	n/a

3.3.2 Detection/quantification limits of commercial CE system

The linear calibration curves for the PA800-CE equipped with a 75 µm ID capillary revealed the LOD and LOQ for thymine, thymidine, FA, stavudine, FLT, and CLT to be in the ranges 2-12 and 13-25 µM, respectively, at their optimal wavelengths for detection (218 and 254nm). The standard deviation in noise for 254 nm and 218 nm were 0.09 mAU and 0.1 mAU, respectively. A complete list of LOD and LOQ for the FLT related compounds is listed in Table 3-2.

Table 3-2 **Limits of detection (LOD), and quantification (LOQ) of FLT samples on commercial CE system.**

Adapted with permission from reference [119].

		Thymidne	Thymine	FA	Stavudine	CLT	FLT
254 nm	LOD	5 µM	5 µM	n/a	7 µM	6 µM	6 µM
	LOQ	13 µM	14 µM	n/a	15 µM	15 µM	20 µM
218 nm	LOD	n/a	n/a	11 µM	n/a	n/a	n/a
	LOQ	n/a	n/a	36 µM	n/a	n/a	n/a

The commercial CE system was also used to determine the LOD and LOQ of β-D-FAC, α-D-FAC and K222. Linear calibration curves at 218 nm revealed the LOD and LOQ to be around 9-12 and 24-32 µM, respectively, for both anomers of FAC. An LOD and LOQ of 120 and 390 µM, respectively, was observed for K222 at 205 nm. A complete list of LOD and LOQ for FAC related compounds is listed in Table 3-3.

An LOD of 120 µM for K222 is better than the typical colormetric-spot test used, where the reference spot is 50 µg/mL (~133 µM) [34], [121], which demonstrates the suitability of CE to be used for K222 detection in PET.

Table 3-3 **Limits of detection (LOD), and quantification (LOQ) analysis of FAC samples on commercial CE system.**

Adapted with permission from reference [119].

		β-FAC	α-FAC	K222
254 nm	LOD	12 µM	9 µM	n/a
	LOQ	29 µM	32 µM	n/a
218 nm	LOD	9 µM	12 µM	180 µM
	LOQ	32 µM	28 µM	570 µM
205 nm	LOD	n/a	n/a	120 µM
	LOQ	n/a	n/a	390 µM

3.3.3 Detection/quantification limits of lab-built CE system

Using the lab-built CE system equipped with the pulsed xenon light source (PX-2) and USB400 spectrometer, the absorbance was measured for several concentrations (0-50 mM) of thymidine in water. The average absorbance for each concentration is plotted versus thymidine concentration in Figure 3-6a. The linear range was found at concentrations below 10 mM (Figure 3-6b). The standard deviation in background absorbance noise of this setup was determined to be 4.0 mAU for 254 nm and 4.1 mAU for 224 nm. Therefore the absorbance values that correspond to the LOD and LOQ of thymidine were 12 mAU and 40 mAU, respectively. Plugging these absorbance values into the linear equation provided in Figure 3-6b, the LOD and LOQ for thymidine were determined to be 210 µM and 750 µM, respectively. A complete list of LOD and LOQ

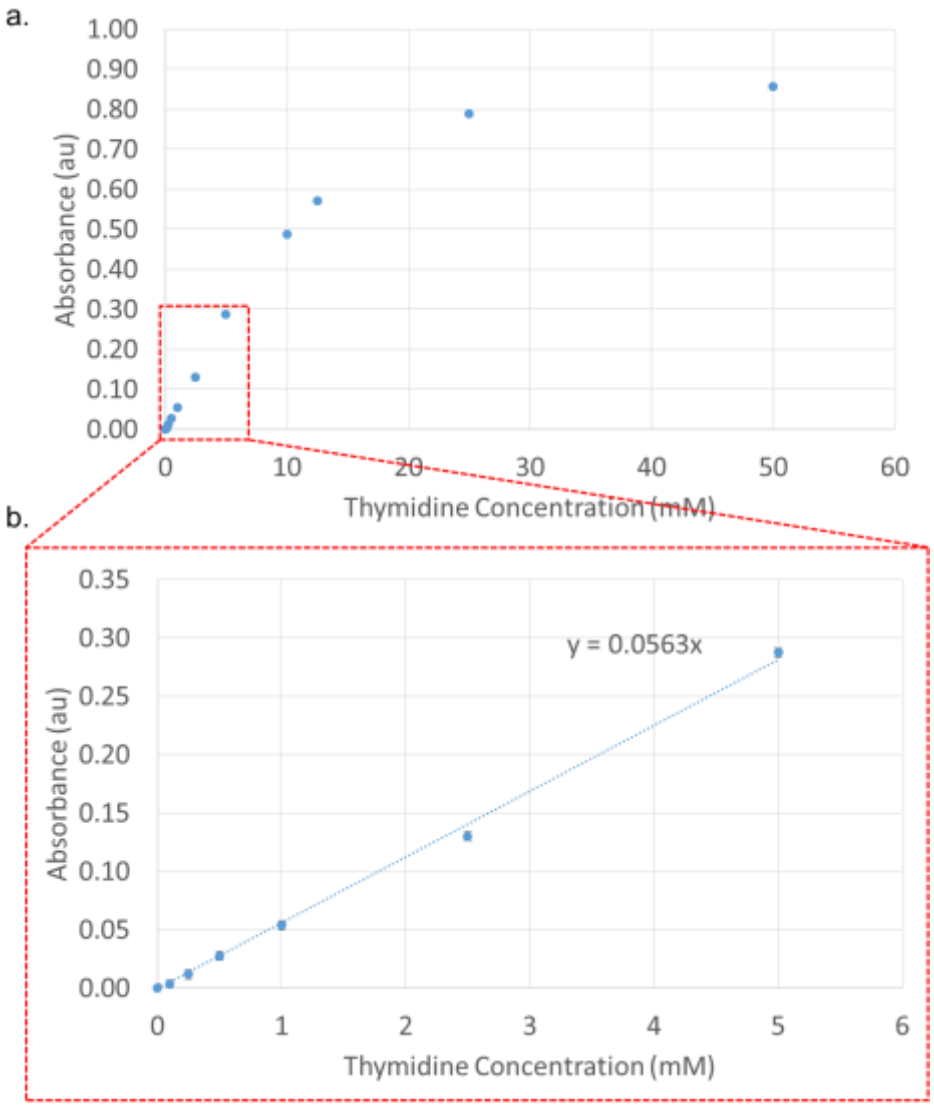

Figure 3-6 **Absorbance vs. Concentration curve with low cost light source and spectrometer**

(a) Absorbance vs. thymidine concentration using PX-2 xenon light source and USB4000 spectrometer with the lab-built CE system, (b) Straight line fit to the linear region.

Table 3-4 **Limit of detection (LOD), and quantitation (LOQ) analysis of FLT samples on lab-built CE system using PX-2 light source and USB4000 spectrometer.**

		Thymidine	Thymine	FA	Stavudine	FLT	CLT
256 nm	LOD	210 µM	260 µM	n/a	310 µM	300 µM	1100 µM
	LOQ	750 µM	850 µM	n/a	1000 µM	1000 µM	3500 µM
224 nm	LOD	n/a	n/a	790 µM	n/a	n/a	n/a
	LOQ	n/a	n/a	2600 µM	n/a	n/a	n/a

for the FLT related compounds using the PX-2 pulsed xenon light source and USB4000

spectrometer is listed in Table 3-4.

The capillary sample cell was then connected to the deuterium light source (DH-2000-BAL) and QE-Pro spectrometer and the measurements repeated. Using this new hardware setup in conjunction with the 75 µm ID capillary, the standard deviation in background absorbance noise was reduced more than 10-fold, i.e. from 4.0 mAU to 0.35 mAU for 254 nm (Figure 3-7). The noise was reduced from 4.1 mAU to 0.67 mAU for 224 nm. The average absorbance for each concentration is plotted versus thymidine concentration in Figure 3-8. This lowered the LOD and LOQ of thymidine to 22 µM and 72 µM, respectively. A complete list of LOD and LOQ for the FLT related compounds using the deuterium DH-2000-BAL light source and QE-Pro spectrometer is listed in Table 3-5.

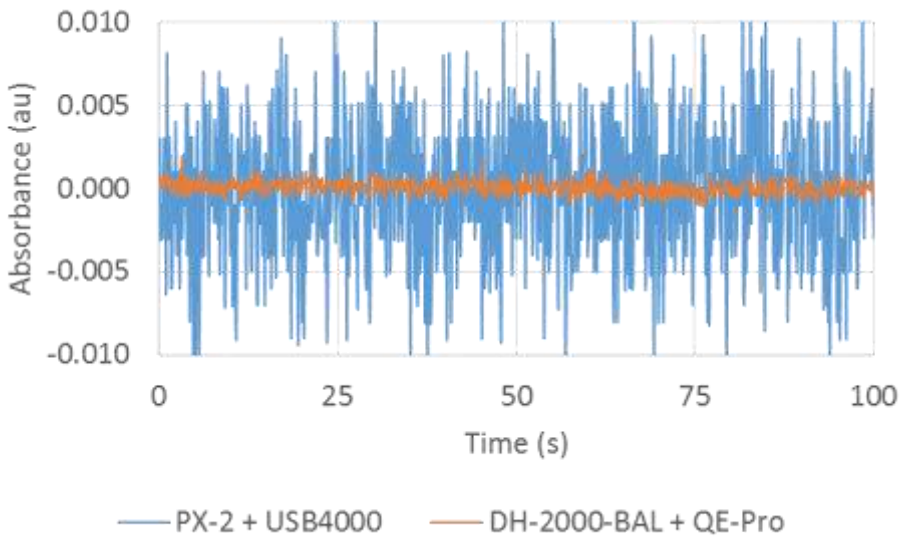

Figure 3-7 **Background absorbance noise at 254 nm for CUV-CCE equipped with PX-2 and USB4000 (blue) and DH-2000-BAL and QE-Pro (orange)**

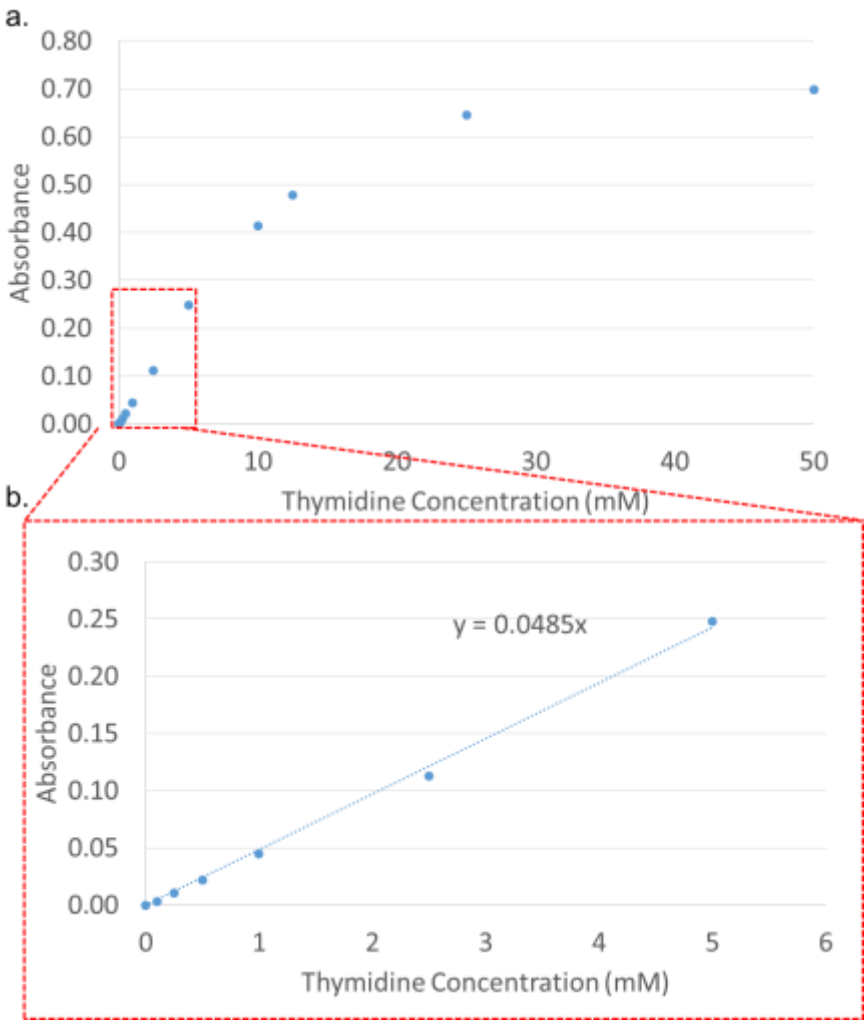

Figure 3-8 **Absorbance vs. Concentration curve with high end light source and spectrometer**

(a) Absorbance vs. Thymidine concentration using DH-2000-BAL deuterium light source and QE-Pro spectrometer with the lab-built CE system, (b) Linear range selected and linear fit equation is plotted.

Table 3-5 **Limit of detection (LOD), and quantitation (LOQ) of FLT samples on lab-built CE system using DH-2000-BAL light source and QE-Pro spectrometer.**

		Thymidine	Thymine	FA	Stavudine	FLT	CLT
256 nm	LOD	22 µM	21 µM	n/a	27 µM	25 µM	75 µM
	LOQ	72 µM	69 µM	n/a	91 µM	84 µM	250 µM
224 nm	LOD	n/a	n/a	54 µM	n/a	n/a	n/a
	LOQ	n/a	n/a	180 µM	n/a	n/a	n/a

3.3.4 Comparison of CE systems and HPLC system

In terms of the LOD, the commercial CE system (Table 3-3 and Table 3-4) and HPLC system (Table 3-5) exhibited similar performance for FLT and β-D-FAC (i.e. ~6 and 9 μM for commercial CE versus ~2 and 5 μM for HPLC). However, the lower LOD of the HPLC could be due to the longer optical path length of 10 mm versus 75 μm on the commercial CE system. K222 was also detectable on the commercial CE system and produced an LOD of 120 μM, whereas K222 could not be detected on the HPLC system. This now demonstrates the feasibility of CE to perform chemical purity analysis both in terms of adequate separation (Section 2.3.3) and adequate detection (this Chapter).

Comparing the commercial CE system to the lab-built system with high performance light source and detector (i.e. DH-2000-BAL and QE-Pro, respectively), the commercial CE system had 4x better LOD for FLT, i.e. FLT: 6 μM for commercial CE system versus 24 μM for lab-built CE system. On the other hand, the lab-built system cost roughly 3x less than the commercial CE system.

The detection limit can be improved with the addition of an extended optical path, as will be shown for the microscale implementation in Chapter 4. In fact, the performance can be improved to that of the commercial CE system and HPLC system. Improved detection may also be possible via alternate modes of detection such as electrochemical detection, radiation detection, and pulsed amperometric detection (PAD) [148]. By lowering LOD to micromolar levels on the microchip CE device, the application of CE to chemical purity testing will be made possible.

3.4 Conclusion

For the analytes involved in FLT syntheses, the LOD of the commercial CE system was similar to that of the HPLC system, despite a much smaller optical path, suggesting that the LOD of an optimized CE system is sufficient for the purposes of PET tracer chemical purity analysis. Though the lab-built system had the worst performance of the three systems tested, it is expected that limits of detection will be improved on the microchip due to the capability of implementing an extended optical path length with relative ease [54], [105], [149]. We show in Chapter 4, that by implementation in a microchip format, where features such as an extended optical path can easily be added, the LOD is lowered to match the commercial CE system, while maintaining lowered cost, and with the added benefit of greatly reduced size.

4 Chapter 4: Integrated Microchip Capillary Electrophoresis Device

4.1 Introduction

In 1990, Manz et al. [150] introduced the concept of micro-total analysis systems (μ-TAS), also known as “Lab-on-a-Chip” (LOC). With these devices, the goal was to integrate the various operations of chemical and biochemical analysis, such as sample handling and introduction, reagent mixing, separation, and detection on a single microfabricated device. Due to CE’s relatively simplistic design and operation, it is well suited to be implemented into such a microchip format. The development and use of microchip capillary electrophoresis (MCE) devices is growing as miniaturization of analytical systems allow the realization of chemical analysis using smaller quantities of samples and faster separation times, while also reducing usage of reagents, solvents, and power [151]–[154].

Several of these advantages have particular relevance for the application of quality control (QC) testing of PET tracers. Faster separation times could reduce the total time for QC testing, reducing the amount of the formulated tracer that is lost to radioactive decay before it can be released for injection into the patient. In addition, the small sample sizes could reduce the amount of sample consumed for QC testing purposes. Furthermore, the possibility of a compact, low-cost system could reduce the instrument costs, space requirements, and radiation shielding needed to perform QC testing.

In Chapter 2, it was established that CE has sufficient separating power to perform chemical purity analysis of example PET tracers. In Chapter 3, it was further established that the limit of detection of CE is also sufficient. In this chapter, we explore the third

aspect of the question of whether it is feasible to use CE for chemical purity analysis of PET tracers, i.e. whether CE with adequate performance can be performed in a miniature, microchip format. In order for a MCE device to be considered as a viable alternative to HPLC system, it must be able perform chemical purity analysis with high sensitivity and repeatability. To address this question, several aspects of CE miniaturization are explored.

First, in Section 4.2, enhancements in optical path length will be explored to ensure that detection limits can be improved on a microchip scale to match or exceed the typical performance of HPLC (current gold standard for chemical purity testing). Sources of noise that affect LOD were also explored, including fluctuation of light source, stability of the optical interface (i.e. between fiber and microchip device), and detector noise. For additive sources, the total noise of the system is the square root of the sum of all other noise sources squared and care is needed to minimize each individual source.

Experiments and discussions so far have not focused on ensuring reproducible amount of sample is injected (and detected), but reproducibility is critical for quantifying the amount of various impurities in the final formulated PET tracer to ensure they are below acceptable limits. Thus, in Section 4.3, techniques for repeatable sample injection are considered.

In order to ensure unambiguous identification of observed peaks, it is important that migration times are analytes are consistent. Different separation channel materials will be explored in Section 4.4 to ensure consistent and repeatable analyte separation in

a small footprint. Consistent migration is also critical in quantitation, as variations in speed of migration can affect determination of area under a peak and thus the estimated quantity of analyte.

Once the microchip detection, injection, and separation components have been tested separately, the complete microchip CE device will be fabricated and characterized (Section 4.5). While the most preferred substrate for some aspects of MCE is glass or quartz due its transparency and its surface stability after conditioning with sodium hydroxide [155], much of the work described here uses optically transparent poly(dimethylsiloxane) (PDMS), due to the possibility of fabricating intricate channel structures [156] and low-dead-volume integrated microvalves [155] via a simple and low-cost process.

4.2 Implementation of on-chip detection

4.2.1 Background

One way to improve the LOD of the optical detector is by increasing the optical detection path length [105] (as discussed in Section 3.1), which increases the absorbance 'signal' in accordance with Beer's Law (Equation 1.8). Figure 3-1 illustrates different methods used to enhance the optical path length of a microchip system. The general strategy is to expand the optical path length between the light source and detector to enhance the amount of light absorption by the analyte. Multi-pass approaches use mirrors around the detection region to reflect the light through the channel multiple times to increase the optical path. Of the many possible approaches to integrate on-chip absorbance detection with extended optical path, a Z-shaped detection cell was selected due to the simplicity of chip fabrication and interfacing of the

illumination and detection optical fibers. A common architecture to integrate the fiber optic cables into the chip for absorbance detection in this configuration is to use an in-plane design where guide channels are included to ensure accurate alignment of both the illuminating and detection fibers with the optical path within the chip [155], [157]. Fabrication and alignment are simpler than non-planar approaches often used for fluorescence detection [158]–[160].

4.2.2 Materials and methods

4.2.2.1 Reagents

Thymine, thymidine, furfuryl alcohol (FA), 2',3'-didehydro-3'-deoxythymidine (stavudine), and 3'deoxy-3'-fluorothymidine (FLT) were purchased from Sigma Aldrich (Milwaukee, WI, USA). Zidovudine impurity B (chlorothymidine, CLT) was purchased from LGC Standards (Wesel, Germany).

4.2.2.2 Microfluidic chip design and fabrication

A series of chips were developed with different optical path lengths in the range of 125 – 1000 μm (Figure 4-1). The chips have an inlet well where the sample is loaded, an approximately Z-shaped path (the center of which is the detection region) and an outlet well where vacuum is applied to clean the chip and to fill the optical path with the sample. All channels were 125 μm deep and 125 μm wide. The wells were 4.75 mm in diameter.

Chips were fabricated by standard replica molding techniques, often referred to as "soft lithography" [161]. 4" silicon wafers (Silicon Valley Microelectronics, Santa Clara, CA USA) were used for the lithography process and were cleaned with oxygen plasma using a Matrix 105 – Downstream Asher (Allwin21, Morgan Hill, CA, USA), and

baked at 150°C for 10 minutes prior to use. Approximately 4 mL of SU-8 2150 negative photoresist (MicroChem, Newton, MA USA) was poured onto a 4" silicon wafer and spun at the following 3 step spin setting: 500:200:5, 1500:500:30, 0:500:0 (speed:acceleration:duration; units are RPM:RPM/s:s). The coated wafer was then soft baked at 65°C for 5 minutes and 95°C for 25 minutes. The wafer was allowed to cool at room temperature for 5 minutes before being placed in the Karl Suss MA150 Mask Aligner (Karl Suss American Inc., Vermon, USA) and set for an exposed energy of 240 mJ/cm^2. Exposure was done through a transparency mask with the pattern shown in Figure 4-1. The exposed wafer was then post baked at 65°C for 5 minutes and 95°C for 11 minutes. The wafer was allowed to cool at room temperature before being developed in SU-8 Developer (MicroChem, Newton, MA USA) for 15 minutes. The wafer was then cleaned using methanol, and dried with compressed nitrogen gas. Finally, the mold was hard baked at 175°C for 15 minutes and at 100°C for 5 minutes. The wafer was then allowed to cool at room temperature for 5 minutes. The final silicon wafer mold contained a negative representation of the desired channel pattern, i.e. ridges where channels are desired. The height of the channel was measured using a Veeco Dektak 150 Surface Profilometer (Bruker, Tustin, AZ, USA).

Once this mold was completed, a 10:1 mass ratio of Momentive RTV615 A:B (New Smyrna Beach, FL, USA) was mixed in a plastic cup for 1 minute and degassed in a desiccator for 2 hours to remove all bubbles. The mold was then placed in a foil lined Pyrex petri dish (140 mm ID) (Product#3160101BO, Corning Inc., Corning, NY), USA). The degassed mixture was then poured onto the silicon wafer mold (~ 5 mm thick layer) and baked in an oven at 80°C overnight.

Once completely cured, the PDMS chips were peeled away from the mold. Metal punches were then used to create the buffer well and sample inlet port in the top portion of the chip. The sample and sample waste well were formed using a 4.75 mm ID catheter punch (HS1871730P1183S, Syneo, West Palm Beach, FL). In addition to the channel that contains the sample, the PDMS extended optical path length detection chip (Figure 4-1) contains alignment channels for easy insertion and alignment of two 125 µm OD fiber optic cables (ThorLabs, Newton, New Jersey, USA) at the two ends of the optical path. One fiber is for illumination for the light source and the other is for detection and leads to the spectrometer. The fibers are collinear with the “jog” in the center region of the channel. These channels are also 125µm wide and 125µm deep. Note that each of the fiber channels has a portion that is collinear with the “jog” as well as a continuation that allows the air initially in the channel to be vented. Using the same depth for the fiber-aligning channels as for the fluid-containing channels simplifies the chip fabrication, requiring a single thickness of photoresist. Due to the elastic property of PDMS, the fibers are held stably in the channels by friction forces (Fig 4-1a). The flat ends of the fibers sit flush against the flat end of the fiber channels, providing efficient optical coupling to the sample channel, another feature of this design.

Since PDMS absorbs strongly in the UV range [162], it was desirable to minimize the thickness of PDMS membrane between the end of the fiber and the sample within the channel. However, the membrane needed to be sturdy enough to allow a fiber optic cable to rest against it, as well as preventing dielectric breakdown when electrophoretic potential is applied (dielectric breakdown of Momentive RTV614 PDMS is 20 V/µm [163]). Therefore, the thickness of the PDMS membrane was designed to be 100 µm

thick to allow %transmission for wavelengths at 220 nm and higher to be above 85%. It can also be noted that this thickness provides an electrical breakdown of up to 2000 V, which should be sufficient to sustain the potential at the detection point in the separation channel (slightly above GND).

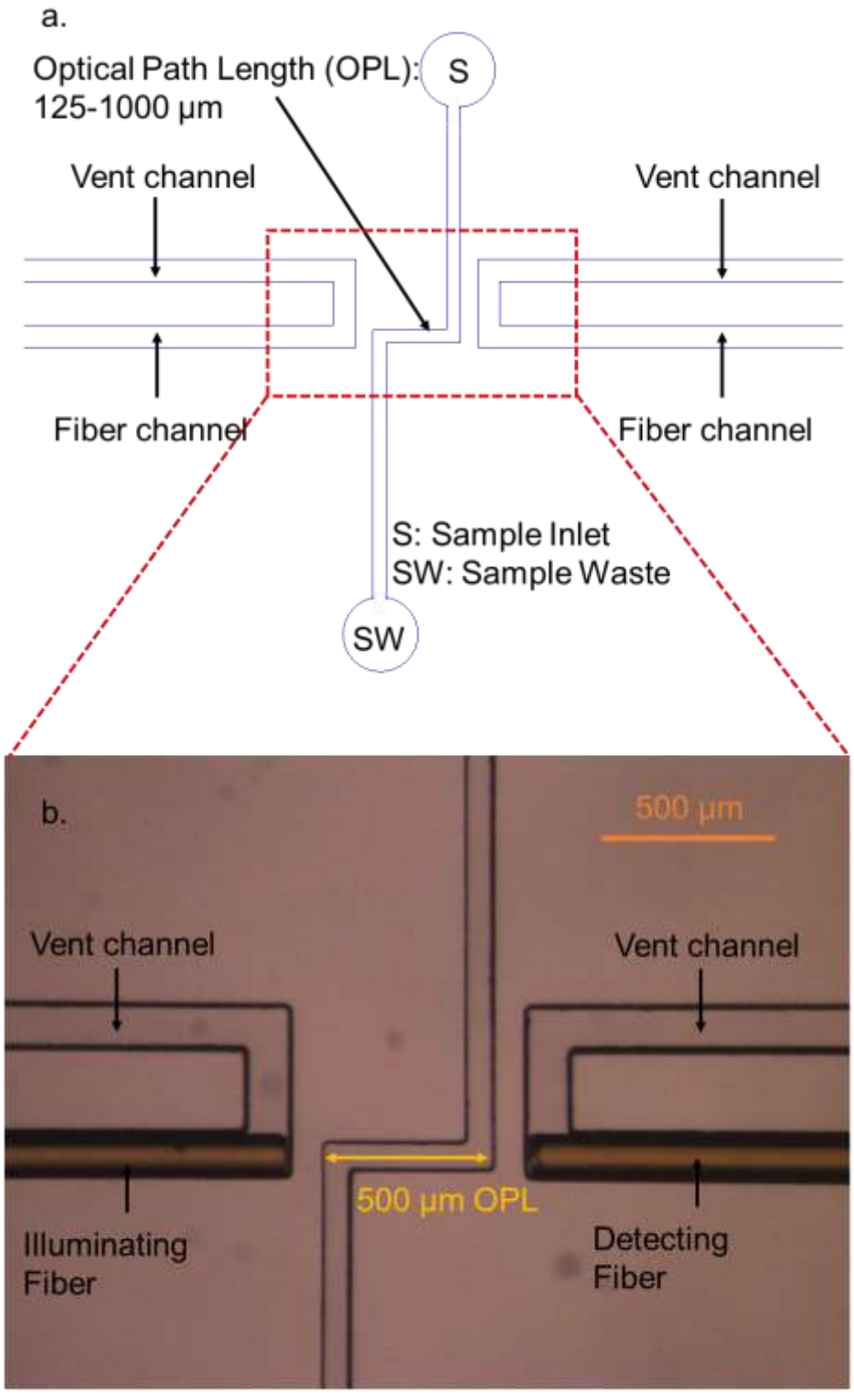

Figure 4-1 **Extended optical path length chip diagram and microscope image**

a) Mask pattern used to make the extended optical path length microchip and b) microscope image of 500 µm optical path length microchip

125, 250, 375, 500, and 1000 µm were fabricated.

4.2.2.3 Evaluation of microfluidic detection chips

Each OPL microfluidic chip was interfaced to the light source and spectrometer to determine LOD and LOQ for thymidine and furfuryl alcohol as described in Section 3.2.3.1. Due to the presence of a common chromophore and thus similar absorption spectrum and molar absorptivity of thymidine, thymine, stavudine, FLT, and CLT, only thymidine was used to initially characterize the various optical path lengths at 256 nm. A wavelength of 224 nm was used for furfuryl alcohol. Wavelengths were chosen as described in Section 2.2.2.1. Once the LOD/LOQ were obtained, a comparison between the different optical path lengths was made. While the optical path length with the lowest LOD/LOQ is desirable, the OPL's effect on separation resolution must also be considered and will be discussed in later.

4.2.3 Results and discussion

Absorbance using the pulsed xenon light source and USB4000 spectrometer is plotted for each optical path length as a function of concentration of thymidine (Figure 4-2a) and furfuryl alcohol (Figure 4-2b). Only data points in the linear range are illustrated The LOD and LOQ were calculated for both compounds for different optical path lengths

and are listed in Table 4-1 along with standard deviation in background absorbance noise.

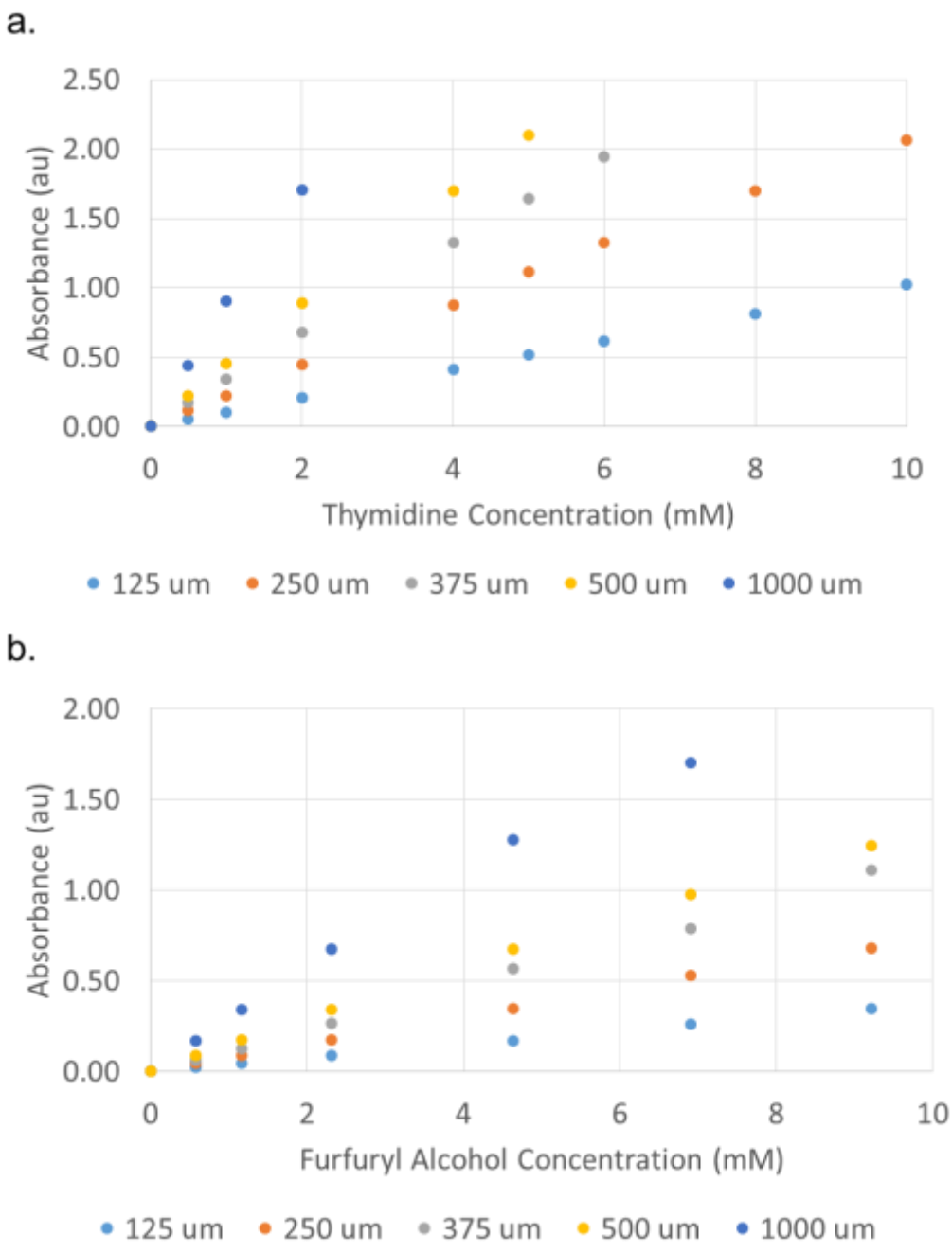

Figure 4-2 **Absorbance vs. concentration in extended optical path chips.**

Graphs show data in the linear range for **a)** thymidine (256 nm) and **b)** furfuryl alcohol (224 nm) in PDMS detection chips with different OPLs using PX-2 xenon light source and USB4000 spectrometer.

Table 4-1 clearly shows a decrease in LOD/LOQ as optical path length is increased. However, while the 1000 µm is shown to have the best performance, there is a potential drawback to using the longest extended optical path length. A longer optical path length causes an increase in peak width because the bands are within the detection region longer, which leads to a decrease in separation resolution. Ro et al. reported a decrease in separation resolution by 5% when increasing the optical path length from 50 µm to 500 µm using a similar Z-shaped detection cell [105]. We have already shown in Section 2.3.1 that baseline resolution was barely achieved for thymidine and thymine (Rs=1.48) using the lab-built CE system and was not baseline resolved for the commercial CE system (Rs=0.77). In order to prevent more substantial decrease in separation resolution, a 500 µm OPL was selected instead of 1000 µm or longer OPL.

Table 4-1 **Extended optical path lengths performance**

Limit of detection (LOD), quantitation (LOQ), and standard deviation in background absorbance noise (Std Dev) analysis for thymidine (256 nm) and furfuryl alcohol (224 nm) on microchip detection chip with various extended optical path lengths using PX-2 xenon light source and USB4000 spectrometer.

Optical path length (µm)		125	250	375	500	1000
Thymidine (256 nm)	Std Dev (mAU)	1.3	1.3	1.2	1.2	1.3
	LOD (µM)	40	18	11	8	5
	LOQ (µM)	130	61	37	28	15
Furfuryl Alcohol (224 nm)	Std Dev (mAU)	1.4	1.3	1.4	1.3	1.4
	LOD (µM)	130	56	36	30	16
	LOQ (µM)	430	190	120	96	54

In order to decrease the LOD and LOQ even further without extending the optical path length, the use of the DH-2000-BAL deuterium light source and QE-Pro spectrometer was explored. Using the 500 µm optical path length microchip equipped with the DH-2000-BAL lamp and QE-Pro spectrometer, solutions of thymidine, thymine,

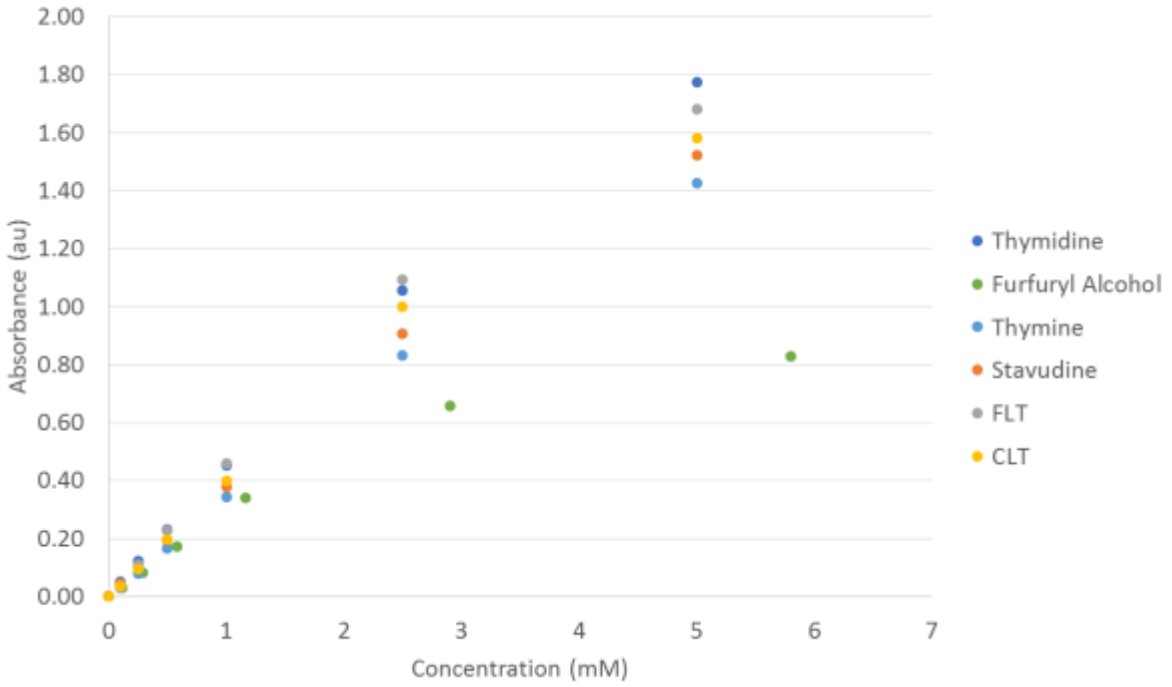

Figure 4-3 **Absorbance vs. concentration for FLT and by-products in PDMS detection chip with OPL of 500 µm using high-performance light source and spectrometer.**

Experiments used the QE-Pro spectrometer and DH-2000-BAL deuterium lamp. Furfuryl alcohol was measured at 224 nm; all other compounds were measured at 254 nm.

furfuryl alcohol, stavudine, FLT, and CLT at various concentrations between 0-5 mM were used to generate calibration curves (Figure 4-3) to calculate the LOD and LOQ of each compound (standard deviation in background absorbance noise was 0.35 mAU at 256 nm and 0.67 mAU for 224 nm). Table 4-2 summarizes the LOD and LOQ for FLT

Table 4-2 **Limits of detection (LOD) and quantification (LOQ) of FLT samples using PDMS optical path length chip (500 µm) and high-performance light source and spectrometer.**

Experiments used the QE-Pro spectrometer and DH-2000-BAL deuterium lamp.

	Analyte	Thymidne	Thymine	FA	Stavudine	CLT	FLT
256 nm	LOD	2 µM	3 µM	n/a	3 µM	3 µM	2 µM
	LOQ	8 µM	10 µM	n/a	10 µM	9 µM	8 µM
224 nm	LOD	n/a	n/a	7 µM	n/a	n/a	n/a
	LOQ	n/a	n/a	23 µM	n/a	n/a	n/a

and its by-products with a 500 µm optical path length with the higher performance light source and detector.

4.2.3.1 Comparison of extended optical path length to CE and HPLC

When compared to both the commercial CE system (Table 3-3) and HPLC system (Table 3-5), the extended optical path length (500 µm) detection chip in conjunction with the high performance (continuous deuterium) light source and high-performance (QE-Pro) spectrometer either matches or surpasses them. Using the microchip with 500 µm optical path length lowered the LOD of FLT below the values of the commercial CE system (2 µM versus 6 µM), while closely matching the values of the HPLC system (2 µM). In the case of furfuryl alcohol, the LOD of the 500 µm detection chip (7 µM) was higher than the value for the commercial CE system (2 µM), while being significantly lower the value for the HPLC system (35 µM). This demonstrates the ability to achieve performance comparable with HPLC using only a low-cost CE setup.

4.2.3.2 Optimization of the OPL

It was shown that the LOD and LOQ of the detection chip can be increased even further simply by extending the length to 1000 µm and presumably beyond; however, this poses separation resolution issues as observed by Ro et al. [105]. By increasing the optical path length, each band of analyte spends longer time in the optical path, effectively increasing the width of the detected peak, and adversely impacting the resolution. If the separation distance between analytes is not large enough, multiple analytes could be present in the optical path at the same time, leading to overlapping peaks in the chromatogram. To estimate the degree to which this could be a factor in the lab-built CE system, migration times from earlier FLT and by-products separation

experiments from Section 2.3.1.2 were used. Using the migration times for the two closest eluting analytes (thymidine and thymine), the physical length of the baseline between the two analytes can be calculated. Thymidine had a migration time of 10.28 minutes over an effective capillary length of 52 cm, corresponding to an elution rate of 5.06 cm/min. Likewise, the elution rate was calculated for thymine (10.51 minutes / 52 cm) as 4.95 cm/min. A 5 second (i.e. 0.083 minute) baseline separation was measured between the two analytes. This can be converted to a length by multiplying by 0.083 minute by thymine's elution rate (4.95 cm/min). This results in a distance of 0.41 cm (4100 µm). Therefore, it may be possible to use a detection chip with an OPL to even larger than 1000 µm pending the separation performance of the 500 µm OPL, which will be tested in Section 4.5.3.1.

4.2.4 Conclusion

With high performance light source and detector, the LOD of the extended OPL detection chip was found to closely match the performance of the HPLC setup for thymidine, thymine, furfuryl alcohol, stavudine, FLT, and CLT. It may also be possible to use a longer OPL with the lower costing PX-2 light source and USB4000 to achieve similar sensitivity levels and keep overall costs to a minimum. Furthermore, the optical detection chip can in principle be integrated with on-chip sample injection and on-chip separation to result in a compact overall microchip CE system. The injection portion is discussed in the next section.

4.3 On-chip sample injection

4.3.1 Background

To achieve high accuracy of chemical purity analysis, the volume of sample injected into the separation channel must be highly reproducible. Automated injection is also important as it increases reproducibility by minimizing human error, especially when working with nanoliter sized sample volumes, and enables minimization of radiation exposure when working with radiopharmaceutical samples. For MCE devices, both electrokinetic and hydrodynamic injection modalities have been studied, each with its own advantages and disadvantages.

Electrokinetic injection is very commonly used for MCE due to its simplicity in terms of system design and operation. By simply applying a relatively low potential for a short period of time between the sample reservoir and sample waste, controlled amounts of sample can be introduced into the separation channel (Figure 4-4). The quantity of the sample injected into the channel is based on the potential and time. In a mixture, the quantity of each analyte injected is not constant, however, because injection also depends on the electroosmotic mobility and the electrophoretic mobility of the individual species in the sample [91]. Thus, an “injection bias” will be present for species with different mobilities, and is especially pronounced if they have different charges [91]. The magnitude of this electrokinetic injection bias has been shown to be as much as 56% when comparing the peak area ratios of two analytes with different electrophoretic mobilites to peak area ratios obtained using hydrodynamic injection [164]. The bias can be accounted for in known samples by careful using internal standards of known concentrations and mobilities to account for the bias [165], [166]. Injection bias results

in the injected sample composition differing from the sample that is being studied. This would lead to under- or over-estimate of the amount of each species when peak areas are quantified. In addition, this biased injection will potentially change the composition of the sample solution over time, as one species will be depleted more rapidly than another, making it challenging to accurately perform repeat measurements. In the case of K222, which has been shown to be positively charged in aqueous solutions, this bias can result in inconsistent quantification over several runs.

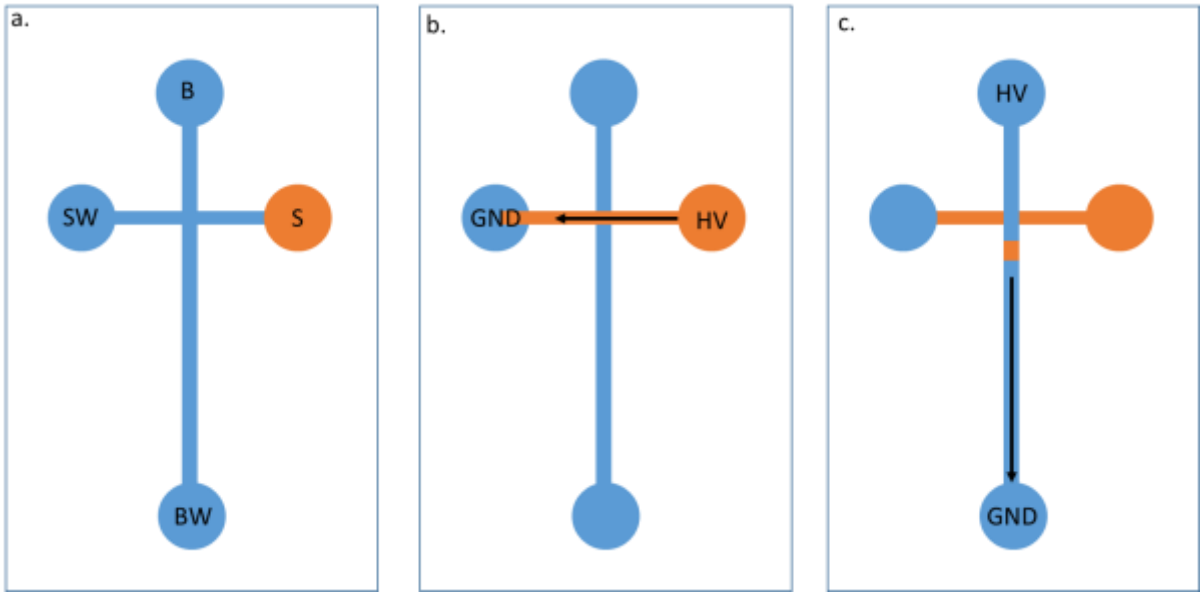

Figure 4-4 **Electrokinetic injection sequence used for MCE device.**

a) Fluidic channel, buffer well (B), buffer waste well (BW), and sample waste well (SW) filled with BGE (blue) and sample well (S) filled with sample (orange). **b)** high voltage (HV) and ground (GND) applied between S and SW to drive sample across the intersection. **c)** HV applied between B and BW to drive sample towards detection region.

In contrast to electrokinetic injection, hydrodynamic injection is performed by the application of a pressure difference between two points to drive sample into the separation channel to produce a sample plug that is representative of the original sample composition. There are several methods to perform hydrodynamic injection on

a microchip, including simpler non-valve based injections, and more complex valve-based injections.

To drive sample hydrodynamically into a MCE chip (illustrated in Figure 4-5) external pumps and valves are typically used [167]. For example, an external syringe pump is use to drive sample from the sample well into cross-sectional channel in the MCE device. Electrophoretic potential can then be applied between the buffer well and buffer waste well to drive the sample towards the detector. However, an additional grounding electrode is commonly needed in the sample waste well to prevent sample within the vicinity of the intersection from entering the separation channel (also known as sample leakage), which can lead to inaccurate injections and peak tailing.

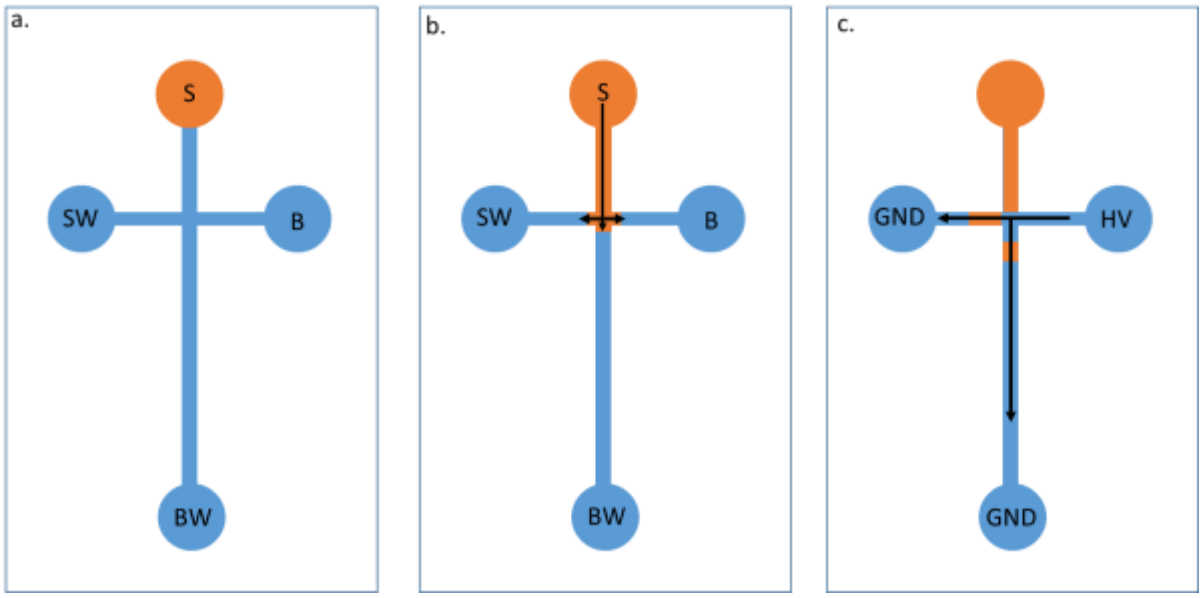

Figure 4-5 **Hydrodynamic injection sequence used for MCE device.**

a) Fluidic channel, buffer well (B), buffer waste well (BW), and sample waste well (SW) filled with BGE (blue) and sample well (S) filled with sample (orange). **b)** external syringe pump used to drive sample from S into the intersection. **c)** high voltage applied between B and BW to drive sample towards detection region and between B and SW to prevent sample leakage.

Luo et al. describes a double-cross injection chip with a control channel for depleting excess sample from the injection region and preventing sample leakage [168]. However, this method requires the use of additional electrodes.

In typical cross injection methods, the injection volume is typically controlled by the channel geometry at the injector. Another means of controlling the volume is to use a split-flow technique [169]. This method is a simple example of a non-valve based hydrodynamic injection technique with controllable sample volume, which takes advantage of the Hagen-Poiseuille law (Equation 4.1) to inject a certain fraction of the total sample volume.

$$Q = \frac{\Delta P d^4 \pi}{128 \eta L} \quad (4.1)$$

Hagen-Poiseulle law states that the volumetric flow rate (Q) of a homogeneous fluid through a capillary tube is directly proportional to the pressure difference between its ends (ΔP) and to the forth power of its inner diameter (d), and inversely proportional to its length (L) and to the viscosity of the fluid (η). Gáspár *et al.* developed a device where the sample inlet was connected to several output channels at a junction [169]. The application of pressure on the sample leads to a pressure at the junction. This creates a pressure difference along all output channels (sample pressure minus atmospheric pressure). By selecting the microchannel widths, an initial sample volume could thus be divided into smaller sub-volumes, the smallest of which was injected into

the separation channel (Figure 4-6). To prevent sample leakage and prevent v_2 from eluting back into the separation channel durng the application of electrophoretic potential, v_2 must be driven hydrodynamically into the HV/waste well during the sample

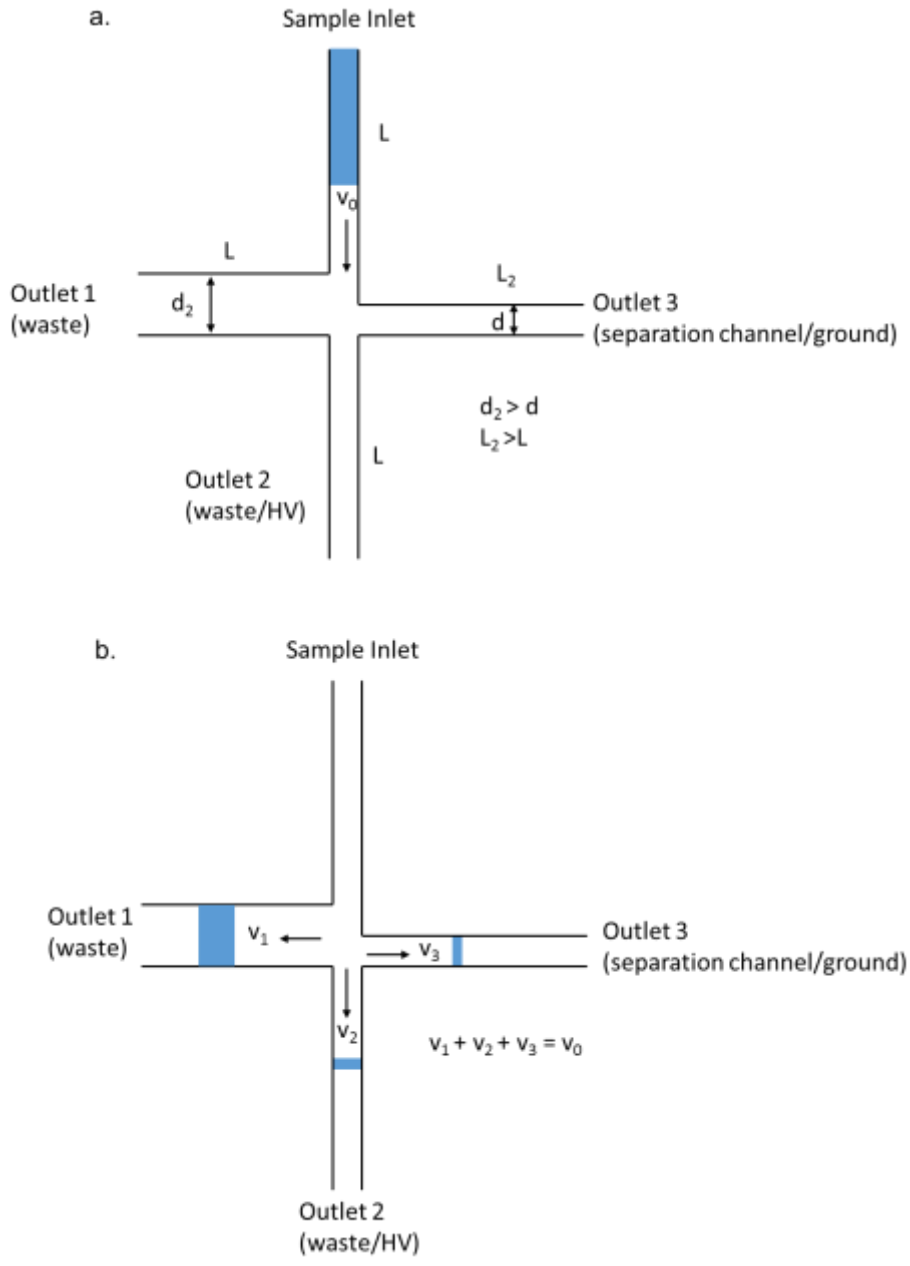

Figure 4-6 **Illustration of hydrodynamic split-flow injector.**

(a) Chip design with varying channel widths and initial sample volume (v_0) (blue) entering chip. (**b)** Sample volume split amongst 3 output channels according to Hagen-Poisuelle law.

injection step. Separation potential can then be applied between outlet 2 and 3 to drive v_3 through the separation channel towards the detector. Although the split-flow injector chip is capable of injecting nanoliter sized volume, and is relatively simple to fabricate compared to valve-based chips, it suffers from inefficient sample usage (most of the initial sample volume injected is sent to waste) and it requires a method to accurately pre-meter the initial sample volume. Also, as sample is hydrodynamically pushed into the microchip, diffusion/mixing of sample with BGE can lead to dispersion and cause undesired band broadening before the sample reaches the intersection due to parabolic flow profile as illustrated in Figure 1-7.

To avoid these issues and the problem of sample leakage describe above, another commonly used hydrodynamic injection approach relies on valve-based microchips, typically made from PDMS. The basic concept is to use a valve to control the timing and quantity of injection. The operating principle of PDMS microvalves is the deflection of a thin PDMS membrane into the fluidic channel of the microchip to restrict

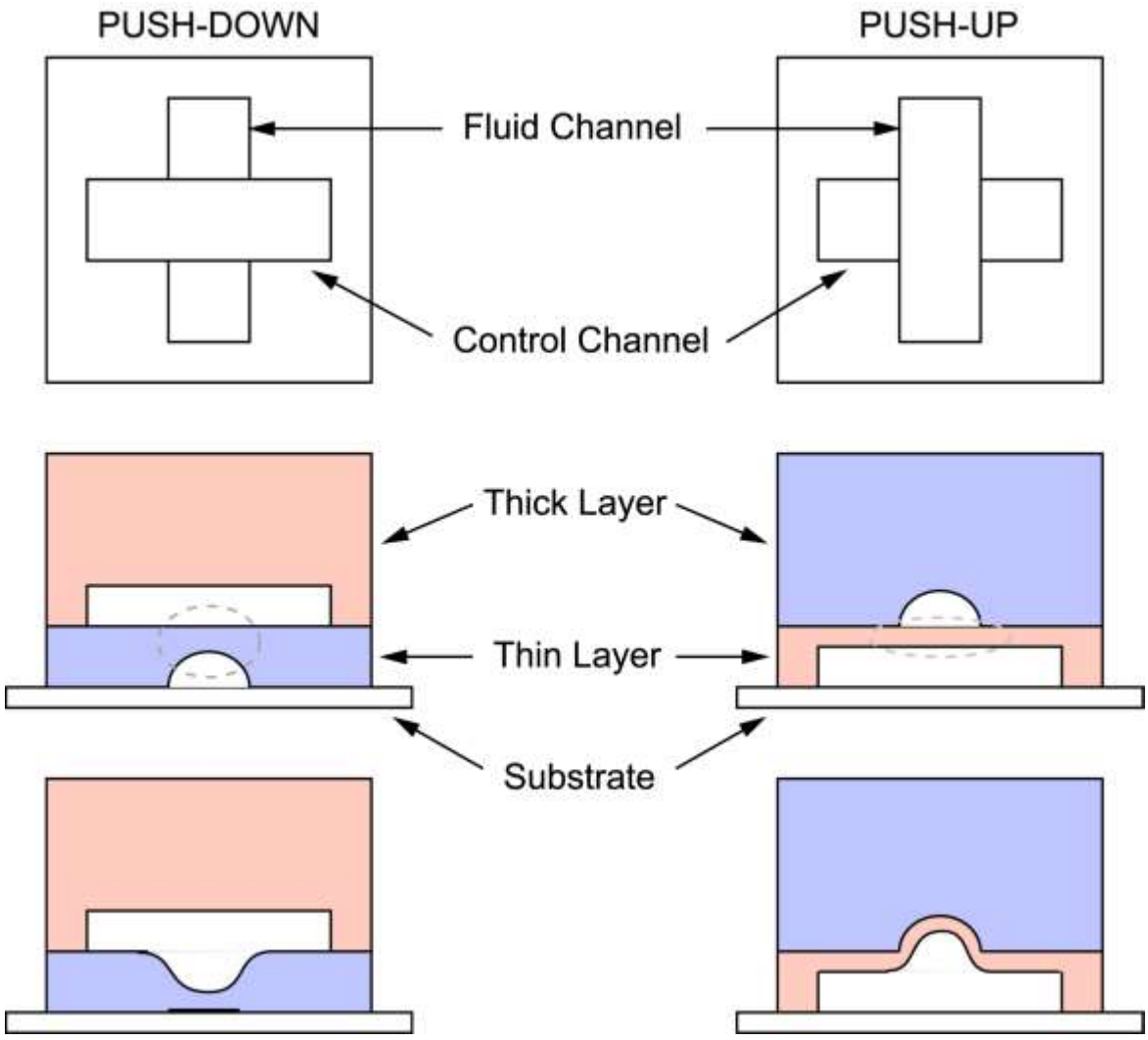

Figure 4-7 **Schematic of two common PDMS microvalve architectures.**

(Left) Three diagrams of *push-down* elastomeric valve. A top-view of the valve is shown in the upper diagram and a side-view is shown below. The fluid channel with rounded profile is in the bottom thin layer and flows beneath the control channel in the thick layer. A dashed circle highlights the thin elastomeric membrane that separates these channels and that is deflected during actuation. The lower diagram shows the valve in the closed state: the control channel is pressurized and deflects the membrane downwards until it completely blocks the fluid channel. A reduced control channel pressure would deflect the membrane only part way, leaving a reduced size opening for the passage of fluid. **(Right)** Corresponding three diagrams for a push-up elastomeric valve. In this case the fluid channel is in the thick layer and flows over the control channel. When actuated, the control channel deflects the intervening elastic membrane upwards, closing off the fluid channel. Typically devices are fabricated from two bonded layers; in both sets of figures, light red indicates the layer with actuation channels and light blue indicates the layer with fluid channels. Note the different shape of the valve membrane in the two cases. The valve membrane in a push-up device is a uniform thickness and is easier to deflect, resulting in lower actuation pressures. Figure provided courtesy of R. Michael van Dam.

flow. The deflection is caused by pressurization of an adjacent ‘control channel’. There

are two main architectures for PDMS microvalves, as shown in Figure 4-7. The left portion of Figure 4-7 illustrates the operation of the push-down valve where control channel is placed on top of the fluidic channel and the right portion illustrates the operation of the push-up valve where the fluidic channel is placed on top of the control channel. In both cases, when the control channel is pressurized, the thin PDMS membrane between the two channels is deflected into the fluidic channel, reducing the size of the fluidic channel. When sufficient pressure is applied to overcome the elasticity of PDMS and the pressure of the fluid in the fluidic channel, the valve is fully closed and completely restricts the flow through that portion of the microchip. Upon release of pressure applied to the control channel, the elastic PDMS membrane springs back to its original position. Figure 4-8 shows the top-view photograph of an open and closed microvalve.

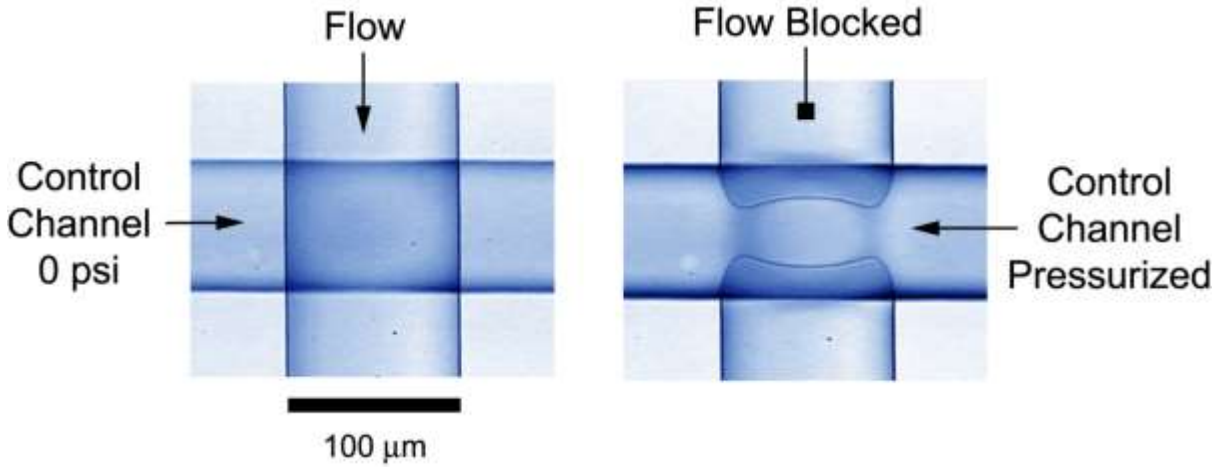

Figure 4-8 **Photograph of an elastomeric microfluidic valve.**

(Left) Photograph of an open PDMS valve. **(Right)** Photograph of same valve closed by pressurizing the control channel. (Reproduced from http://www.fluidigm.com/nanoflex.htm with permission. Copyright Fluidigm Corporation.)

In the case of the push-down valve, the elastic membrane is deflected downwards into the fluidic channel [170], whereas, the membrane is deflected upwards

into the fluidic channel for the push-up valve [171]. Typically the push-up configuration allows the control channel to be fully actuated with significantly lower pressures due to the shape of the membrane [171]. In order for the elastic membrane to completely close the fluidic channel, the fluidic channel must be rounded in shape to prevent fluid to leak from the corners. Rounded channels can be fabricated using photoresist that is reflowed during processing (described in Section 4.3.2.1).

The use of pneumatic PDMS microvalves strategically placed around a T-shaped fluidic channel to hydrodynamically inject controlled amounts of a sample into a separation channel (Figure 4-9) has been studied by several groups [98], [155], [172]. Figure 4-9 shows a simple T-shaped MCE device with 3 microvalves (v1, v2, and v3). By opening v2 and v3, sample can be pushed hydrodynamically into the intersection, while preventing sample from entering the channel towards the buffer well by keeping v1 closed. Then by closing both v2 and v3, and opening v1, electrophoretic potential can be applied between the buffer well and buffer waste well to drive the sample towards the detector. Sample leakage is prevented by valves v2 and v3. This is not a typical chip arrangement, but is simply for illustrative purposes.

These valve-based approaches exhibit highly repeatable sample injection, yielding relative standard deviation (%RSD) of the peak area as low as 1.77% (n=15) [98], which is below what has been suggested as an appropriate acceptance criterion for peak area reproducibility (2%) [173]. Though this approach eliminates analyte-dependent electrokinetic bias, it can still suffer from other types of bias. For example, a higher viscosity sample will flow more slowly than a low viscosity sample, and the amount injected in a given time that the valve is open will be lower for the former. It

could also suffer from chip-to-chip variation, due to small manufacturing differences or small differences in the whole system that affect the valve response time.

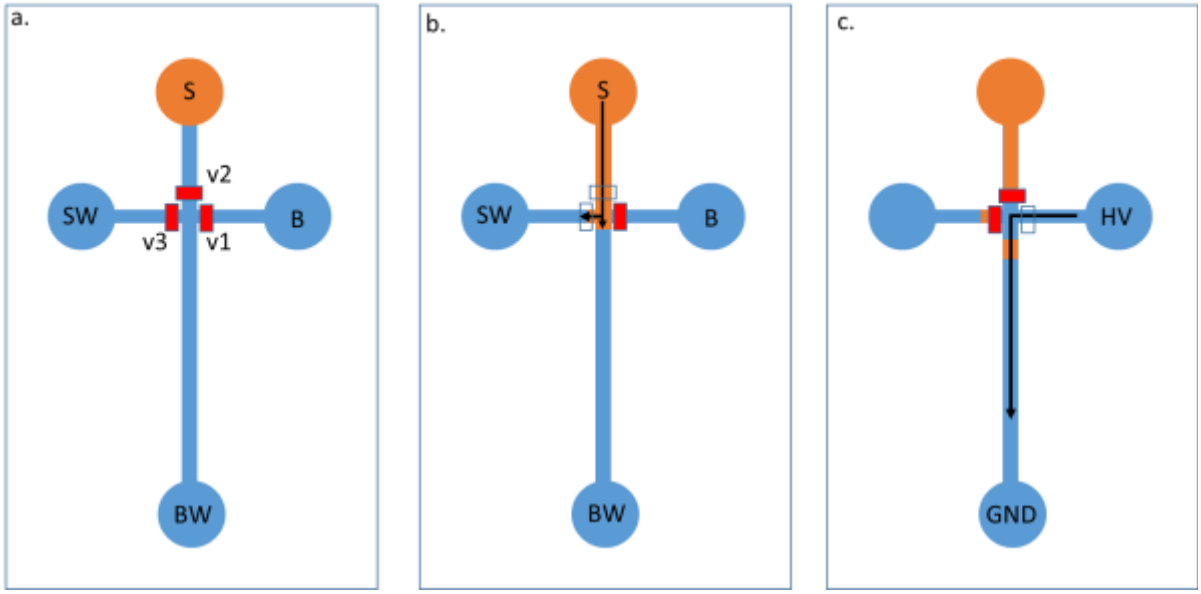

Figure 4-9 **Microvalve-controlled hydrodynamic injection sequence used for MCE device.**

a) Fluidic channel, buffer well (B), buffer waste well (BW), and sample waste well (SW) filled with BGE (blue) and sample well (S) filled with sample (orange). Device has three microvalves (v1, v2, v3). **b)** Sample is hydrodynamically injected into the intersection (v2, v3 open) (v1 closed). **c)** HV is applied between B and BW to drive sample towards detection region (v2, v3 closed) (v1 open).

To avoid the influence of both kinds of bias, we developed another novel type of microvalve injector. Using PDMS microvalves placed around the separation channel, a fixed volume can be confined within the separation channel in a loading step, and then this full volume can be injected into the separation channel. This method does not allow as much flexibility in injected sample volume (e.g. as can be done by tuning sample driving pressure, or valve opening time in other approaches), but was expected to give more reproducible injections, since the amount injected is metered volumetrically rather than by time and pressure, and thus should not depend on the fluid properties.

The goal of this study was to compare the reproducibility of two valve-based sample injection methods (time dependent and fixed volume injection) to determine the best approach for the integrated device for chemical purity analysis. Thus, the peak area of a single analyte injection was used to determine the %RSD. Since experience had shown some issues with the stability of the PDMS surface and thus variability in EOF (see Section 4.4), which can affect the peak area, the chips were designed to connect to a conventional capillary. Because the conventional capillary has more stable EOF, the measured peak area as the sample passes through the detector can be assumed to reflect the amount of sample injected.

4.3.2 Materials and methods

4.3.2.1 Reagents

Sodium phosphate monobasic (NaH_2PO_4), sodium phosphate dibasic dihydrate (Na_2HPO_4), sodium dodecyl sulfate (SDS), sodium hydroxide (NaOH), and thymidine were purchased from Sigma Aldrich (Milwaukee, WI, USA).

4.3.2.2 Microfluidic chip design and fabrication

Schematics of the time-dependent volume and fixed volume injection chips are shown in Figure 4-10. The time-dependent volume chip (Figure 4-10a) relies on the valve opening time (and pressure applied to sample) to achieve a controlled injection volume. The fixed volume chip (Figure 4-10b) relies on volumetric filling of a valve-enclosed chamber to achieve a controlled injection volume. Operation of the chips are shown in Figures 4-13 and 4-14, respectively. Each chip was fabricated using the technique known as multilayer soft lithography [174], from two patterned layers of PDMS that are aligned and bonded together. These chips use the “push-up” valve architecture.

The control layer channels were 15 µm deep and 75 µm wide and were rectangular in cross section. The flow layer was 20 µm deep and 75 µm wide and was rounded in cross section to enable complete channel sealing using the on-chip pneumatic valve [170].

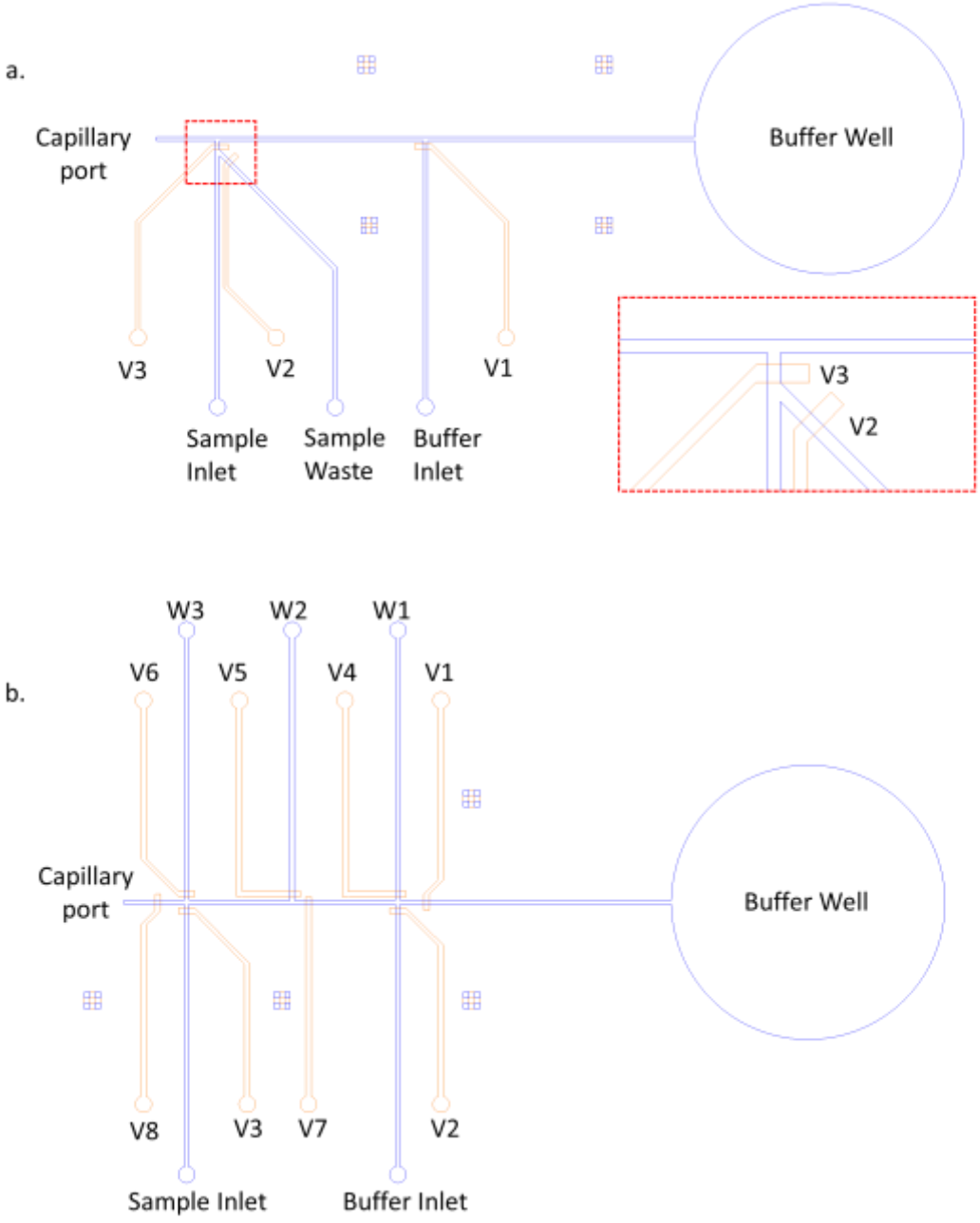

Figure 4-10 **Mask Patterns of Microvalve-based Injection Chips**

(a) Time-dependent sample volume injector with three microvalves controlled by pressure applied at ports V1-V3. Inset region shows zoomed in view of microvalves V2 and V3. (**b)** Fixed sample volume injector with eight microvalves (V1-V8) and three waste outlets (W1-W3). Control lines are shown in orange and fluidic lines are shown in blue. Both chips are designed to inject towards the left side, which will be connected to an external capillary (Capillary port).

To fabricate the control layer mold, 4” silicon wafers (Silicon Valley

Microelectronics, Santa Clara, CA USA) were used for the lithography process. They were first cleaned with oxygen plasma using a Matrix 105 – Downstream Asher (Allwin21, Morgan Hill, CA, USA), and baked at 150°C for 10 minutes prior to use. Approximately 4 mL of SU-8 2010 negative photoresist (MicroChem, Newton, MA USA) was poured onto a 4” silicon wafer and spun at the following 3 step spin setting: 500:200:5, 1500:500:30, 0:500:0 (speed:acceleration:duration; units are RPM:RPM/s:s). The coated wafer was then soft baked at 95°C for 3 minutes. The wafer was allowed to cool at room temperature for 5 minutes before being placed in the Karl Suss MA150 Mask Aligner (Karl Suss American Inc., Vermon, USA) and set for an exposed energy of 140 mJ/cm^2. The exposed wafer was then post baked at 95°C for 4 minutes. The wafer was allowed to cool at room temperature, and then developed by immersion in SU-8 Developer (MicroChem, Newton, MA USA) for 3 minutes. The wafer was then cleaned using methanol, and dried with compressed nitrogen gas. Finally, the mold was hard baked at 175°C for 15 minutes and at 100°C for 5 minutes. The wafer was then allowed to cool at room temperature for 5 minutes. The height of the channel was measured using a Veeco Dektak 150 Surface Profilometer (Bruker, Tustin, AZ, USA).

To fabricate the fluidic mold, 4” silicon wafers (Silicon Valley Microelectronics, Santa Clara, CA USA) were used for the lithography process and were cleaned as described above. Approximately 6 mL of hexamethydisilazane (HMDS) (Sigma-Aldrich, St. Louis, MO USA) was poured onto the wafer and spun at the following setting 3 step spin setting: 400:200:18, 1000:500:45, 0:500:0 (speed:acceleration:duration; units are RPM:RPM/s:s) as an adhesion promoter. Approximately 6 mL of SPR 220-7.0 positive photoresist (MicroChem, Newton, MA USA) was then poured onto the 4” silicon wafer

and spun at the following setting 3 step spin setting: 400:200:30, 1000:500:80, 0:500:0 (speed:acceleration:duration; units are RPM:RPM/s:s). The coated wafer was then soft baked at 105°C for 6 minutes. The wafer was allowed to cool at room temperature for 5 minutes before being placed in the Karl Suss MA150 Mask Aligner (Karl Suss American Inc., Vermon, USA) and set for exposed energy of 720 mJ/cm^2. After exposure, the coated wafer was set aside for a 3 hours rehydration step. The exposed wafer was then post baked at 110°C for 5 minutes. The wafer is then set aside for 45 minutes at room temperature for rehydration. The wafer was then developed by immersing in CD-26 (MicroChem, Newton, MA USA) for 30 minutes. The wafer was then rinsed gently with water and dried with compressed nitrogen gas.

Once developed, a reflow process (to achieved parabolic channel profile) was performed. This was accomplished by placing the wafer on a 65°C hot plate and allowing it to gradually heat up to 140°C. Once at 140°C the wafer was left there for 40 minute before removing and cooling at room temperature for 5 minutes. This was followed by a hard bake by placing the wafer on a 135°C hot plate and allowing it to gradually heat up to 190°C. Once at 190°C the wafer was left there for 3 hours (channel features became blackened) before removing and cooling at room temperature for 5 minutes. The height of the channel was then measured using a Veeco Dektak 150 Surface Profilometer.

Once both molds were completed, a 20:1 mass (~45 g) ratio of RTV615 A:B (Momentive, New Smyrna Beach, FL, USA) was measured out and mixed in a plastic cup for 1 minute. The mixture was then placed into a vacuum desiccator for 2 hours to remove air bubbles. The degassed mixture was then poured onto the control mold and

spun 2500 RPM (acceleration: 1000 RPM/s) for 1 min. A 5:1 (~50 g) mass ratio of RTV615 A:B was measured out and mixed in a plastic cup for 1 minute and placed into a vacuum desiccator to remove air bubbles. The fluidic mold was then placed in a foil lined Pyrex petri dish (140 mm ID) (Product#3160101BO, Corning Inc., Corning, NY), USA) before pouring the mixture onto it (~ 5 mm thick layer). Both layers were then baked at 80°C for 20 minutes. The fluidic layer was then removed from the wafer mold, trimmed to the size of the chip, and aligned onto the control layer with the assistance of alignment marks. Scotch tape was used to keep the surface of the chip clean before alignment (810 Scotch Tape, 3M, Saint Paul, MN, USA). The alignment was done using a Stemi SV 11 microscope (Zeiss Oberkochen, Germany) equipped with a KL 1500 LCD lamp (Schott, Southbridge, MA, USA). The layers were placed in contact so that there were no air bubbles between them. The aligned chips were placed back in the 80°C oven for a minimum of 2 hours to allow the layers to bond together.

To create the bottom substrate for the chip, a 10:1 mass ratio (~50 g) of RTV615 A:B (Momentive, New Smyrna Beach, FL, USA) was prepared and mixed in a plastic cup for 1 minute and placed into a vacuum desiccator to remove air bubbles. A blank silicon wafer was then placed in a foil lined Pyrex petri dish (140 mm ID) (Product#3160101BO, Corning Inc., Corning, NY), USA) before pouring the mixture onto it (~ 5 mm thick layer). The bottom substrate was then placed in an 80°C oven for 2 hours. The bottom substrate was then removed from the blank mold and set aside for later use.

Once the control layer and fluid layer bonding was complete, the chips were removed from the control wafer mold. A Schmidt manual press (Press Type 3/6,

Schmidt, Cranberry Twp., PA, USA) equipped with metal punches was then used to create a buffer well, ports for fluidic and control lines, and a port for a fused silica capillary. The buffer well was formed using a 4.75 mm ID catheter punch (HS1871730P1183S, Syneo, West Palm Beach, FL). A 720 µm ID catheter punch (CR0350255N20R4, Syneo, West Palm Beach, FL) was then used for all other ports except the capillary port. A 330 µm ID punch ID punch (CR0180115N26R4, Syneo, West Palm Beach, FL) was used to create a port for insertion of a capillary. (Using a capillary provided a simple way to connect detectors and measure the peak areas of injected analytes.) A 75 µm I.D., 375 µm O.D. Teflon coated fused-silica capillary with a total length of 20 cm from Polymicro (Phoenix, AZ, USA) was inserted into the capillary port with the capillary end not quite flush with the surface, but ~ 1 mm back from the surface of the PDMS chip. The combined chip (fluid and control layers) was then bonded to the flat PDMS substrate using a Corona Discharge bonder (LM4816-11MS-MSA, Enercon Industries). The completed chip was then baked at 80°C for a minimum of 2 hours.

The thickness of the membrane valve between the control and fluidic was determined as follows. The full thickness of PDMS deposited on the control layer mold after curing was measured as 30 µm using a Veeco Dektak 150 Surface Profilometer. Using the control layer mold feature height measurement 15 µm, the membrane was determined to be 15 µm thick. In operation, approximately 35 psi was needed to fully actuate the valve, which was visually inspected using Nikon SMZ 1500 stereomicroscope (Nikon, Los Angeles, CA, USA). Pressure was transferred into the control channel using polytetrafluoroethylene (PTFE) tubing (#30 AWG, Cole Palmer,

Vernon Hills, Illinois, USA). The pressure was supplied by a house compressed air house supply line.

4.3.2.3 Microchip and capillary conditioning

To condition the hybrid capillary-microchip, water was pushed into the chip though the buffer inlet port via pressure (10 psi) for 30 min to purge all air from the fluidic channels. Afterwards, the PDMS end of the hybrid capillary-microchip was placed in a 3" petri dish with a water dampened Kimwipe (Kimberly-Clark, Roswell, GA, USA), to prevent the chip from drying out, and was sealed and left overnight. 1 M NaOH was then pushed into the chip though the buffer inlet port for 30 minutes to ensure previous liquid is thoroughly removed. The PDMS end was resealed and left overnight to allow complete conditioning of the fused silica capillary and PDMS (to form hydroxyl groups [175]). When the chip was ready to be used, water was first pushed into the chip though the buffer inlet port for 30 minutes to eliminate the NaOH, followed by the BGE (e.g., 30 mM phosphate buffer with 100 mM SDS) for 30 minutes.

4.3.2.4 Microvalve operation and control

The microvalve channels in the control layer of the PDMS device could be filled with either water or air; however, to prevent air from entering the fluidic channel (by permeation through the PDMS valve membrane), the microvalves were filled with water. This was accomplished by connecting each control channel port via #30 PTFE tubing to a vial filled with water and pressurizing at 20 psi until all trapped air in each control channel was eliminated [170]. Once the microvalves are filled with water, the water vial is removed, and the tubing is connected via a valve to the operating pressure line (35 psi).

Each on-chip pneumatic valves was actuated by a computer controlled external solenoid valve (SMC S070B-5DG, SMC, Yorba Linda, CA, USA) [176]. These 3-way valves either direct pressure to the control channel (causing closure of the on-chip valve), or vent the pressure from the control channel (allowing the on-chip valve to open via elastic restoration of the PDMS membrane). A custom-written LabView program was used to control the timing of valve operations for sample injection. The sample was contained in a septum sealed vial with a fixed pressure inlet (1.5 psi) plus an outlet tubing (#30 PTFE tubing) connected to the sample inlet port of the fluidic layer of the chip. The vial end of the tubing was immersed below the liquid sample. Before injection, sample and BGE priming steps were performed to remove any air trapped in the tubing and microchannels as shown later in Figures 4-13 and 4-14.

For the time-dependent volume chip, it is important to know the characteristic response time of the valves (both the solenoid valve controlling air pressure, as well as the on-chip microvalve). To estimate the actual actuation time (time fluidic channel is open to allow sample injection) of the microvalves, an Autolab potentiostat (PGSTAT101, Metrohm, The Netherlands) was used to apply a small voltage (5 V) between the buffer well (ground) and buffer inlet (5 V) of the microchip injector. The potentiostat would then measure the current while the microvalve was momentarily opened for various durations (100, 200 and 400 ms). When the fluidic path was open, an electrical circuit would be established and a stable current would be recorded. When the path was closed, the current would fall back to zero. By taking the difference of the duration of the steady current plateau and the programmed valve actuation time, an estimated delay time could be calculated. Figure 4-11 shows the plot of current vs. time

for 400 ms valve actuation time. The plateau was measured to be 380 ms long, giving an estimated microvalve delay time of 20 ms. A similar result was observed for the 100

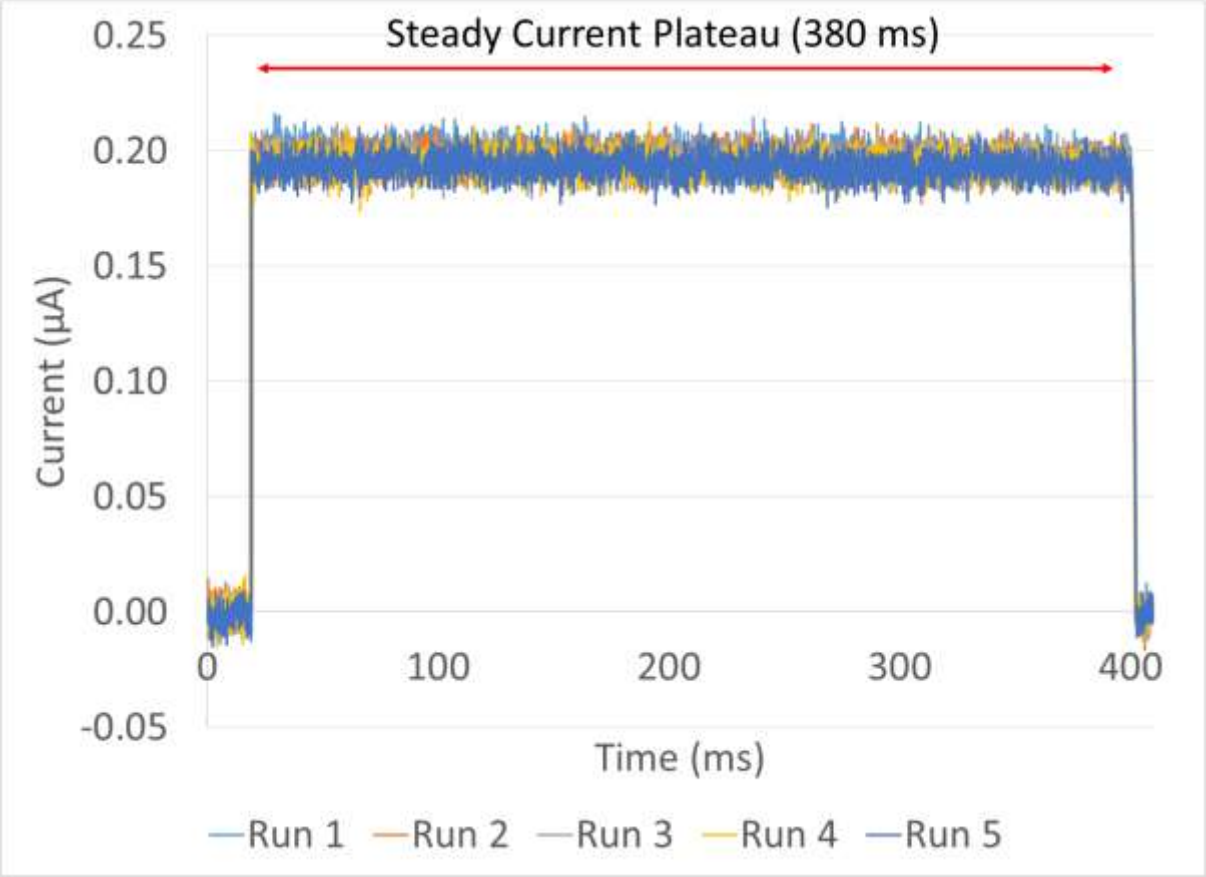

Figure 4-11 **Measurement of microvalve response time.**

A potential of 5 V was applied between buffer well (ground) and buffer inlet (5V). Current was measured during the actuation (fluidic channel unrestricted) of the microvalve for 400 ms. A steady current plateau of 380 ms was measured, giving the microvalve a response time of 20 ms.

and 200 ms actuation test (data not shown). Therefore, to allow for adequate microvalve actuation time, the operation time for the time dependent volume injector was kept at 100 ms and above (5x the estimated delay time of the microvalve).

4.3.2.5 Microvalve injection and detection

To assess the repeatability of injection, the sample was injected within the chip and then electrokinetically transported through the separation capillary (length: 20 cm, ID: 75 µm) and through the detector (effective length: 16 cm). Detection occurred in the CUV-CCE sample cell (Ocean Optics, Dunedun, FL, USA) coupled to the PX-2 pulsed xenon light source and USB4000 spectrometer. A schematic illustrating the experimental setup is shown in Figure 4-12. The same setup is also used for the fixed volume injection chip.

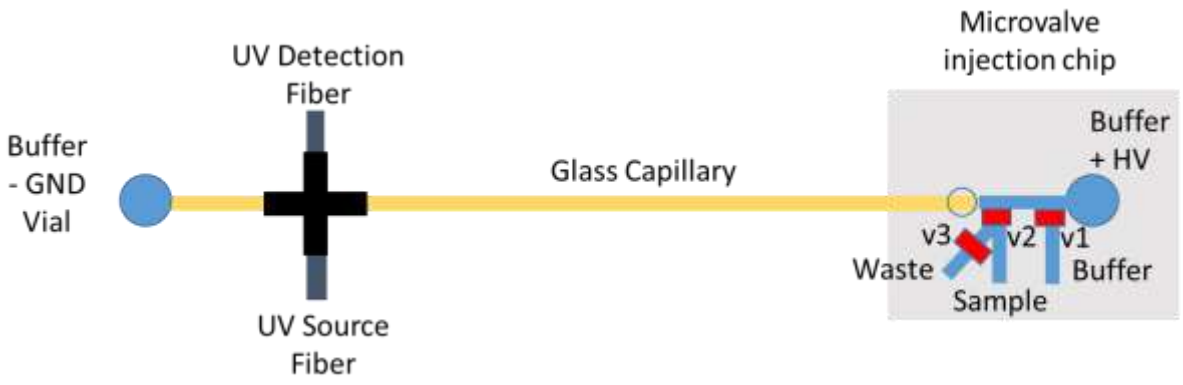

Figure 4-12 **Schematic of experiment setup to determine repeatability of injection of PDMS microvalve injection chip.**

The chip is connected to a fused silica capillary. The capillary is inserted into a CUV-CCE sample cell (Ocean Optics, Dunedun, FL, USA) for detection.

4.3.2.5.1 Time-dependent volume injection

Time dependent volume injection was achieved by opening the flow path between the sample inlet and separation channel for a preset amount of time at a fixed pressure. A low sample pressure of 1.5 psi was selected to closely mimic the pressure used by Kelly et al. [155], and to ensure a relatively long injection time to minimize error

in the duration the microvalve remains open. A schematic of the time-dependent volume injection method is shown in Figure 4-13.

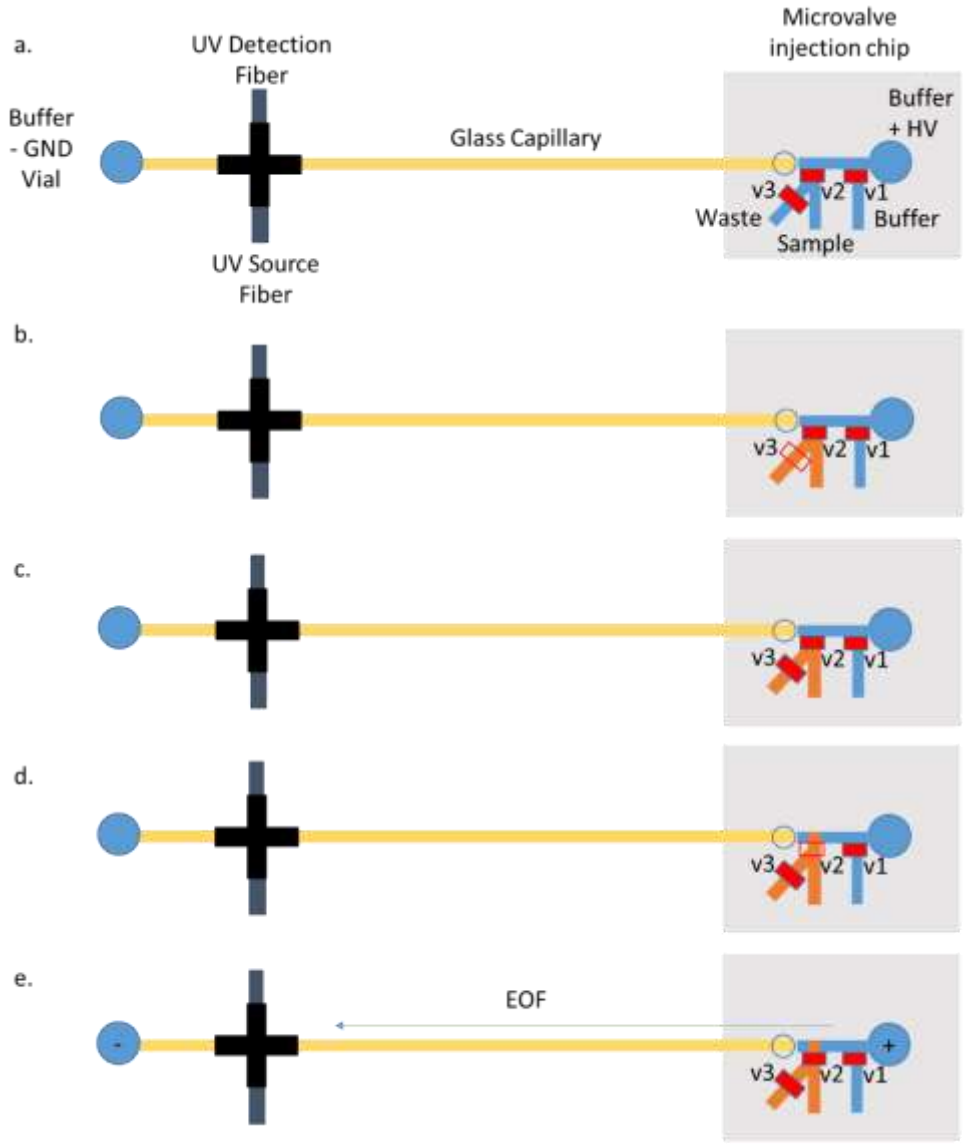

Figure 4-13 **Schematic of time dependent volume microvalve CE chip valve actuation and injection process.**

a) Micro-valve CE chip prefilled with running buffer. Micro-valves (v1 and v2) closed upon completion of filling with buffer. **b)** v3 opened to allow filling of sample channel with the sample solution (priming). **c)** v3 closed. **d)** v2 opened momentarily to inject sample into separation channel. **e)** v2 closed, and then CE potential is applied and sample is driven by EOF (blue arrow) towards UV detector.

4.3.2.5.2 Fixed volume injection

For the fixed volume injection chip, the injected volume was determined by prefilling a fixed volume chamber (to volumetrically measure the sample) prior to injection and application of the separation potential. The fixed volume injection chip is comprised of two fixed volume chambers in the injection chip. The dimension of the combined metered portion separation channel is 75 μm wide, 20 μm high, and 4 mm long. This allows a sample volume of 3 nL (half volume) or 6 nL (full volume) to be injected. These volumes could be tuned by changing the chip design, if needed. Only a single volume is needed for chemical purity analysis, but this chip included the option for different volumes as this would enable later optimization of the injection volume.

The procedure for half volume injection is shown in Figure 4-14. The operation of full-volume loading is similar to half-volume loading, except v3, v7, and v4 are opened in step d of Figure 4-14. The sequence of microvalve actuation steps for injection is performed in such a way that the sample pressure (1.5 psi) is not “trapped” in the separation channel. The trapped pressure could otherwise distort the channel and change its volume, due to the elastic nature of PDMS. Once the sample is loaded in the fixed volume, the sample inlet is sealed by actuating v3. An allotted time (~5 s) is then elapsed to allow the sample pressure to be released through sample waste. The waste outlet is then sealed by actuating either v5 (half-volume injection) or v4 (full-volume injection). After the simultaneous opening of v1, v7, and v8, electrophoretic potential is applied. Note that it is important to ensure these valves are fully open prior to applying the separation potential, otherwise it is possible for the full voltage to be momentarily applied across the slowest one of the valves, leading to dielectric breakdown and damage to the chip.

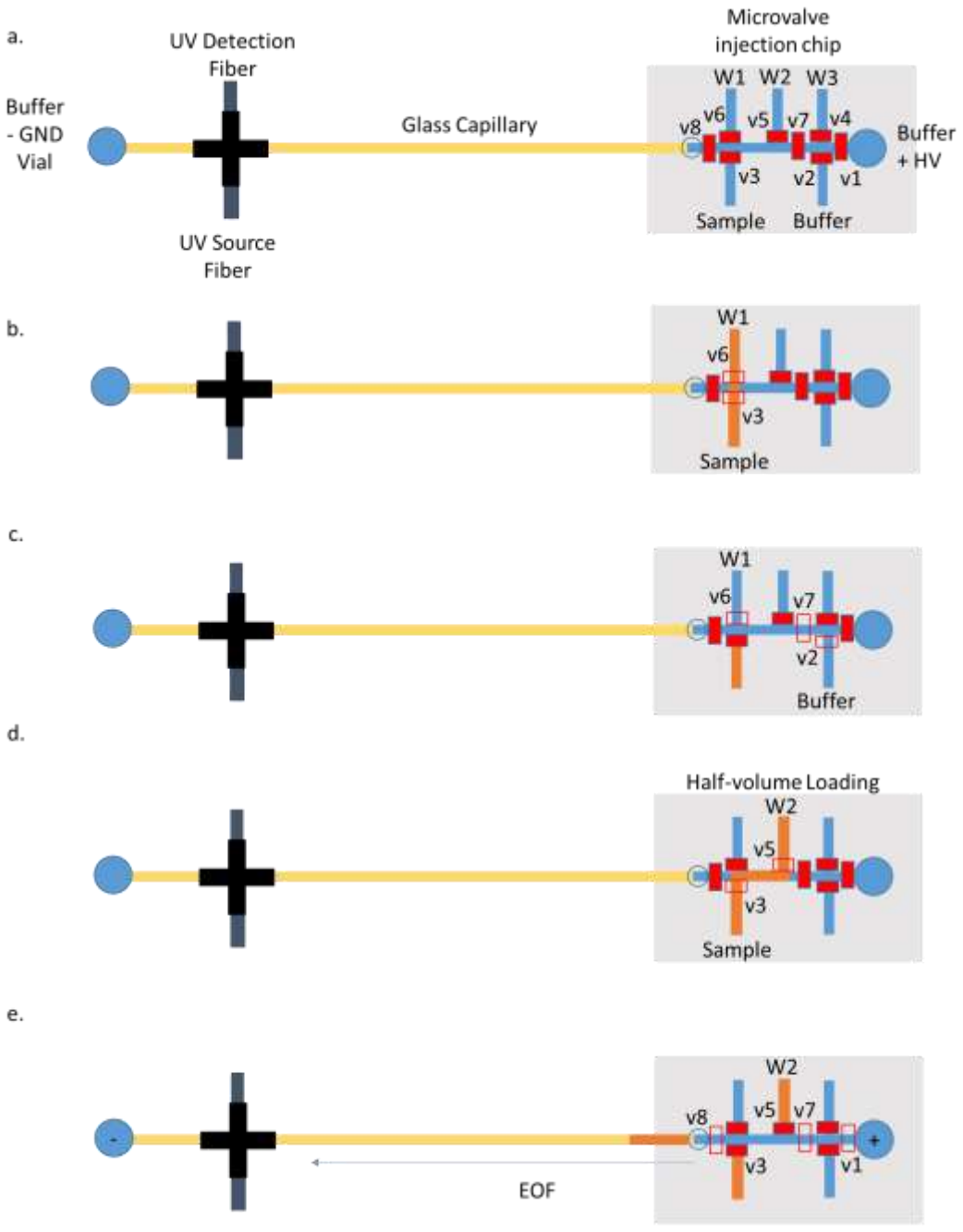

Figure 4-14 **Schematic of fixed volume microvalve CE chip valve actuation and injection process.**

a) Fixed volume chip primed with BGE. **b)** Sample is primed from the sample inlet (v3, v6 open, then closed after operation). **c)** BGE is primed from the buffer inlet (v2, v7, v6 open, then closed after operation). This step is optional. **d)** The half-chamber is then loaded with sample from the sample inlet (v3, v5 open). When filled, v3 is closed first, then v5, to avoid trapping any pressure inside the chamber. **e)** The sample is then separated by applying electrophoretic potential (after v1, v7, v8 are fully open).

4.3.2.5.3 Detection and analysis

For both chips, to drive the injected sample towards the detector, a field of 200 V/cm (4 kV) was applied across the microchip using a 0-30 kV power supply obtained from Information Unlimited (Amherst, NH, USA) via platinum electrodes placed in the reservoirs and a stable current was achieved. Chromatograms were collected from the time of injection until the sample had passed the detector. Data analysis was performed using OriginPro 8.5 as described in Section 2.2.2.2.

4.3.3 Results and discussion

4.3.3.1 Time-dependent volume injection

Using a sample pressure of 1.5 psi, a range of injection times was investigated to determine when the maximum peak height would level off, which would signify the point where the sample plug was wide enough that its true concentration was being measured at the peak center, rather than a more dilute version due to diffusive broadening. We arbitrarily chose this as the valve opening time. Figure 4-15 shows peak height for injection times ranging from 200 to 1000 ms of 5 mM thymidine sample

(in water) monitored at 256 nm. It can be seen that the absorbance begins to level off at an actuation time just below 600 ms.

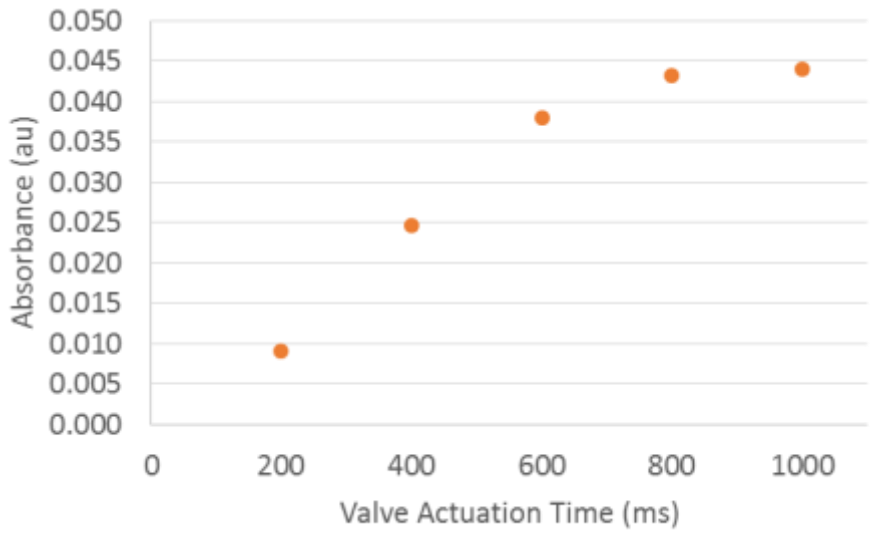

Figure 4-15 **Plot of Absorbance (au) versus Valve Actuation Time (ms)**

Maximum absorbance (peak height) is shown to start leveling off around 600 ms, and achieve a near-maximum value at 800 ms, which would potentially signify an optimal injection time as the center of the sample plug would closely representative the pure sample with minimal diffusive effects

Successive injections were then run at 800 ms microvalve actuation times. For each, the peak area was determined, and then the %RSD in peak area of all runs could be computed. Figure 4-16 shows an overlay of eight successive injections of 5 mM thymidine at 800 ms. The peak areas were calculated for each run, and exhibited a peak area %RSD of 3.9% (n=8). This result is higher than the value published by Li et al. (%RSD of 1.77%, n=15) for a very similar chip design and operation [98]. This poorer performance could be attributed dead volume within the capillary-chip junction (which could cause undesired band broadening [177], [178] and a lower signal that is more susceptible noise), or perhaps due to a difference in noise between the setups (e.g.

optical detection system). Optimization of the capillary junction and other system aspects will be explored in Chapter 5.

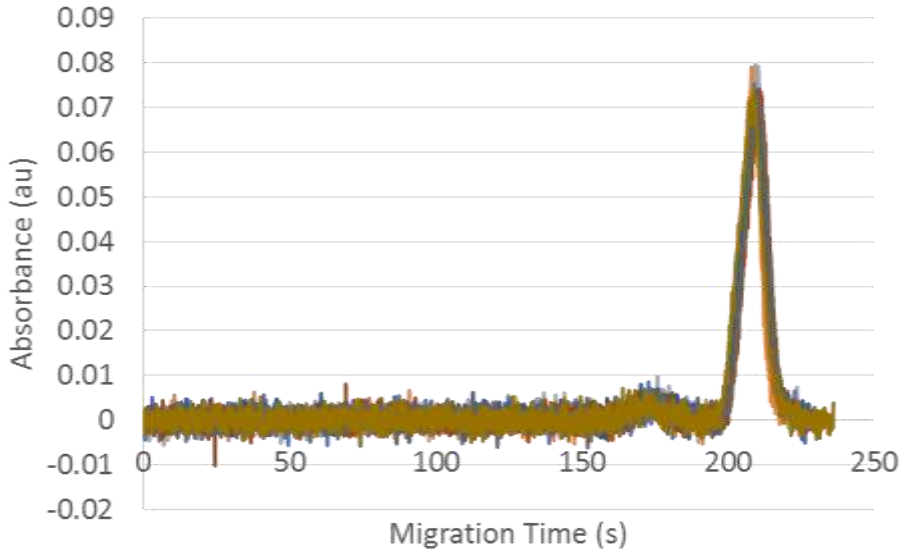

Figure 4-16 **Overlay of successive injections of 5 mM thymidine using time-dependent volume injector (n=8)**

4.3.3.2 Fixed volume injection

The fixed volume chip was then used to inject successive half-volume (3 nL) into the separation channel. Figure 4-17 shows an overlay of 11 successive half-volume injections of 5 mM thymidine, resulting in a peak area %RSD of 1.7% (n=11). Successive full-volumes (6 nL) of 5 mM thymidine was also performed, resulting in a peak area %RSD of 2.0% (n=9). Both of these results are similar to that reported by Li et al. (%RSD of 1.77%, n=15), using a time-dependent valve-based approached [98]. If the issues described in the previous section were addressed (capillary-chip junction, and noise in optical system), it is expected that the fixed volume approach could give superior %RSD performance.

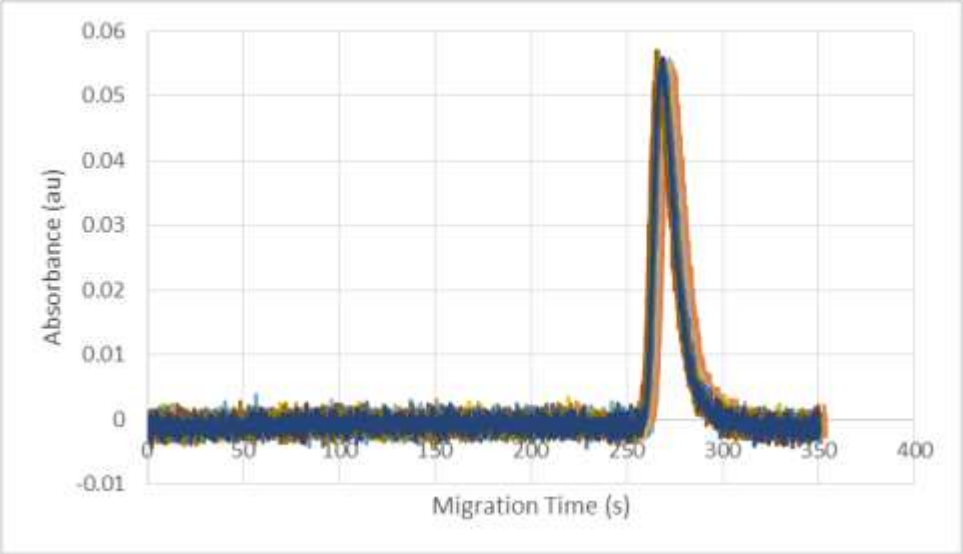

Figure 4-17 **Overlay of 8 successive injections of 5 mM thymidine using fixed volume (3 nl) injection chip (n=11).**

4.3.3.3 Comparison of time dependent and fixed volume injection

The chip and setup for the fixed volume approach are more complex; however, once the chip and setup have been assembled, operation is automated and there would be negligible difference to the operator. Comparing peak area %RSD between time-dependent and fixed volume injection shows ~2 fold improvement for fixed volume injections (3.9% for time-dependent volume versus 1.7% for fixed volume). While the fixed volume chip requires additional valves, the extra complexity of these valves is almost negligible, and the reduction in peak area %RSD is highly favorable. While the time-dependent method showed worse performance than has been reported in literature for the same injection method, it is likely this could be improved by reducing the dead volume within the capillary junction and improving the optical system. If the same improvements are then made in the fixed volume chip, then it is expected that the %RSD of the fixed volume chip (currently comparable to literature report of time-dependent injection) would be better than the value reported in literature. It is also

expected that the fixed volume chip will have a better chip-to-chip performance compared to the time-dependent volume chip as the fixed volume injection method will not be affected by any variability in chip-to-chip valve fabrication or other aspects of the system that can affect response time. This potential advantage will be explored in the future.

4.3.4 Conclusion

The use of microvalves to hydrodynamically inject sample into the separation channel has been shown to be highly repeatable (%RSD = 1.7% for the fixed volume injection method), comparable to best reports in the CE literature (e.g. 1.77% [98]). This %RSD is also below a value (2%) that has been suggested as an acceptance criterion for peak area reproducibility in CE [173]. Due to a novel injector design, further improvements in %RSD are expected after optimization of the capillary/microchip interface and the overall optical system. The prospects for improvement are discussed in Chapter 5.

4.4 On chip sample separation

4.4.1 Background

Having established adequate performance of detection and injection in the microchip format, the third component is to implement the separation itself in the microchip.

To achieve high peak separation resolution, unambiguous determination of species, and accurate peak area, the EOF within the separation channel should be highly uniform. Any spatial or temporal variations in the EOF within the channel could cause peak broadening or shifts in migration time. MCE chips are usually constructed

from either glass or PDMS. PDMS is highly favorable due to its relatively low cost and ease of fabrication, especially during the design phase, when many iterations of the design are needed. Furthermore, the use of PDMS would enable seamless integration of the separation channel with the microvalve-based injection and detection portions of the chip. PDMS can be conveniently bonded by air plasma oxidation (via corona discharge). Corona plasma treatment also modifies the hydrophilic PDMS surface to a more hydrophilic surface, which is needed for stable EOF. Unfortunately, however, it has been shown that the generated hydrophilic surface is fairly short lived [161], [179], regardless of how the surface is made hydrophilic [94], [180]–[182]. Instability of the hydrophilicity results in poor peak separation performance [94], [155], [169], [183], [184]. PDMS is also known to adsorb various materials onto its surface or absorb hydrophobic analytes into the bulk [185], which can also create variations in EOF, affect the amount of sample remaining in solution, or lead to cross-contamination.

Another popular material choice for electrophoresis is fused silica, typically in the form of capillaries. Fused silica has many positive characteristic such as good mechanical and optical properties, high electrical insulation, good EOF stability, and low chemical reactivity. However, fused silica microchips are relatively more expensive and difficult to fabricate than PDMS. Patterning of fused silica typically requires the use of harsh and dangerous chemicals, such as Piranha (a mixture of sulfuric acid and hydrogen peroxide) for cleaning and buffered hydrofluoric acid for etching [186]–[188]. Furthermore, bonding of the fused silica chip to a substrate (to close the channel) can be challenging [189]–[192]. Another downside of glass microchips of course is the

difficulty in integrating microvalves with tiny dead volumes, making it challenging to integrate the valve-based injection approaches investigated in Section 0.

To best leverage the advantages of both platforms, several groups have worked on integrating fused silica capillaries into PMDS microfluidic devices [155], [193], [194]. Koczka and Gáspár integrated a separation capillary into a split flow injection chip by creating a capillary insertion port that is perpendicular to the sample loading channel [194]. This simply approach requires no modification of the typical PDMS chip fabrication process as the capillary is inserted into a narrower version of the same kind of port as normally used for insertion of tubing, and was adopted for our initial studies. However, as will be discussed in Chapter 5, it turns out that this geometry has a significant dead volume and leads to substantial peak broadening. Other, more sophisticated approaches for integrating capillaries into PDMS chips have also been demonstrated. *Kelly et al.* fabricated a PDMS pneumatic injection chip with a fused silica separation capillary that connects to the side of the chip such that the inside of the capillary is collinear with the sample loading channel [155]. *Dimov et al.* incorporated a fused silica separation capillary entirely within the PDMS chip itself by fixing a capillary filled with water to the bottom of the chip substrate and pouring uncured PDMS over it before curing the chip [193]. The trapped water within the capillary not only prevents uncured PDMS from entering the capillary, but as the water evaporates during the curing process, the gas creates air bubbles on both ends of the capillary to indicate where the inlets and outlets of the chip should be made.

In this section, the separation properties of both PDMS and fused silica are explored to determine an optimal configuration for the purposes of this feasibility study.

In particular, one configuration consists of a 20 cm long PDMS separation channel with integrated detection region; the other configuration consists of a 20 cm long capillary connected to a PDMS detection chip.

4.4.2 Materials and Methods

4.4.2.1 Reagents

Sodium phosphate monobasic (NaH_2PO_4), sodium phosphate dibasic dihydrate (Na_2HPO_4), sodium dodecyl sulfate (SDS), sodium hydroxide (NaOH), thymidine, furfuryl alcohol (FA), 2',3'-didehydro-3'-deoxythymidine (stavudine), and 3'deoxy-3'-fluorothymidine (FLT) were purchased from Sigma Aldrich (Milwaukee, WI, USA). Zidovudine impurity B (chlorothymidine, CLT) was purchased from LGC Standards (Wesel, Germany).

As described in Section 2.2.1, these compounds are well-known impurities and byproducts from the synthesis and purification of [^{18}F]FLT [24], [116]. Sample one was made with a mixture of 5 mM thymidine and 5.8 mM FA to incorporate analytes with different maximum wavelength absorbance (256 for thymidine and 224 for FA) to clearly identify the peaks. Sample two was made with a mixture of thymidine, FLT, and CLT (5 mM each) in order to bracket FLT with the fastest (thymidine) and slowest (CLT) eluting analytes (as observed in Section 2.3.1.2). Samples were made in 18 MΩ deionized water. The separation buffer was 100 mM SDS in 30 mM phosphate buffer (PB), designated as SDS-PB. All buffers were degassed prior to use.

4.4.2.2 Overview

In order to assess the separation performance in PDMS and fused silica, samples one and two were separated in both setups, and the chromatograms analyzed

to calculate separation resolution on both chips. The consistency of migration time was also measured (%RSD) to determine the stability of EOF and the surface over time.

As described earlier, reports have shown drift in migration time using PDMS for CE separation [94], [188]. Using a similar MCE chip design as illustrated in Figure 4-4, Vickers *et al.* observed a ~14% change in migration time for analytes using a PDMS separation channel after ~60 minutes of continuous run time [94]. Thus, a study was performed to examine this drift over at least 60 min in both setups. (Even in the capillary setup, the presence of the microinjector chip means that ~1 cm of the separation pathway is made from PDMS.)

Finally, a mathematical technique to correct for migration time drift was then investigated to determine the potential to overcome small amounts of drift. The correction technique, described by Bidulock et al. [195], uses two internal standards within the solution to bracket the analyte of interest. Using this technique, Bidulock not only corrected the migration time, and reported a decrease in standard deviation in migration time from 3.60% to 0.57% [195].

4.4.2.3 Microfluidic chip design and fabrication

4.4.2.3.1 Full PDMS chip

The wafer mold containing the design for the full PDMS chip was fabricated as described in Section 4.2.2.2 using SU-2150 negative photoresist. Figure 4-18a illustrates the design used to create the mold, which features a 20 cm long serpentine channel (16 cm effective length) to match the length of the fused silica capillary used in Section 4.3.2.2. All channels were 125 µm deep and 125 µm wide to reduce fabrication complexity, while allowing insertion of 125 µm OD fiber optic cables (ThorLabs).

Tapered turns are implemented (Figure 4-18b) to reduce peak skewing around turns [196]. Paegel *et al.* [196] demonstrated that a 4:1 ratio (width of straight channel:width of curved channel) produced highest separation resolution compared to smaller ratios tested (2:1 and 1:1) when using serpentine turns.

The PDMS chip was fabricated as described in Section 4.2.2.2. All four wells on the PDMS chip were formed using a 4.75 mm ID catheter punch (HS1871730P1183S, Syneo, West Palm Beach, FL). The PDMS CE chip contains alignment channels for

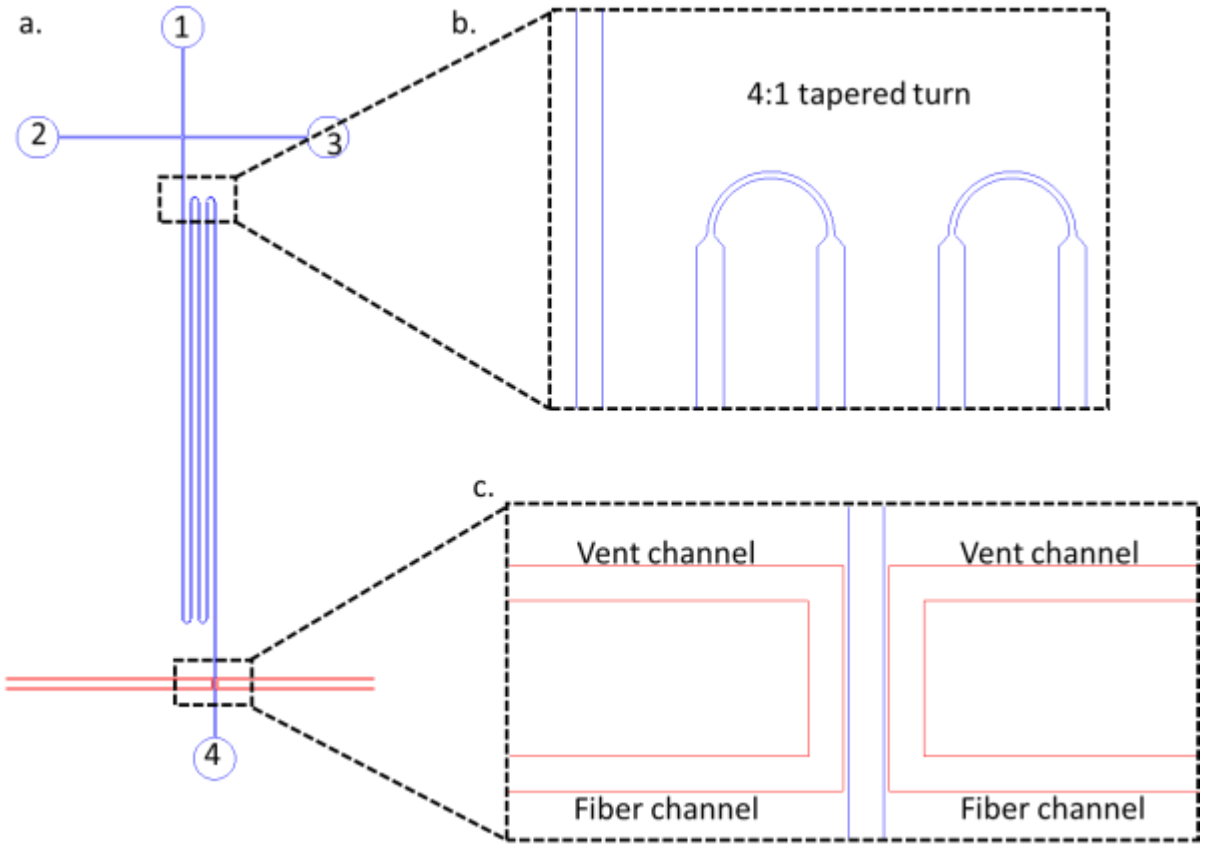

Figure 4-18 **Mask design used for full PDMS separation chip.**

a) Entire chip schematic showing fluidic channel (blue) and optical fiber alignment channels (red). Four wells indicated are 1: Buffer well, 2: Sample well, 3: Sample waste, 4: Buffer waste. **b)** Inset showing zoomed in view of 4:1 tapered turns used to reduce peak skewing. **c)** Inset showing zoomed in view of fiber alignment channels, and (non-extended) 125 µm OPL.

easy insertion and alignment of two 125 µm OD fiber optic cables – an illuminating fiber and a detection fiber (Figure 4-18c), as described in Section 4.2.2.2. A PX-2 Pulsed Xenon source (Ocean Optics) provided UV illumination through a 125 µm optical path length (to simplify design and maximize separation resolution) and the detection fiber was coupled to a USB4000 spectrometer (Ocean Optics).

4.4.2.3.1.1 Performing separation in the PDMS microchannel

The conditioning of the PDMS microchip was performed as described in Section 4.3.2.3.

During the experiment, the PDMS chip and samples were maintained at room temperature (22°C). Due to the desire to investigate first with a simple chip architecture, valve-based injection was not used here. Instead, samples were injected electrokinetically at 200 V/cm for 5 s and separation was performed at 200 V/cm (4 kV) using a 0-30 kV power supply obtained from Information Unlimited (Amherst, NH, USA) as shown in Figure 4-4. Sample was driven from sample well (S) towards sample waste (SW) electrokinetically to fill up the intersection with sample by applying potential. Based on the geometry, the injected volume is expected to be <1% of the volume of the separation channel (i.e. a 125 µm segment compared to the 20 cm channel length). The sample plug was then driven towards the detection region by applying potential between the buffer well (B) and buffer waste well (BW). While electrokinetic injection does potentially pose an injection bias, this experiment is concerned only with separation of analytes (which should not be affected by this issue), and not their quantitation. Detection was performed as described in Section 4.2.2.2. Data analysis was performed as described in Section 4.2.2.3.

4.4.2.3.2 Fused silica capillary chip

Fabrication of the fused silica capillary chip was identical to the method described in Section 4.3.2.2, using a hybrid device consisting of a capillary connected to a PDMS microvalve-based injector chip. A 75 µm I.D., 375 µm O.D. Teflon-coated fused-silica capillary (Polymicro, Phoenix, AZ, USA) was used, with a total length of 20 cm (16 cm to detector window, similar to full PDMS chip described in the previous section). A PDMS injector chip with the time-dependent injection design (Figure 4-10) was used to simplify fabrication and setup.

4.4.2.3.2.1 Performing separation in the fused silica channel

The conditioning of the PDMS microchip was performed as described in Section 4.3.2.3. During the experiment, the capillary and samples were maintained at room temperature (22°C). Injection was performed hydrodynamically as described in Section 4.3.2.5 and illustrated in Figure 4-12, but using a 400 ms actuation time to improve separation performance. A potential of 200 V/cm was applied for separation. Since quantification of concentrations/amounts of analytes wasn't important for these studies, detection was performed using a USB4000 spectrometer coupled to a PX-2 pulsed xenon light source using a CUV-CCE sample cell (all purchased from Ocean Optics, Dunedun, FL, USA). Absorption maxima at 224 and 254 nm were monitored. Data analysis was performed as described in Section 2.2.2.2.

4.4.2.3.3 Migration time drift correction technique

The correction technique, described by Bidulock et al. [195], relies on maintaining the same relative distance between pairs of peaks. Effectively, the time axis (x-axis) is scaled. Mathematically, the migration time (x) for the middle peak is calculated from:

$$x = \frac{t_1\,(t_3 - t_2) + t_3(t_2 - t_1)}{t_3 - t_1} \quad (4.2)$$

where t_1 is the migration time for the first eluting peak, t_2 is the uncorrected migration time for middle peak, and t_3 is the migration time for last eluting peak.

From here, the ratio of original migration time to new migration time can be calculated (t_2:x), and the time axis for the whole chromatogram can be scaled accordingly.

This method can correct for EOF difference between one CE separation run and another.

4.4.3 Results and discussion

4.4.3.1 PDMS channel separation

Using sample mixture one, the separation of 5 mM thymidine and 5.8 mM FA was attempted on the full PDMS chip. Though the migration time appeared consistent with results in the silica capillary (see next section), no separation was observed (Figure 4-20). Futhermore, there was noticeable tailing of the peaks, possibly due to analytes sticking or absorbing to the PDMS surface. A reduction in analyte concentration and the use of longer separation channels was attempted to improve separation of the two analytes, but the results were similar (data not shown). Smaller volume injections (<5 s) were also attempted, but produced similar results (data not shown).

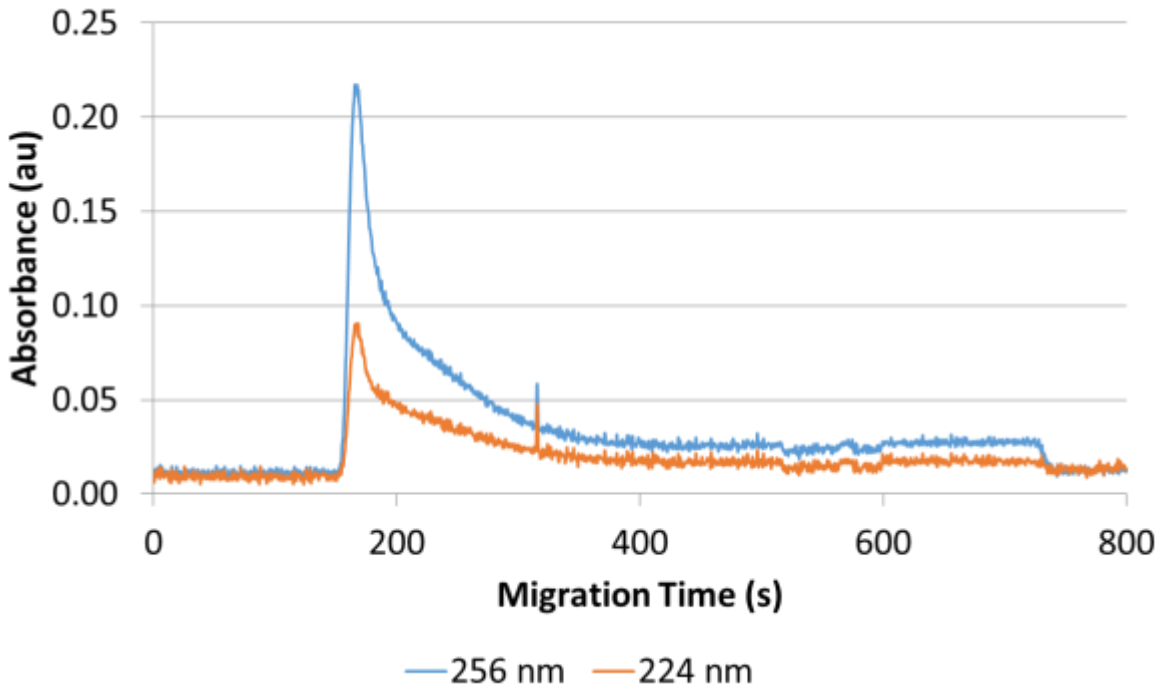

Figure 4-19 **Separation performance of the PDMS separation channel.**

Single Injection of sample containing 5 mM Thymidine and 5.8 mM FA in 30 mM PB with 100 mM SDS into the PDMS separation channel.

Though others have shown that the sticking of analytes to PDMS can be mitigated by coating the PDMS surface with silica [197], this solution was not tried here, and it is unclear if in fact this is the issue. It is also possible that the conditioning of the PDMS channels was very unstable, adversely affecting the resolution. No further experiments were performed with the PDMS.

4.4.3.2 Fused silica channel separation

Using sample one, the separation of 5 mM thymidine and 5.8 mM FA was attempted on the hybrid PDMS fused silica chip. In this case, slight separation between thymidine (peak 1) and FA (peak 2) was achieved (Rs = 0.75) as shown in Figure 4-21. Migration time of the peaks shown in Figure 4-21 was measured at 174 seconds for thymidine (visible in both wavelengths) and 193 seconds for furfuryl alcohol. Note that

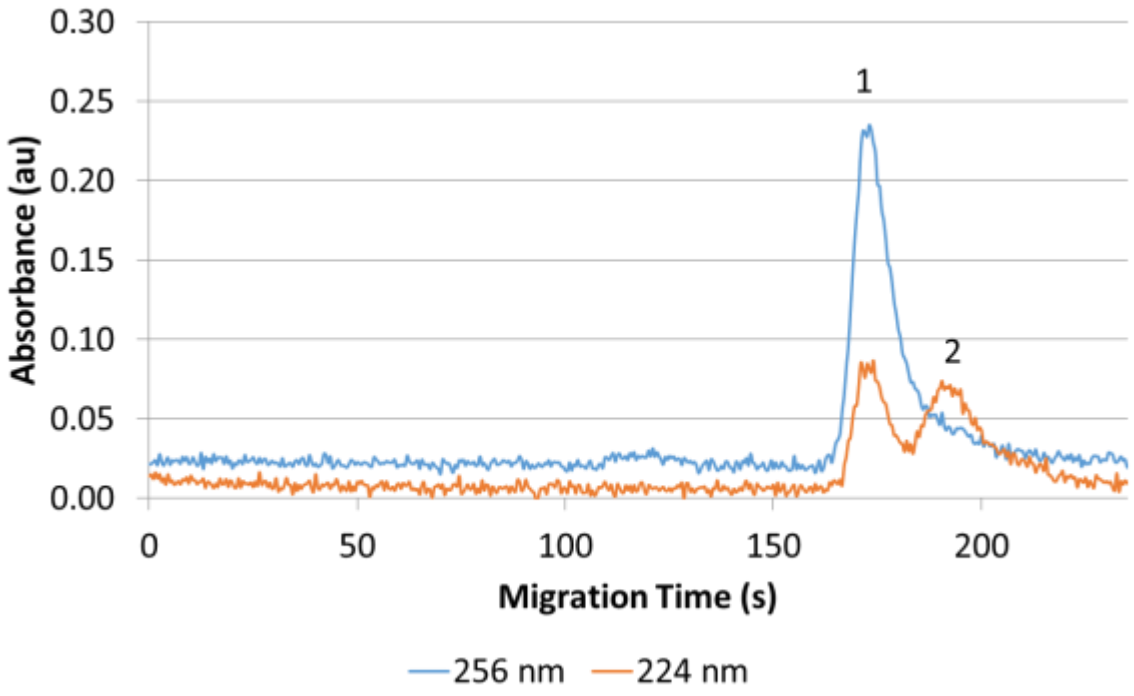

Figure 4-20 **Separation performance of the silica capillary (with PDMS injector).**

Single Injection of sample containing 5 mM Thymidine (peak 1) and 5.8 mM FA (peak 2) in 30 mM PB with 100 mM SDS into the PDMS separation channel.

the migration time of thymidine matches closely the peaks in Figure 4-20 (169 seconds), suggesting that similar EOF occurs in the PDMS channel despite the long tailing of the peaks.

When compared to the migration time obtained using a 60 cm capillary (52 cm effective length, Section 2.3.1.2, thymidine had a migration time of 617 s, resulting in an elution rate of 0.084 cm/s. This is comparable to the elution rate of thymidine obtained using the 20 cm (16 cm effective length) capillary used here (0.092 cm/s). To prevent issues noticed due to excess Joule heating, the use of a smaller ID capillary (50 µm) will be explored and discussed in Section 5.4.

While baseline separation was not achieved, likely due to the shorter capillary length compared to that used in Chapter 2, the fused silica capillary clearly performed better than the full PDMS chip.

The separation resolution was also evaluated between FLT and the slowest and fastest eluting analytes (CLT and thymidine, respectively). Using the fused silica chip, the sample containing thymidine, FLT and CLT (5 mM each) was used, resulting in baseline separation ($R_s > 1.5$) of all 3 compounds (Figure 4-22). The resolution R_s between the two closest peaks (thymidine and FLT) was calculated to be 2.1, and the resolution between FLT and CLT was 3.1. While this demonstrated the ability of the fused silica chip to obtain baseline separation between these three compounds, future optimizations will be required to obtain baseline resolution between all 6 related FLT compounds (thymidine, thymine, FA, stavudine, FLT, and CLT).

To calculate the %RSD in migration time, four successive injections were performed. These experiments resulted in a migration time %RSD of <1% for each of

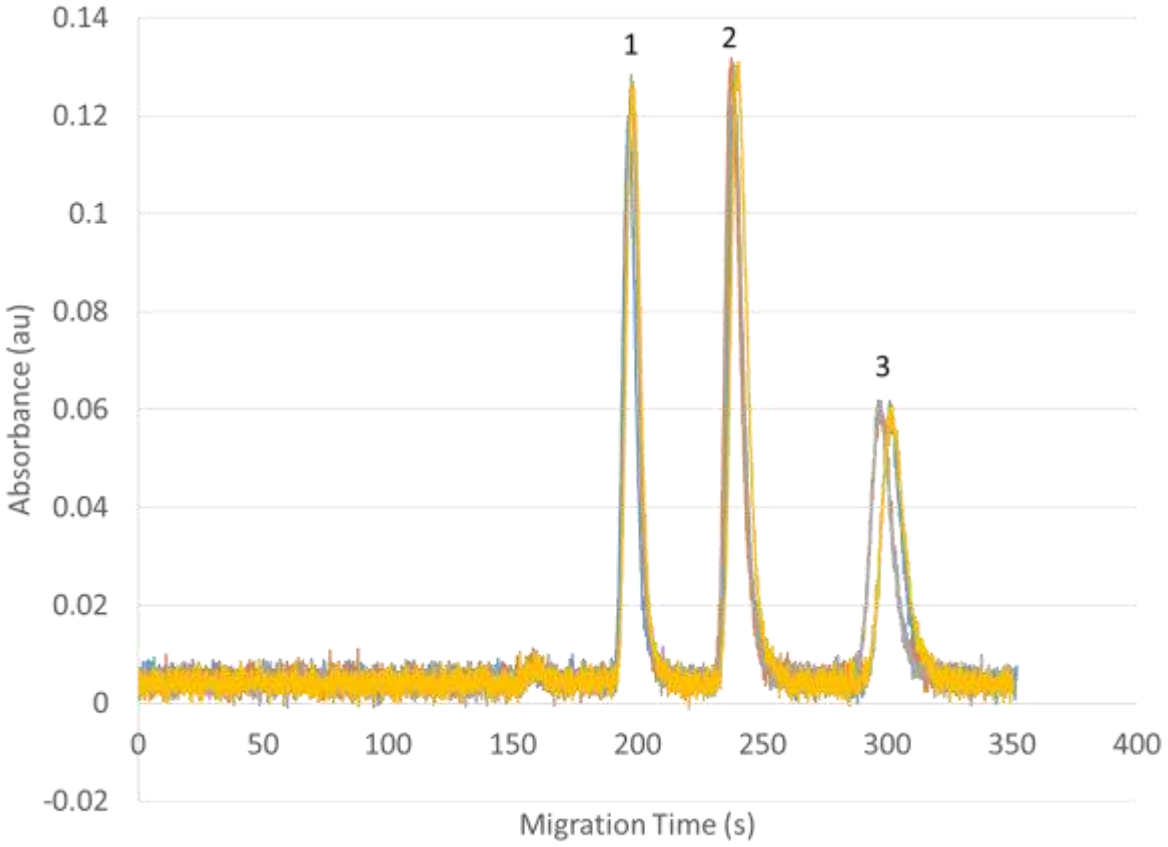

Figure 4-21 **Overlay of 4 successive injections using time dependent volume injector**

5 mM thymidine (peak 1), 5 mM FLT (peak 2), and 5 mM CLT (peak 3). Separation was performed in a fused silica capillary. Injections performed at 1.5 psi for 400 ms.

the three compounds. Peak area %RSD was also calculated to compare to results observed in Section 4.3.3.1 using the time-dependent volume injector. The results here were similar, i.e. ~ 3.3 - 3.6% for the three different species, compared to 3.9% observed previously. Table 4-3 summarizes peak area %RSD, peak width, migration time (t_m), and t_m %RSD.

Table 4-3 **Peak area %RSD, peak width (s), migration time (t_m), and t_m %RSD for thymidine, FLT, and CLT (5 mM each) for separation performed on hybrid PDMS fused silica capillary chip (n=4).**

Experiments used the PX-2 xenon light source and USB4000 spectrometer. Results are from n=4 experiments.

	Thymidine	FLT	CLT
Peak area %RSD	3.3	3.3	3.6
Peak width (s)	20±0	20±1	19±1
t_m (s)	197	239	300
Reproducibility (t_m) %RSD	0.36	0.44	0.83

4.4.3.3 Extended study on migration time drift using hybrid fused silica MCE chip

Due to the presence of PDMS for a portion of the separation channel, 12 successive runs were performed using sample two to see if a migration time drift would be observed, as has previously been reported in PDMS channels. Each run lasted about 7 minutes, corresponding to a total run time of ~84 minutes. Figure 4-23 shows an overlay of all 12 runs. Although it is not clear from an overlay, successive experiments showed a steady shift to slower migration times. This is most noticeable for the slowest eluting compound (CLT), which is possibly due to the fact that CLT spends the most time in the PDMS portion of the MCE device. Figure 4-24 shows a drift (increase) in migration time for thymidine, FLT, and CLT shows over the 12 runs. CLT exhibited the highest RSD% in migration time (1.60%). An overall change of 3.3% in migration time from run 1 to run 12 (289 seconds to 300 seconds) was calculated for CLT. This is much lower that the reported 14% by Vickers *et al.* [94], and is possibly

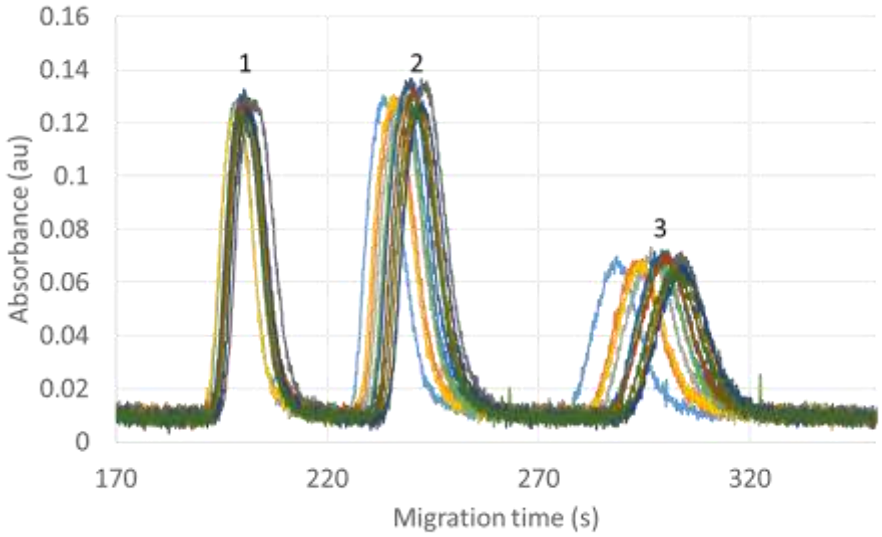

Figure 4-23 **Overlay of 12 successive sample injections using time dependent volume injector**

5 mM thymidine (peak 1), 5 mM FLT (peak 2), and 5 mM CLT (peak 3). Separation was performed in a fused silica capillary. About 1cm of the separation channel is formed by the outlet of the PDMS injection chip. Injections were performed at 1.5 psi sample pressure for 400 ms duration.

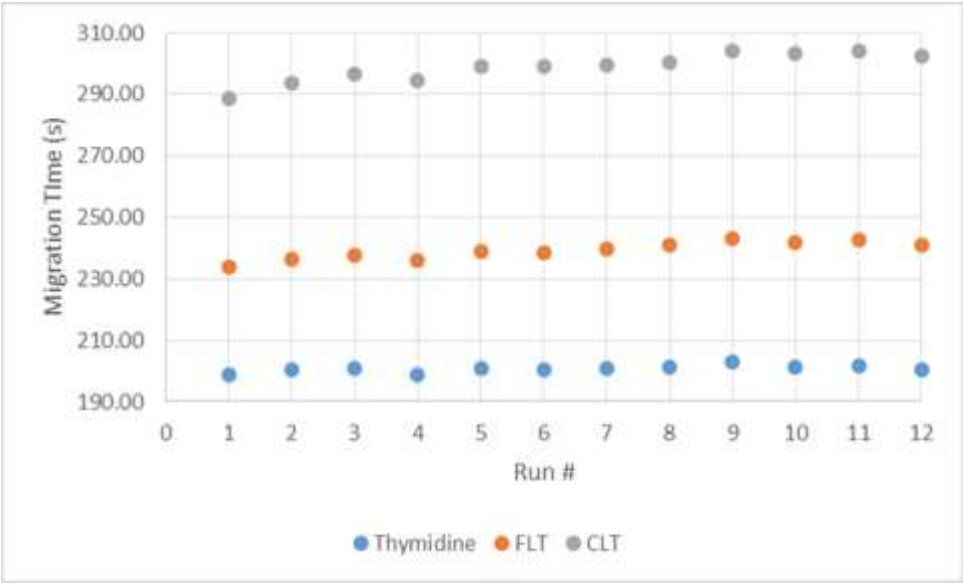

Figure 4-22 **Trend in migration time for successive CE runs using PDMS injector and silica capillary separation channel.**

t_m for thymidine, FLT, and CLT shown to increase over the course of 12 successive runs.

due to the shorter length of PDMS material along the separation channel (~1 cm here

versus 4.2 cm [198]).

Using the migration time correction technique described in Section 4.4.2.2, the time axis was adjust for each chromatogram. The new overlay of the 12 chromatograms after correction is shown in Figure 4-25. Improvements in %RSD for migration time were seen (<1% for all compounds) and peak area (<2% for all compounds). These results are summarized in Table 4-5. This shows the possibility to use the migration time correction to adjust for drift caused by unstable surface PDMS conditioning.

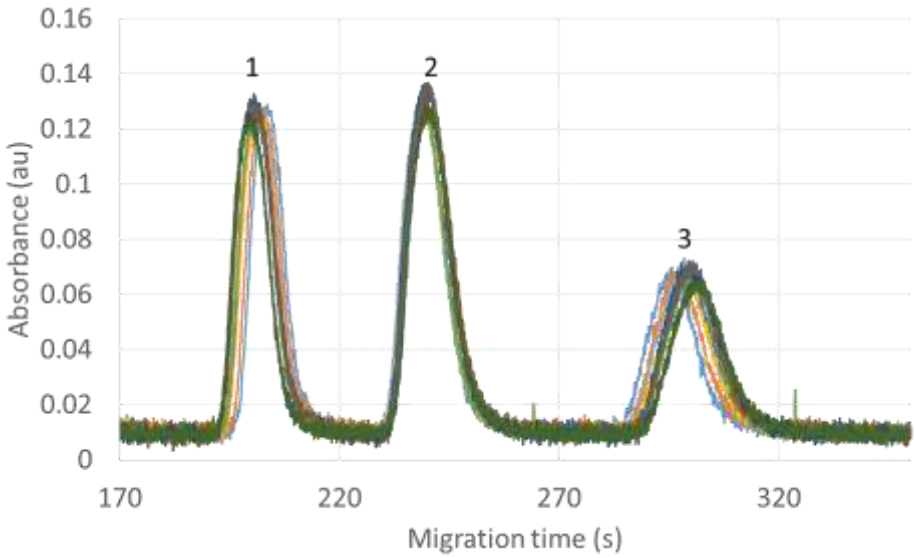

Figure 4-24 **Time corrected overlay of 12 successive injections**

5 mM thymidine (peak 1), 5 mM FLT (peak 2), and 5 mM CLT (peak 3) using time dependent volume injector. Separation was performed in a fused silica capillary. Injections performed at 1.5 psi at 400 ms.

In order for this migration time correction technique to be useful, it is necessary to have at least 3 components in the mixture that can be unambiguously identified. For samples containing less than 3 compounds, the use of internal standards would be needed. In the case of the analysis of purified FLT, the impurity profile may be different from run to run. To avoid ambiguity, perhaps thymidine and CLT could be spiked in as internal standards to bracket FLT and allow the use of the correction technique and adjustment of the time-axis. A second run would also have to be performed with different standards so that thymidine and CLT could be accurately quantified.

Typically, in QC analysis of PET tracers, only a single run is performed, in which case drift shouldn't be an issue, as our observations show that EOF is very consistent for the first 4-6 runs immediately after conditioning the capillary. However, multiple runs may be desirable in order in increase confidence in the data, and then this would become a consideration. Multiple runs are generally not possible with HPLC due to the long duration of each analysis run including cleaning time (that prevents high throughput), and the high cost of the system (that prevents the use of multiple HPLC systems). However, due to the rapid analysis time of CE, and the possibility of integrating multiple CE channels in a compact device, such approach might be practical with CE..

Table 4-4 **%RSD of migration time (t_m), peak height, and peak area for 12 successive separation thymidine, FLT, and CLT (5 mM each) performed on hybrid PDMS fused silica capillary chip after correction technique.**

	Migration time (t_m) (s)			Peak height (au)			Peak area (au*s)		
	Thymidine	FLT	CLT	Thymidine	FLT	CLT	Thymidine	FLT	CLT
%RSD	**0.14**	**0.03**	**0.21**	**2.07**	**2.71**	**3.56**	**1.74**	**1.21**	**1.48**

4.4.4 Conclusion

While a single microchip containing the injector, separation channel, and detection region would be desired, we observed extremely poor separation in the PDMS channel, perhaps due to unstable EOF and/or the stickiness/absorbing properties of the PDMS channels. Since the performance of the PDMS channel does not appear adequate for separation of the mixed FLT sample (and possibly other PET tracers samples) without significant further efforts, a hybrid microdevice construction was instead selected. The incorporation of a fused silica capillary increases the number and complexity of assembly steps and possible places for errors to occur (e.g. capillary clogging, dead-volume at capillary interface, capillary breakage), as well as an overall larger MCE device than a single integrated chip. However, it provides a highly stable separation medium compared to PDMS. While the separation of only 3 compounds (thymidine, FLT, and CLT) was displayed, the full separation of all 6 compounds of interest in FLT samples could be achieved on a longer fused silica capillary (as explored in Section 4.5.3.1).a

4.5 Integrated hybrid microchip CE device

4.5.1 Overview

In previous sections, I have shown that microfluidic detection and microfluidic injection perform as well or better than macroscale counterparts, and that a capillary can be integrated with the microfluidic device and achieve reproducible separation.

In this section, the performance of a device with all components integrated together is explored. For simplicity, the time-dependent volume microvalve injector as described in Section 4.3.3.1 was used for injection, though this could be swapped for

the fixed volume injector in the future. The 500 μm OPL chip as described in Section 4.2.2.2 was used for detection. The separation performance was tested on the complete hybrid MCE device using similar FLT samples used in Section 2.2.2.2.

4.5.2 Materials and methods

4.5.2.1 Reagents

Similar reagents were used as described in Section 2.2.1.

4.5.2.2 Microfluidic system design and fabrication

A schematic of the complete hybrid MCE device is shown in Figure 4-26. The time-dependent volume injection chip and extended optical path length chip are connected together with a fused silica capillary. Each of the PDMS chips (microvalve

and optical path length chips) were fabricated as described in Sections 4.3.2.2 and 4.2.2.2, respectively.

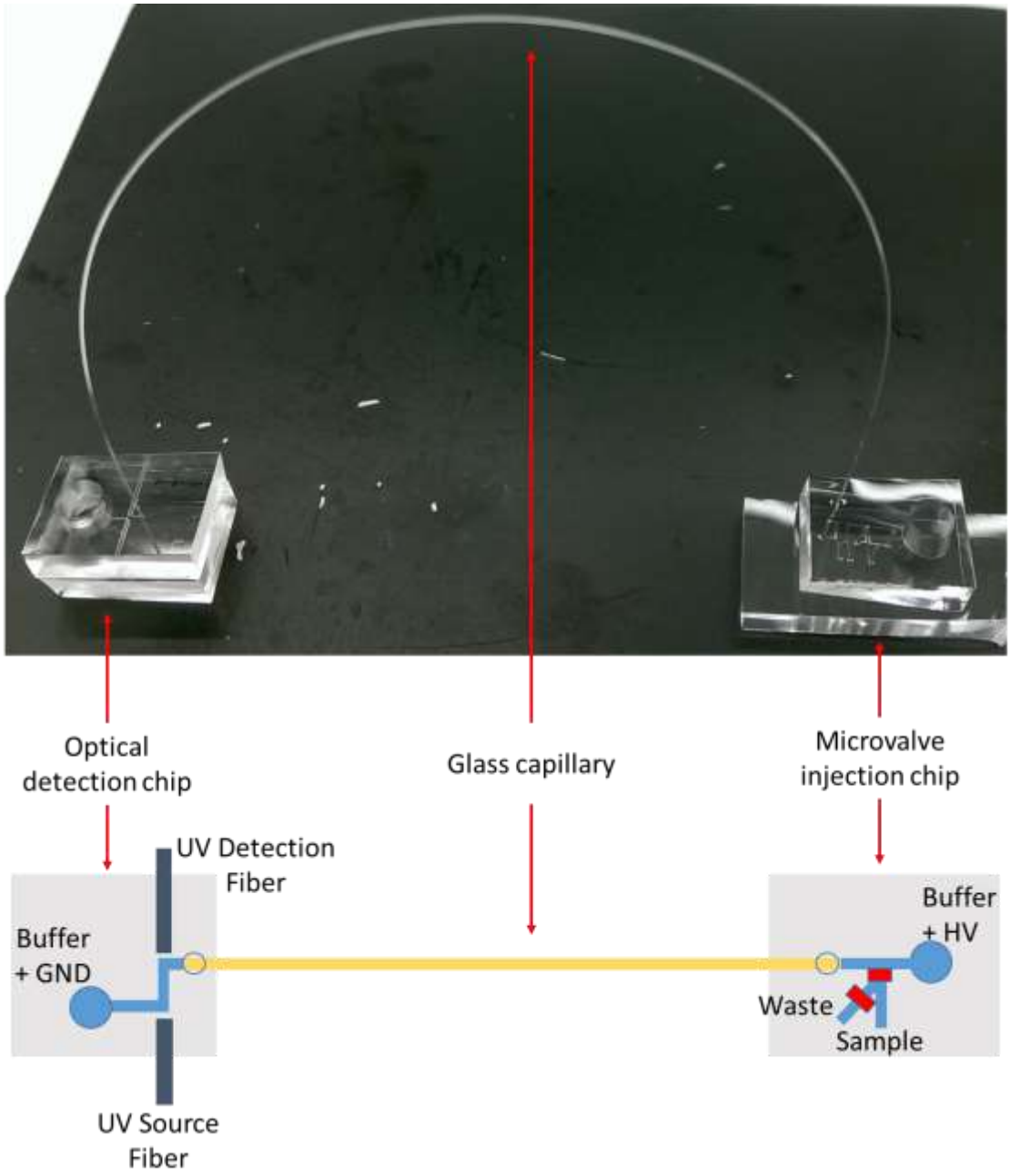

Figure 4-25 **Image and schematic of complete hybrid MCE device**

Photo (top) and schematic (bottom) of hybrid CE platform incorporating optical detection, micro-valve injector, and glass capillary separation channel.

The assembled device, with capillary joining the two chips, was prepared as follows. One end of the capillary was inserted through the capillary port of the injection chip before bonding to the substrate, with the capillary first inserted until flush with channel surface of the PDMS chip, then pulled ~1 mm back from the surface. The microvalve chip was then corona plasma bonded to the PDMS slab substrate and baked at 80°C for 2 hours to maximize bonding. Once removed from the oven, the other end of the capillary was inserted through the capillary port of the optical path length chip before bonding to its substrate. The optical path length chip was then corona plasma bonded to a bottom PDMS substrate.

4.5.2.3 Microchip and capillary conditioning

The conditioning of the PDMS microchip was performed as described in Section 4.3.2.3.

4.5.2.4 Microchip operation

The microvalves were operated as discussed in Section 4.3.2.4.

Absorbance measurements and data analysis were performed as described in Section 2.2.2.2.

4.5.2.4.1 Performing separation in complete hybrid MCE device

Sample was injected for 400 ms at 1.5 psi, and separation voltage was set at 200 V/cm (4 kV). Fused silica length was 20 cm, with an effective length of about 21 cm include a section of separation channel inside the injection chip. Optical fibers were inserted into the extended optical path length chip and coupled to the PX-2 pulsed xenon light source, and USB4000 spectrometer.

The complete hybrid MCE device was first tested with the separation of thymidine, FLT, and CLT (5 mM each in water). It was later tested with a sample containing all six FLT related analytes: 1 mM thymidine, 1 mM thymine, 2.3 mM FA, 1 mM stavudine, 1 mM FLT and 1 mM FLT. A BGE of 30 mM phosphate and 100 mM SDS (pH 7.4) was used for all separations of the 3-component and 6-component sample mixtures.

Since the results of Section 4.4 suggested that the 20 cm capillary may be insufficient, a hybrid MCE device with a 60 cm capillary was also fabricated (61 cm effective length) to improve separation resolution. Maintaining the separation voltage at 200 V/cm, a 6 compound FLT sample was injected. The sample consisted of 5 mM thymidine, 2 mM thymine, 2.5 mM furfuryl alcohol, 5 mM stavudine, 2.6 mM FLT, and 1.4 mM CLT.

4.5.3 Results and discussion

4.5.3.1 Complete hybrid MCE device performance

Using the complete hybrid MCE device with a 20 cm fused silica capillary, the sample containing thymidine, FLT, and CLT (5 mM each) was injected and separated as shown in Figure 4-27.

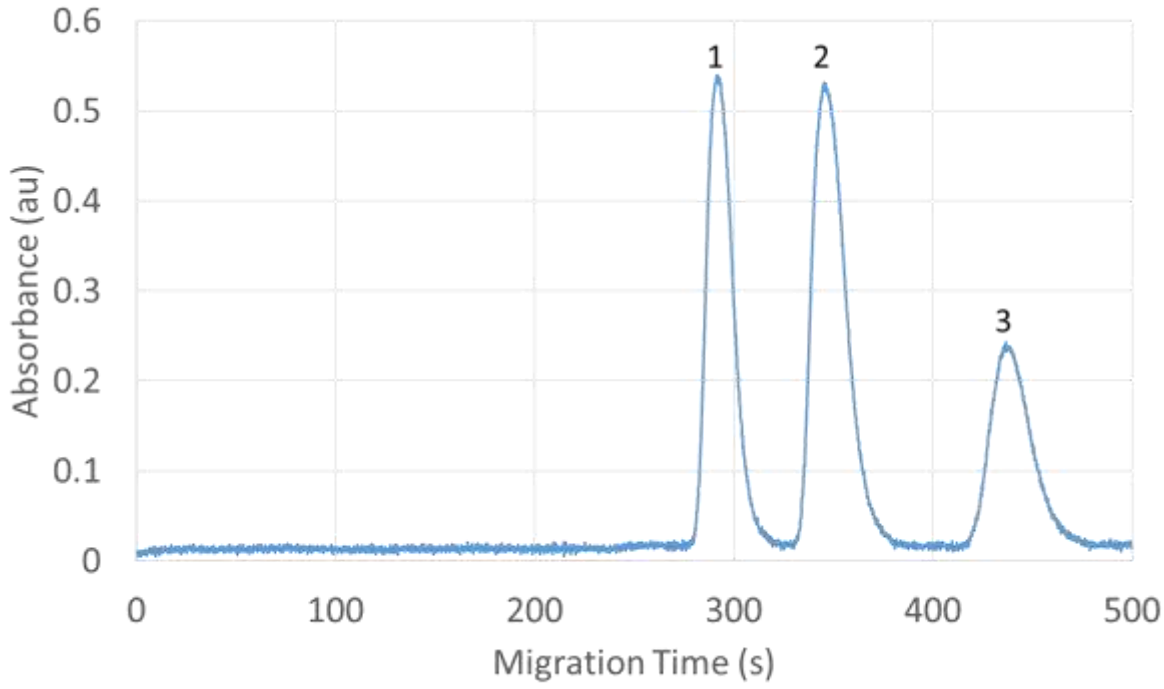

Figure 4-26 **CE electropherogram of 5 mM thymidine (peak 1), 5 mM FLT (peak 2), and 5 mM CLT (peak 3) separated on complete hybrid MCE device with 20 cm capillary and 500 µm OPL.**

The resolution, Rs, between the two closest peaks (thymidine and FLT) was calculated to be 1.4 (not quite baseline separation), and that between FLT and CLT was 2.0. These separation resolutions are lower than those obtained in Section 4.4.3.2 with use of the MCE device without the detection chip (Rs = 2.1 between thymidine and FLT and Rs = 3.1 between FLT and CLT). This is most like due to effects associated with an additional capillary junction needed to connect the detection chip. This added junction

adds additional dead volume, known to cause band broadening [177], [178]. Possible improvements to reduce dead volume will be discussed in Section 0.

The hybrid MCE device was then used to attempt the separate 6 FLT related compounds (thymidine, thymine, FA, stavudine, FLT and CLT) as shown in Figure 4-28, which was used to compare to the performance using a longer separation capillary. As expected, baseline separation was not achieved between any compounds except FLT and CLT (Rs = 3.0 for peak 3 and 4). Note that due to the use of lower concentrations, and likely a different alignment of the optical system, the signal is a little too low for accurate analysis of separation; these issues were corrected for future analyses.

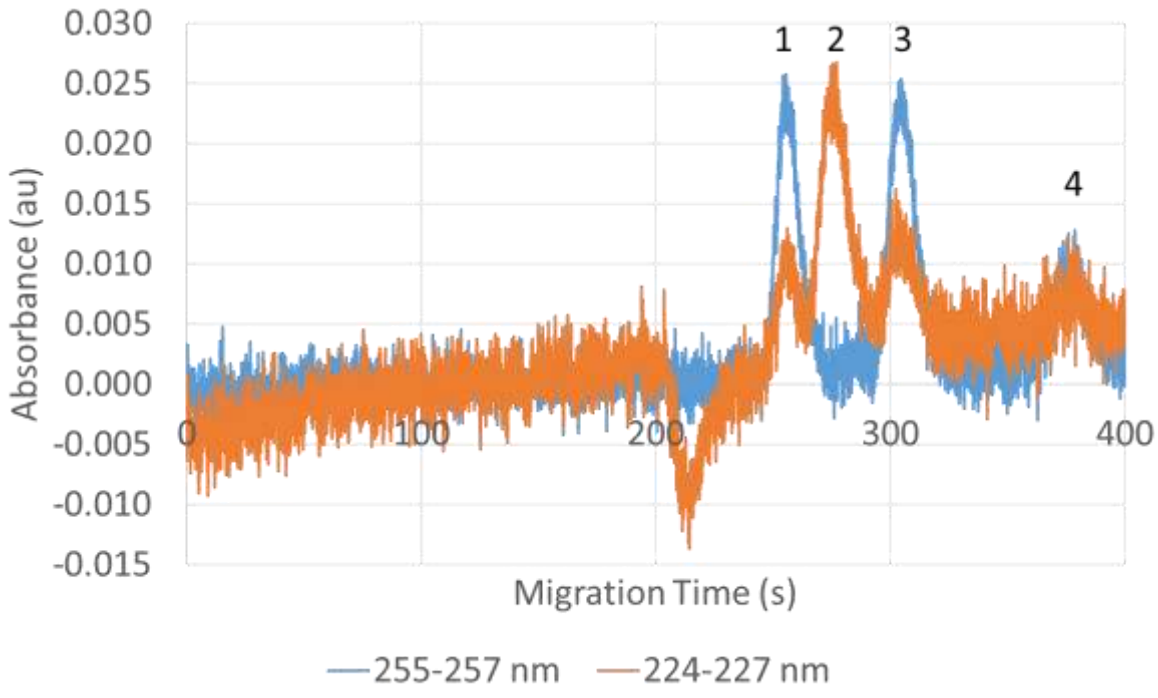

Figure 4-27 **CE electropherogram of 6 FLT related compounds using complete hybrid MCE device with 20 cm capillary and 500 µm OPL resulting in poor separation resolution.**

1 mM thymidine and 1 mM thymine (peak 1), 2.3 mM FA (peak 2), 1 mM stavudine and 1 mM FLT (peak 3), and 1 mM CLT (peak 4).

To improve separation resolution, separation was attempted in the device with 60 cm capillary. As shown in Section 2.3.1.2, baseline separation of the 6-component FLT mixture could be achieved in a capillary (75 µm) with 52 cm effective length, coupled to a capillary UV detection cell. In the hybrid microchip, the separation of the 6 FLT related compounds (thymidine, thymine, FA, stavudine, FLT and CLT) was improved using a 60 cm capillary (62 cm effective length including PDMS separation channel) compared to the use of a 20 cm capillary (21 cm effective length including PDMS separation channel). As shown in Figure 4-29, Rs increases to 5.2 for FLT and CLT compared to 3.0 in the chip with 20 cm capillary). Unfortunately, thymidine, thymine, and furfuryl alcohol were still not fully separated. The performance of separation between these

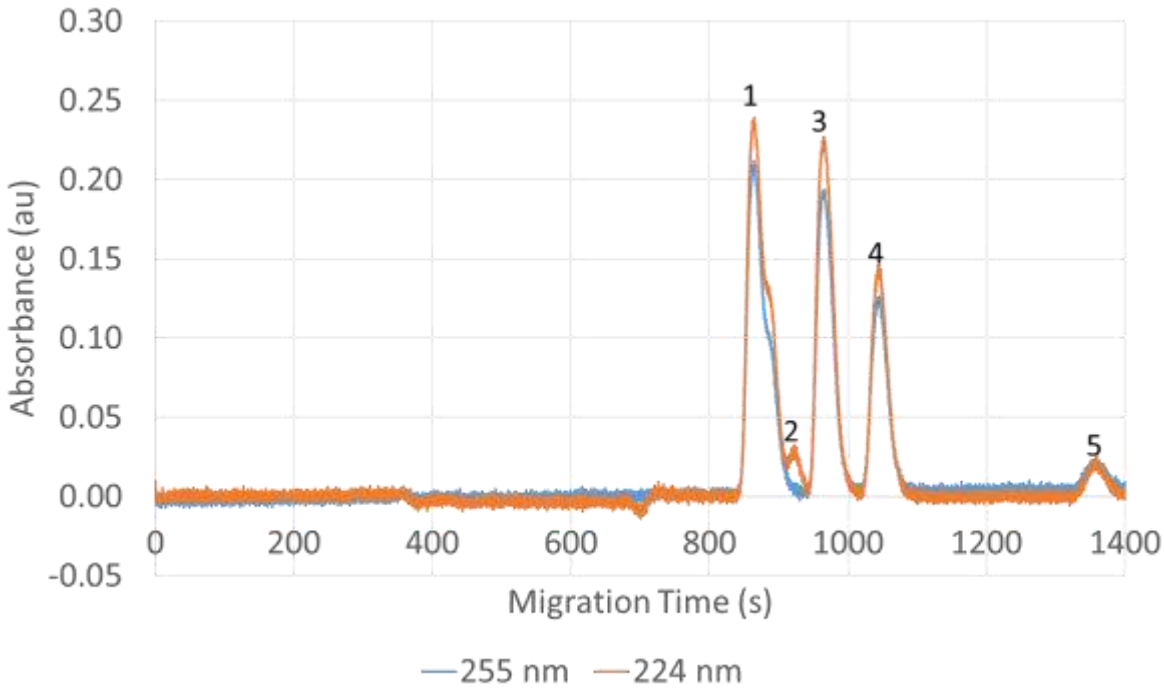

Figure 4-28 **CE electropherogram of 6 FLT related compounds using complete hybrid MCE device with 60 cm capillary (61 cm effective length) and 500 µm OPL.**

5 mM thymidine (peak 1), 2 mM thymine (peak 1), 2.5 mM furfuryl alcohol (peak 2), 5 mM stavudine (peak 3), 2.6 mM FLT (peak 4), and 1.4 mM CLT (peak 5) using time dependent volume injector.

analytes using the hybrid MCE device was worse than that shown on the lab-built CE system (Section 2.3.1.2) using a similar capillary length. (In fact, the effective length was slightly longer in the hybrid MCE device.)

While the separation resolution of the complete hybrid MCE was lower than that obtained using a capillary, this work has shown that the three components (injection chip, separation capillary, and detection chip) could be integrated together and achieve separation of several chemical species. As will be discussed in Chapter 5, several optimizations to the geometry of the device to lower dead volume are expected to remedy the poor separation resolution, and enable baseline separation of all components of the FLT mixture. Overall, a novel hybrid MCE device was fabricated and demonstrated the ability to perform the three key components to CE (injection, separation, and detection), with the ability to obtain LOD/LOQ comparable to HPLC systems at a fraction of the cost and in a much smaller footprint.

4.5.4 Conclusion

The use of a hybrid MCE device to link together the microscale CE operations of sample injection, separation, and detection has been demonstrated. While the MCE device yielded poor separation resolution compared to results shown in Section 2.3.1.2 (baseline separation only achieved for CLT and FLT peaks on MCE device compared to baseline separation for all compounds using lab-built CE device), the feasibility of using MCE to chemical purity analysis has been established. Improvements to the design of the hybrid MCE device (discussed in Chapter 5) are expected to resolve this one issue and enhance the separation resolution to a level sufficient for analysis of FLT and other PET tracers.

5 Chapter 5: Hybrid MCE Device Optimizations and Future Work

5.1 Introduction

In chapter 4, the three main components of CE operation (injection, separation, and detection) were implemented successfully into a proof of concept hybrid MCE device and its performance was demonstrated on a sample containing a mixture of FLT and related by-products. However, several areas need improvement and optimization before a hybrid MCE device (instead of an HPLC system) can routinely be used to perform chemical purity tests for PET tracers. Specifically, improvements in separation resolution are necessary. Improvements in peak area repeatability and migration time repeatability are also desirable.

There are several relatively simple parameters of the hybrid MCE device that can be tweaked to optimize the first of these (i.e. separation resolution), including capillary length, electrophoretic field, injection volume, and optical path length. However, adjusting these parameters can have a negative impact on other performance areas of the hybrid MCE device, and thus the tradeoffs need to be considered on the whole system level. For example, an increase in separation resolution can possibly be achieved by reducing the optical path length, however, this would also increase the LOD of the detection portion of the hybrid MCE device as discussed in Section 4.2. Increasing the length of silica capillary can also improve separation resolution (as described by Equation 5.2), but this would increase the analytical time as eluting analytes would need to travel further before being detected. Furthermore, it may become challenging to find a power supply capable of supplying the potential needed to achieve the same electric field strength over the longer capillary. Applying a larger

electrophoretic field can increase separation resolution as well as decrease analytical times due to the dependence of electrophoretic mobility on electrophoretic potential (Equation 1.6). However, this may also increase Joule heating, which can negatively affect peak area and migration time %RSD values due to the dependence of EOF and viscosity on temperature, which will be discussed in Section 5.4. These tradeoffs are discussed in more detail in Section 0. It is also suspected that a large dead-volume at the chip-to-capillary interface may lead to substantial peak broadening that can adversely affect resolution. This issue will be further discussed in Section 0.

In terms of peak area variability and migration time repeatability, it is suspected that the dead volume near the microvalves in the fixed volume injection microchip may lead to substantial variability in injection amount (and thus peak area). This issue will be discussed in Section 0. Additional aspects of the hybrid MCE device can also be modified to improve performance. Several potentially addressable issues where observed during the design, fabrication, conditioning, and operation of the device. These issues include substantial Joule heating under some conditions (Section 5.4), and separation channel conditioning instability and contamination (Section 0).

5.2 Identification of major factors affecting separation resolution

5.2.1 Background

In this section, fundamental equations used to gauge the separation performance of CE will be explored. In particular, the concept of theoretical plates and plate height will be discussed. In capillary or column chromatography, the number of theoretical plates (N) is a measure of separation efficiency of the system, and can be calculated as for each eluting peak as

$$N = 5.54\left(\frac{t_m}{w_{1/2}}\right)^2 \quad (5.1)$$

where t_m is migration time, and $w_{1/2}$ is peak full width at half the maximum value of the peak height [199]. Theoretical plates can be seen as imaginary segments in the separation capillary/column in which complete equilibration of analytes between stationary and mobile phase occur. The performance of a separation process depends on having a large series of consecutive equilibrium stages. The higher the number of theoretical plates, the greater the separation efficiency [200].

Another measure of efficiency is plate height (H), which arises from the same concept of equilibrium stages, and is defined as

$$H = \frac{L}{N} \quad (5.2)$$

where L is the distance from injection to detection, i.e. the effective length of the separation channel. Basically, H can be seen as the length of each theoretical plate. As a band passes through a theoretical plate, equilibration leads to the band broadening equivalent to the plate height. Therefore, keeping the value of H minimal is desirable. H can also be broken down into individual contributing components, which are due to the injection (H_{inj}), detection (H_{det}), diffusion (H_{diff}), and geometry (H_{geo}) of the CE device and can be summed up as shown in Equation 5.3 [201].

$$H = H_{inj} + H_{det} + H_{diff} + H_{geo} \quad (5.3)$$

By reducing the overall plate height of the system, band broadening is reduced, and an improvement in separation can be achieved, corresponding to an increase number of theoretical plates. However, several components of H are more easily

controlled than others. Both the injection and detection components can be controlled by adjusting the injection plug length (l_{inj}) and the detection OPL (l_{det}), respectively, as shown in Equation 5.4 and 5.5 [201].

$$H_{inj} = \frac{l_{inj}^2}{12L} \quad (5.4)$$

$$H_{det} = \frac{l_{det}^2}{12L} \quad (5.5)$$

Equation 5.4 shows that the H_{inj} component of the plate height depends on the square of the injection plug length. Intuitively, it makes sense that the length of the initial plug will play a role in the final peak width. Reducing the injection plug length will lead to significant reduction of H_{inj}. Similarly, Equation 5.5 shows that the H_{det} component depends on the square of the detection length (i.e. length of OPL). Again, this makes intuitive sense, as a longer detection region increases the length of time the sample is visible to the detector, and thus increases the peak width. Reducing the OPL will thus significantly reduce H_{det}.

The contribution of axial diffusion to the band broadening is described using Einstein equation (Equation 5.7) [200], [201], where D_m is the diffusion coefficient of the analyte and v is the linear velocity of the analyte.

$$H_{diff} = \frac{2D_m}{v} \quad (5.7)$$

While the diffusion coefficient of the eluting analytes are constant, velocity of the analyte can be controlled by adjusting the applied electrophoretic potential (E) as

previously shown in Equation 1.6 and discussed in Section 1.2.1. The higher the voltage, the higher the speed, and the less time is permitted for diffusive broadening, thus reducing H_{diff}.

The contribution due to the geometry of the hybrid MCE device is the most difficult to calculate as it depends on the geometry of the entire separation channel, including dead volume, and channel geometry (e.g. serpentine channel, straight channel, turn angles, etc). It is described by Equation 5.8, where n is the number of identical turns, ω is the width at the top of the channel (peak of the turn), θ is the turn angle, σ_{ni} is band broadening (variance) from non-ideal behavior of injected sample and Joule heating, and σ_{dv} represents the variance due to dead volume [177], [201]. Both σ_{ni} and σ_{dv} are of unknown form that depends of geometric shape of the channel, channel material, and electric field gradients [177].

$$H_{geo} = n\frac{(\omega\theta)^2}{12L} + \frac{\sigma_{ni}^2}{L} + \frac{\sigma_{dv}^2}{L} \quad (5.8)$$

To see where there is the most room for improvement, the efficiency of separation of FLT and by-products performed on three CE systems (lab-built CE, commercial CE, and hybrid MCE with 60 cm capillary) will be calculated and compared to each other. The migration time and full width half max from the fastest and slowest eluting analytes will be used to calculate the range of N, H, H_{inj}, and H_{det}. By taking the ratios of H_{inj}/H, and H_{det}/H, the relative contributions from the injector and detector can be estimated, potentially guiding where optimization efforts should be focused for maximal impact.

5.2.2 Separation efficiency of lab-built CE system

The fastest and slowest eluting analytes were thymidine and CLT, respectively. The migration time of thymidine was 611 seconds, and had a $w_{1/2}$ of 5 seconds. Using these values, with an effective capillary length of 52 cm, the number of theoretical plates was calculated to be 82400, and the plate height was 6.31 µm. To calculate H_{inj}, the length of the injected plug (l_{inj}) needed to be determined. This was estimated estimating the velocity (L/t_m) of thymidine and multiplying it by the injection time (5 seconds), resulting in a plug length of 0.43 cm. (This assumes the injection voltage for EK injection was the same as the separation voltage, which was the case here.) Using Equation 5.4, H_{inj} was calculated to be 2.91 µm. To calculate H_{det}, the OPL of 75 µm was used in Equation 5.5, giving a value of 9.0e-4 µm. The contributions from the injection plug length and detection OPL to H were then calculated to be 46% and 0.014%, respectively. This leaves ~54% of band broadening associated with the geometry and diffusion.

A similar calculation was performed for CLT, resulting in an 18% contribution for the injection and 0.014% for the detector. A summary of calculated values (N, H, H_{inj}, H_{det}, H_{inj}/H, and H_{det}/H is given in Table 5-1.

Table 5-1 **Lab-built CE system separation efficiency.**

Migration time, peak full width half max $w_{1/2}$, number of theoretical plates (N), plate height (H), injection plate height (H_{inj}), detection plate height (H_{det}), and contribution percentage of H_{inj} and H_{det} for lab-built CE system.

	Thymidine	CLT
t_m (s)	611	980
$w_{1/2}$ (s)	5	8
N	82400	82800
H (μm)	6.31	6.28
H_{inj} (μm)	2.91	1.13
H_{det} (μm)	9.01e-4	9.01e-4
H_{inj}/H (%)	46	18
H_{det}/H (%)	0.014	0.014

5.2.3 Separation efficiency of commercial CE system

Using similar equations in Section 5.2.3, the values of N, H, H_{inj}, H_{det}, H_{inj}/H, and H_{det}/H were calculated for thymidine and CLT. The effective length used for the commercial system was 21 cm with an injection time of 2.5 seconds, and an OPL of 75 µm. A summary of calculated values (N, H, H_{inj}, H_{det}, H_{inj}/H, and H_{det}/H) for thymidine and CLT are summarized in Table 5-2.

Table 5-2 **Commercial CE system separation efficiency.**

Migration time, peak full width half max $w_{1/2}$, number of theoretical plates (N), plate height (H), injection plate height (H_{inj}), detection plate height (H_{det}), and contribution percentage of H_{inj} and H_{det} for commercial CE system.

	Thymidine	CLT
t_m (s)	131	252
$w_{1/2}$ (s)	2	3
N	42100	39100
H (µm)	8.86	5.37
H_{inj} (µm)	6.39	5.37
H_{det} (µm)	2.23e-3	2.23e-3
H_{inj}/H (%)	72	32
H_{det}/H (%)	0.025	0.042

5.2.4 Separation efficiency of hybrid MCE system

Similarly, the values of N, H, H_{inj}, H_{det}, H_{inj}/H, and H_{det}/H were calculated for the hybrid MCE device, but the stavudine peak was characterized instead of thymidine due to the incomplete separation between thymidine and thymine. The effective length used for the hybrid MCE system was 62 cm, and the OPL was 500 µm. The injected plug length (using 400 ms actuation time at 1.5psi) was estimated as follows. Using the data from Section 4.2.3, an absorbance value of 1.52 was obtained for 5 mM stavudine using

a 500 µm OPL when detection region was uniformly filled with this analyte. The peak area for 5 mM stavudine during separation (Section 4.5.3.1) was measured to be 5.35 (au*s). Using the conservation of mass (i.e., area of stavudine plug remains constant during elution), the length of an original, "step" plug could be estimated. Taking the area of 5.35 (au*s) and dividing it by pure absorbance signal of 1.52 au resulted in an equivalent plug length of 3.5 seconds. Stavudine had an elution velocity of 0.066 cm/s; therefore, multiplying 0.066 cm/s by 3.5 s gave a linear plug length of 0.224 cm. CLT had an elution velocity of 0.045 cm/s; therefore, multiplying 0.045 cm/s by 3.5 s gave a linear plug length of 0.160 cm. A summary of calculated values (N, H, H_{inj}, H_{det}, H_{inj}/H, and H_{det}/H) are summarized in Table 5-3.

Table 5-3 **Hybrid MCE system separation efficiency.**

Migration time, peak full width half max $w_{1/2}$, number of theoretical plates (N), plate height (H), injection plate height (H_{inj}), detection plate height (H_{det}), and contribution percentage of H_{inj} and H_{det} for hybrid MCE system.

	Stavudine	CLT
t_m (s)	966	1360
$w_{1/2}$ (s)	22	45
N	10700	5050
H (µm)	58	122
H_{inj} (µm)	0.67	0.34
H_{det} (µm)	0.034	0.034
H_{inj}/H (%)	1.16	0.279
H_{det}/H (%)	0.058	0.027

5.2.5 Separation efficiency comparison of CE systems

By comparing the number of theoretical plates obtained for all three CE systems it is clear that hybrid MCE device had the lowest efficiency, which is approximately 16-

fold lower than the lab-built CE system (N_{CLT} = 82800 for lab-built CE system, N_{CLT} = 5050 for hybrid MCE) and 8-fold lower than the commercial CE system (N_{CLT} = 39100 for commercial CE system, N_{CLT} = 5050 for hybrid MCE) when comparing CLT. This lower efficiency is due to the wider peak obtained on the hybrid MCE device caused by band broadening. For example, the CLT peak width on hybrid MCE device is 6-fold higher than on the lab-built CE system.

By converting N to H, we are able to determine the major contributing factors to band broadening. Table 5-3 also shows that the combined contributions to peak broadening from the injector and detector in the hybrid MCE device are less than 2% combined for stavudine, and less than 1% combined for CLT. This indicates that the major contributors to the broadening of peak width are due to either diffusion of the analytes or to the geometry of the hybrid MCE device. Since H was low and relatively similar in value for the lab-built CE and commercial CE systems (6.31 µm and 8.86 µm, respectively, for thymidine, and 6.28 µm and 5.37 µm, respectively, for CLT), the ~10-22 fold increase in H for the hybrid MCE device is most likely *not* due to H_{diff}. This is because H_{diff} is expected to be similar across all systems since similar analytes, BGE, and temperature were used. Also, the elution velocity was very similar for the lab-built CE system and hybrid MCE device (elution rate of CLT = 0.053 cm/s on lab-built CE system, elution rate of CLT = 0.045 cm/s on hybrid MCE device). Thus the *maximum* possible contribution of H_{diff} is expected to be on the order of ~6 µm, based on the total *H* for the lab-built and commercial CE systems. Therefore, it can be assumed that the major contribution to peak broadening in the hybrid MCE device is the geometry of the hybrid MCE device itself. In order to improve the performance of the hybrid MCE

device, optimizations in the geometry should first be explored to reduce band broadening.

5.2.6 Conclusion

By comparing the separation efficiency of FLT and related by products performed on the three CE systems used it was determined that the hybrid MCE device yielded the worst performance. It was also determined that the H_{geo} component of H was most likely the main source of band broadening, using data from the other CE systems to argue that H_{diff} cannot be a major factor. Therefore, several improvements to the geometry of the hybrid MCE device will be discussed in the following sections.

5.3 Dead volume reduction

5.3.1 Background

One possible contributor to peak broadening related to the geometry of the hybrid MCE device is dead volume within the fluidic path. Dead volume can occur when there are sudden changes in geometry (e.g. sudden broadening, sharp corners, etc.). The flow speed can be very inhomogeneous, leading to dispersion. Dead volume within the microfluidic device has been shown to distort peak shape and increase band broadening [177], [178], and it has been reported that a dead volume of just 0.7 nL (with sample plug ~0.18 nL) can have adverse effects (reducing plate number from 40000 to 15000) on the efficiency of separation [177]. This was done by detecting a specified peak at two locations (first on the injection chip itself, and again within a capillary connected to the injection chip via tapered junction containing the dead volume) and comparing the measured N values. When the dead volume of 0.7 nL was removed within the junction, an increase in plate number as much as ~2.4x was observed for

another specified peak (47000 to 112000) [177]. In the case of the hybrid MCE device, there is likely a substantial dead volume at the interface between the chip and the capillary. In fact, there are two junctions: one between the injection chip and the capillary, and another between the capillary and the detection chip. It is suspected that this dead volume leads to substantial dispersion at each interface, leading to peak broadening. By minimizing the dead volume within these interfaces, a decrease in peak width and increase separation performance is expected.

The effect of dead volume at the capillary-chip junctions is discussion in the next section. Dead volume near the microvalves is discussed in the subsequent section; this dead volume can affect the peak area repeatability.

5.3.2 Capillary junction

In this section, I describe experiments performed to determine the effect of dead volume at the capillary junction. Figure 5-1 illustrates the capillary junction within the microchip injector. The inset on the right of figure 5-1 highlights the the non-uniformity in dimensions along the fluid path at the capillary-to-chip junction. This non-uniformity creates dispersion [177], as the flow velocity decreses as the channel widens and causes the peak to widen laterally and become shorter in the axial direction. Any difference in flow across the channel cross section can then lead to peak dispersion. An appoximate volume of 90 nL is contained in the capillary junction as the fluidic flow experiences a change in channel dimensions (20 µm (H) x 75 µm (W)) PDMS fluidic channel to 1mm section of 330 µM ID capillary port to 75 µm ID capillary).

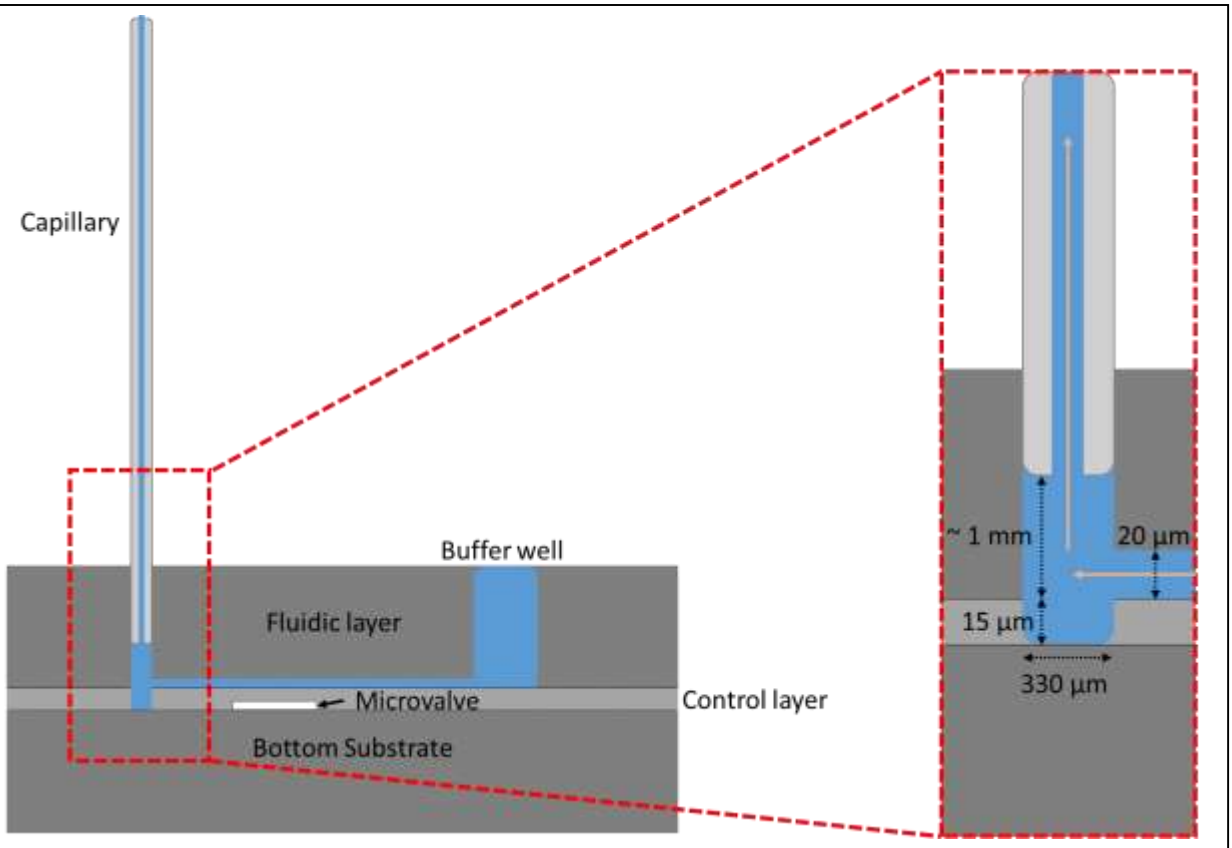

Figure 5-1 **Schematic of 90° fused silica capillary/PDMS chip junction.**

Inset shows enhanced view of capillary junction with light orange arrows representing fluidic flow in the injection chip to capillary junction. Flow would be in the opposite direction in the capillary to detection chip junction. Approximate volume of capillary junction is ~90 nL.

To investigate the effect of the capillary junction, two configurations were compared: (i) electrokinetic injection into a capillary connected to the PDMS detection chip (500 µm OPL), and (ii) the full hybrid MCE device consisting of PDMS injection chip, capillary, and PDMS detection chip (500 µm OPL). The first has a single capillary-chip junction, while the latter has two. (The flow behaviour at both junctions is presumed to be the same as the geometry is identical, and only the flow is reversed.) Note that the results in Section 5.2.4 suggest that the contribution of injection plug length to the peak broadening is very small compared to other sources. Thus, this difference between the two setups can be neglected.

5.3.2.1 Materials and methods

5.3.2.1.1 Reagents

Reagents used are as described in Section 4.5.2.1.

5.3.2.1.2 Microchip fabrication

The single-junction chip fabrication was performed as described in Section 4.5.2.2, but without using the microvalve injector. The full hybrid chip was already evaluated in Section 4.5.3. Figure 5-2 compares the hybrid MCE device with the experimental setup here (i.e. no injector).

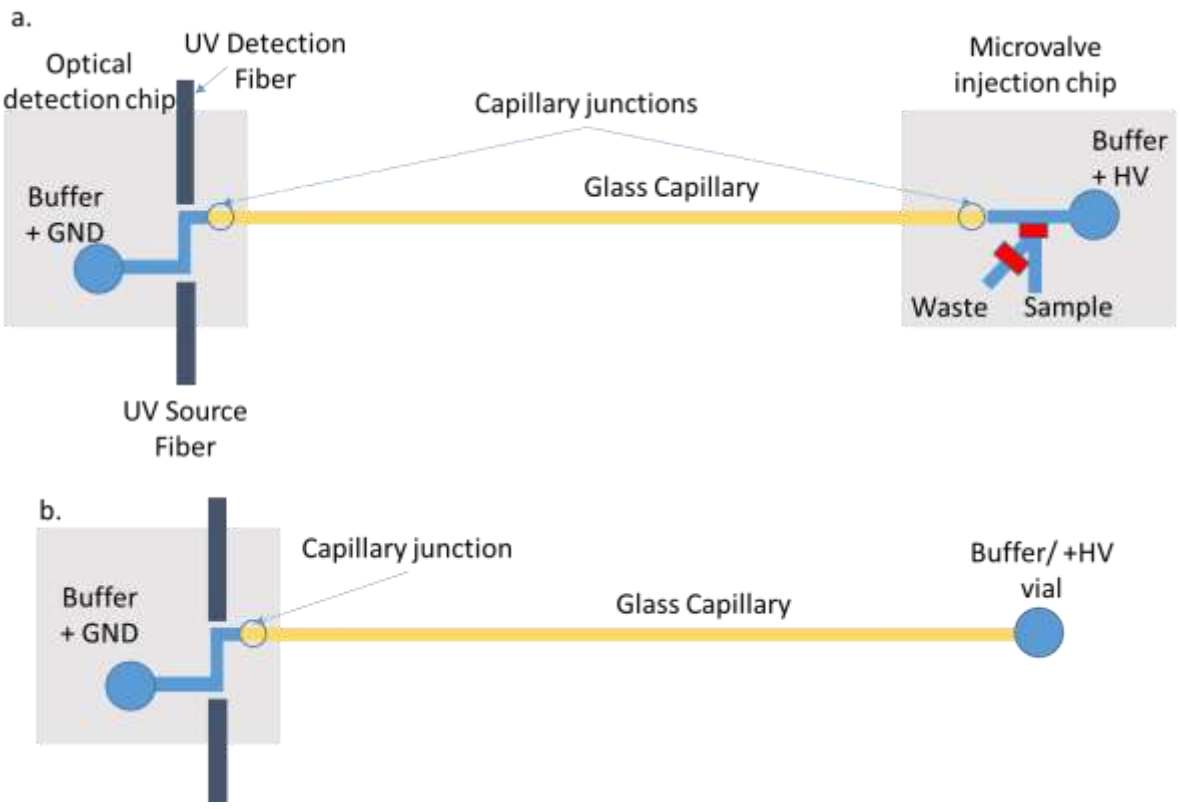

Figure 5-2 **Schematic of a) complete hybrid MCE device with two capillary-chip junctions, and b) experimental setup here incorporating only a single junction.**

Hydrodynamic microvalve injection is performed in the top device, while electrokinetic injection is performed in the bottom one.

5.3.2.1.3 Microchip and capillary conditioning

Conditioning was performed as described in Section 4.5.2.3.

5.3.2.1.4 Microchip operation and data analysis

Microchip operation and data analysis as performed in Section 4.5.2.4, however, due to lack in microvalve injector, electrokinetic injection was performed using 200 V/cm for 5 seconds.

5.3.2.2 Results and Discussion

Using the extended optical path length chip with a 60 cm fused silica separation channel, a similar FLT sample as used in Section 4.5.3 was injected electrokinetically and detected. The sample consisted of 5 mM thymidine, 2 mM thymine, 2.5 mM furfuryl

alcohol, 5 mM stavudine, 2.6 mM FLT, and 1.4 mM CLT. The separation chromatogram

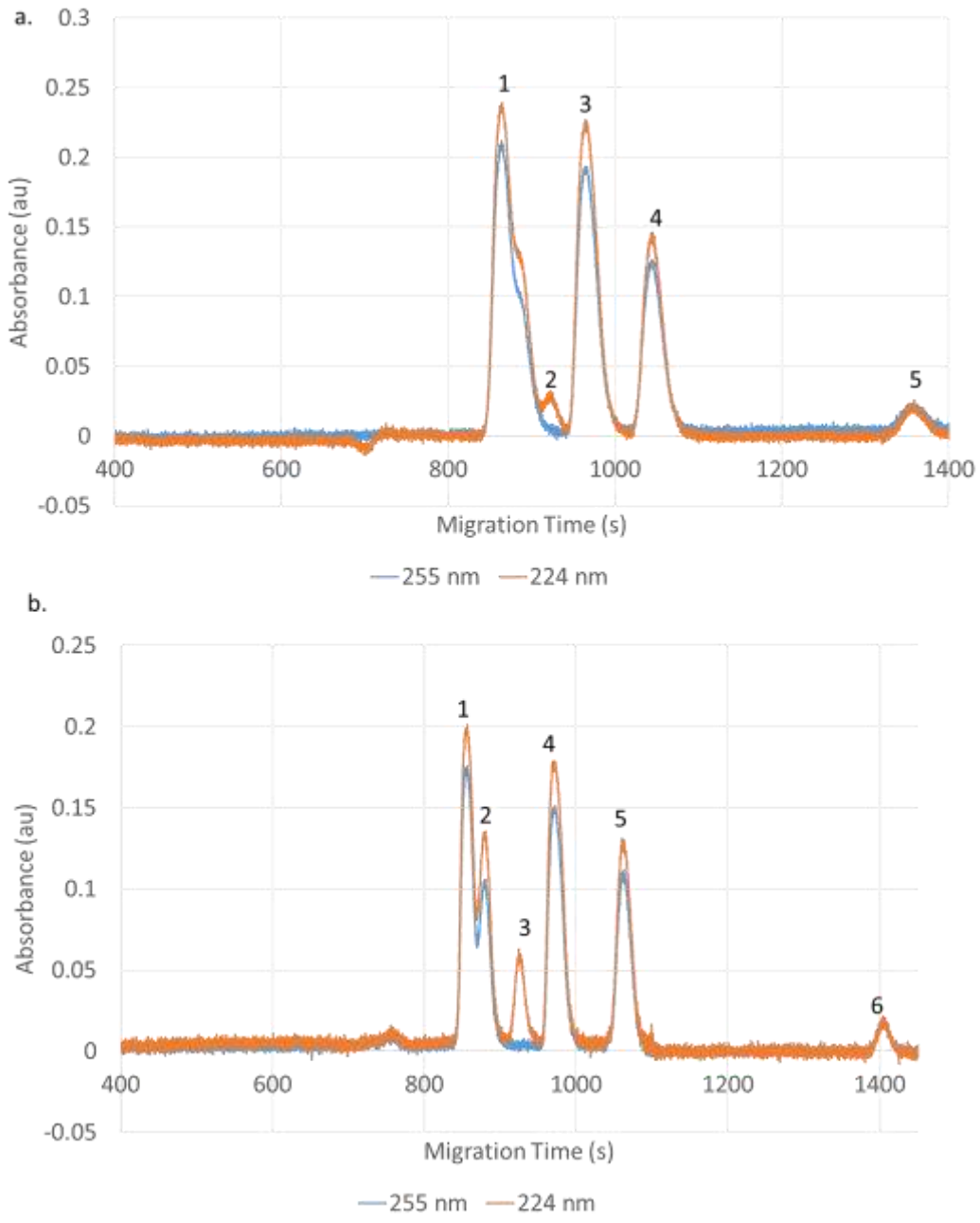

Figure 5-3 **Effect of capillary-chip junctions on separation efficiency**

CE electropherograms of (**a)** complete hybrid chip with two capillary junction [peaks: 5 mM thymidine (peak 1), 2 mM thymine (peak 1), 2.5 mM furfuryl alcohol (peak 2), 5 mM stavudine (peak 3), 2.6 mM FLT (peak 4), and 1.4 mM CLT (peak 5)] and **b)** hybrid chip with only a single capillary junction [peaks: 5 mM thymidine (peak 1), 2 mM thymine (peak 2), 2.5 mM furfuryl alcohol (peak 3), 5 mM stavudine (peak 4), 2.6 mM FLT (peak 5), and 1.4 mM CLT (peak 6)]. Both chips equipped with 60 cm fused silica capillary and 500 µm OPL PDMS detection chip.

using two capillary junctions is shown in Figure 5-3a, while Figure 5-3b shows the separation chromatogram using one capillary junction.

Figure 5-3 shows an improved resolution between thymidine and thymine when using one capillary junction compared to two. Also, improvement in separation resolution was obtained for stavudine and CLT compared to the complete hybrid MCE device as number of theoretical plates increase and plate height decreased for both compounds (summarized in Table 5.4b). Separation resolution between FLT and CLT also increased from 5.06 to 8.56. In the lab-built CE system with no capillary/PDMS chip junctions (Section 2.3.1.2), baseline resolution was achieved between thymidine and thymine, and separation resolution between FLT and CLT was 15. This shows the potential improvements to be gained by reducing dead volume on the hybrid MCE device.

Table 5-4 shows a summary of performance for t_m, $w_{1/2}$, N, and H for setups using zero, one, and two capillary junctions, which clearly shows a very significant increase in band broadening as more junctions are added. This demonstrates the importance of minimizing dead volume within the MCE device. Therefore, in order to effectively use a fused silica capillary for separation purposes, in conjunction with valve-based injector and extended optical path detector, improvements in the capillary junction must be further explored.

Table 5-4 **Migration time, peak full width half max $w_{1/2}$, number of theoretical plates (N), plate height (H), injection plate height (H_{inj}), and detection plate height (H_{det})**

(a) Results for setup with no capillary junction (capillary only); (**b)** Results for setup with one capillary junction (capillary and OPL chip); and (**c)** Results for setup with two capillary junctions (capillary, OPL chip, and injection chip). All setups used a 60 cm capillary.

a.

No cap. junc.	Thymidine	CLT
t_m (s)	611	980
$w_{1/2}$ (s)	5.0	8.0
N	82400	82800
H (μm)	6.31	6.28

b.

1 cap. junc	Stavudine	CLT
t_m (s)	973	1404
$w_{1/2}$ (s)	17	28
N	17800	13900
H (μm)	35	43

c.

2 cap. junc	Stavudine	CLT
t_m (s)	966	1360
$w_{1/2}$ (s)	22	45
N	10700	5050
H (μm)	58	122

Efforts to make the capillary flush with the bottom of the junction to reduce or eliminate dead volume was attempted, but this change caused problems during the bonding process between the chip and the bottom substrate. As the capillary is moved

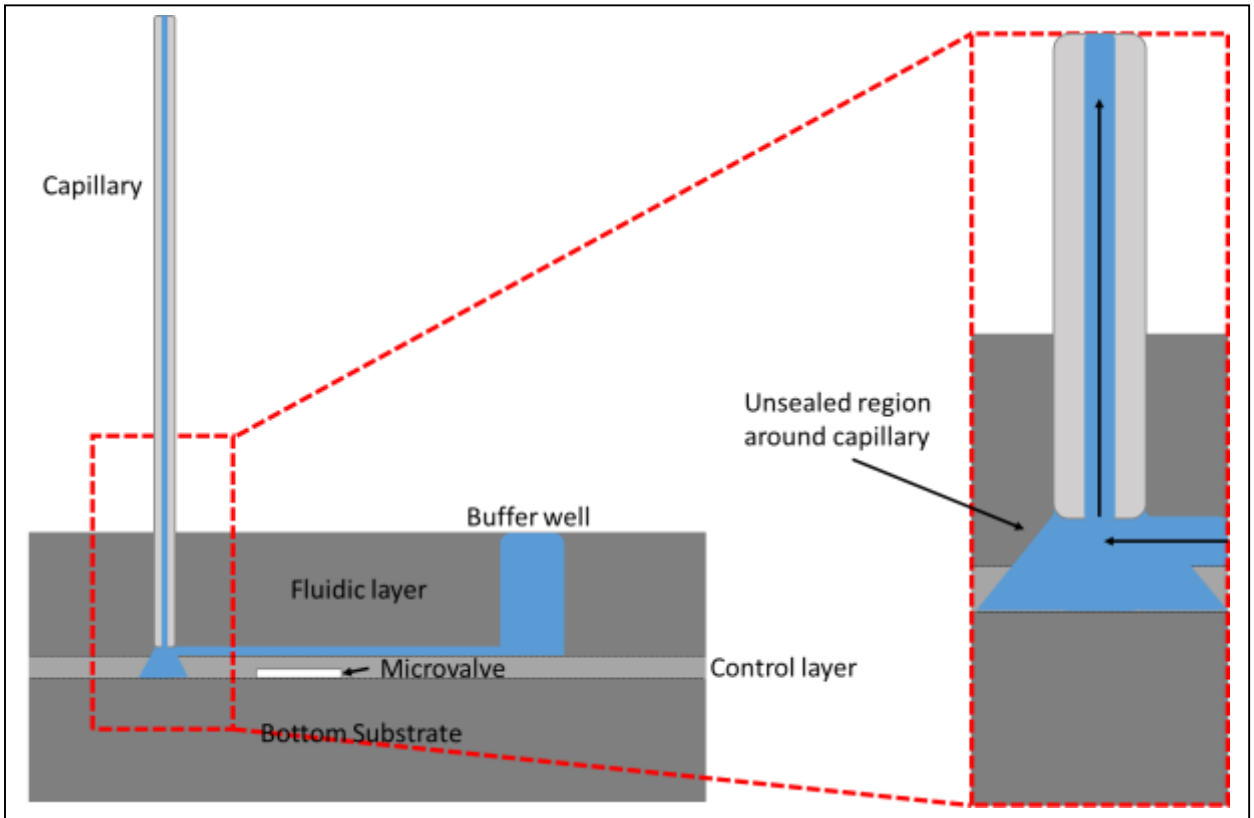

Figure 5-4 **Schematic of 90° fused silica capillary/PDMS chip junction when capillary is inserted too closely to the bottom of the port.**

Stress at the junction leads to poor bonding in the vicinity of the capillary. Inset shows zoomed in view of the region of poor bonding.

closer to the bottom edge of the port, additional stress is created on the PDMS port due to the larger capillary OD compared to the port diameter (capillary OD: 365 µm, capillary port diameter: 330 µm). This added stress made it difficult for region around the port to remain in contact with the bottom PDMS substrate, resulting is poor bonding in that region, and potentially increased junction volume, as shown in Figure 5-4.

Other geometries have been reported for interfacing capillaries and PDMS chips to reduce the dead volume, but fabrication is more complicated. For example, Kelly *et al.* reported a horizontal capillary/PDMS junction [155] that can eliminate the junction dead volume. In this design, the interior of the capillary is collinear with the microchannel within the PDMS chip as illustrated in Figure 5-5. Ideally, the fluidic channel dimensions will be kept uniform between the silica capillary (i.e. the internal diameter) and PDMS chip (i.e. the microchannel) throughout the entire junction to minimize dead volume. However, this increases the complexity of chip fabrication, as this would require multiple photoresist depositions on the wafer molds to create a

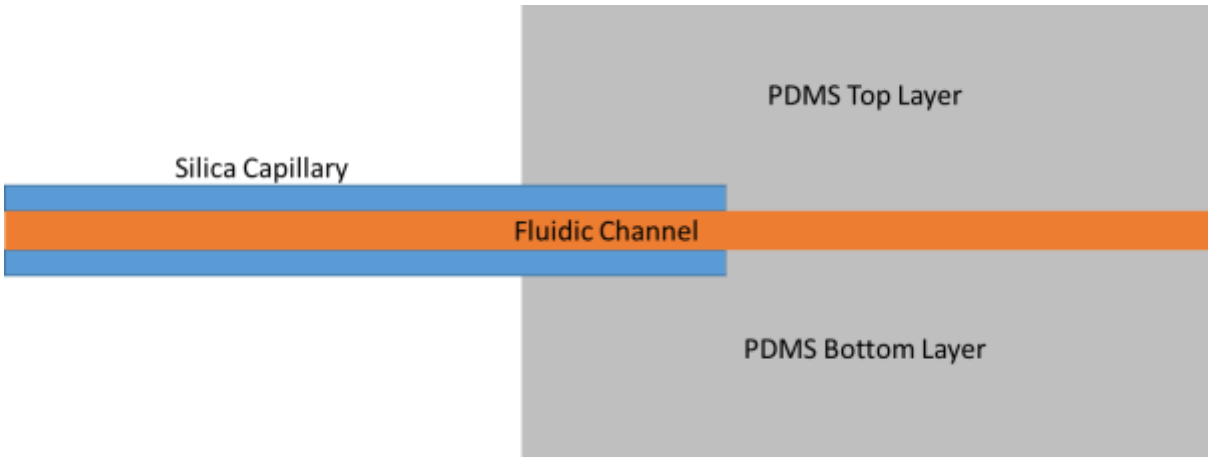

Figure 5-5 **Illustration of in-plane capillary junction**

In-plane design is used to help eliminate dead volume by keeping the fluidic channel dimension uniform between silica capillary and PDMS chip.

features with multiple heights. DeLaMarre *et al.* also uses a horizontal capillary junction, but avoids the use of using multiple photoresist depositions by simply tapering the outer wall of the fused silica capillary using a ceramic cleaving stone [202]. By tapering the outer walls, the silica capillary can then be inserted directly into the fluidic channel which it meets the edge of the microfluidic chip. However, initial attempts in our lab to replicate the tapered end proved difficult as the capillary was prone to breaking and cracking during the tapering process. Dimov *et al.* also employed the use of a horizontal capillary, but by embedding it completely within the PDMS mold itself [193], [203]. This was done by first filling the capillary with water, and then securing it onto a silicon wafer. PDMS was then poured onto the entire wafer and baked as normal (80ºC for 2 hours). The water provided two benefits as it would prevent the capillary from clogging up with PDMS, and would also evaporate out both ends of the capillary during the curing process creating two air bubbles within the PDMS. Input and output ports could then be punched out at the locations of the air bubble, creating an opening for the fluidic path. Future work will explore the various designs and implementations of a horizontal capillary junction to determine a practical solution to resolve the issues at this interface in the hybrid MCE device.

5.3.2.3 Conclusion

By reducing the dead volume within the fluidic pathway of the hybrid MCE device, an increase in separation resolution was achieved. The next step would be to perform a comparison of suitable junction designs in terms of fabrication complexity and performance.

5.3.3 PDMS microvalve optimization

5.3.3.1 Background

The use of microvalves to perform fixed volume injection has been shown in Section 4.3.3.2 to provide high reproducibility of peak area (%RSD = 1.7% for 3 nL injection using PDMS fixed volume injector chip). However, the performance was expected to be superior to a literature report using time-dependent valve injection [98]. The lack of improved performance may be due to dead-volumes created due to suboptimal positioning of microvalves in the fixed volume injector.

Figure 5-6a illustrates the current design and placement of the microvalves (orange) in the fixed volume chip. The dead volumes are located between the microvalves and the fluidic intersection. After the chip is first filled with BGE, sample is then loaded, however, the dead volume of BGE remains between the microvalves and the intersection, which can later cause undesired diffusion and mixing between BGE and sample. Using positioning and alignment techniques described by Thorsen et al., the ability to reduce the distance between microvalves and fluidic intersections to 0-25 μm has been demonstrated [133].

Therefore, to reduce the dead volume around the microvalves in the fixed volume injector, the microvalves were designed to be closer to the intersections of the fluidic channel (blue). In order to move the microvalves closer, the amount that the valves overlap the two sides of the channel must be reduced. Using a similar approach to that reported by Tseng *et al.* [204], a tapered shape was chosen to allow close valve positioning, while maintaining sufficient separation between adjacent valves to allow for bonding (Figure 5-6b). An estimated dead volume reduction was calculated as follows.

Keeping the channel height and width the same in both designs, the only change was the dead volume length indicated in Figure 5-6a. By taking the ratio of the length from the old and new design, an estimation in dead volume was calculated. The old design

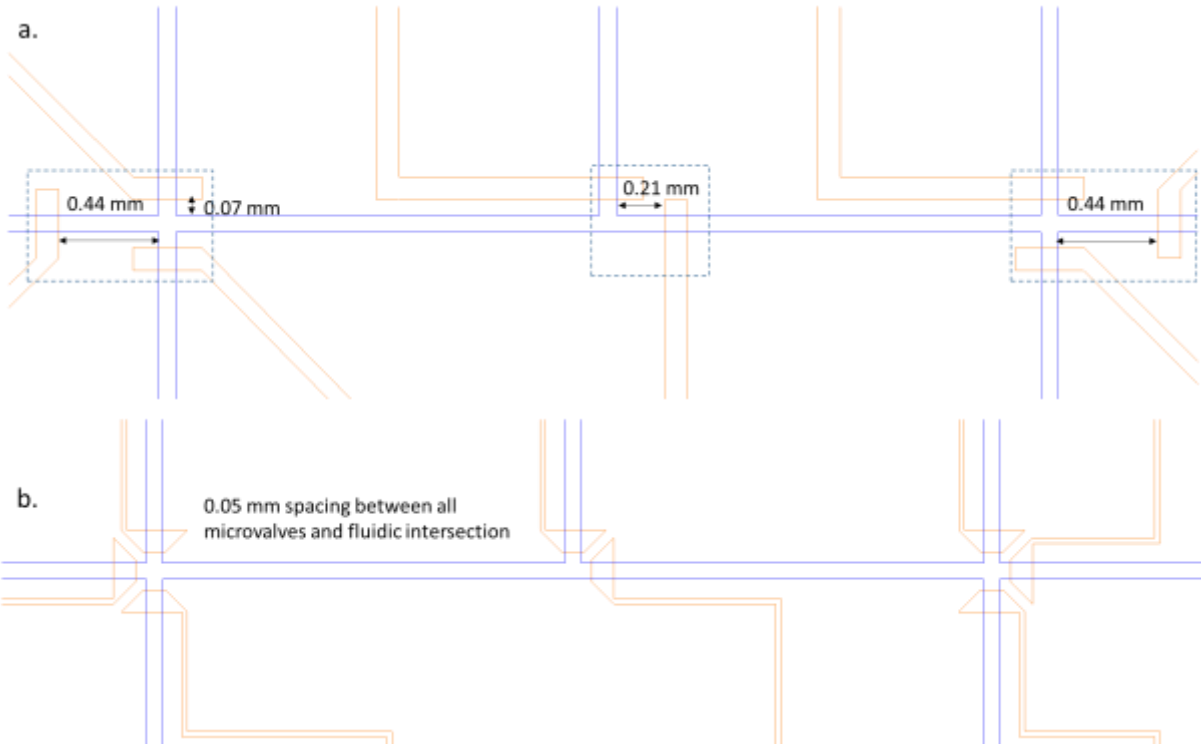

Figure 5-6 **Illustration of improved microvalve placement**

a) current design and placement of microvalve in fixed volume injector (red box highlights dead volume), and b) proposed new design with smaller dead volume.

had an overall total dead volume length of 3 mm, whereas the new design has a total length of 0.4 mm. This results in a 7.5-fold reduction in dead volume (3 mm / 0.4 mm) within the highlighted region in Figure 5-6. Using the channel dimensions of 75 µm width and 20 µm depth, this is a reduction in dead volume of 4.5 nL to 0.6 nL.

The performance of this new design versus the original design will be compard in future work.

5.4 Mitigating Joule heating

5.4.1 Background

In this section, the observed effects of Joule heating (described in Section 1.2.5) and possible improvements will be discussed. Joule heating occurs within the CE/MCE device as the electrical resistance within the fluidic path of the device generates heat during the application of electrophoretic potential. Excess heating can affect electrophoretic mobilities by as much as 2% / °C; therefore, methods to control CE temperature can be vital to achieving high migration time reproducibility [93]. Excess Joule heating has also been shown to cause formation of gas bubbles within the fluidic channel, which interrupts electrical current during application of electrophoretic potential and/or causes electrical arcing, which damages the chip.

The generation of heat within the fluidic channel of the MCE device produced some observable issues during development. Initially, the PDMS microvalve injector chip was corona plasma bonded to a flat 1”x3” glass slide. The use of a glass slides were initially used as it was readily available, bonded strongly to PDMS after plasma treatment, and provided a highly sturdy substrate for the PDMS chips. However, during the operation of glass slide based chips, noticeable fogging and condensation was visible within the bulk PDMS adjacent to the fluidic channel of the PDMS chip after about 30 minutes of use that continued to get worse over time. This led to the formation of vapor bubbles within the channels, which disrupted electrical current after around 40 minutes of use (Figure 5-7). This, in turn, caused electrical arcing within the fluidic channel, sometimes damaging the chip, and led to inconsistent application of voltage

and thus varying EOF. It was suspected that Joule heating was likely the cause of these issues.

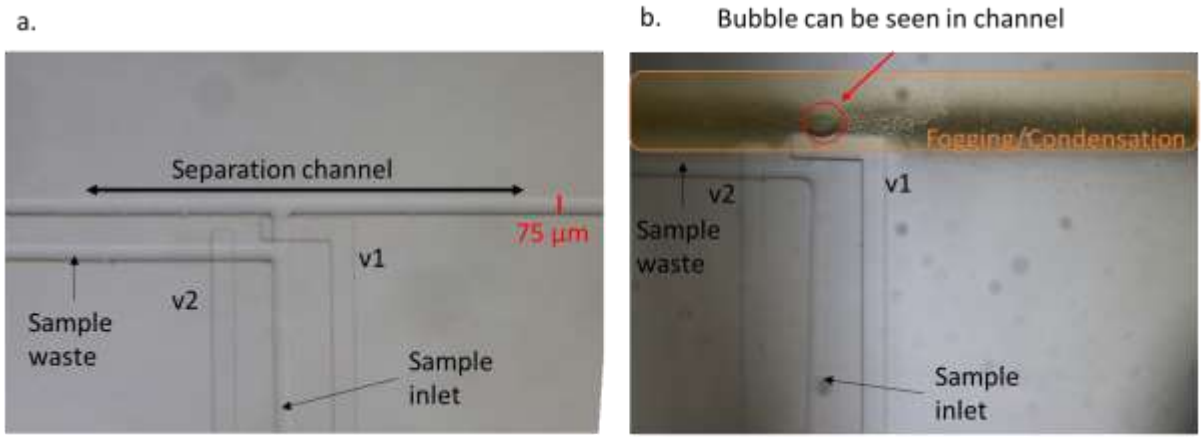

Figure 5-7 **Image of microvalve chip**

a) before CE operation and **b)** after 40 mins of use. Microvalves (v1, v2) shown.

The power dissipation can be estimated using Ohm's Law (Equation 5.9) and the power equation (Equation 5.10), where V is voltage (V) applied between high voltage (HV) and ground, I is current (A), R is resistance (Ω) of the BGE solution contained within the separation channel (Equation 5.11), ρ is the resistivity of the BGE, L is the length of the fluidic channel, w is the width of the channel, h is the height of the channel, and P is power (W), which will be discussed in Section 5.4.2.2.3.

$$V = IR \quad (5.9)$$

$$P = \frac{V^2}{R} \quad (5.10)$$

$$R = \frac{\rho L}{\pi (wh)^2} \quad (5.11)$$

These equations can be used to calculate how much heat must be removed during separation if cooling is the means used to ensure a stable temperature. Several

methods including the use of a heat sink, and the implementation of liquid-cooling channels were explored in our setup.

The equations also show that Joule heating can be reduced by changes in operating parameters. For example, power is reduced by reducing the applied voltage; however, this would have an adverse effect on separation time and resolution. Power can also be reduced by increasing the resistance of the capillary (e.g., by increasing L, increasing ρ, or decreasing the dimensions). However, increasing L would affect separation time, and decreasing dimensions would reduce the sample volume that can be injected. Reduction of capillary dimensions was explored in our setup.
Finally, the chip material was also explored in our setup. By changing the bottom substrate of the injection chip to PDMS instead of glass, a more gas-permeable device was produced that was more tolerant of vapor formation (i.e. vapor can escape rather than being trapped and leading to fogging and gas bubble formation).

5.4.2 Materials and methods

5.4.2.1 Reagents

Reagents used are as described in Section 4.5.2.1.

5.4.2.2 Approaches for cooling the chip

5.4.2.2.1 Heat Sink

An aluminum plate, the size of a 96 well plate, was cooled in a 4°C refrigerator for several hours. The aluminum plate was then placed underneath the PDMS chip similar to that used in Section 4.4.2.3.1 during the application of electrophoretic potential (200 V/cm). The PDMS chip was fabricated with a glass slide bottom layer. A thin film of water was place between the glass slide and aluminum plate to ensure good

thermal contact over the entire surface. The use of a heat sink would thermally transfer heat away from the fluidic separation channel during the application of electrophoretic potential.

5.4.2.2.2 Cooling Channels

Cooling channels (inspired by Beckman Coulter CE system) were designed into the chip described in Section 4.4.2.3.1, as shown in Figure 5-8. The use of the cooling channels would allow water to be continuously flushed alongside the fluidic separation channels (~200 µm away to avoid possible electrical breakdown of PDMS (20 V/µm) [163]), and to remain thin enough to allow adequate thermal transfer) to carry generated heat away from the separation channel. Using an applied voltage of 4 kV, the region

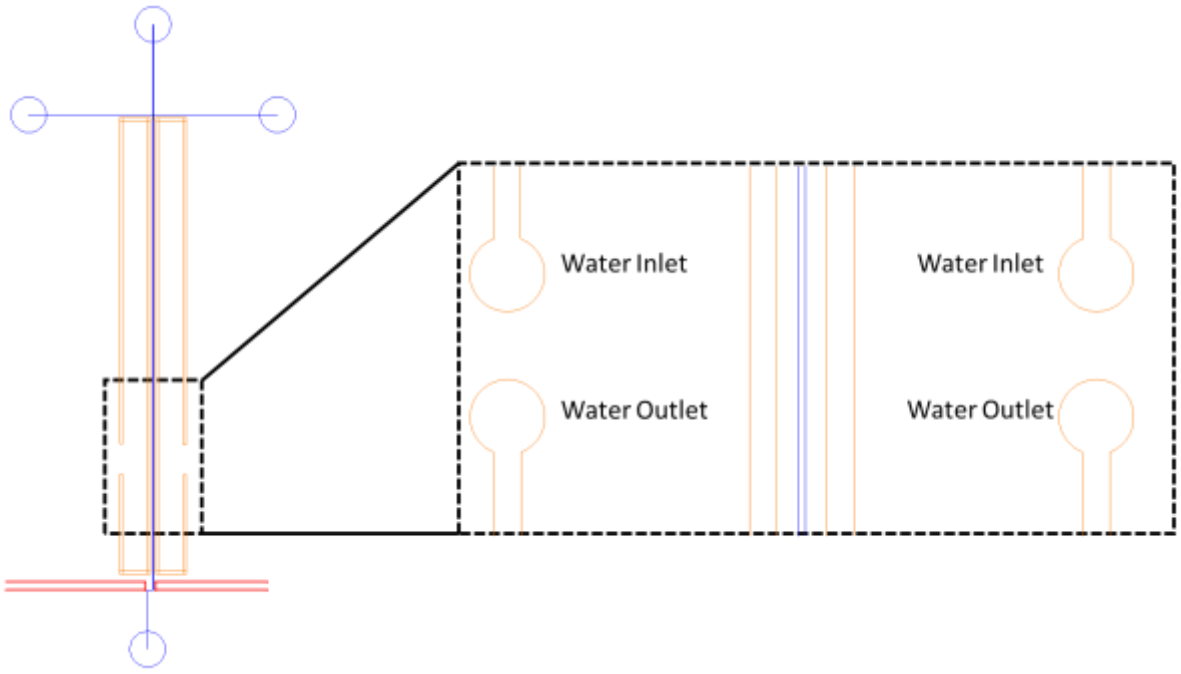

Figure 5-8 **Mask pattern for PDMS CE microchip with cooling channels (orange) alongside the separation channel (blue).**

Fiber optic alignment channels shown in red. Inset on right shows ports for coolant (water). Though this chip design has multiple inlets and outlets for the coolant, it is possible that these could be connected by channels on the chip.

along the cooling channel will experience only a fraction of the applied potential, thereby, avoiding any electrical breakdown of the PDMS wall. Due to the geometry of the T-channel design, and the presence of fiber optic alignment channels, wrapping the cooling channel along the whole fluidic separation path was not practical. Water was driven through the cooling channels using a syringe pump. Figure 5-9 shows a simplified schematic of the cooling channel in the chip to illustrate flow of coolant (H_2O) alongside fluidic channel to transfer heat away from the chip.

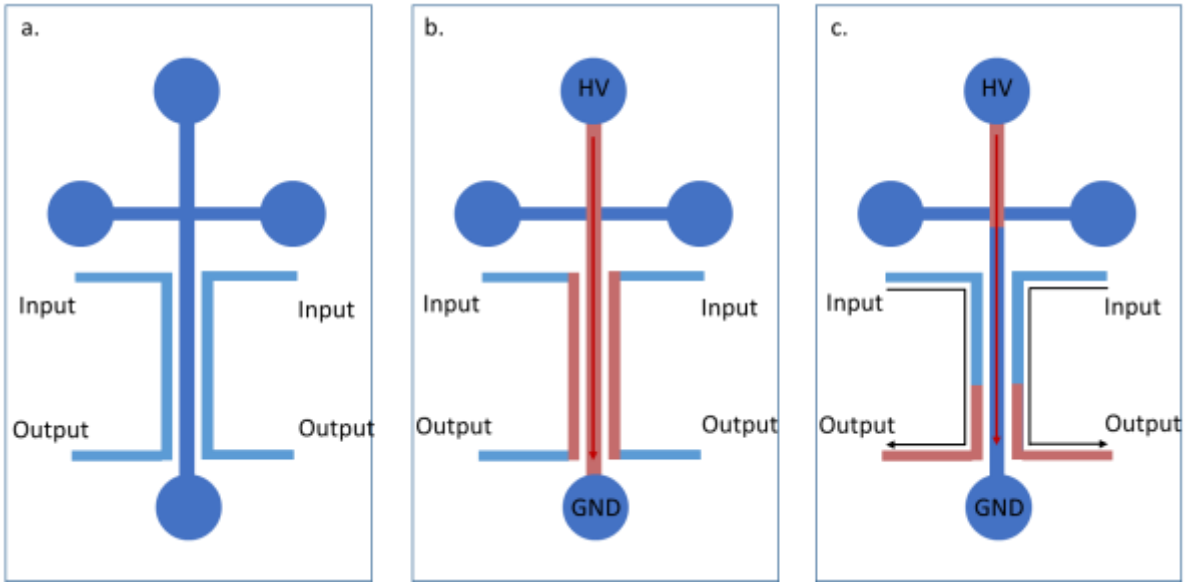

Figure 5-9 **Simplified schematic of PDMS CE microchip with cooling channels showing coolant (light blue) alongside fluidic channel**

a) High voltage (HV) not applied, BGE (dark blue) within fluidic channel unheated. **b)** HV applied, EOF flow represented by red arrow, BGE within separation channel and coolant along separation channel is heated (light red) **c)** Coolant (water) flow, represented by black arrow carrying away heated liquid, restores temperature of separation channel.

5.4.2.2.3 Power Reduction

To reduce the amount of heat generated within the PDMS portion of the chip a smaller ID capillary (50 µm) was used to increase the electrical resistance of the capillary and thus reduce the power consumption within the PDMS chip. A time-

dependent volume injection chip was attached to a 50 µm ID fused silica capillary (fabrication process was similar to that described in Section 4.3.2.2) to test the effects of the power reduction. The reduction in power consumption was calculated using Ohm's Law (Equation 5.9) and the power equation (Equation 5.10).

The resistance of a 20 cm capillary was measured using a digital multimeter (2831E, BK Precision, Yorba Linda, CA, USA). By inserting each end of the BGE filled capillary into two 2 mL vials filled with BGE (30 mM PB width 100 mM SDS), a potential of 4 kV was applied, and a current of 80 µA was measured, resulting in a calculated resistance of 50 MΩ. Using a time-dependent volume injector chip with a 20 cm long capillary (75 µm ID) (Section 4.3.3.1) filled with BGE, a separation voltage of 4 kV was applied, and a current of 55 µA was measured using the digital multimeter. The total voltage drop is divided among the capillary and the injection chip. Using the resistance of 50 MΩ, a voltage drop of 2800 V was calculated for capillary. This means there was a 1200 V drop across the time-dependent volume injection chip, which was difficult to measure directly due to the small dimensions of the capillary port. Using Ohm's law, the resistance of the time-dependent injection chip was calculated to be 22 MΩ. This corresponds to a power dissipation of 0.066 W within the time dependent volume injector chip. When the same injection chip was fabricated using a 50 µm ID capillary, a current of 30 µA was measured using 4 kV over the whole chip. Using the same resistance for the time-dependent volume injector chip previously obtained (22 MΩ), this corresponded to a voltage drop of 660 V over the PDMS chip, and a power dissipation of 0.020 W in the PDMS chip. Therefore, by replacing the 75 µm ID capillary with a 50

μm ID capillary, a 3.3x reduction in power was achieved, which is expected to a lead to a corresponding slowdown in the temperature increase, all else being equal.

5.4.2.2.4 Bottom Substrate Material

The vapor formation due to Joule heating created additional problems when a microvalve control layer was used. Upon microscopic inspection of the hybrid MCE chip with glass substrate after 40 minutes of use, it was apparent that the vapor was becoming trapped between the non-permeable glass slide and the PDMS control layer. The generated vapor could condensate between the two layers as it cooled when contacting the cooler substrate. (To determine the location of the issue, the fluidic layer was carefully removed to keep the control layer intact and attached to the glass slide. The condensate could then be clearly seen between the glass slide and the control layer on the microscope.)

The condensate caused blistering and deformation of the control layer, which could cause irreproducible volume injections as the fluidic channel was compressed by the blisters, and would completely disrupt electrical current if the channel became completely pinched off (Figure 5-10).

It was suspected that using a gas-permeable substrate could potentially eliminate this problem. To test this hypothesis, the glass slide was replaced with a flat PDMS slab in the injector chip. By preventing condensation it is suspected that an additional cooling effect is also gained; the prevention of condensation within the chip means that the heat carried by the vapor is not deposited in the chip, nor the latent heat of condensation. However, it is unclear whether the evaporation may adversely affect the buffer composition and lead to adverse effects.

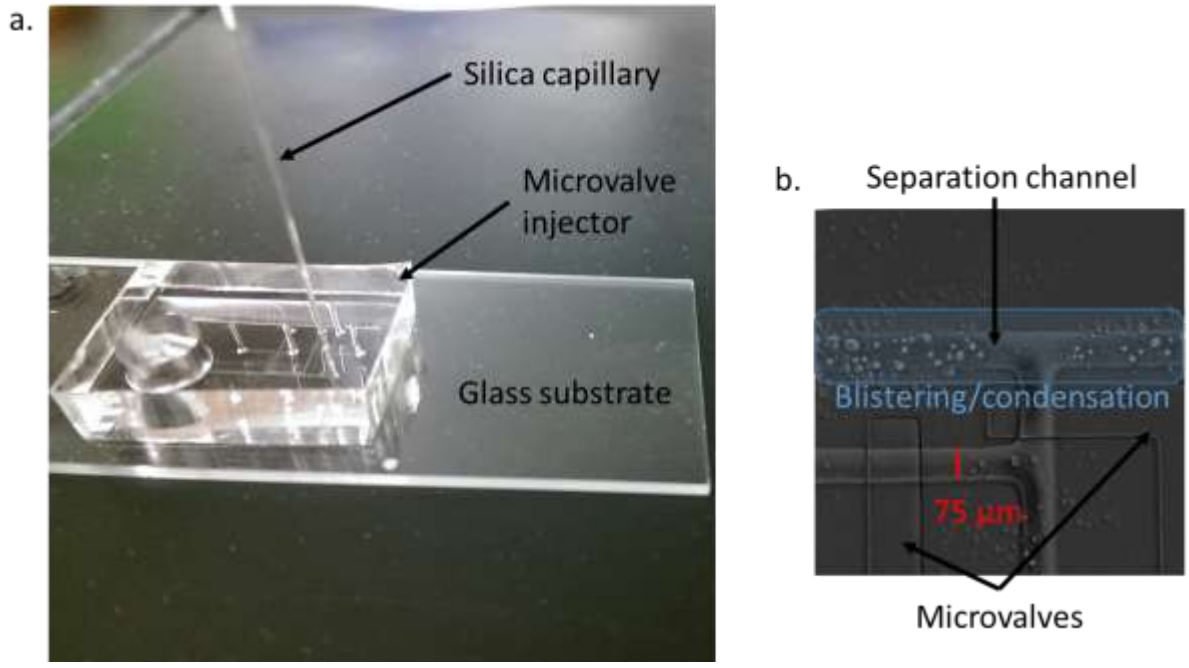

Figure 5-10 **PDMS microvalve chip on glass substrate**

(a) Image of PDMS microvalve chip with glass slide substrate. (b) Image of blistering and condensation between control layer and glass slide substrate after 40 minutes of electrophoretic potential (4 kV). Note that image (b) was taken after removal of the PDMS fluidic layer. An outline of the fluidic layer is still seen, however, due to the partially-cured nature of the layers when they are assembled during fabrication. The different appearance of the image compared to other images is due to the use of oblique lighting here to enhance contrast.

5.4.3 Results and discussion

5.4.3.1 Heat Sink

By placing the 4^{o} C aluminum plate under a full PDMS MCE device during the application of electrophoretic potential, a reduction of fogging and condensation was noticed. However, this generated an additional issue as the BGE solution (30 mM PB and 100 mM SDS) contained in the wells began to freeze and crystalize, which disrupted the electrical connections of the CE system shown in Figure 5-11. To

effectively use the heat sink, a higher temperature set point for the aluminum block would be required.

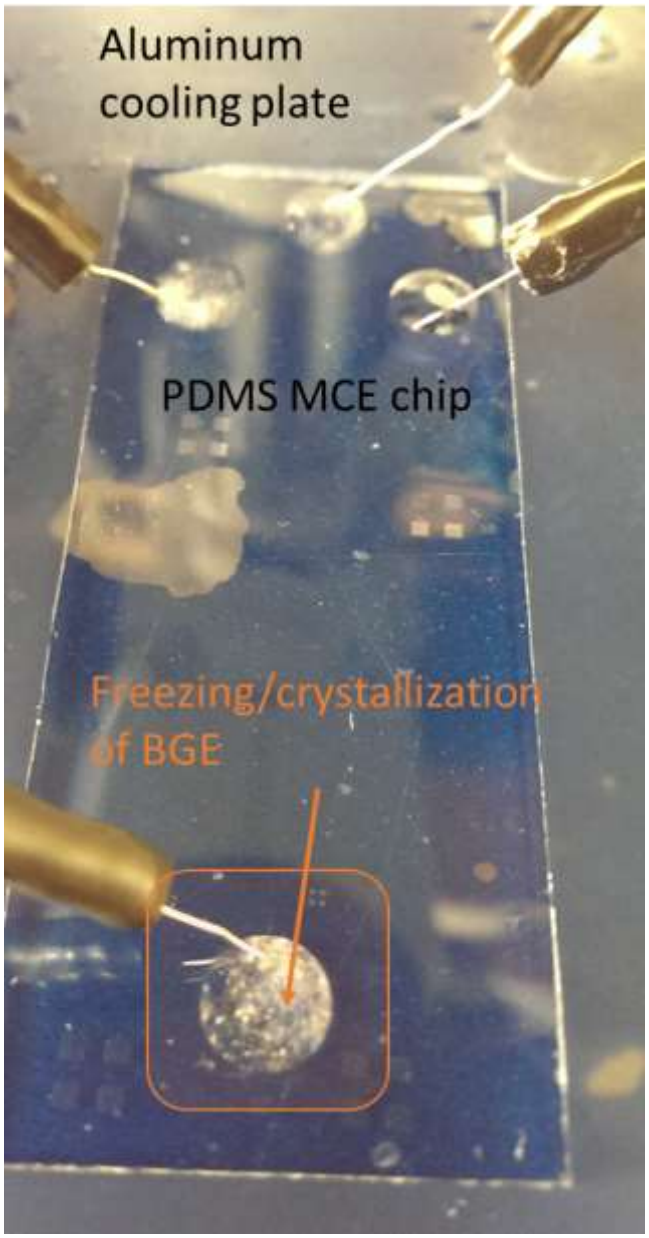

Figure 5-11 **Image of PDMS MCE chip placed on top of 4° C aluminum plate.**

Highlighted orange region shows freezing/crystallization of BGE (30 mM phosphate buffer with 100 mM SDS) causing disruption in application of electrophoretic potential (4 kV).

5.4.3.2 Cooling Channels

The implementation of cooling channels alongside the fluidic channels was tested and resulted in reduced fogging and condensation within the fluidic channel. Figure 5-12 shows a reduction in channel fogging in the area alongside the cooling

channels, while still showing fogging in regions without cooling channels. While the cooling channels generated positive results, the use of circulating coolant adds complexity, and therefore, simpler methods to mitigate Joule were explored.

5.4.3.3 Power Reduction

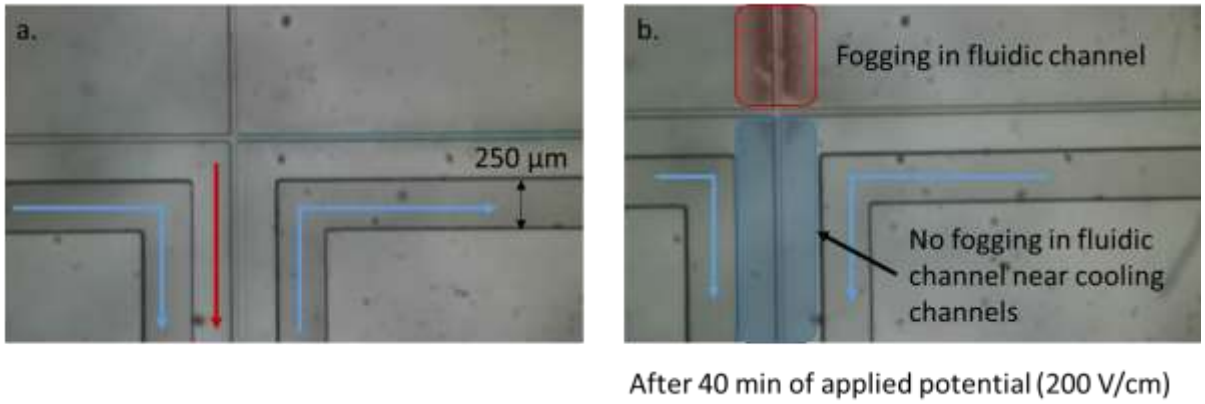

Figure 5-12 **Effect of cooling channels on fogging near separation channel**

(a) Image of PDMS MCE with cooling channel before application of electrophoretic potential. Blue arrows indicate direction of coolant flow, and red arrow indicates direction of EOF through the separation channel. (**b)** Same chip after 40 minutes of electrophoretic potential (4 kV). Red box highlights channel region where fogging is noticeable and blue box highlights region where no channel fogging noticed.

To lower the voltage drop across the PDMS portion of the hybrid MCE device, a fused capillary with a smaller ID (50 µm vs. 75 µm) was tested. The use of the 50 µm ID capillary reduced the power within the PDMS microvalve chip by 3-fold (as calculated above) from 0.066 W to 0.020 W. The effect of this change was extension of the operating time of the hybrid MCE device from 40 minutes (after which failure normally occurred) to >180 minutes with minimal fogging within the fluidic channel as shown in Figure 5-13. This new operating time is significantly longer than the expected 120 minutes of use (i.e. 3 x 40 minutes). This may be because the reduced power dissipation can be partly removed at ambient conditions rather than all the heat energy

going toward increasing the chip temperature. The higher power dissipation of 0.066 W was most likely generating heat too quickly, causing the chip to fail.

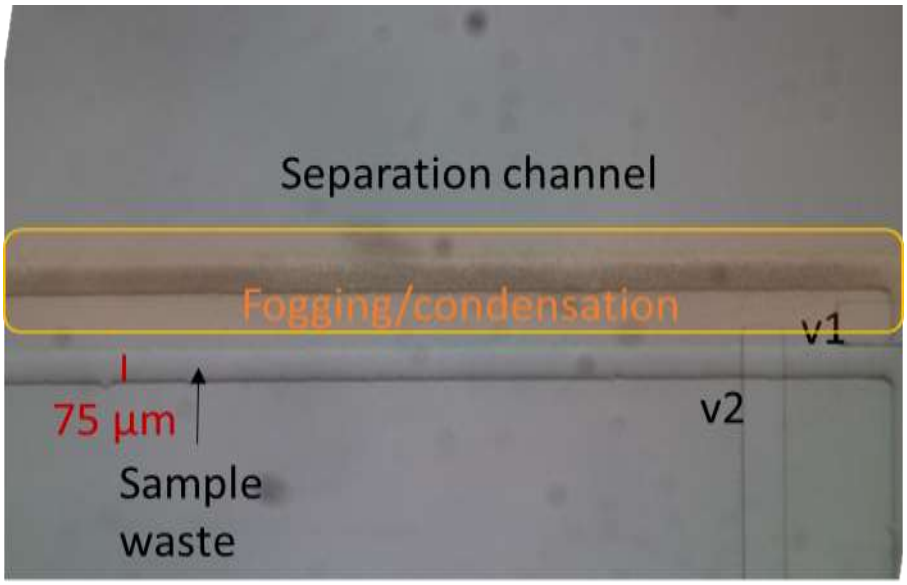

Figure 5-13 **Image of time-dependent injection chip after 180 minutes of application of electrophoretic potential (4 kV) using a 50 µm ID fused silica capillary (20 cm).**

Minimal fogging was noticed within fluidic channel.

5.4.3.4 Gas-permeable (PDMS) bottom substrate

By replacing the glass slide with a flat PDMS bottom layer, vapor generated from Joule heating was able to dissipate in all directions out of the chip. This significantly reduced the amount of fogging and eliminated blistering as vapor no longer seemed to condense between the control layer and bottom substrate. This increased operating time of the hybrid MCE device with PDMS substrate to >180 minutes (Figure 5-14) compared to only 40 minutes before chip failure in the chip with glass substrate (Figure 5-10).

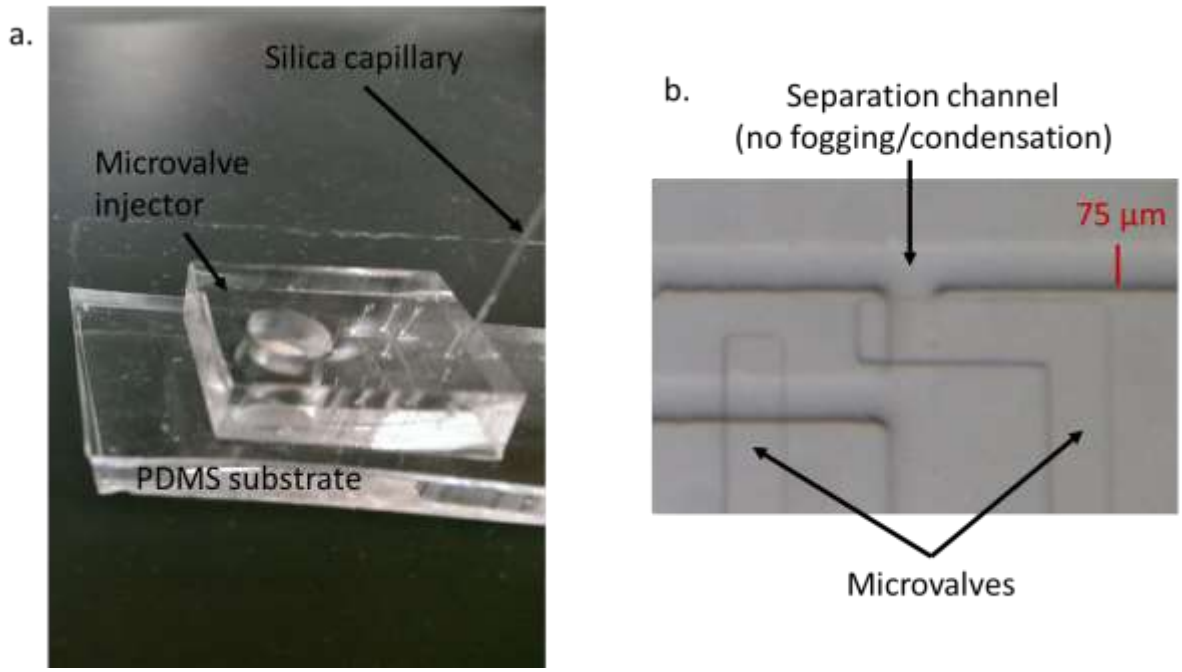

Figure 5-14 **Full PDMS microvalve chip**

(a) Image of PDMS microvalve chip with PDMS substrate. (b) Image of control layer and glass slide substrate after 180 minutes of electrophoretic potential (4 kV).

5.4.4 Conclusion

The value of mitigating Joule heating in improving operating time and robustness of the hybrid MCE device has been demonstrated. By implementing the described methods to remove excess heat, the chip can be operated for a longer time, and presumably the temperature within the chip is more constant, which should lead to more consistent behavior.

By effectively eliminating excess heat, the use of higher separation potential may become practical (though not yet tested), which could help improve separation resolution, and analysis times.

5.5 Improving Surface Conditioning and Reducing Channel Contamination

5.5.1 Background and Discussion

Channel conditioning instability and contamination (due to the absorption of analytes) of the separation channel can cause undesired changes to the EOF during separation. This change in EOF adversely affects peak area and migration time reproducibility. As shown by Vickers *et al.*, a drift of 14% in migration time (from 65 seconds to 75 seconds) was observed over successive CE runs spanning around 60 minutes in a PDMS chip [94]. This causes inconsistencies in detected peak width, migration time, and calculated area. In Section 4.4.3.3, we reported a drift of 3.3% of 289 seconds, in the hybrid MCE device, comprising a 21 cm separation channel of which ~1 cm was PDMS and 20 cm was a silica capillary.

While both silica and PDMS are susceptible to surface fouling [185], [205], it is most predominate in PDMS due to its permeable nature [169]. Furthermore, because PDMS is a polymer, rearrangements of the surface are possible due to motion of polymer chains, or movement of unreacted monomers or oligomers [94]. By exploring alternative silica and PMDS surface conditioning and/or modification methods, an improvement in separation resolution and reduction peak area and migration time %RSD can likely be achieved.

In terms of PDMS surface conditioning/stability, Vickers *et al.* found that the use of oxygen plasma treatment and extraction of unreacted oligomers improved the formation and stability of SiO_2 groups on the PDMS surface for up to 7 days, and reduced the migration time drift to just 4% (from 53 seconds to 55 second) over 4 hours of continuous use (previously 14% drift over 1 hour for untreated/extracted PDMS) [94].

Recently, Fantona *et al.* published a one-step in-mold method to chemically modify the PDMS surface, where thin films of ionic and non-ionic surfactants are patterned, transferred to a pre-polymer, and subsequently immobilized onto the PDMS surface, resulting in a stable hydrophilic PDMS surface for up to 11 days [182].

Another method to decrease migration time %RSD is to suppress EOF. By suppressing the potentially unstable EOF, the velocity of the eluting analytes will only be dependent on their electrophoretic mobilities as described by Equation 1.6. These mobilities remains constant as long as fluidic viscosity is unchanged (Equation 1.3). Schulze *et al*. describe the use of poly(ethylene glycol) (PEG) to coat glass channels in order to suppress the unstable EOF, resulting in a migration time %RSD reduction of as much as 3-fold (1.25% in uncoated channel versus 0.4% using channel coated with 5% PEG solution) [206]. By coating the glass channel/capillary with PEG, EOF was suppressed due the ability of PEG to mask the silanol groups in the inner surface of the capillary [207]. However, by suppressing the EOF, the analysis time was increased 3-fold (37 seconds for uncoated channel versus 106 seconds for channel coated with 5% PEG solution [206]). Therefore, care must be taken to implement surface modifications in order to maximize desired performance parameters. The use of additional surface modifications also increases the complexity and cost of MCE device fabrication as more steps, reagents, and time are needed.

Future work will explore various surface coating and modification methods in order to improve the performance, stability, and reproducibility of the hybrid MCE device. Though the stability of the hybrid MCE device is probably already sufficient over the timespan needed for QC testing of chemical purity of PET tracers (a few minutes),

enhanced stability would be useful to enable replicate tests. Furthermore, enhanced understanding of surface stability will be critical in ensuring repeatable performance from one chip to another. In addition, improved understanding of PDMS stability may lead to the possibility of integrating the separation completely into a PDMS format, enabling integration of injection, separation, and detection in a single PDMS chip without the need for a capillary. This would have significant benefits in terms of cost, complexity, size, and robustness of the MCE platform.

5.6 Concluding remarks

Though positron emission tomography (PET) is the most sensitive and well-suited tool for many types of experiments in the study of cancer biology and its treatment, the difficulty and high cost of production of the needed tracers severely limits their accessibility and diversity. This bottleneck slows the discovery and development of new tracers, new diagnostics for cancer, and hinders the use of tracers in research. Simpler and lower cost production of PET tracers, performed at the site of use, could open the door for more researchers to integrate PET into their research. The study and use of PET is important as it has been proven to be highly useful in clinical applications, and has the potential to assist the development and use of modern medicine.

Unique characteristics of microfluidic platforms can eliminate these obstacles by enabling production of PET tracers in the biology lab or the clinic with minimal infrastructure or specially-trained personnel. Microfluidic platforms for radiosynthesis have been actively pursued during the past several years to utilize the advantages of lower cost and reduced complexity. Once the developments of these microfluidic radiosynthesizers has been established, the quality control testing process will still

remain a bottleneck. Therefore, the miniaturization of an effective QC device must also be realized. The use of miniaturization to reduce the equipment size and shielding needed for the chemical purity analysis of PET tracers is expected to be a key part of streamlining the QC testing process, and ultimately the overall tracer production process.

The work contained in this thesis has demonstrated the feasibility of using a miniaturized CE platform to perform chemical purity analysis on PET related compounds using smaller and potentially more affordable device. The separation of PET related compounds such as FLT and related by-products (thymidine, thymine, FA, stavudine, and CLT) has been demonstrated. Also, the separation of both FAC isomers (β-D-FAC and α-D-FAC) has been demonstrated along with the separation and detection of K222. The lowered analytical times (<2 minutes) and LOD (120 μM) obtained for K222 compared to the typical colormetric-spot test used (analytical time: 5-15 minutes, LOD 133 μM) demonstrates that CE can be extended to tracers without strong UV absorbance and can be used to combine multiple QC tests into a single platform. Also, with the potential of adding multiple detection modules to the hybrid MCE device (i.e. radiation, and electrochemical detectors), its use and application can also be expanded (i.e. radiochemical purity analysis). The miniaturized format of the hybrid MCE device will also allow it to be integrated into a microscale device (i.e. miniaturized radiosynthesizer) to perform a large subset of required QC tests.

However, before the full potential can be realized, a thorough optimization process must be performed on the current hybrid MCE device before it can be routinely used as a replacement for HPLC (the current standard method for chemical purity analysis).

While the use the fixed volume microvalve injection chip allowed for high injection reproducibility (peak area %RSD as low as 1.7%) and the detection chip with extended optical path length achieved high sensitivity (LOD: 2-7 µM for FLT and related by-products), both matching the performance of commercial CE and HPLC systems, the dead volume within the capillary junctions proved to hinder optimal separation of tested analytes. Though baseline separation was achieved in a CE device, this was not successfully translated to the hybrid MCE chip due, primarily, to dead volume at the chip-capillary junctions that leads to dispersion effects. Design optimizations to reduce dead volume and improve the geometry of the hybrid MCE device will allow for improvements in separation resolution, peak area and migration time %RSD, and robustness.

The work I have completed in my doctoral program has given me valuable insight and experience in the field of microfluidics, electrophoresis, and quality testing. I hope to continue to expand my knowledge in these fields as I move forward in my future endeavors.

6 Appendix

6.1 Absorbance data for detection/quantification limits of HPLC system

This section contains calibration curves (absorbance versus concentration) for the experiments described in Section 3.3.1.

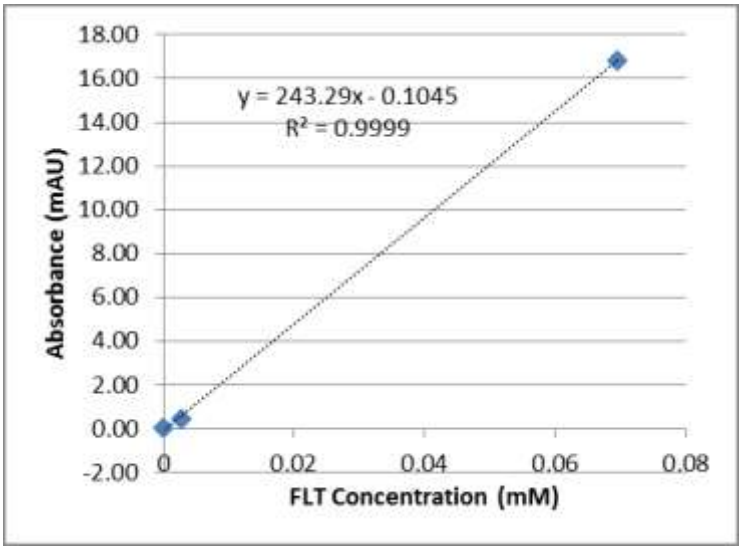

Figure 6-1 **Absorbance vs. FLT Concentration (StDev noise: 0.5 mAU)**

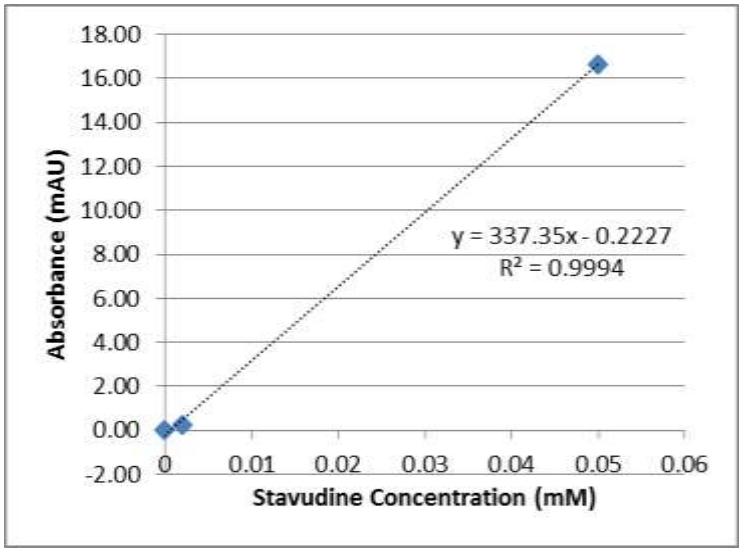

Figure 6-2 **Absorbance vs. Stavudine Concentration (StDev noise: 0.5 mAU)**

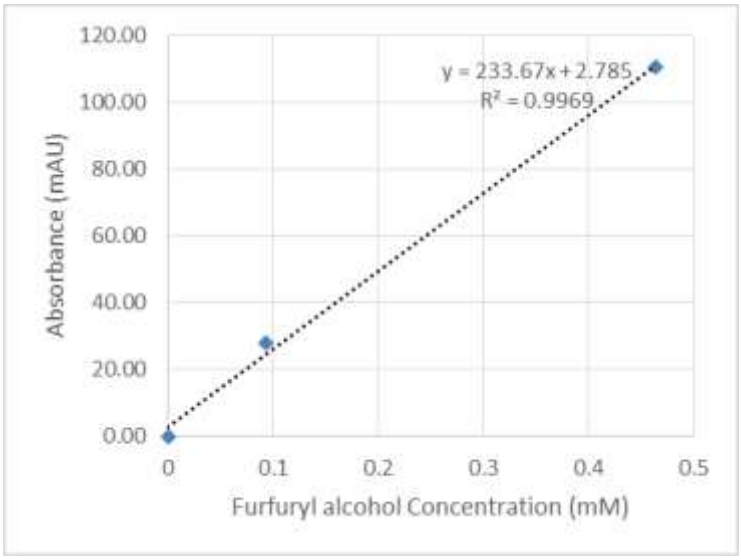

Figure 6-3 **Absorbance vs. FA Concentration (StDev noise: 0.1 mAU)**

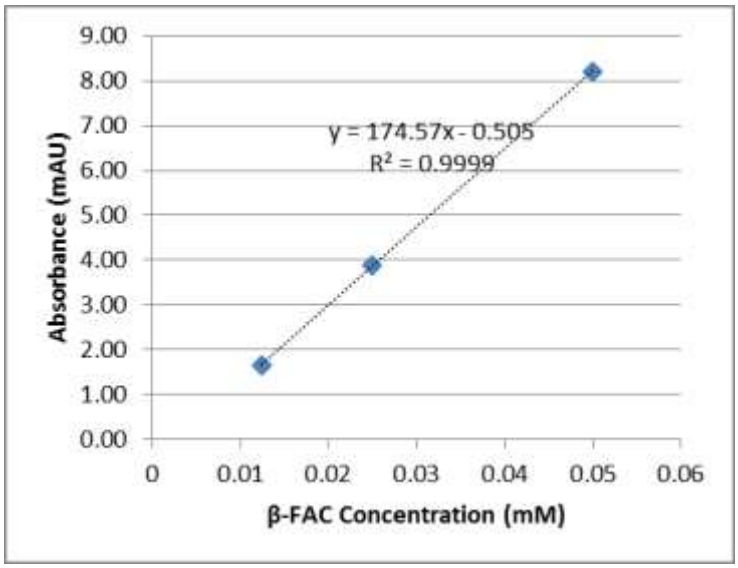

Figure 6-4 **Absorbance vs. β-FAC Concentration (StDev noise: 0.1 mAU)**

6.2 Absorbance data for detection/quantification limits of commercial CE system

This section contains calibration curves (absorbance versus concentration) for the experiments described in Section 3.3.2.

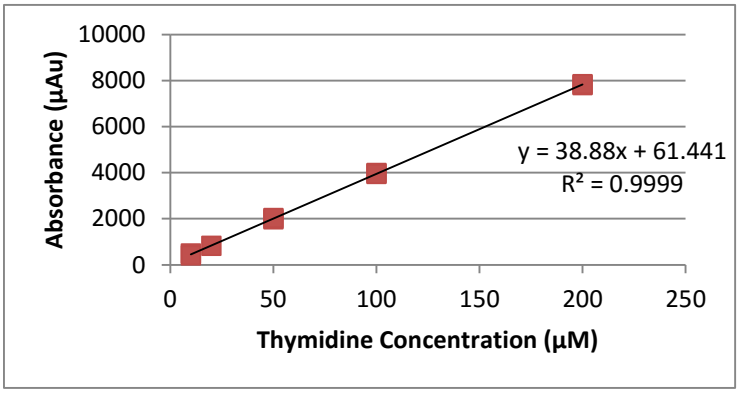

Figure 6-5 **Absorbance vs. Thymidine Concentration (StDev noise: 0.09 mAU)**

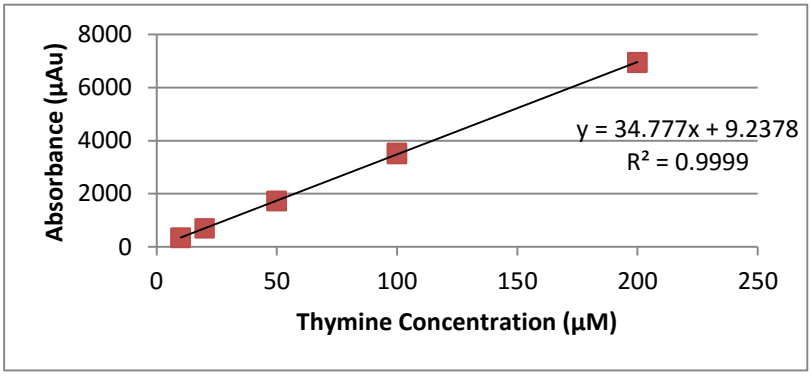

Figure 6-6 **Absorbance vs. Thymine Concentration (StDev noise: 0.09 mAU)**

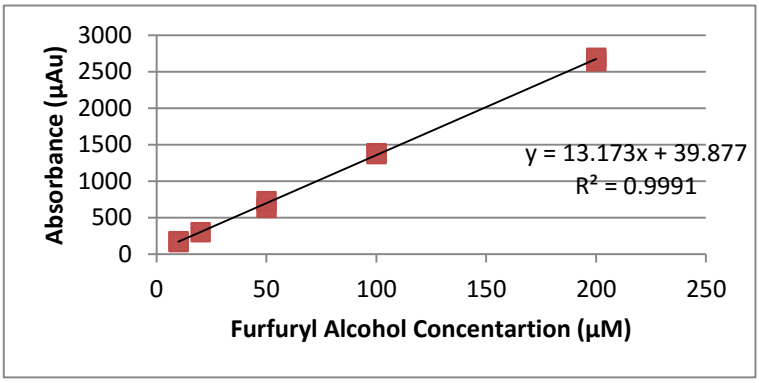

Figure 6-7 **Absorbance vs. FA Concentration (StDev noise: 0.1 mAU)**

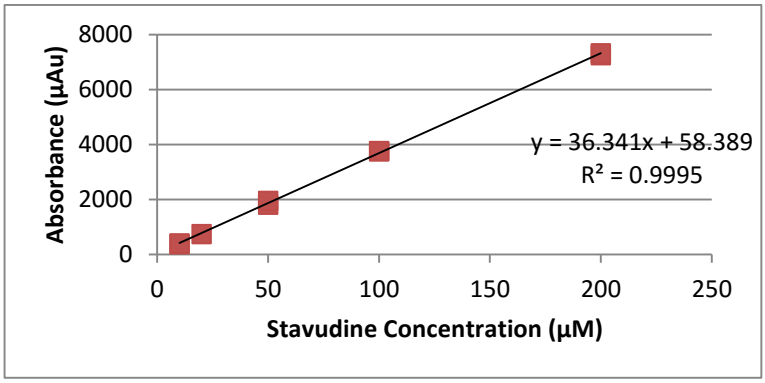

Figure 6-8 **Absorbance vs. Stavudine Concentration (StDev noise: 0.09 mAU)**

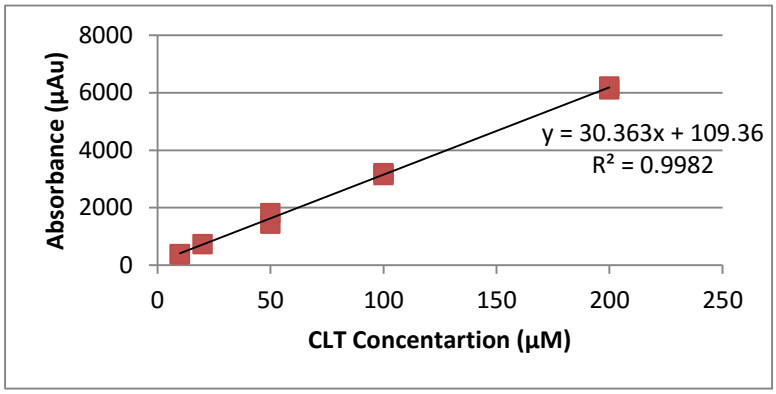

Figure 6-9 **Absorbance vs. CLT Concentration (StDev noise: 0.09 mAU)**

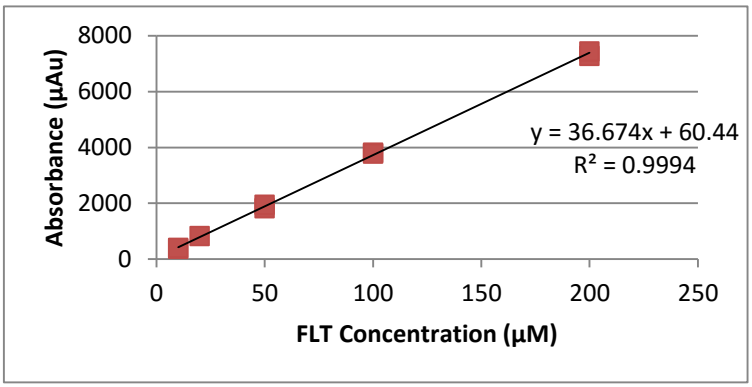

Figure 6-10 **Absorbance vs. FLT Concentration (StDev noise: 0.09 mAU)**

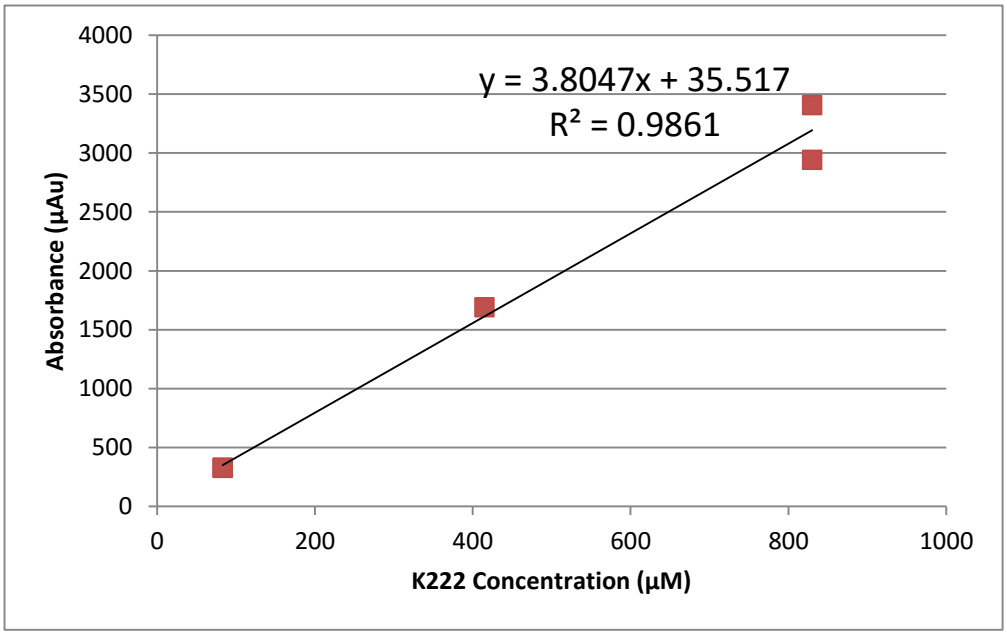

Figure 6-11 **Absorbance vs. Thymidine Concentration (StDev noise: 0.1 mAU)**

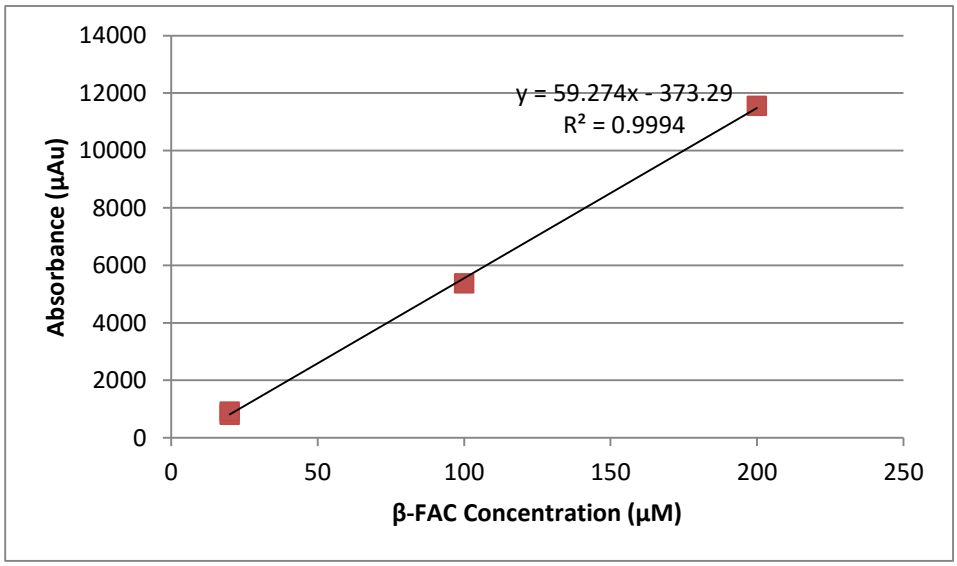

Figure 6-12 **Absorbance vs. Thymidine Concentration (StDev noise: 0.1 mAU)**

6.3 Absorbance data for detection/quantification limits of lab-built CE system

This section contains calibration curves (absorbance versus concentration) for the experiments described in Section 3.3.3.

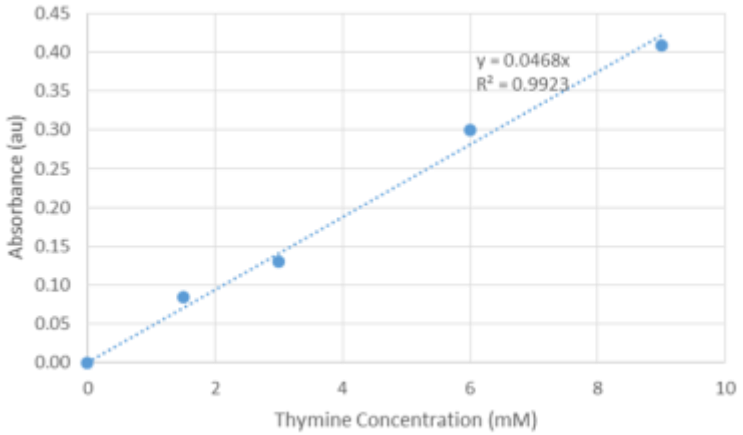

Figure 6-13 **Absorbance vs. Thymine Concentration (PX-2 xenon light source + USB4000) (StDev noise: 4 mAU)**

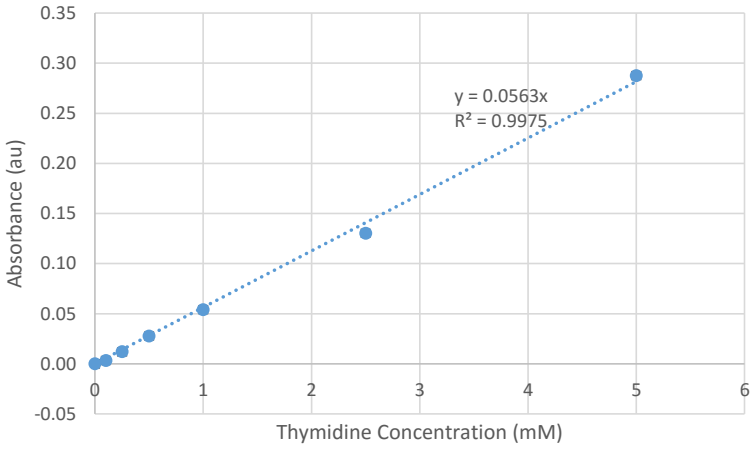

Figure 6-14 **Absorbance vs. Thymidine Concentration (PX-2 xenon light source + USB4000) (StDev noise: 4 mAU)**

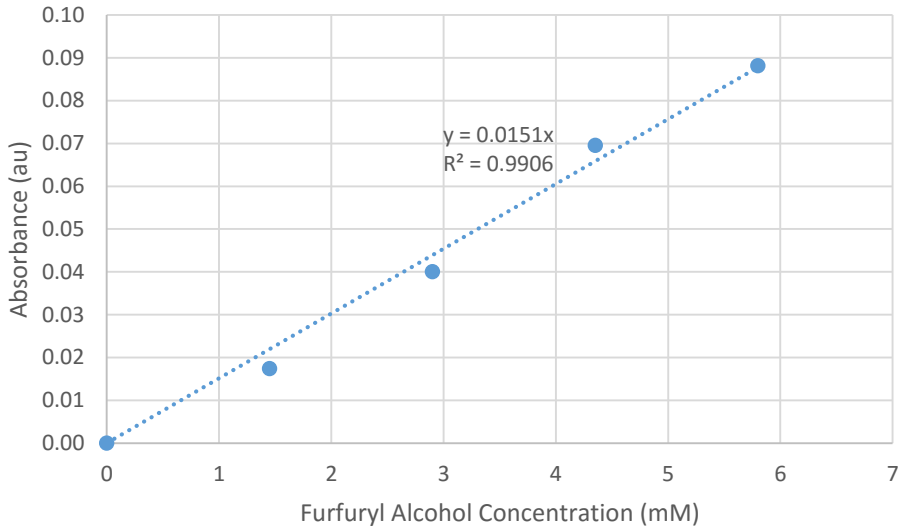

Figure 6-15 **Absorbance vs. FA Concentration (PX-2 xenon light source + USB4000) (StDev noise: 4.1 mAU)**

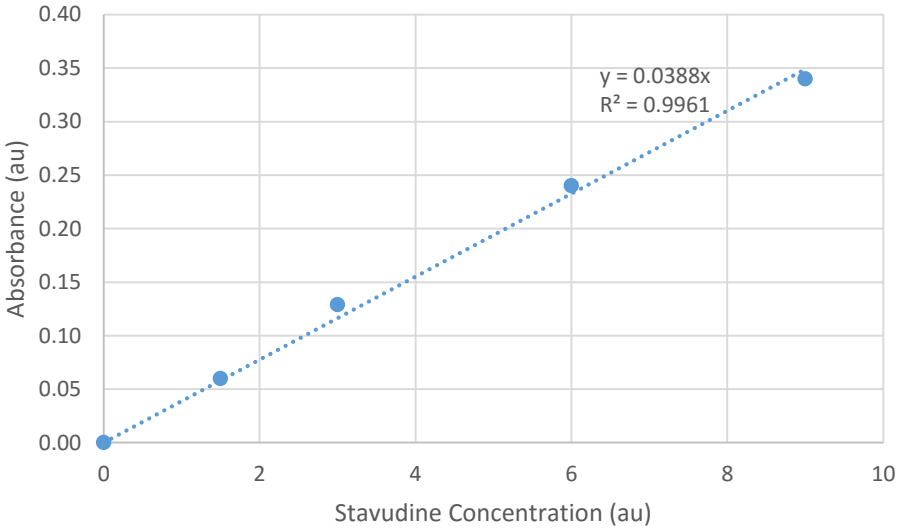

Figure 6-16 **Absorbance vs. Stavudine Concentration (PX-2 xenon light source + USB4000) (StDev noise: 4 mAU)**

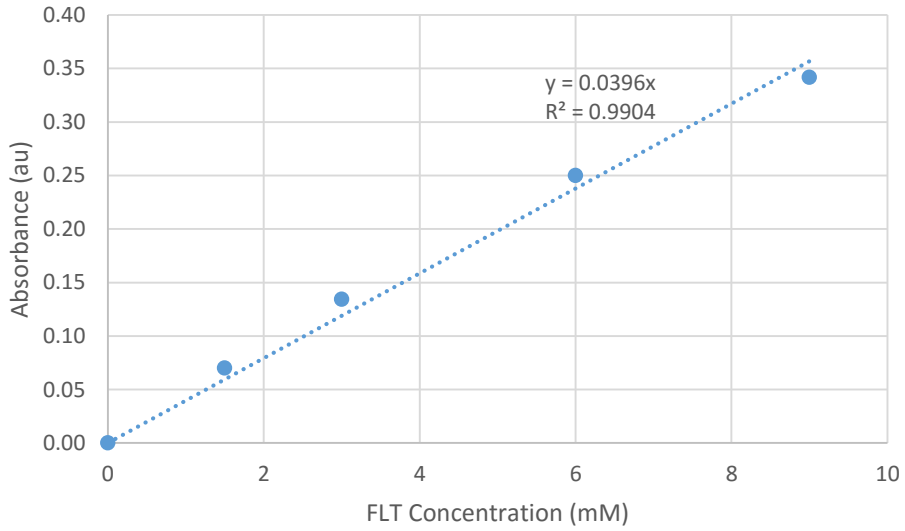

Figure 6-17 **Absorbance vs. FLT Concentration (PX-2 xenon light source + USB4000) (StDev noise: 4 mAU)**

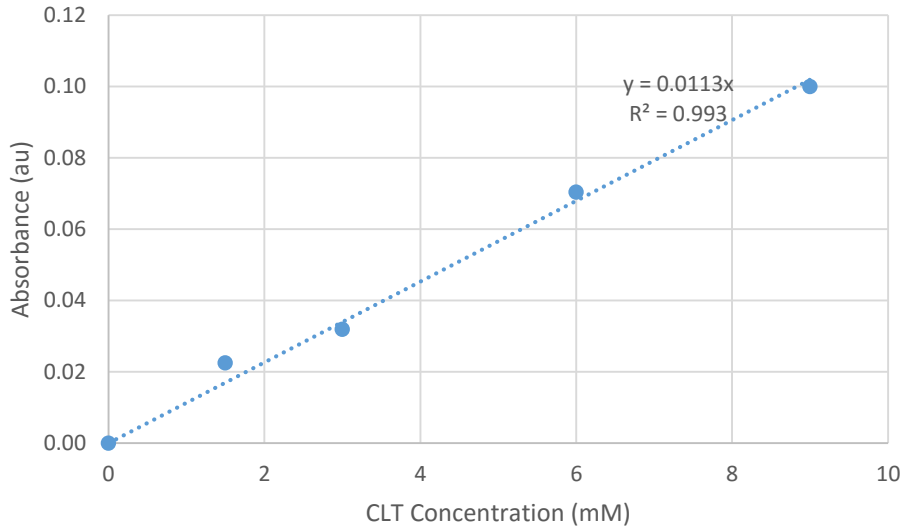

Figure 6-18 **Absorbance vs. CLT Concentration (PX-2 xenon light source + USB4000) (StDev noise: 4 mAU)**

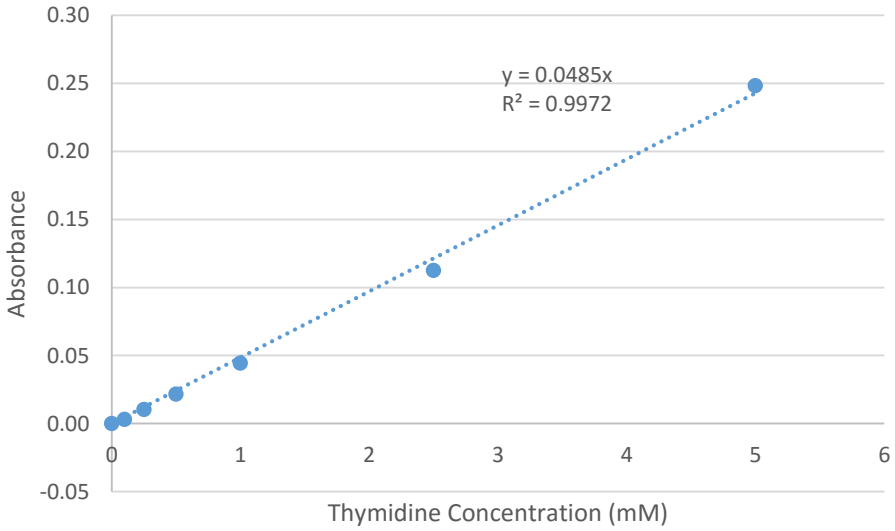

Figure 6-19 **Absorbance vs. Thymidine Concentration (DH-2000-BAL deuterium light source + QePro) (StDev noise: 0.35 mAU)**

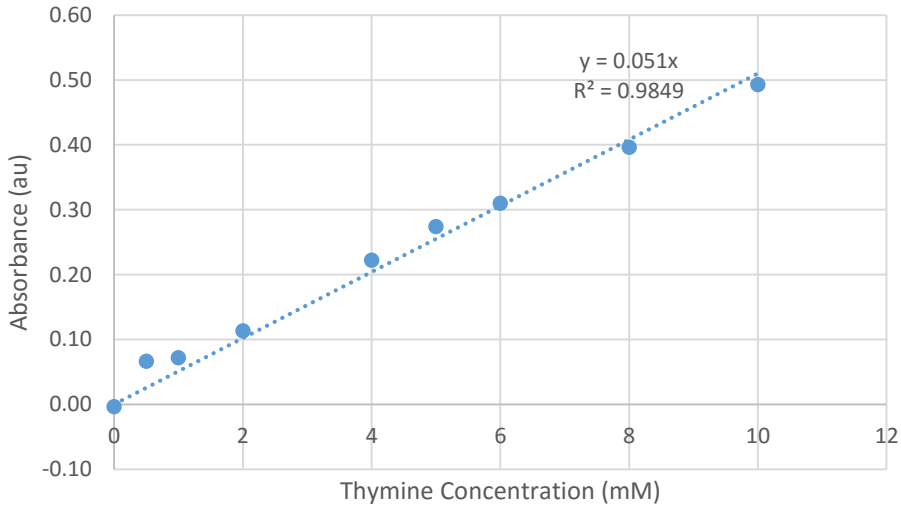

Figure 6-20 **Absorbance vs. Thymine Concentration (DH-2000-BAL deuterium light source + QePro) (StDev noise: 0.35 mAU)**

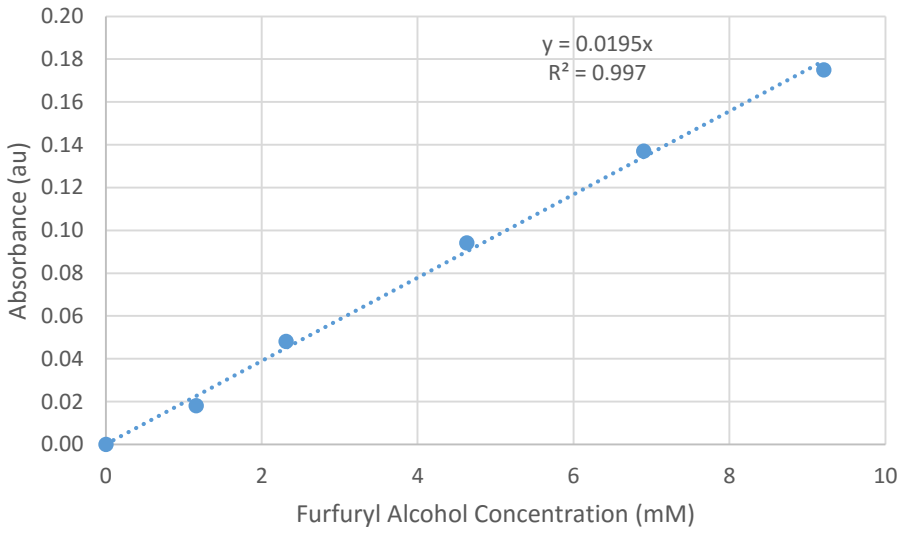

Figure 6-21 **Absorbance vs. FA Concentration (DH-2000-BAL deuterium light source + QePro) (StDev noise: 0.67 mAU)**

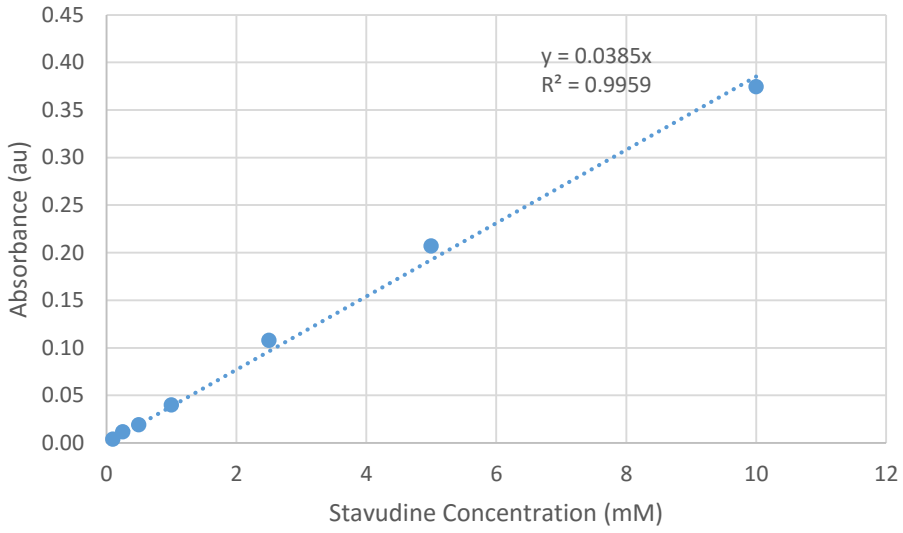

Figure 6-22 **Absorbance vs. Stavudine Concentration (DH-2000-BAL deuterium light source + QePro) (StDev noise: 0.35 mAU)**

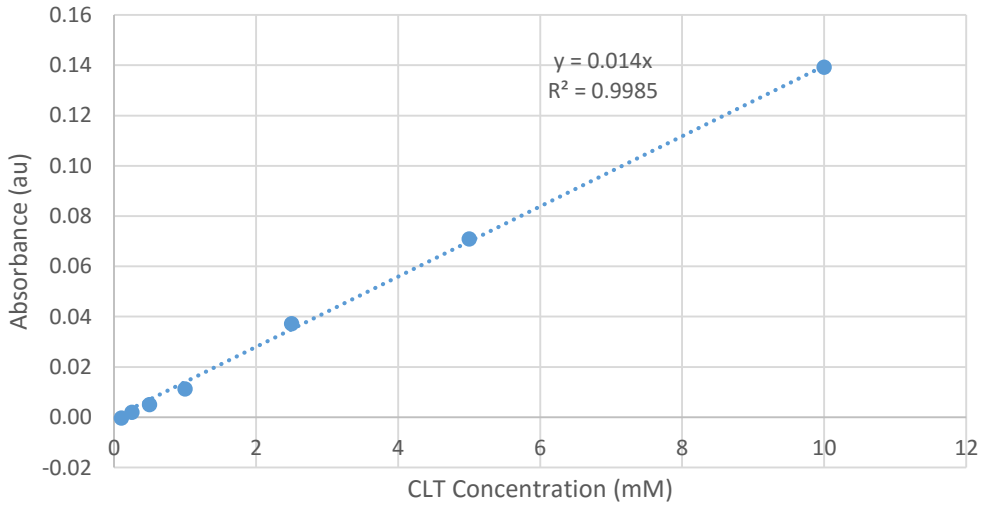

Figure 6-23 **Absorbance vs. CLT Concentration (DH-2000-BAL deuterium light source + QePro) (StDev noise: 0.35 mAU)**

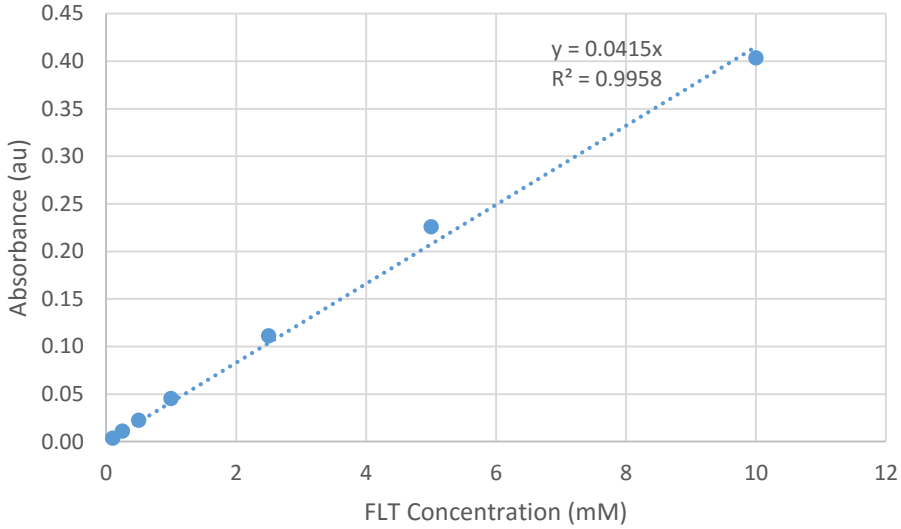

Figure 6-24 **Absorbance vs. FLT Concentration (DH-2000-BAL deuterium light source + QePro) (StDev noise: 0.35 mAU)**

6.4 Absorbance Data for Extended Optical Path Length Chip (Section 4.2)

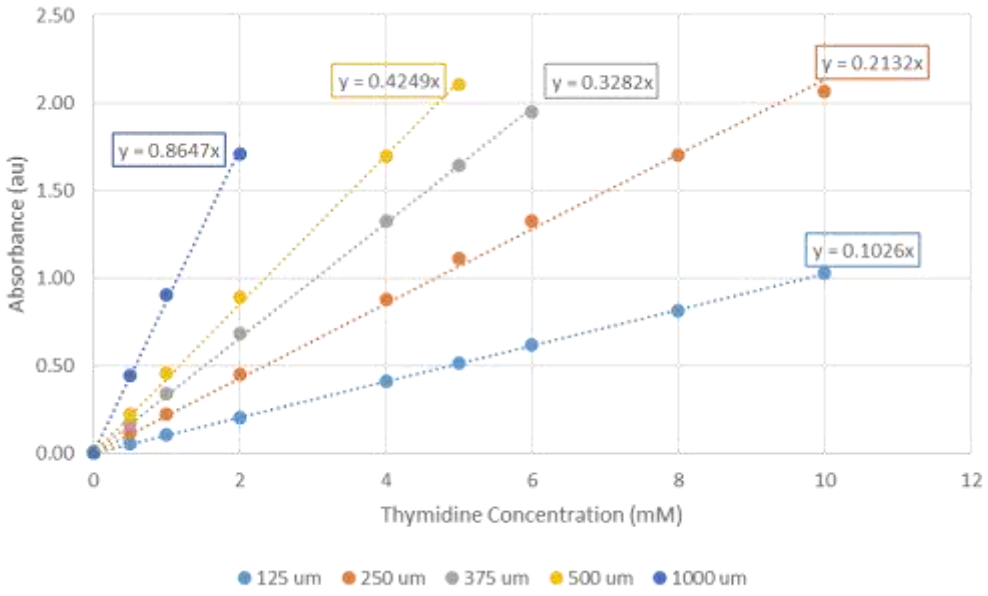

Figure 6-25 **Extended OPL Chip with Thymidine (PX-2 Xenon Light source + USB 4000) (StDev noise listed in Table 4-1)**

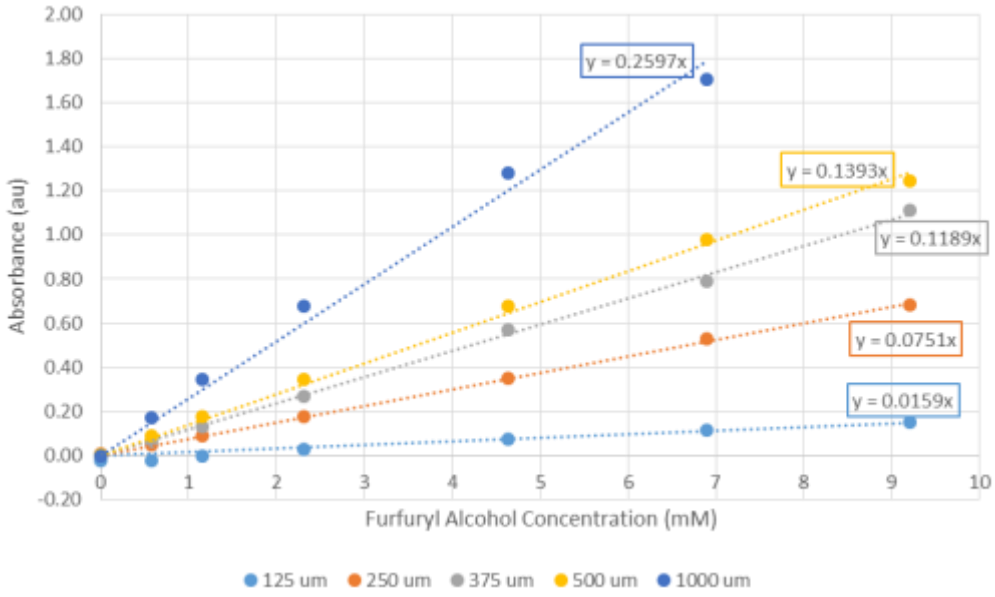

Figure 6-26 **Extended OPL Chip with FA (PX-2 Xenon Light source + USB 4000) (StDev noise listed in Table 4-1)**

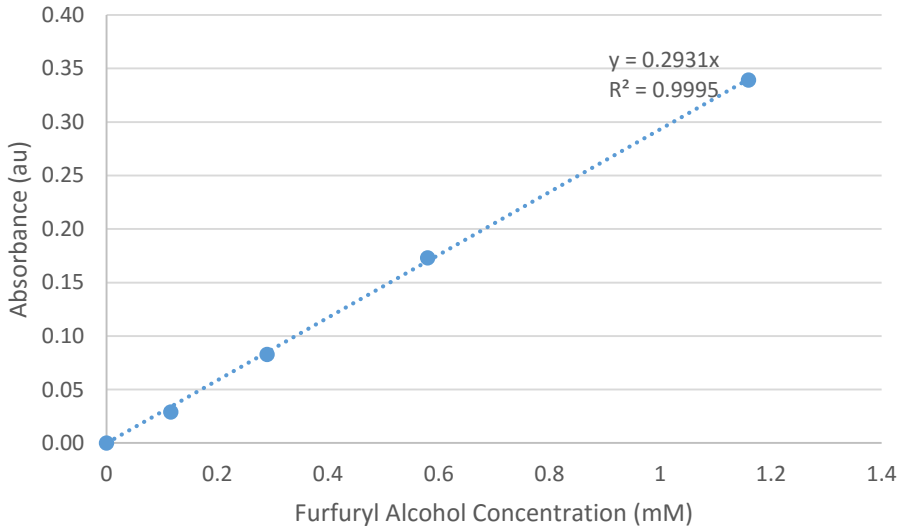

Figure 6-27 **500 µm OPL Chip with FA (DH-2000-BAL deuterium light source + QePro) (StDev noise: 0.67 mAU)**

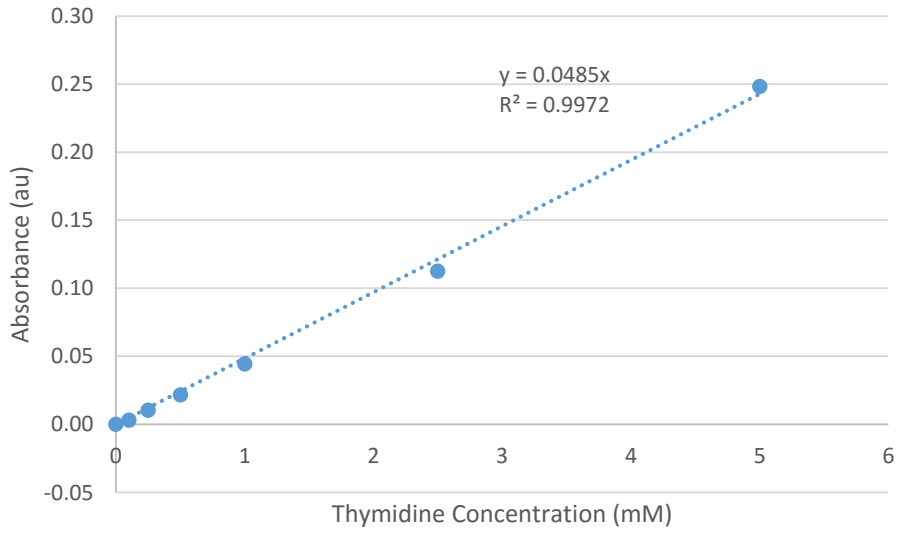

Figure 6-28 **500 µm OPL Chip with Thymine (DH-2000-BAL deuterium light source + QePro) (StDev noise: 0.35 mAU)**

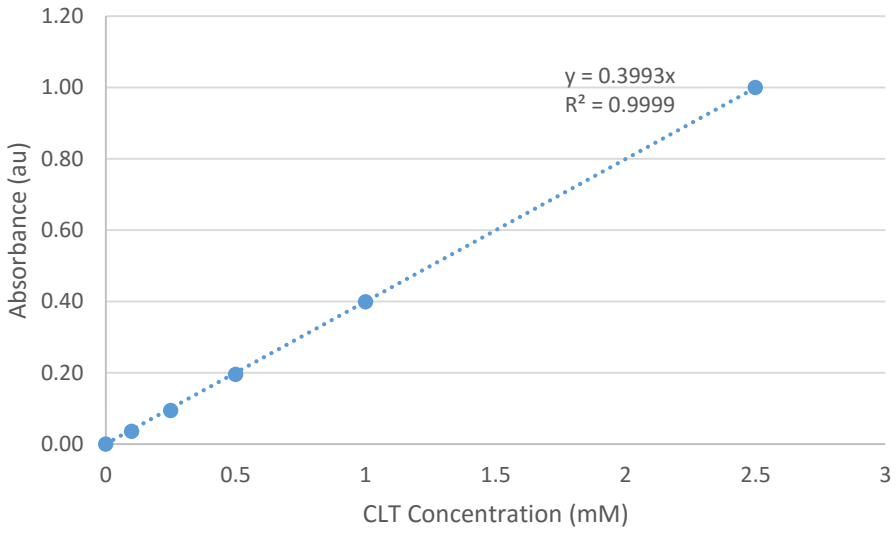

Figure 6-29 **500 µm OPL Chip with CLT (DH-2000-BAL deuterium light source + QePro) (StDev noise: 0.35 mAU)**

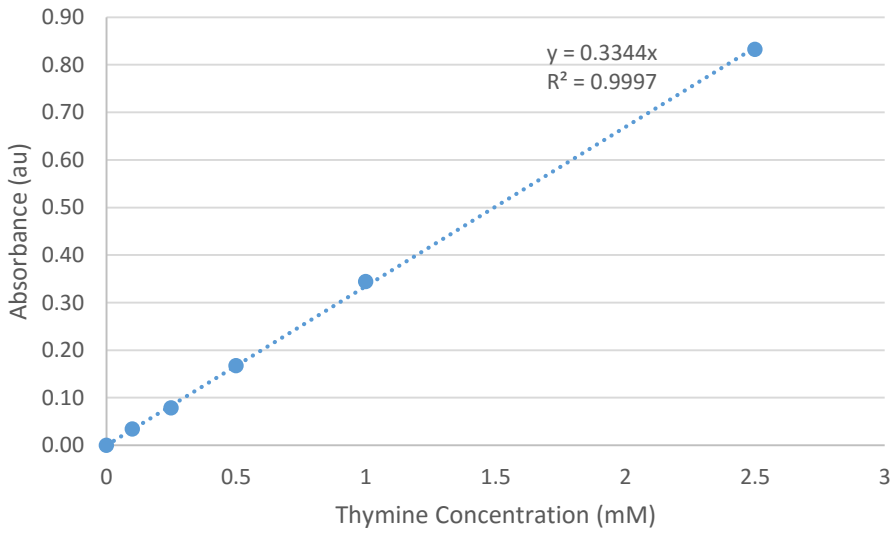

Figure 6-30 **500 µm OPL Chip with Thymine (DH-2000-BAL deuterium light source + QePro) (StDev noise: 0.35 mAU)**

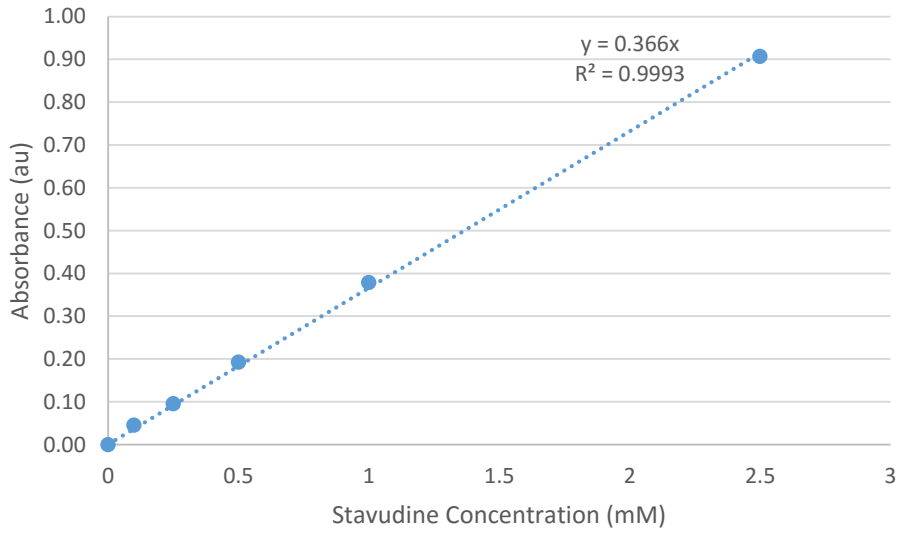

Figure 6-31 **500 µm OPL Chip with Stavudine (DH-2000-BAL deuterium light source + QePro) (StDev noise: 0.35 mAU)**

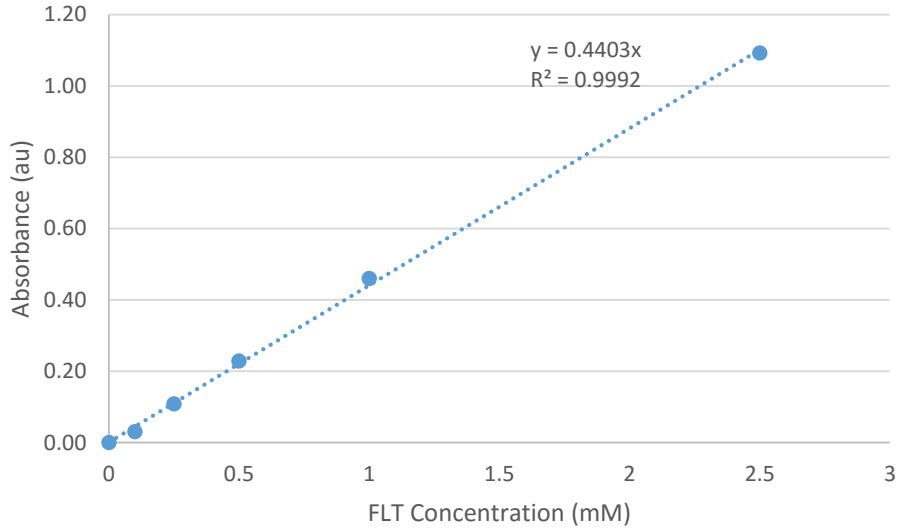

Figure 6-32 **500 µm OPL Chip with FLT (DH-2000-BAL deuterium light source + QePro) (StDev noise: 0.35 mAU)**

7 References

[1] M. E. Phelps, “PET: The Merging of Biology and Imaging into Molecular Imaging,” *J NucI Med*, vol. 41, no. 4, pp. 661–681, 2000.

[2] A. J. Fleming, S. P. Smith, C. M. Paul, N. C. Hall, B. T. Daly, A. Agrawal, and D. E. Schuller, “Impact of [18F]-2-Fluorodeoxyglucose–Positron Emission Tomography/Computed Tomography on Previously Untreated Head and Neck Cancer Patients,” *The Laryngoscope*, vol. 117, no. 7, pp. 1173–1179, 2007.

[3] S. Vallabhajosula, “18F-Labeled Positron Emission Tomographic Radiopharmaceuticals in Oncology: An Overview of Radiochemistry and Mechanisms of Tumor Localization,” *Seminars in Nuclear Medicine*, vol. 37, no. 6, pp. 400–419, Nov. 2007.

[4] M. E. Rodnick, B. G. Hockley, P. Sherman, C. Quesada, M. R. Battle, A. Jackson, K. E. Linder, S. Macholl, W. J. Trigg, M. R. Kilbourn, and P. J. H. Scott, “Novel fluorine-18 PET radiotracers based on flumazenil for GABAA imaging in the brain,” *Nuclear Medicine and Biology*, vol. 40, no. 7, pp. 901–905, Oct. 2013.

[5] A. Snellman, J. Rokka, F. R. Lopez-Picon, O. Eskola, I. Wilson, G. Farrar, M. Scheinin, O. Solin, J. O. Rinne, and M. Haaparanta-Solin, “Pharmacokinetics of [18F]flutemetamol in wild-type rodents and its binding to beta amyloid deposits in a mouse model of Alzheimer’s disease,” *Eur J Nucl Med Mol Imaging*, vol. 39, no. 11, pp. 1784–1795, Nov. 2012.

[6] S. Liu, D. Li, H. Shan, F. P. Gabbaï, Z. Li, and P. S. Conti, “Evaluation of 18F-labeled BODIPY dye as potential PET agents for myocardial perfusion imaging,” *Nuclear Medicine and Biology*, vol. 41, no. 1, pp. 120–126, Jan. 2014.

[7] H. F. Wehrl, M. S. Judenhofer, S. Wiehr, and B. J. Pichler, “Pre-clinical PET/MR: technological advances and new perspectives in biomedical research,” *Eur J Nucl Med Mol Imaging*, vol. 36, no. 1, pp. 56–68, Feb. 2009.

[8] M. E. Phelps, *PET: Molecular Imaging and Its Biological Applications*, 1st ed. Springer Science & Business Media, 2004.

[9] E. O. Aboagye, P. M. Price, and T. Jones, “In vivo pharmacokinetics and pharmacodynamics in drug development using positron-emission tomography,” *Drug Discovery Today*, vol. 6, no. 6, pp. 293–302, Mar. 2001.

[10] S. Chen, J. Lei, R. M. van Dam, P.-Y. Keng, and C.-J. “CJ” Kim, “Planar alumina purification of 18F-labeled radiotracer synthesis on EWOD chip for positron emission tomography (PET),” in *Proceedings of the 16th International Conference on Miniaturized Systems for Chemistry and Life Sciences*, Okinawa, Japan, 2012, pp. 1771–1773.

[11] S. Banister, D. Roeda, F. Dolle, and M. Kassiou, “Fluorine-18 Chemistry for PET: A Concise Introduction,” *Current Radiopharmaceuticalse*, vol. 3, no. 2, pp. 68–80, Apr. 2010.

[12] S. Vallabhajosula, L. Solnes, and B. Vallabhajosula, “A Broad Overview of Positron Emission Tomography Radiopharmaceuticals and Clinical Applications: What Is New?,” *Seminars in Nuclear Medicine*, vol. 41, no. 4, pp. 246–264, Jul. 2011.

[13] M.-C. Lasne, C. Perrio, J. Rouden, L. Barré, D. Roeda, F. Dolle, and C. Crouzel, “Chemistry of β +-Emitting Compounds Based on Fluorine-18,” in *Contrast Agents II*, vol. 222, W. Krause, Ed. Berlin, Heidelberg: Springer Berlin Heidelberg, 2002, pp. 201–258.

[14] W. A. Weber and R. Figlin, “Monitoring Cancer Treatment with PET/CT: Does It Make a Difference?,” *J Nucl Med*, vol. 48, no. 1_suppl, p. 36S–44, Jan. 2007.

[15] P. Marchand, V. Bekaert, A. Ouadi, P. Laquerriere, D. Brasse, and H. Curien, “Forty Years of 18F-Labeled Compound Development in an Open Access Database,” *J Nucl Med*, vol. 54, no. 1, p. 15N–17N, Jan. 2013.

[16] “Radiosynthesis Database of PET Probes (RaDaP).” [Online]. Available: http://www.nirs.go.jp/research/division/mic/db2/. [Accessed: 15-Aug-2012].

[17] J. R. Grierson and A. F. Shields, “Radiosynthesis of 3’-deoxy-3’-[18F]fluorothymidine: [18F]FLT for imaging of cellular proliferation in vivo,” *Nuclear Medicine and Biology*, vol. 27, no. 2, pp. 143–156, Feb. 2000.

[18] S. Niedermoser, M. Pape, F. J. Gildehaus, C. Wängler, M. Hartenbach, R. Schirrmacher, P. Bartenstein, and B. Wängler, “Evaluation of an automated double-synthesis module: efficiency and reliability of subsequent radiosyntheses of FHBG and FLT,” *Nuclear Medicine and Biology*, vol. 39, no. 4, pp. 586–592, May 2012.

[19] J. Mukherjee, Z.-Y. Yang, T. Brown, R. Lew, M. Wernick, X. Ouyang, N. Yasillo, C.-T. Chen, R. Mintzer, and M. Cooper, “Preliminary assessment of extrastriatal dopamine d-2 receptor binding in the rodent and nonhuman primate brains using the high affinity radioligand, 18F-fallypride,” *Nuclear Medicine and Biology*, vol. 26, no. 5, pp. 519–527, Jul. 1999.

[20] N. T. Vandehey, J. M. Moirano, A. K. Converse, J. E. Holden, J. Mukherjee, D. Murali, R. J. Nickles, R. J. Davidson, M. L. Schneider, and B. T. Christian, “High-affinity dopamine D2/D3 PET radioligands 18F-fallypride and 11C-FLB457: A comparison of kinetics in extrastriatal regions using a multiple-injection protocol,” *J Cereb Blood Flow Metab*, vol. 30, no. 5, pp. 994–1007, May 2010.

[21] M. Guillaume, A. Luxen, B. Nebeling, M. Argentini, J. C. Clark, and V. W. Pike, “Recommendations for fluorine-18 production,” *International Journal of Radiation Applications and Instrumentation. Part A. Applied Radiation and Isotopes*, vol. 42, no. 8, pp. 749–762, 1991.

[22] N. Satyamurthy, B. Amarasekera, C. W. Alvord, J. R. Barrio, and M. E. Phelps, “Tantalum [18O]Water Target for the Production of [18F]Fluoride with High Reactivity for the Preparation of 2-Deoxy-2-[18F]Fluoro-D-Glucose,” *Molecular Imaging & Biology*, vol. 4, no. 1, pp. 65–70, Jan. 2002.

[23] J.-H. Chun, S. Telu, S. Lu, and V. W. Pike, “Radiofluorination of diaryliodonium tosylates under aqueous-organic and cryptand-free conditions,” *Org Biomol Chem*, vol. 11, no. 31, pp. 5094–5099, Aug. 2013.

[24] C. Pascali, A. Bogni, L. Fugazza, C. Cucchi, O. Crispu, L. Laera, R. Iwata, G. Maiocchi, F. Crippa, and E. Bombardieri, “Simple preparation and purification of ethanol-free solutions of 3′-deoxy-3′-[18F]fluorothymidine by means of disposable solid-phase extraction cartridges,” *Nuclear Medicine and Biology*, vol. 39, no. 4, pp. 540–550, May 2012.

[25] P. Y. Keng, M. Esterby, and R. M. van Dam, “Emerging Technologies for Decentralized Production of PET Tracers,” in *Positron Emission Tomography - Current Clinical and Research Aspects*, C.-H. Hsieh, Ed. Rijeka, Croatia: InTech, 2012, pp. 153–182.

[26] M. Lazari, J. Collins, B. Shen, M. Farhoud, D. Yeh, B. Maraglia, F. T. Chin, D. A. Nathanson, M. Moore, and R. M. van Dam, “Fully Automated Production of Diverse 18F-Labeled PET Tracers on the ELIXYS Multireactor Radiosynthesizer Without Hardware Modification,” *J. Nucl. Med. Technol.*, vol. 42, no. 3, pp. 203–210, Sep. 2014.

[27] M. R. Javed, S. Chen, J. Lei, J. Collins, M. Sergeev, H.-K. Kim, C.-J. Kim, R. M. van Dam, and P. Y. Keng, “High yield and high specific activity synthesis of [18F]fallypride in a batch microfluidic reactor for micro-PET imaging,” *Chem. Commun.*, vol. 50, no. 10, pp. 1192–1194, 2014.

[28] W.-Y. Tseng, J. S. Cho, X. Ma, A. Kunihiro, A. Chatziioannou, and R. M. van Dam, “Toward reliable synthesis of radiotracers for positron emission tomography in PDMS microfluidic chips: Study and optimization of the [18F] fluoride drying process,” in *Technical Proceedings of the 2010 NSTI Nanotechnology Conference and Trade Show*, Anaheim, CA, 2010, vol. 2, pp. 472–475.

[29] P. Y. Keng, H. Ding, S. Chen, S. Sadeghi, G. J. Shah, M. E. Phelps, N. Satyamurthy, C.-J. Kim, and R. M. van Dam, “Digital microfluidics: Toward a bench-top platform for on-demand radiosynthesis of diverse PET tracers,” presented at the 240th ACS National Meeting, Boston, MA, 22-Aug-2010.

[30] S. Chen, M. R. Javed, H.-K. Kim, J. Lei, M. Lazari, G. J. Shah, M. van Dam, P. Y. Keng, and C.-J. Kim, “Radiolabelling diverse positron emission tomography (PET) tracers using a single digital microfluidic reactor chip,” *Lab Chip*, vol. 14, pp. 902–910, 2014.

[31] P. Y. Keng and R. M. van Dam, “Digital Microfluidics: A New Paradigm for Radiochemistry,” *Mol. Imag.*, vol. 14, pp. 579–594, 2015.

[32] S. Yu, “Review of 18F-FDG synthesis and quality control,” *Biomed Imaging Interv J*, vol. 2, no. 4, p. e57, 2006.

[33] E. Fermi, “Quality Control of PET Radiopharmaceuticals,” in *Molecular Imaging: Radiopharmaceuticals for PET and SPECT*, Springer Berlin Heidelberg, 2009, pp. 197–204.

[34] R. Nakao, T. Ito, M. Yamaguchi, and K. Suzuki, “Simultaneous analysis of FDG, ClDG and Kryptofix 2.2.2 in [18F]FDG preparation by high-performance liquid chromatography with UV detection,” *Nucl. Med. Biol.*, vol. 35, no. 2, pp. 239–244, Feb. 2008.

[35] “QC1,” *http://www.qc1.com*. [Online]. Available: http://www.qc1.com/. [Accessed: 01-Dec-2012].

[36] “Trace-ability, Inc. - SBIR Source,” *SBIRSource.com*. [Online]. Available: http://sbirsource.com/sbir/firms/26162-trace-ability-inc. [Accessed: 26-Dec-2015].

[37] A. I. Anzellotti, A. R. McFarland, D. Ferguson, and K. F. Olson, “Towards the Full Automation of QC Release Tests for [18F]fluoride-labeled Radiotracers,” *Current Organic Chemistry*, vol. 17, no. 19, pp. 2153–2158, Oct. 2013.

[38] R. Nutt, A. M. Giamis, and A. McFarland, “Quality Control Module for Biomarker Generator System.”

[39] A. Arora, G. Simone, G. B. Salieb-Beugelaar, J. T. Kim, and A. Manz, “Latest developments in micro total analysis systems,” *Analytical chemistry*, vol. 82, no. 12, pp. 4830–4847, 2010.

[40] D. E. Patabadige, S. Jia, J. Sibbitts, J. Sadeghi, K. Sellens, and C. T. Culbertson, “Micro Total Analysis Systems: Fundamental Advances and Applications,” *Analytical chemistry*, 2015.

[41] C. Liu, Y. Mo, Z. Chen, X. Li, O. Li, and X. Zhou, “Dual fluorescence/contactless conductivity detection for microfluidic chip,” *Analytica chimica acta*, vol. 621, no. 2, pp. 171–177, 2008.

[42] M. Vázquez, C. Frankenfeld, W. K. T. Coltro, E. Carrilho, D. Diamond, and S. M. Lunte, “Dual contactless conductivity and amperometric detection on hybrid

PDMS/glass electrophoresis microchips," *Analyst*, vol. 135, no. 1, pp. 96–103, 2010.

[43] M. U. Kopp, H. J. Crabtree, and A. Manz, "Developments in technology and applications of microsystems," *Current Opinion in Chemical Biology*, vol. 1, no. 3, pp. 410–419, Oct. 1997.

[44] K. Schult, A. Katerkamp, D. Trau, F. Grawe, K. Cammann, and M. Meusel, "Disposable Optical Sensor Chip for Medical Diagnostics: New Ways in Bioanalysis," *Anal. Chem.*, vol. 71, no. 23, pp. 5430–5435, Dec. 1999.

[45] M. Ávila, M. Zougagh, A. Escarpa, and Á. Ríos, "Fast single run of vanilla fingerprint markers on microfluidic-electrochemistry chip for confirmation of common frauds," *Electrophoresis*, vol. 30, no. 19, pp. 3413–3418, Oct. 2009.

[46] S.-H. Chen and J. M. Gallo, "Use of capillary electrophoresis methods to characterize the pharmacokinetics of antisense drugs," *Electrophoresis*, vol. 19, no. 16–17, pp. 2861–2869, Nov. 1998.

[47] Á. Ríos, M. Zougagh, and M. Avila, "Miniaturization through lab-on-a-chip: Utopia or reality for routine laboratories? A review," *Analytica Chimica Acta*, vol. 740, pp. 1–11, Aug. 2012.

[48] P. Neuži, S. Giselbrecht, K. Länge, T. J. Huang, and A. Manz, "Revisiting lab-on-a-chip technology for drug discovery," *Nat Rev Drug Discov*, vol. 11, no. 8, pp. 620–632, Aug. 2012.

[49] S. Archibald, N. Pamme, N. Brown, and M. Tarn, "Integrated microfluidic lab-on-a-chip systems for 18F radiotracer synthesis, purification and quality control," *J Nucl Med*, vol. 56, no. supplement 3, pp. 167–167, May 2015.

[50] A. P. Lewis, A. Cranny, N. R. Harris, N. G. Green, J. A. Wharton, R. J. K. Wood, and K. R. Stokes, "Review on the development of truly portable and in-situ capillary electrophoresis systems," *Meas. Sci. Technol.*, vol. 24, no. 4, p. 042001, Apr. 2013.

[51] J. Wang, “Electrochemical Detection for Capillary Electrophoresis Microchips: A Review,” *Electroanalysis*, vol. 17, no. 13, pp. 1133–1140, 2005.

[52] G. M. Whitesides, “The origins and the future of microfluidics,” *Nature*, vol. 442, no. 7101, pp. 368–373, Jul. 2006.

[53] D. Janasek, J. Franzke, and A. Manz, “Scaling and the design of miniaturized chemical-analysis systems,” *Nature*, vol. 442, no. 7101, pp. 374–380, Jul. 2006.

[54] S. Götz and U. Karst, “Recent developments in optical detection methods for microchip separations,” *Anal Bioanal Chem*, vol. 387, no. 1, pp. 183–192, Jan. 2007.

[55] J. W. Jorgenson and K. D. Lukacs, “Zone electrophoresis in open-tubular glass capillaries,” *Anal. Chem.*, vol. 53, no. 8, pp. 1298–1302, Jul. 1981.

[56] J. W. Jorgenson and K. D. Lukacs, “Free-zone electrophoresis in glass capillaries.,” *Clinical Chemistry*, vol. 27, no. 9, pp. 1551–1553, Sep. 1981.

[57] E. Tamizi and A. Jouyban, “The potential of the capillary electrophoresis techniques for quality control of biopharmaceuticals—A review,” *Electrophoresis*, vol. 36, no. 6, pp. 831–858, Mar. 2015.

[58] R. Jankowsky, B. Noll, and B. Johannsen, “Capillary electrophoresis of 99mtechnetium radiopharmaceuticals,” *Journal of Chromatography B: Biomedical Sciences and Applications*, vol. 724, no. 2, pp. 365–371, Mar. 1999.

[59] S. L. Pimlott and A. Sutherland, “Molecular tracers for the PET and SPECT imaging of disease,” *Chem. Soc. Rev.*, vol. 40, no. 1, pp. 149–162, 2011.

[60] A. B. Bergamo, J. A. Fracassi da Silva, and D. P. de Jesus, “Simultaneous determination of aspartame, cyclamate, saccharin and acesulfame-K in soft drinks and tabletop sweetener formulations by capillary electrophoresis with capacitively coupled contactless conductivity detection,” *Food Chemistry*, vol. 124, no. 4, pp. 1714–1717, Feb. 2011.

[61] C. Liu, G. Fang, Q. Deng, Y. Zhang, J. Feng, and S. Wang, “Determination of metolcarb in food by capillary electrophoresis immunoassay with a laser-induced fluorescence detector,” *Electrophoresis*, vol. 33, no. 9–10, pp. 1471–1476, May 2012.

[62] B. S. Sekhon, “An overview of capillary electrophoresis: pharmaceutical, biopharmaceutical and biotechnology applications,” *J Pharm Educ Res*, vol. 2, no. 2, pp. 2–36, 2011.

[63] L. Suntornsuk, “Recent advances of capillary electrophoresis in pharmaceutical analysis,” *Anal Bioanal Chem*, vol. 398, no. 1, pp. 29–52, Sep. 2010.

[64] M. Pioch, S.-C. Bunz, and C. Neusüß, “Capillary electrophoresis/mass spectrometry relevant to pharmaceutical and biotechnological applications,” *Electrophoresis*, vol. 33, no. 11, pp. 1517–1530, Jun. 2012.

[65] I. Kohler, J. Schappler, and S. Rudaz, “Microextraction techniques combined with capillary electrophoresis in bioanalysis,” *Anal Bioanal Chem*, vol. 405, no. 1, pp. 125–141, Sep. 2012.

[66] J. Eijkel, “Chip-based capillary electrophoresis platforms: toward point-of-care applications,” *Bioanalysis*, vol. 7, no. 11, pp. 1385–1387, Jun. 2015.

[67] H. Zhang, J. Gavina, and Y.-L. Feng, “Understanding mechanisms of pressure-assisted electrokinetic injection: Application to analysis of bromate, arsenic and selenium species in drinking water by capillary electrophoresis-mass spectrometry,” *Journal of Chromatography A*, vol. 1218, no. 20, pp. 3095–3104, May 2011.

[68] R. J. Flaherty, B. Nshime, M. DeLaMarre, S. DeJong, P. Scott, and A. W. Lantz, “Cyclodextrins as complexation and extraction agents for pesticides from contaminated soil,” *Chemosphere*, vol. 91, no. 7, pp. 912–920, May 2013.

[69] J. W. Jorgenson and K. D. Lukacs, “Capillary zone electrophoresis,” *Science*, vol. 222, no. 4621, pp. 266–272, Oct. 1983.

[70] O. Koji and T. Shigeru, “Micellar electrokinetic chromatography,” *Mol Biotechnol*, vol. 9, no. 3, pp. 253–271, Jun. 1998.

[71] V. Dolník, “Capillary gel electrophoresis,” *J. Micro. Sep.*, vol. 6, no. 4, pp. 315–330, Jul. 1994.

[72] R. Rodriguez-Diaz, T. Wehr, and M. Zhu, “Capillary isoelectric focusing,” *Electrophoresis*, vol. 18, no. 12–13, pp. 2134–2144, Jan. 1997.

[73] D. Kaniansky and J. Marák, “On-line coupling of capillary isotachophoresis with capillary zone electrophoresis,” *Journal of Chromatography A*, vol. 498, pp. 191–204, 1990.

[74] M. M. Dittmann and G. P. Rozing, “Capillary electrochromatography — a high-efficiency micro-separation technique,” *Journal of Chromatography A*, vol. 744, no. 1–2, pp. 63–74, Sep. 1996.

[75] X. Huang, M. J. Gordon, and R. N. Zare, “Current-monitoring method for measuring the electroosmotic flow rate in capillary zone electrophoresis,” *Anal. Chem.*, vol. 60, no. 17, pp. 1837–1838, Sep. 1988.

[76] J. E. Melanson, N. E. Baryla, and C. A. Lucy, “Dynamic capillary coatings for electroosmotic flow control in capillary electrophoresis,” *TrAC Trends in Analytical Chemistry*, vol. 20, no. 6–7, pp. 365–374, Jun. 2001.

[77] S. F. Y. Li, *Capillary Electrophoresis: Principles, Practice and Applications*. Elsevier, 1992.

[78] C. L. Rice and R. Whitehead, “Electrokinetic Flow in a Narrow Cylindrical Capillary,” *J. Phys. Chem.*, vol. 69, no. 11, pp. 4017–4024, Nov. 1965.

[79] T. Tsuda, M. Ikedo, G. Jones, R. Dadoo, and R. N. Zare, “Observation of flow profiles in electroosmosis in a rectangular capillary,” *Journal of Chromatography A*, vol. 632, no. 1–2, pp. 201–207, Feb. 1993.

[80] U. Tallarek, E. Rapp, T. Scheenen, E. Bayer, and H. Van As, “Electroosmotic and Pressure-Driven Flow in Open and Packed Capillaries: Velocity Distributions and Fluid Dispersion,” *Anal. Chem.*, vol. 72, no. 10, pp. 2292–2301, May 2000.

[81] K. D. Lukacs and J. W. Jorgenson, “Capillary zone electrophoresis: Effect of physical parameters on separation efficiency and quantitation,” *J. High Resol. Chromatogr.*, vol. 8, no. 8, pp. 407–411, Aug. 1985.

[82] B. B. VanOrman, G. G. Liversidge, G. L. McIntire, T. M. Olefirowicz, and A. G. Ewing, “Effects of buffer composition on electroosmotic flow in capillary electrophoresis,” *J. Micro. Sep.*, vol. 2, no. 4, pp. 176–180, Jul. 1990.

[83] S. Hjertén, “Zone broadening in electrophoresis with special reference to high-performance electrophoresis in capillaries: An interplay between theory and practice,” *Electrophoresis*, vol. 11, no. 9, pp. 665–690, Jan. 1990.

[84] J. H. Knox and K. A. McCormack, “Temperature effects in capillary electrophoresis. 1: Internal capillary temperature and effect upon performance,” *Chromatographia*, vol. 38, no. 3–4, pp. 207–214, Feb. 1994.

[85] J. H. Knox and K. A. McCormack, “Temperature effects in capillary electrophoresis 2: Some theoretical calculations and predictions,” *Chromatographia*, vol. 38, no. 3–4, pp. 215–221, Feb. 1994.

[86] C. A. Lucy and R. S. Underhill, “Characterization of the Cationic Surfactant Induced Reversal of Electroosmotic Flow in Capillary Electrophoresis,” *Anal. Chem.*, vol. 68, no. 2, pp. 300–305, Jan. 1996.

[87] K. K.-C. Yeung and C. A. Lucy, “Suppression of Electroosmotic Flow and Prevention of Wall Adsorption in Capillary Zone Electrophoresis Using Zwitterionic Surfactants,” *Anal. Chem.*, vol. 69, no. 17, pp. 3435–3441, Sep. 1997.

[88] S. Terabe, “Capillary Separation: Micellar Electrokinetic Chromatography,” *Annual Review of Analytical Chemistry*, vol. 2, no. 1, pp. 99–120, 2009.

[89] D. S. Burgi and R. L. Chien, “Optimization in sample stacking for high-performance capillary electrophoresis,” *Anal. Chem.*, vol. 63, no. 18, pp. 2042–2047, 1991.

[90] R. Aebersold and H. D. Morrison, “Analysis of dilute peptide samples by capillary zone electrophoresis,” *Journal of Chromatography A*, vol. 516, no. 1, pp. 79–88, Sep. 1990.

[91] J. P. Landers, *Handbook of Capillary Electrophoresis, Second Edition*. CRC Press, 1996.

[92] K. D. Altria, “Overview of capillary electrophoresis and capillary electrochromatography,” *Journal of Chromatography A*, vol. 856, no. 1–2, pp. 443–463, Sep. 1999.

[93] R. J. Nelson, A. Paulus, A. S. Cohen, A. Guttman, and B. L. Karger, “Use of peltier thermoelectric devices to control column temperature in high-performance capillary electrophoresis,” *Journal of Chromatography A*, vol. 480, pp. 111–127, 1989.

[94] J. A. Vickers, M. M. Caulum, and C. S. Henry, “Generation of Hydrophilic Poly(dimethylsiloxane) for High-Performance Microchip Electrophoresis,” *Anal. Chem.*, vol. 78, no. 21, pp. 7446–7452, Nov. 2006.

[95] J. P. Schaeper and M. J. Sepaniak, “Parameters affecting reproducibility in capillary electrophoresis,” *Electrophoresis*, vol. 21, no. 7, pp. 1421–1429, Apr. 2000.

[96] T. Faller and H. Engelhardt, “How to achieve higher repeatability and reproducibility in capillary electrophoresis,” *Journal of Chromatography A*, vol. 853, no. 1–2, pp. 83–94, Aug. 1999.

[97] X. Huang, W. F. Coleman, and R. N. Zare, “Analysis of factors causing peak broadening in capillary zone electrophoresis,” *Journal of Chromatography A*, vol. 480, pp. 95–110, 1989.

[98] M. W. Li, B. H. Huynh, M. K. Hulvey, S. M. Lunte, and R. S. Martin, “Design and characterization of poly(dimethylsiloxane)-based valves for interfacing continuous-flow sampling to microchip electrophoresis,” *Anal. Chem.*, vol. 78, no. 4, pp. 1042–1051, Feb. 2006.

[99] A. J. Gaudry, Y. H. Nai, R. M. Guijt, and M. C. Breadmore, “Polymeric Microchip for the Simultaneous Determination of Anions and Cations by Hydrodynamic Injection Using a Dual-Channel Sequential Injection Microchip Electrophoresis System,” *Anal. Chem.*, vol. 86, no. 7, pp. 3380–3388, Apr. 2014.

[100] A. Llobera, R. Wilke, and S. Büttgenbach, “Optimization of poly(dimethylsiloxane) hollow prisms for optical sensing,” *Lab on a Chip*, vol. 5, no. 5, p. 506, 2005.

[101] A. Llobera, S. Demming, R. Wilke, and S. Büttgenbach, “Multiple internal reflection poly(dimethylsiloxane) systems for optical sensing,” *Lab on a Chip*, vol. 7, no. 11, p. 1560, 2007.

[102] L. J. Gimbert and P. J. Worsfold, “Environmental applications of liquid-waveguide-capillary cells coupled with spectroscopic detection,” *TrAC Trends in Analytical Chemistry*, vol. 26, no. 9, pp. 914–930, Oct. 2007.

[103] J.-Z. Pan, B. Yao, and Q. Fang, “Hand-held Photometer Based on Liquid-Core Waveguide Absorption Detection for Nanoliter-scale Samples,” *Analytical Chemistry*, vol. 82, no. 8, pp. 3394–3398, Apr. 2010.

[104] A. Llobera, R. Wilke, and S. B�ttgenbach, “Poly(dimethylsiloxane) hollow Abbe prism with microlenses for detection based on absorption and refractive index shift,” *Lab on a Chip*, vol. 4, no. 1, p. 24, 2004.

[105] K. W. Ro, K. Lim, B. C. Shim, and J. H. Hahn, “Integrated Light Collimating System for Extended Optical-Path-Length Absorbance Detection in Microchip-Based Capillary Electrophoresis,” *Analytical Chemistry*, vol. 77, no. 16, pp. 5160–5166, Aug. 2005.

[106] E. González-Peñas, C. Leache, A. López de Cerain, and E. Lizarraga, “Comparison between capillary electrophoresis and HPLC-FL for ochratoxin A quantification in wine,” *Food Chemistry*, vol. 97, no. 2, pp. 349–354, Jul. 2006.

[107] H. J. Gaus, A. G. Beck-Sickinger, and E. Bayer, “Optimization of capillary electrophoresis of mixtures of basic peptides and comparison with HPLC,” *Anal. Chem.*, vol. 65, no. 10, pp. 1399–1405, May 1993.

[108] E. R. Castro and A. Manz, “Present state of microchip electrophoresis: State of the art and routine applications,” *Journal of Chromatography A*, vol. 1382, pp. 66–85, Feb. 2015.

[109] N. Nuchtavorn, W. Suntornsuk, S. M. Lunte, and L. Suntornsuk, “Recent applications of microchip electrophoresis to biomedical analysis,” *Journal of Pharmaceutical and Biomedical Analysis*.

[110] H. Herman, G. Flores, K. Quinn, M. Esterby, G. J. Shah, M. E. Phelps, N. Satyamurthy, and R. M. van Dam, “Multi-pot radiosynthesizer capable of high-pressure reactions for production of [18F]FAC and analogs,” presented at the Society of Nuclear Medicine Annual Meeting, San Antonio, TX, 04-Jun-2011.

[111] C. G. Radu, C. J. Shu, E. Nair-Gill, S. M. Shelly, J. R. Barrio, N. Satyamurthy, M. E. Phelps, and O. N. Witte, “Molecular imaging of lymphoid organs and immune activation using positron emission tomography with a new 18F-labeled 2′-deoxycytidine analog,” *Nat Med*, vol. 14, no. 7, pp. 783–788, Jul. 2008.

[112] C. J. Shu, D. O. Campbell, J. T. Lee, A. Q. Tran, J. C. Wengrod, O. N. Witte, M. E. Phelps, N. Satyamurthy, J. Czernin, and C. G. Radu, “Novel PET Probes Specific for Deoxycytidine Kinase,” *Journal of Nuclear Medicine*, vol. 51, no. 7, pp. 1092–1098, Jul. 2010.

[113] K. W. Pankiewicz, “Fluorinated nucleosides,” *Carbohydrate Research*, vol. 327, no. 1–2, pp. 87–105, Jul. 2000.

[114] Z. Li, H. Cai, and P. S. Conti, “Automated synthesis of 2′-deoxy-2′-[18F]fluoro-5-methyl-1-β-d-arabinofuranosyluracil ([18F]-FMAU) using a one reactor radiosynthesis module,” *Nucl. Med. Biol.*, vol. 38, no. 2, pp. 201–206, Feb. 2011.

[115] D. A. Armbruster, M. D. Tillman, and L. M. Hubbs, “Limit of detection (LQD)/limit of quantitation (LOQ): comparison of the empirical and the statistical methods exemplified with GC-MS assays of abused drugs.,” *Clinical Chemistry*, vol. 40, no. 7, pp. 1233–1238, Jul. 1994.

[116] M. Lazari, K. M. Quinn, S. B. Claggett, J. Collins, G. J. Shah, H. E. Herman, B. Maraglia, M. E. Phelps, M. D. Moore, and R. M. van Dam, “ELIXYS - a fully automated, three-reactor high-pressure radiosynthesizer for development and routine production of diverse PET tracers,” *EJNMMI Res*, vol. 3, no. 1, p. 52, Dec. 2013.

[117] J. Vindevogel and P. Sandra, “Simultaneous pH and ionic strength effects and buffer selection in capillary electrophoretic techniques,” *Journal of Chromatography A*, vol. 541, pp. 483–488, 1991.

[118] P. D. Grossman, Ed., *Capillary Electrophoresis: Theory and Practice*. Academic Press, 1992.

[119] S. Cheung, J. Ly, M. Lazari, S. Sadeghi, P. Y. Keng, and R. M. van Dam, “The separation and detection of PET tracers via capillary electrophoresis for chemical identity and purity analysis,” *Journal of Pharmaceutical and Biomedical Analysis*, vol. 94, pp. 12–18, Jun. 2014.

[120] Z. Chen and S. Ghosal, “Electromigration dispersion in Capillary Electrophoresis,” *Bull Math Biol*, vol. 74, no. 2, pp. 346–355, Feb. 2012.

[121] J. C. Hung, “Comparison of Various Requirements of the Quality Assurance Procedures for 18F-FDG Injection*,” *Journal of Nuclear Medicine*, vol. 43, no. 11, pp. 1495 –1506, Nov. 2002.

[122] B. H. Mock, W. Winkle, and M. T. Vavrek, “A color spot test for the detection of Kryptofix 2.2.2 in [18F]FDG preparations,” *Nuclear Medicine and Biology*, vol. 24, no. 2, pp. 193–195, Feb. 1997.

[123] D. A. Skoog, F. J. Holler, and T. A. Nieman, *Principles of instrumental analysis*. Saunders College Pub., 1998.

[124] W. Deng, X. Zhang, Z. Sun, J. Yin, Z. Zhou, L. Han, and S. Zhao, “HPLC-ELSD Determination of Kryptofix 2.2.2 in the Preparations of 2-Deoxy-2-[18F]fluoro-d-glucose and other Radiopharmaceuticals,” *Chromatographia*, vol. 75, no. 11–12, pp. 629–633, Jun. 2012.

[125] S. J. Oh, C. Mosdzianowski, D. Y. Chi, J. Y. Kim, S. H. Kang, J. S. Ryu, J. S. Yeo, and D. H. Moon, “Fully automated synthesis system of 3′-deoxy-3′-[18F]fluorothymidine,” *Nuclear Medicine and Biology*, vol. 31, no. 6, pp. 803–809, Aug. 2004.

[126] R. T. Kennedy, I. German, J. E. Thompson, and S. R. Witowski, “Fast analytical-scale separations by capillary electrophoresis and liquid chromatography,” *Chemical reviews*, vol. 99, no. 10, pp. 3081–3132, 1999.

[127] K. D. Altria, “Improved Performance in Capillary Electrophoresis using Internal Standards,” *LC-GC Europe*, vol. 15, no. 9, p. 588, Sep. 2002.

[128] G. . Wynia, G. Windhorst, P. . Post, and F. . Maris, “Development and validation of a capillary electrophoresis method within a pharmaceutical quality control environment and comparison with high-performance liquid chromatography,” *Journal of Chromatography A*, vol. 773, no. 1–2, pp. 339–350, Jun. 1997.

[129] A. E. Bruno, B. Krattiger, F. Maystre, and H. M. Widmer, “On-column laser-based refractive index detector for capillary electrophoresis,” *Analytical Chemistry*, vol. 63, no. 23, pp. 2689–2697, 1991.

[130] K. Swinney and D. J. Bornhop, “Detection in capillary electrophoresis,” *Electrophoresis*, vol. 21, no. 7, pp. 1239–1250, 2000.

[131] J. A. F. da Silva, C. L. do Lago, D. P. de Jesus, and W. K. T. Coltro, “Capacitively Coupled Contactless Conductivity Detection (C4D) Applied to Capillary Electrophoresis (CE) and Microchip Electrophoresis (MCE),” in *Capillary Electrophoresis and Microchip Capillary Electrophoresis*, C. D. García, K. Y. Chumbimuni-Torres, and E. Carrilho, Eds. John Wiley & Sons, Inc., 2013, pp. 145–160.

[132] P. Kubáň and P. C. Hauser, “Ten years of axial capacitively coupled contactless conductivity detection for CZE - a review,” *ELECTROPHORESIS*, vol. 30, no. 1, pp. 176–188, 2009.

[133] W. Lu and R. M. Cassidy, “Pulsed amperometric detection of carbohydrates separated by capillary electrophoresis,” *Analytical Chemistry*, vol. 65, no. 20, pp. 2878–2881, Oct. 1993.

[134] J. Fedorowski and W. R. LaCourse, “A review of pulsed electrochemical detection following liquid chromatography and capillary electrophoresis,” *Analytica chimica acta*, vol. 861, pp. 1–11, 2015.

[135] M. L. Marina, A. Ríos, and M. Valcárcel, *Analysis and Detection by Capillary Electrophoresis*. Newnes, 2005.

[136] T. Tsuda, J. V. Sweedler, and R. N. Zare, “Rectangular capillaries for capillary zone electrophoresis,” *Anal. Chem.*, vol. 62, no. 19, pp. 2149–2152, Oct. 1990.

[137] D. N. Heiger, P. Kaltenbach, and H.-J. P. Sievert, “Diode array detection in capillary electrophoresis,” *ELECTROPHORESIS*, vol. 15, no. 1, pp. 1234–1247, Jan. 1994.

[138] Y. Xue and E. S. Yeung, “Characterization of Band Broadening in Capillary Electrophoresis due to Nonuniform Capillary Geometries,” *Anal. Chem.*, vol. 66, no. 21, pp. 3575–3580, Nov. 1994.

[139] T. Wang, J. H. Aiken, C. W. Huie, and R. A. Hartwick, “Nanoliter-scale multireflection cell for absorption detection in capillary electrophoresis,” *Anal. Chem.*, vol. 63, no. 14, pp. 1372–1376, Jul. 1991.

[140] G. J. M. Bruin, G. Stegeman, A. C. Van Asten, X. Xu, J. C. Kraak, and H. Poppe, “Optimization and evaluation of the performance of arrangements for UV detection in high-resolution separations using fused-silica capillaries,” *Journal of Chromatography A*, vol. 559, no. 1–2, pp. 163–181, Oct. 1991.

[141] S. E. Moring, R. T. Reel, and R. E. J. van Soest, “Optical improvements of a Z-shaped cell for high-sensitivity UV absorbance detection in capillary electrophoresis,” *Anal. Chem.*, vol. 65, no. 23, pp. 3454–3459, Dec. 1993.

[142] A. Mainka and K. Bächmann, “UV detection of derivatized carbonyl compounds in rain samples in capillary electrophoresis using sample stacking and a Z-shaped

flow cell," *Journal of Chromatography A*, vol. 767, no. 1–2, pp. 241–247, Apr. 1997.

[143] K. W. Kim Suhyeon, "Extended path length post-column flow cell for UV-visible absorbance detection in capillary electrophoresis," *Journal of Chromatography A*, vol. 680, no. 1, pp. 109–116, 1994.

[144] "Enhanced UV-Visible Absorbance Detection in Capillary Electrophoresis Using Modified T-Shaped Post-Column Flow Cell," *Bulletin of the Korean Chemical Society*, vol. 23, no. 2, pp. 295–300, Feb. 2002.

[145] Ocean Optics, "PX2 Pulsed Xenon Lamp Stability." ocean optics, 08-Jul-2002.

[146] Ocean Optics, "DH-2000-BAL," *Ocean Optics*. [Online]. Available: http://oceanoptics.com/product/dh-2000-bal/. [Accessed: 28-Dec-2015].

[147] D. A. Skoog, F. J. Holler, and S. R. Crouch, *Principles of Instrumental Analysis*. Thomson Brooks/Cole, 2007.

[148] K. Ramni, K. Navneet, U. Ashutosh, S. O. P, and T. Arti, "High Performance Liquid Chromatography Detectors – A Review," 2011.

[149] C. M. Rushworth, J. Davies, J. T. Cabral, P. R. Dolan, J. M. Smith, and C. Vallance, "Cavity-enhanced optical methods for online microfluidic analysis," *Chemical Physics Letters*, vol. 554, pp. 1–14, Dec. 2012.

[150] A. Manz, N. Graber, and H. M. Widmer, "Miniaturized total chemical analysis systems: A novel concept for chemical sensing," *Sensors and Actuators B: Chemical*, vol. 1, no. 1–6, pp. 244–248, Jan. 1990.

[151] B. Graß, A. Neyer, M. Jöhnck, D. Siepe, F. Eisenbeiß, G. Weber, and R. Hergenröder, "A new PMMA-microchip device for isotachophoresis with integrated conductivity detector," *Sensors and Actuators B: Chemical*, vol. 72, no. 3, pp. 249–258, Feb. 2001.

[152] A. Ríos, A. Escarpa, M. C. González, and A. G. Crevillén, “Challenges of analytical microsystems,” *TrAC Trends in Analytical Chemistry*, vol. 25, no. 5, pp. 467–479, May 2006.

[153] S. Ahuja and M. Jimidar, *Capillary Electrophoresis Methods for Pharmaceutical Analysis*. Elsevier, 2011.

[154] K. Sueyoshi, F. Kitagawa, and K. Otsuka, “Recent progress of online sample preconcentration techniques in microchip electrophoresis,” *J. Sep. Science*, vol. 31, no. 14, pp. 2650–2666, Aug. 2008.

[155] R. T. Kelly, C. Wang, S. J. Rausch, C. S. Lee, and K. Tang, “Pneumatic Microvalve-Based Hydrodynamic Sample Injection for High-Throughput, Quantitative Zone Electrophoresis in Capillaries,” *Anal. Chem.*, vol. 86, no. 13, pp. 6723–6729, 2014.

[156] E. Kim, Y. Xia, and G. M. Whitesides, “Polymer microstructures formed by moulding in capillaries,” *Nature*, vol. 376, no. 6541, pp. 581–584, Aug. 1995.

[157] Z. Liang, N. Chiem, G. Ocvirk, T. Tang, K. Fluri, and D. J. Harrison, “Microfabrication of a planar absorbance and fluorescence cell for integrated capillary electrophoresis devices,” *Analytical Chemistry*, vol. 68, no. 6, pp. 1040–1046, 1996.

[158] G. Jiang, S. Attiya, G. Ocvirk, W. E. Lee, and D. J. Harrison, “Red diode laser induced fluorescence detection with a confocal microscope on a microchip for capillary electrophoresis,” *Biosensors and Bioelectronics*, vol. 14, no. 10–11, pp. 861–869, Jan. 2000.

[159] M. Vaculovičová, M. Akther, P. Maaskant, D. Brabazon, and M. Macka, “Fibre coupled micro-light emitting diode array light source with integrated band-pass filter for fluorescence detection in miniaturised analytical systems,” *Analytica Chimica Acta*, vol. 871, pp. 85–92, Apr. 2015.

[160] T. Endo, K. Yamamoto, K. Sueyoshi, and H. Hisamoto, “Development of Microchip Electrophoresis-Integrated Nanoimprinted Photonic Crystal,” *Sensors and Materials*, vol. 27, no. 5, pp. 425–433, 2015.

[161] D. C. Duffy, J. C. McDonald, O. J. A. Schueller, and G. M. Whitesides, “Rapid Prototyping of Microfluidic Systems in Poly(dimethylsiloxane),” *Anal. Chem.*, vol. 70, no. 23, pp. 4974–4984, Dec. 1998.

[162] B. Ma, X. Zhou, G. Wang, Z. Dai, J. Qin, and B. Lin, “A hybrid microdevice with a thin PDMS membrane on the detection window for UV absorbance detection,” *ELECTROPHORESIS*, vol. 28, no. 14, pp. 2474–2477, Jul. 2007.

[163] Momentive, “Momentive RTV615 Data sheet.” Momentive.

[164] X. Huang, M. J. Gordon, and R. N. Zare, “Bias in quantitative capillary zone electrophoresis caused by electrokinetic sample injection,” *Anal. Chem.*, vol. 60, no. 4, pp. 375–377, Feb. 1988.

[165] P. Kuban, K. Tennberg, R. Tryzell, and B. Karlberg, “Calibration principles for flow injection analysis–capillary electrophoresis systems with electrokinetic injection,” *Journal of Chromatography A*, vol. 808, no. 1–2, pp. 219–227, May 1998.

[166] E. V. Dose and G. A. Guiochon, “Internal standardization technique for capillary zone electrophoresis,” *Anal. Chem.*, vol. 63, no. 11, pp. 1154–1158, Jun. 1991.

[167] C.-C. Lin, C.-C. Chen, C.-E. Lin, and S.-H. Chen, “Microchip electrophoresis with hydrodynamic injection and waste-removing function for quantitative analysis,” *Journal of Chromatography A*, vol. 1051, no. 1–2, pp. 69–74, Oct. 2004.

[168] Y. Luo, D. Wu, S. Zeng, H. Gai, Z. Long, Z. Shen, Z. Dai, J. Qin, and B. Lin, “Double-Cross Hydrostatic Pressure Sample Injection for Chip CE: Variable Sample Plug Volume and Minimum Number of Electrodes,” *Anal. Chem.*, vol. 78, no. 17, pp. 6074–6080, Sep. 2006.

[169] A. Gáspár, P. I. Koczka, H. Carmona, and F. A. Gomez, “Split injection: A simple introduction of subnanoliter sample volumes for chip electrophoresis,” *Microchemical Journal*, vol. 99, no. 2, pp. 180–185, Nov. 2011.

[170] M. A. Unger, H.-P. Chou, T. Thorsen, A. Scherer, and S. R. Quake, “Monolithic Microfabricated Valves and Pumps by Multilayer Soft Lithography,” *Science*, vol. 288, no. 5463, pp. 113–116, Apr. 2000.

[171] V. Studer, G. Hang, A. Pandolfi, M. Ortiz, W. F. Anderson, and S. R. Quake, “Scaling properties of a low-actuation pressure microfluidic valve,” *Journal of Applied Physics*, vol. 95, no. 1, pp. 393–398, Jan. 2004.

[172] A. L. Bowen and R. S. Martin, “Integration of on-chip peristaltic pumps and injection valves with microchip electrophoresis and electrochemical detection,” *Electrophoresis*, vol. 31, no. 15, pp. 2534–2540, Aug. 2010.

[173] C. Cianciulli and H. Wätzig, “Analytical instrument qualification in capillary electrophoresis,” *Electrophoresis*, vol. 33, no. 11, pp. 1499–1508, Jun. 2012.

[174] M. A. Unger, H.-P. Chou, T. Thorsen, A. Scherer, and S. R. Quake, “Monolithic Microfabricated Valves and Pumps by Multilayer Soft Lithography,” *Science*, vol. 288, no. 5463, pp. 113–116, Apr. 2000.

[175] I. Hoek, F. Tho, and W. M. Arnold, “Sodium hydroxide treatment of PDMS based microfluidic devices,” *Lab on a Chip*, vol. 10, no. 17, p. 2283, 2010.

[176] T. Thorsen, S. J. Maerkl, and S. R. Quake, “Microfluidic Large-Scale Integration,” *Science*, vol. 298, no. 5593, pp. 580–584, Oct. 2002.

[177] N. H. Bings, C. Wang, C. D. Skinner, C. L. Colyer, P. Thibault, and D. J. Harrison, “Microfluidic devices connected to fused-silica capillaries with minimal dead volume,” *Analytical chemistry*, vol. 71, no. 15, pp. 3292–3296, 1999.

[178] C.-H. Chiou and G.-B. Lee, “Minimal dead-volume connectors for microfluidics using PDMS casting techniques,” *Journal of Micromechanics and Microengineering*, vol. 14, no. 11, p. 1484, 2004.

[179] I.-J. Chen and E. Lindner, “The Stability of Radio-Frequency Plasma-Treated Polydimethylsiloxane Surfaces,” *Langmuir*, vol. 23, no. 6, pp. 3118–3122, Mar. 2007.

[180] D. Belder, A. Deege, H. Husmann, F. Kohler, and M. Ludwig, “Cross-linked poly(vinyl alcohol) as permanent hydrophilic column coating for capillary

electrophoresis," *ELECTROPHORESIS*, vol. 22, no. 17, pp. 3813–3818, Sep. 2001.

[181] L. Gitlin, P. Schulze, S. Ohla, H.-J. Bongard, and D. Belder, "Surface modification of PDMS microfluidic devices by controlled sulfuric acid treatment and the application in chip electrophoresis," *Electrophoresis*, Sep. 2014.

[182] A. Fatona, Y. Chen, M. Reid, M. A. Brook, and J. M. Moran-Mirabal, "One-step in-mould modification of PDMS surfaces and its application in the fabrication of self-driven microfluidic channels," *Lab Chip*, vol. 15, no. 22, pp. 4322–4330, 2015.

[183] J. Kim, M. K. Chaudhury, M. J. Owen, and T. Orbeck, "The Mechanisms of Hydrophobic Recovery of Polydimethylsiloxane Elastomers Exposed to Partial Electrical Discharges," *Journal of Colloid and Interface Science*, vol. 244, no. 1, pp. 200–207, Dec. 2001.

[184] N. A. Lacher, N. F. de Rooij, E. Verpoorte, and S. M. Lunte, "Comparison of the performance characteristics of poly(dimethylsiloxane) and Pyrex microchip electrophoresis devices for peptide separations," *Journal of Chromatography A*, vol. 1004, no. 1–2, pp. 225–235, Jul. 2003.

[185] G. Ocvirk, M. Munroe, T. Tang, R. Oleschuk, K. Westra, and D. J. Harrison, "Electrokinetic control of fluid flow in native poly(dimethylsiloxane) capillary electrophoresis devices," *Electrophoresis*, vol. 21, no. 1, pp. 107–115, Jan. 2000.

[186] V. Dolník, S. Liu, and S. Jovanovich, "Capillary electrophoresis on microchip," *ELECTROPHORESIS*, vol. 21, no. 1, pp. 41–54, 2000.

[187] Y. Chen and A. Pépin, "Nanofabrication: Conventional and nonconventional methods," *ELECTROPHORESIS*, vol. 22, no. 2, pp. 187–207, Jan. 2001.

[188] W. K. T. Coltro, S. M. Lunte, and E. Carrilho, "Comparison of the analytical performance of electrophoresis microchannels fabricated in PDMS, glass, and polyester-toner," *Electrophoresis*, vol. 29, no. 24, pp. 4928–4937, Dec. 2008.

[189] H. Nakanishi, T. Nishimoto, N. Nakamura, S. Nagamachi, A. Arai, Y. Iwata, and Y. Mito, "Fabrication of electrophoresis devices on quartz and glass substrates using

a bonding with HF solution," in *, Tenth Annual International Workshop on Micro Electro Mechanical Systems, 1997. MEMS '97, Proceedings, IEEE*, 1997, pp. 299–304.

[190] B. Renberg, K. Sato, T. Tsukahara, K. Mawatari, and T. Kitamori, "Hands on: thermal bonding of nano-and microfluidic chips," *Microchimica Acta*, vol. 166, no. 1–2, pp. 177–181, 2009.

[191] L. Chen, G. Luo, K. Liu, J. Ma, B. Yao, Y. Yan, and Y. Wang, "Bonding of glass-based microfluidic chips at low- or room-temperature in routine laboratory," *Sensors and Actuators B: Chemical*, vol. 119, no. 1, pp. 335–344, Nov. 2006.

[192] Z.-J. Jia, Q. Fang, and Z.-L. Fang, "Bonding of glass microfluidic chips at room temperatures," *Analytical chemistry*, vol. 76, no. 18, pp. 5597–5602, 2004.

[193] I. K. Dimov, A. Riaz, J. Ducrée, and L. P. Lee, "Hybrid integrated PDMS microfluidics with a silica capillary," *Lab on a Chip*, vol. 10, no. 11, p. 1468, 2010.

[194] P. I. Koczka and A. Gaspar, "Application of a capillary-assembled microfluidic system for separation of cephalosporins," *ELECTROPHORESIS*, vol. 35, no. 17, pp. 2534–2537, Sep. 2014.

[195] A. C. E. Bidulock, A. van den Berg, and J. C. T. Eijkel, "Improving chip-to-chip precision in disposable microchip capillary electrophoresis devices with internal standards," *ELECTROPHORESIS*, vol. 36, no. 6, pp. 875–883, Mar. 2015.

[196] B. M. Paegel, L. D. Hutt, P. C. Simpson, and R. A. Mathies, "Turn Geometry for Minimizing Band Broadening in Microfabricated Capillary Electrophoresis Channels," *Analytical Chemistry*, vol. 72, no. 14, pp. 3030–3037, Jul. 2000.

[197] A. R. Abate, D. Lee, C. Holtze, A. Krummel, and W. D. Do T, "Functionalized glass coating for PDMS microfluidic devices," *Lab-on-a-Chip Technology: Fabrication and Microfluidics, Caister Academic Press*, 2009.

[198] Y. Liu, J. C. Fanguy, J. M. Bledsoe, and C. S. Henry, "Dynamic Coating Using Polyelectrolyte Multilayers for Chemical Control of Electroosmotic Flow in

Capillary Electrophoresis Microchips," *Anal. Chem.*, vol. 72, no. 24, pp. 5939–5944, 2000.

[199] Council of Europe, "2.2.47. Capillary Electrophoresis," *European Pharmacopoeia*. pp. 74–79, Jan-2005.

[200] J. C. Giddings, "Generation of Variance, 'Theoretical Plates,' Resolution, and Peak Capacity in Electrophoresis and Sedimentation," *Separation Science*, vol. 4, no. 3, pp. 181–189, Jun. 1969.

[201] S. C. Jacobson, R. Hergenroder, L. B. Koutny, R. J. Warmack, and J. M. Ramsey, "Effects of Injection Schemes and Column Geometry on the Performance of Microchip Electrophoresis Devices," *Anal. Chem.*, vol. 66, no. 7, pp. 1107–1113, 1994.

[202] M. F. DeLaMarre and S. A. Shippy, "Development of a simplified microfluidic injector for analysis of droplet content via capillary electrophoresis," *Analytical chemistry*, vol. 86, no. 20, pp. 10193–10200, 2014.

[203] I. K. Dimov, A. Riaz, J. Ducrée, and L. P. Lee, "Hybrid integrated platform of PDMS microfluidics and Silica Capillary for effective CE and ESI-MS coupling," in *Solid-State Sensors, Actuators and Microsystems Conference, 2009. TRANSDUCERS 2009. International*, 2009, pp. 1281–1284.

[204] W.-Y. Tseng, J. S. Cho, A. Chatziioannou, and R. M. van Dam, "Interdigitated evaporation chip for efficient solvent exchange in microchannels," in *Proceedings of the 16th International Conference on Miniaturized Systems for Chemistry and Life Sciences*, Okinawa, Japan, 2012, pp. 2008–2010.

[205] J. K. Towns and F. E. Regnier, "Impact of polycation adsorption on efficiency and electroosmotically driven transport in capillary electrophoresis," *Analytical Chemistry*, vol. 64, no. 21, pp. 2473–2478, 1992.

[206] M. Schulze and D. Belder, "Poly(ethylene glycol)-coated microfluidic devices for chip electrophoresis," *ELECTROPHORESIS*, vol. 33, no. 2, pp. 370–378, Jan. 2012.

[207] R. Zeng, Z. Luo, D. Zhou, F. Cao, and Y. Wang, “A novel PEG coating immobilized onto capillary through polydopamine coating for separation of proteins in CE,” *ELECTROPHORESIS*, vol. 31, no. 19, pp. 3334–3341, Oct. 2010.